



The  
University  
Of  
Sheffield.

**Microstructure Development of Complex Phase Steels During  
Thermomechanical Processing**

**By:**

Luis Fernando Romano Acosta

A thesis submitted in partial fulfilment of the requirements for the degree of  
Doctor of Philosophy

The University of Sheffield  
Faculty of Engineering  
Department of Materials Science and Engineering

November 2020

Sheffield, United Kingdom

# ACKNOWLEDGEMENTS

I would like to acknowledge to CONACYT (Mexican National Council of Science and Technology) and the Roberto Rocca education program for the financial support provided to carry out this project. I would also wish to acknowledge to Ternium Mexico SA de CV for providing the material and the valuable discussions on this research.

Moreover, my sincere thanks go to my supervisor, Prof. Eric Palmiere, for giving me the chance to join his research team at the University of Sheffield to receive an outstanding academic career. I will always be in debt with him for his strong support, guidance and advice through all process to pursue my PhD degree.

I would also like to express my gratitude to the members of the department of materials science and engineering and its professional staff for their time dedicated to help and train me in the labs. Special thanks are given to Dean Haylock for all his support and camaraderie in the thermomechanical lab. I am very grateful to Neil Hind, Tes Monaghan, Le Ma, Cheryl Shaw, Colm O'Regan, John Nutter, Dawn Bussey and all who taught, advised or helped me in some way to fulfil this work.

I feel blessed for having met amazing colleagues and friends in the department during my time in Sheffield. I would like to express my thanks to Bhushan Rakshe, Eduardo Pineda, Marta Muniz, Piyanut Muangtong, Carlos Brambila, Daniel Olguin, Karol Rodriguez, and the others for their continuous support, mentoring and endlessly scientific and social talks.

Thanks to my immediate family who have always motivated and encouraged me and to whom I dedicate this thesis. Thanks to my mother, Rosy Acosta, for all her love, wisdom and values instilled from young and for everything she has done for me. To my sister, Rosy Garcia; my niece, Andrea Rangel and my granny, Consuelo. Their unconditional support is my source to achieve my goals.

Last but not least, I wish to record my deepest appreciation for my partner Diana Paez, a loyal friend who persistently support me throughout the full period. I will always be thankful to her for having believed in me. This work is also dedicated to her.

# Table of Contents

ACKNOWLEDGEMENTS .....	I
List of Figures .....	VI
List of Tables .....	XII
CHAPTER 1 ABSTRACT .....	1
CHAPTER 2 INTRODUCTION .....	3
2.1. Statement of Objectives .....	5
CHAPTER 3 BACKGROUND .....	7
3.1. Advanced High Strength Steels (AHSS).....	7
3.1.1. Complex Phase (CP) steels.....	11
3.1.2. Challenge of CP steels today .....	17
3.2. Thermomechanical Processing (TMP).....	17
3.2.1. Prior Austenite Grain.....	20
3.2.2. Deformation: strain, temperature and strain rate .....	21
3.2.3. Controlled cooling .....	24
3.3. Restoration mechanisms on microstructural evolution .....	26
3.3.1. Recovery .....	28
3.3.2. Recrystallization .....	29
3.3.3. Grain growth.....	32
3.4. Summary .....	32
CHAPTER 4 EXPERIMENTAL PROCEDURE.....	34
4.1. As-received material: Phases and Microstructure Characterization .....	34
4.1.1. Quantitative Metallography.....	35
4.1.2. X-Ray Diffraction.....	41

4.2. Critical Processing Temperatures.....	42
4.2.1. Thermodynamic Analysis.....	43
4.2.2. Determination of Phase Transformation Temperatures.....	43
4.2.3. Recrystallization-Stop Temperature ( $T_{5\%}$ ) .....	48
4.3. Hot Rolling Simulation .....	55
4.3.1. Plane Strain Compression (PSC) Testing.....	56
4.4. Characterization after PSC Testing.....	59
4.4.1. Microstructure Evolution through TMP .....	60
4.4.2. Analysis of Crystallographic texture and deformation by Electron Backscattered Diffraction (EBSD).....	61
4.4.3. Evaluation of Mechanical Properties.....	61
CHAPTER 5 RESULTS .....	66
5.1. Initial Characterization.....	66
5.2. Phase Transformation Temperatures.....	70
5.3. Recrystallization-Stop Temperature ( $T_{5\%}$ ).....	74
5.3.1. Flow Stress of Double and Single Hit Tests.....	75
5.3.2. Fraction Softening calculations .....	78
5.3.3. Microstructure evaluation of Double and Single Hit Tests .....	80
5.4. Hot Rolling Simulation .....	84
5.4.1. Microstructure Evolution of Deformed Austenite.....	85
5.4.2. Finishing Rolling + Runout table simulation .....	87
5.5. Identification and Quantification of Transformation Products .....	91
5.6. Mechanical properties evaluation.....	104
CHAPTER 6 DISCUSSION.....	109
6.1. Effect of Prior Austenite Grain on Final Product.....	109
6.1.1. Defining $T_{5\%}$ .....	110



6.1.2. Precipitation vs Recrystallization .....	114
6.2. Designing a Thermomechanical Schedule for CP800.....	119
6.2.1. Effect of TMP parameters on microstructure evolution.....	123
6.3. Comparison of Laboratory simulation vs Industrial TMP Schedule.....	132
CHAPTER 7 CONCLUSIONS .....	137
CHAPTER 8 FUTURE WORK .....	140
CHAPTER 9 REFERENCES .....	142
APPENDIX I Microstructures by Electron Microscopy .....	163
AI.1. SC1.....	164
AI.1a. SC1 Secondary electrons .....	164
AI.2 SC2.....	165
AI.2a. SC2 Secondary electrons .....	165
AI.2b. SC2 TEM thin foil.....	166
AI.3 SC3.....	168
AI.3a. SC3 Secondary electrons .....	168
AI.3b. SC3 TEM thin foil.....	169
AI.4 SC4.....	170
AI.4a. SC4 Secondary electrons .....	170
AI.4b. SC4 TEM thin foil.....	171
AI.5. SC5.....	172
AI.5a. SC5 Secondary electrons .....	172
AI.5b. SC5 TEM thin foil.....	173
AI.6 Quench.....	174
AI.6a. Quench Secondary electrons .....	174
AI.6b. Quench TEM thin foil .....	175
APPENDIX II Electron Backscattered Diffraction Mapping .....	176

AII.1 EBSD maps from SC1 ..... 177  
AII.2 EBSD maps from SC2 ..... 179  
AII.3 EBSD maps from SC3 ..... 181  
AII.4 EBSD maps from SC4 ..... 184  
AII.5 EBSD maps from SC5 ..... 186  
AII.6 EBSD maps from Quench after the fourth pass ..... 188

# List of Figures

FIGURE 3.1 GLOBAL FORMABILITY DIAGRAM FOR AHSS GRADES [10].....	7
FIGURE 3.2 FUTURE STEEL VEHICLE MATERIAL USAGE [15].....	9
FIGURE 3.3 STRESS VS ELONGATION DIAGRAM FOR DIFFERENT STEEL TYPES AND THEIR APPLICATIONS ON BODY CAR STRUCTURE [15].....	10
FIGURE 3.4 A) SCHEMATIC CP STEEL MICROSTRUCTURE [15] B) MICROSTRUCTURE OF A CP STEEL WITH A BAINITE/MARTENSITE MATRIX [25].....	12
FIGURE 3.5 ENGINEERING FLOW STRESS CURVES FOR DIFFERENT CP STEEL GRADES AND A CONVENTIONAL STEEL [24].....	13
FIGURE 3.6 THE INCREASE IN $T_{5\%}$ TEMPERATURE WITH AN INCREASE IN THE LEVEL OF MICROALLOYING SOLUTES IN A 0.07C, 1.40MN, 0.25SI STEEL [33].....	16
FIGURE 3.7 HOT ROLLING PROCESSING OF STEEL SLABS [40] .....	19
FIGURE 3.8 THREE STAGES OF THE CONTROLLED ROLLING PROCESS AND THE CHANGE IN MICROSTRUCTURE [63] .....	23
FIGURE 3.9 CCT DIAGRAM INDICATING THE RANGES OF COOLING RATES FOR PRODUCING DIFFERENT MICROSTRUCTURES. M = MARTENSITE; B = BAINITE; F = FERRITE; P = PEARLITE [10].....	25
FIGURE 3.10 SCHEMATIC DIAGRAM OF THE RESTORATION MECHANISM FROM DEFORMED METAL. A) DEFORMED STATE, B) RECOVERED, C) PARTIALLY RECRYSTALLIZED, D) FULLY RECRYSTALLIZED, E) GRAIN GROWTH AND F) ABNORMAL GRAIN GROWTH [60].....	27
FIGURE 3.11 STAGES OF MICROSTRUCTURE EVOLUTION DURING THE RECOVERY PROCESS [60] ....	28
FIGURE 3.12 THE CHARACTERISTICS OF FLOW STRESS AND MICROSTRUCTURAL CHANGES WHEN DYNAMIC RECOVERY IS THE ONLY RESTORATION MECHANISM [90].....	29
FIGURE 3.13 A SCHEMATIC DIAGRAM OF THE RECRYSTALLIZATION PROCESS. DOTTED LINES REPRESENT PREVIOUS GRAIN BOUNDARIES AND THE SOLID LINES ARE THE NEW RECRYSTALLIZED GRAINS [60].....	30
FIGURE 3.14 SCHEMATIC DIAGRAMS OF FLOW STRESS A) DUE TO DIFFERENT METALLURGICAL PHENOMENA. B) MICROSTRUCTURE EVOLUTION THROUGH DEFORMATION DEPENDING ON THE PROCESSING PARAMETERS [33, 91] .....	31

FIGURE 4.1 SECTIONED AS-RECEIVED CP800 TRANSFER BAR. ....	35
FIGURE 4.2 SATURATED PICRIC ACID SOLUTION. BEFORE (LEFT) AND AFTER (RIGHT) MATURING..	37
FIGURE 4.3 SCHEMATIC CONFIGURATION OF HEATING METHODS FOR CLASSICAL DILATOMETRY TESTING USING A) INDUCTION HEATING AND B) RESISTANCE HEATING [112] .....	44
FIGURE 4.4 DILATOMETER USED TO MEASURE THE LENGTH CHANGE OF THE SAMPLES.....	45
FIGURE 4.5 DILATOMETER SAMPLE OF CP800 AFTER MACHINING. LENGTH IS PARALLEL TO THE ROLLING DIRECTION. THE SCALE SHOWN IS IN MM .....	45
FIGURE 4.6 SCHEMATIC HEAT TREATMENT FOR DILATOMETER TESTS.....	46
FIGURE 4.7 DILATOMETRY CURVE FOR A MICROALLOYED STEEL OBTAINED THROUGH THERMOMECHANICAL SIMULATOR GLEEBLE 3800 [114] .....	47
FIGURE 4.8 THERMOMECHANICAL ROUTE OF THE DOUBLE HIT TESTS .....	50
FIGURE 4.9 THERMOMECHANICAL COMPRESSION MACHINE FOR PLANE STRAIN COMPRESSION (PSC TEST).....	51
FIGURE 4.10 GEOMETRY OF THE PSC SAMPLES .....	52
FIGURE 4.11 PSC METALLOGRAPHY TO MEASURE THE RECRYSTALLIZED FRACTION BY POINT COUNT METHOD. METALLOGRAPHY SHOWING 50% OF AUSTENITE RECRYSTALLIZED AREA..	55
FIGURE 4.12 REPRESENTATIVE DIAGRAM OF PLANE STRAIN COMPRESSION TESTING. ....	56
FIGURE 4.13 SCHEMATIC TMP ROUTE FOR CP800. COLOURED LINES REPRESENT WATER QUENCH SPECIMENS FOR THE EVALUATION OF AUSTENITE MICROSTRUCTURE EVOLUTION .....	58
FIGURE 4.14 THE THREE PLANES IN A ROLLED PRODUCT. ROLLING DIRECTION IS INDICATED WITH THE DOUBLE-SIDED ARROW. PSC SPECIMEN AFTER DEFORMATION AND ALL SECTIONING STEPS TO MOUNT THE LONGITUDINAL FACE INDICATED BY THE RED ARROW. BAR SCALES ARE IN MM. .....	59
FIGURE 4.15 TENSION MACHINE ZWICK ROELL Z050 .....	64
FIGURE 4.16 TENSILE SPECIMEN FROM PSC SPECIMEN BEFORE AND AFTER THE TENSILE TEST. PINS ARE ATTACHED AT THE CENTRE FOR EXTENSION MEASUREMENTS. SCALE BAR IS IN CENTIMETRES.....	65
FIGURE 5.1 AS-RECEIVED CP800 TRANSFER BAR MICROSTRUCTURE. ETCHANT: 2% NITAL.....	67
FIGURE 5.2 PAGB OF CP800 AS-RECEIVED TRANSFER BAR. PAGS = $46 \pm 5.7$ MM. ETCHANT: AQUEOUS PICRIC ACID SOLUTION.....	67

FIGURE 5.3 SEM IMAGES OF THE AS-RECEIVED CP800 TRANSFER BAR. BACKSCATTERED ELECTRONS (LEFT) AND SECONDARY ELECTRONS (RIGHT). .....	68
FIGURE 5.4 TEM BRIGHT FIELD IMAGE OF LATH MARTENSITE OF THE AS-RECEIVED CP800 TRANSFER BAR. ....	69
FIGURE 5.5 X-RAY DIFFRACTION PATTERN OF THE AS-RECEIVED CP800 TRANSFER BAR.....	69
FIGURE 5.6 PHASE TRANSFORMATION MEASURED BY DILATOMETRY FOR CP800 COOLED AT 10 °C/s. ....	72
FIGURE 5.7 THERMODYNAMIC EQUILIBRIUM DIAGRAMS CALCULATED BY A) JMatPRO AND B) THERMOCALC FOR CP800 CHEMICAL COMPOSITION.....	73
FIGURE 5.8 CONTINUOUS COOLING TRANSFORMATION DIAGRAM FROM JMatPRO® FOR THE CP800. AUSTENITISATION TEMPERATURE: 1000 °C, PAGES: 45 MM. RED ASTERISKS REPRESENT ACTUAL DILATOMETRY MEASUREMENTS.....	74
FIGURE 5.9 FLOW STRESS CURVES OF SINGLE AND DOUBLE HIT TESTS AT 920 °C, 950 °C, 980 °C AND 1000 °C. DEFORMATION PARAMETERS OF SET 1: TOTAL STRAIN 0.5, INTERPASS TIME 20 s, STRAIN RATE 10 s <sup>-1</sup> .....	76
FIGURE 5.10 FLOW STRESS CURVES OF SINGLE AND DOUBLE HIT TESTS AT 980°C, 1000°C AND 1020°C. DEFORMATION PARAMETERS OF SET 2: TOTAL STRAIN 0.5, INTERPASS TIME 4 s, STRAIN RATE 10 s <sup>-1</sup> .....	77
FIGURE 5.11 FLOW STRESS CURVES OF DOUBLE HIT TESTS AT 950°C AND 980°C. DEFORMATION PARAMETERS OF SET 3: TOTAL STRAIN 0.8, INTERPASS TIME 4 s, STRAIN RATE 10 s <sup>-1</sup> .....	78
FIGURE 5.12 SOFTENING % OF DOUBLE HIT TESTS AT DIFFERENT DEFORMATION TEMPERATURES. SET 1: E=0.25; INTERPASS TIME = 20 s. SET 2: E=0.25; INTERPASS TIME = 4 s. SET 3: E=0.40; INTERPASS TIME = 4 s .....	79
FIGURE 5.13 PRIOR AUSTENITE GRAIN BOUNDARIES OF SINGLE AND DOUBLE HIT DEFORMED SPECIMENS AT DIFFERENT TEMPERATURES. DEFORMATION PARAMETERS OF SET 1: TOTAL STRAIN 0.5, INTERPASS TIME 20 s, STRAIN RATE 10 s <sup>-1</sup> .....	81
FIGURE 5.14 PRIOR AUSTENITE GRAIN BOUNDARIES OF DOUBLE HIT TESTS AT DIFFERENT TEMPERATURES. DEFORMATION PARAMETERS OF SET 2: TOTAL STRAIN 0.5, INTERPASS TIME 4 s, STRAIN RATE 10 s <sup>-1</sup> .....	82

FIGURE 5.15 PRIOR AUSTENITE GRAIN BOUNDARIES OF SINGLE AND DOUBLE HIT TESTS AT DIFFERENT TEMPERATURES. DEFORMATION PARAMETERS OF SET 3: STRAIN PER PASS 0.4, INTERPASS TIME 4 s, STRAIN RATE $10\text{ s}^{-1}$ .....	82
FIGURE 5.16 FLOW STRESS CURVES AND MICROSTRUCTURE EVOLUTION OF AUSTENITE DURING TMP .....	87
FIGURE 5.17 FLOW STRESS AND CORRESPONDING MICROSTRUCTURE OF SPECIMENS THAT FOLLOW THE FULL TMP SCHEDULE WITH CONTROLLED COOLING .....	90
FIGURE 5.18 SEM SE MICROGRAPHS OF SPECIMENS AFTER FULL TMP SCHEDULE AND CONTROLLED COOLING .....	92
FIGURE 5.19 TEM IMAGES OF SC2 .....	93
FIGURE 5.20 TEM IMAGES OF SC3 .....	94
FIGURE 5.21 TEM IMAGES OF SC4 .....	95
FIGURE 5.22 TEM IMAGES OF SC5 .....	96
FIGURE 5.23 A) BC MAP, $GB = 5^\circ$ AND B) BS MAP OF SC3 AND THEIR DISTRIBUTION OF PIXELS ...	98
FIGURE 5.24 GRAIN AVERAGED BAND CONTRAST MAP OF SC3. $GB = 5^\circ$ AND ITS DISTRIBUTION..	99
FIGURE 5.25 GRAIN ORIENTATION SPREAD MAP OF SC3 AND ITS DISTRIBUTION HISTOGRAM .....	100
FIGURE 5.26 GRAIN BOUNDARIES MISORIENTATION MAP OF SC3 AND THE MISORIENTATION DISTRIBUTION. BLACK LINES REPRESENT MISORIENTATION HIGHER THAN $5^\circ$ AND BLUE LINES FROM $2^\circ$ TO $5^\circ$ .....	101
FIGURE 5.27 INVERSE POLE FIGURE MAP OF SC3 AND THE ORIENTATION CODE .....	102
FIGURE 5.28 MAPS OF PHASES SEGMENTATION OF A) QUENCH AFTER 4 <sup>TH</sup> PASS, B) SC1, C) SC2, D) SC3, E) SC4 AND F) SC5. COLOUR REPRESENTATION: RED = RETAINED AUSTENITE, BLACK = MARTENSITE, BLUE = BAINITIC FERRITE AND YELLOW = POLYGONAL FERRITE.....	103
FIGURE 5.29 SEM SE IMAGE OF SC3 SHOWING THE INDENTATION LEFT FOR THE VICKERS HARDNESS MEASUREMENT .....	104
FIGURE 5.30 AFM IMAGE OF SC3 ALONG WITH THE NANOHARDNESS MEASUREMENTS FOR DIFFERENT FEATURES IN MICROSTRUCTURE .....	105
FIGURE 5.31 AFM IMAGE OF SC5 ALONG WITH THE NANOHARDNESS MEASUREMENTS FOR DIFFERENT FEATURES IN MICROSTRUCTURE.....	106

FIGURE 5.32 TENSILE ENGINEERING FLOW STRESS AT ROOM TEMPERATURE OF SPECIMENS WITH FULL TMP SCHEDULE .....	107
FIGURE 6.1 SOFTENING PERCENTAGE CALCULATED BY METHOD C FOR THE 3 SETS OF DOUBLE HIT TESTS. $T_{5\%}$ AND $T_{95\%}$ ARE REPRESENTED AS 20 AND 60% SOFTENING .....	112
FIGURE 6.2 TEMPERATURE GRADIENT BETWEEN $T_{5\%}$ AND $T_{95\%}$ AS A FUNCTION OF STRAIN PER PASS [120] .....	113
FIGURE 6.3 PRECIPITATION START TIME-TEMPERATURE CURVES FOR DIFFERENT AMOUNTS OF STRAIN FROM 0.20 TO 0.80 .....	115
FIGURE 6.4 RECRYSTALLIZATION TIME-TEMPERATURE CURVES FOR A) START 5% OF RECRYSTALLIZATION AND B) COMPLETE 95% OF RECRYSTALLIZATION VARYING THE AMOUNT OF STRAIN FROM 0.20 TO 0.80 .....	116
FIGURE 6.5 INTERACTION OF THE PRECIPITATION-RECRYSTALLIZATION CURVES CALCULATED BY THE MODEL FOR A) SET 1&2 $E=0.25$ , B) $E=0.30$ AND C) SET 3 $E=0.40$ .....	117
FIGURE 6.6 MODELLED $T_{5\%}$ AND $T_{95\%}$ AS A FUNCTION OF STRAIN FOR THE CP COMPOSITION .....	118
FIGURE 6.7 CCT DIAGRAM FROM JMatPro® FOR CP STEEL USING THE CONDITIONS AFTER THE LAST PASS OF THE TMP SCHEDULE. AUSTENITISATION TEMPERATURE: 850°C, PAGES: 3 $\mu\text{M}$ .....	122
FIGURE 6.8 SCHEMATIC AUSTENITE MICROSTRUCTURES AS A FUNCTION OF THE PROCESSING PARAMETERS SUCH AS DEFORMATION TEMPERATURE, AMOUNT OF STRAIN AND THE INTERPASS TIME. FIGURE ADAPTED FROM [31] .....	124
FIGURE 6.9 JMatPro® SIMULATION OF THE EVOLUTION OF AUSTENITE DECOMPOSITION AND MECHANICAL PROPERTIES FOLLOWING THE COOLING STRATEGY OF SC3 .....	128
FIGURE 6.10 CORRELATION BETWEEN VOLUME FRACTION OF PHASES WITH THE MECHANICAL PROPERTIES DEVELOPED IN THE DIFFERENT TMP SCHEDULES .....	130
FIGURE 6.11 UTS BY %RA PRODUCT OF THE SPECIMENS SUBJECTED TO THE DIFFERENT TMP SCHEDULES .....	132
FIGURE 6.12 GENERAL FULL TMP PROCESSING OF STEEL IN AN INDUSTRIAL MILL .....	133
FIGURE 6.13 EQUIVALENT STRAIN DISTRIBUTION AFTER THE PSC DEFORMATION OBSERVED IN THE LONGITUDINAL DIRECTION. MICROSTRUCTURE NEAR THE TOP AND BOTTOM SURFACES	

EXHIBIT MORE EQUIAXIAL AUSTENITE GRAINS WHILE AT THE CENTRE IS COMPLETELY  
ELONGATED STRUCTURE. ETCHANT: SATURATED PICRIC ACID SOLUTION ..... 135

FIGURE 6.14 MICROSTRUCTURE OBSERVATION AT A) TOP AND C) BOTTOM NEAR THE SURFACE OF  
THE PSC SPECIMEN AND B) AT THE CENTRE OF THE SPECIMEN. ETCHANT: 2% NITAL ..... 136



# List of Tables

TABLE 3.1 MAXIMUM AMOUNT (WT%) OF CHEMICAL ELEMENTS IN COMMERCIAL CP STEELS [26]	14
TABLE 3.2 MECHANICAL PROPERTY REQUIREMENT FOR CP STEEL GRADES [26]	16
TABLE 4.1 SPECIFICATION AND CAPABILITIES OF PHILIPS FEI TECNAI T20	40
TABLE 4.2 EQUATIONS OF $A_{R3}$ DESCRIBED BY DIFFERENT AUTHORS. ALLOY CONTENT IS SPECIFIED IN WEIGHT %	48
TABLE 4.3 DEFORMATION PARAMETERS TO EVALUATE $T_{5\%}$ ON DOUBLE HIT TESTS	49
TABLE 4.4 TMC GENERAL SPECIFICATIONS	51
TABLE 4.5 DIFFERENT METHODS TO CALCULATE THE FRACTION SOFTENING OF A DOUBLE HIT TEST. .....	53
TABLE 4.6 EMPIRICAL EQUATIONS TO ESTIMATE $T_{5\%}$ . ALLOY CONTENT IS SPECIFIED IN WEIGHT % .....	54
TABLE 4.7 STRATEGIES TO OBTAIN CP MICROSTRUCTURE DURING THERMOMECHANICAL PROCESSING. ....	59
TABLE 5.1 CHEMICAL COMPOSITION OF AS-RECEIVED CP800 TRANSFER BAR. ....	70
TABLE 5.2 SUMMARY OF DILATOMETRY TESTS FOR THE CP800. ....	71
TABLE 5.3 ESTIMATION OF $A_{R3}$ FOR THE CP800 CHEMICAL COMPOSITION AND INITIAL PAGES OF 46 MM. ....	73
TABLE 5.4 PRIOR AUSTENITE GRAINS MICROSTRUCTURE OF SINGLE AND DOUBLE HIT TESTS	83
TABLE 5.5 GRAIN SIZE MEASUREMENTS OF THE DEFORMED SPECIMENS. ....	83
TABLE 5.6 $T_{5\%}$ ESTIMATION FOR THE CP800. ....	84
TABLE 5.7 ACTUAL MEASUREMENTS OF STRAIN AND TEMPERATURE PER DEFORMATION PASS OF THE SPECIMENS WITH THE FULL TMP SCHEDULE	91
TABLE 5.8 ACTUAL MEASUREMENTS DURING COOLING ON SPECIMENS OF FULL TMP SCHEDULE. COOLING RATE 1 CONSIDER FROM THE LAST DEFORMATION PASS UNTIL THE HOLDING TEMPERATURE. COOLING RATE 2 INCLUDES AFTER THE HOLDING TEMPERATURE UNTIL ROOM TEMPERATURE	91
TABLE 5.9 VOLUME FRACTION OF PHASES IN DIFFERENT SPECIMENS ANALYSED BY EBSD.....	103

TABLE 5.10 MECHANICAL PROPERTIES CALCULATED FROM THE TENSILE TESTS.....	108
TABLE 6.1 VOLUME FRACTION AND MECHANICAL PROPERTIES PREDICTION BASED ON THE DIFFERENT COOLING STRATEGIES AFTER THE FINISHING ROLLING. CALCULATIONS MADE BY JMATPRO® SOFTWARE.....	128

# CHAPTER 1

## ABSTRACT

Population growth and continuous infrastructural development have brought a high demand for private automotive vehicles, which is expected to continue rising in the coming years. As a result, there will be a larger number of vehicles in transit and therefore the probabilities of crash collisions and CO<sub>2</sub> emissions into the environment will also increase. For this reason, the technological development of steels for automotive applications is increasingly important. CO<sub>2</sub> emissions can be reduced by improving fuel consumption lowering the weight of vehicles. Therefore, automakers are investing in research to develop lighter and stronger automotive components which meet the safety requirements, without increasing production costs.

Complex phase (CP) steels have been introduced as candidates to improve steel properties through thermomechanical controlled processing (TMP). This thesis focuses on investigating different TMP schedules in a CP steel composition to evaluate the microstructure evolution and mechanical properties. The potential of the alloying elements has been assessed to develop a stronger steel grade through TMP. The effect of deformation parameters and cooling conditions on the final product was also considered in the analysis.

Small specimens of CP steel underwent to four-pass TMP routes, simulating deformations conditions during finishing rolling. This was done in a TMP machine under the module of plane strain compression. The TMP routes were designed by defining the critical processing parameters such as transformation temperatures and recrystallization-stop temperature. The TMP explores the influence of the conditioning of the austenite during the finishing rolling and the subsequent development of the microstructure in the run-out table. An extensive characterization was done for the as-received material and the post-processed specimens.

The deformation parameters and the cooling strategies led to the development of microstructures corresponding to certain mechanical properties and volume fraction of phases. The higher tensile strength and higher amount of bainite were achieved in the specimen deformed at lower last-pass temperature but higher holding temperature during the step cooling. This generated

high dislocation density with deformation bands and therefore high  $S_v$  to facilitate transformation products.

The heavily deformed and non-recrystallized austenite structure is ideal to create fine-grained products which increase the tensile strength. This is also favourable to start ferrite transformation in a relatively short time. Alloying elements play a key role in the microstructure development through TMP, e.g. Nb addition delays austenite recrystallization, retaining a high  $S_v$ .

Most of the TMP schedules designed in this work developed the mechanical properties and microstructure to be considered as CP for automotive applications.

# CHAPTER 2

## INTRODUCTION

Today, the production of cars is rapidly growing. Therefore, the number of vehicles transiting on the roads is increasing along with the possibility of automobiles crashes. At the same time, the worldwide concern of the carbon dioxide (CO<sub>2</sub>) emissions from vehicles enhance due to the high impact on global warming. The transport sector is responsible for almost 16% of the total carbon dioxide emissions into the environment [1, 2].

One way that has recently been proposed to tackle this problem without affecting the production of vehicles is to improve the performance of new cars and trucks by reducing their weight to reduce fuel consumption, and in consequence, the CO<sub>2</sub> emissions. This would also produce an economic advantage for the consumer [3, 4]. For this reason, technological development in the automotive industry is of high importance. There are several approaches to achieve this goal without significantly increasing the processing cost. For instance, stronger steels for crash impact can be produced, allowing to reduce the thickness of the components to produce a lighter structure that does not expose the safety of the passengers [5].

The need to increase passenger safety, as well as vehicle fuel efficiency, are a constant cause of debate for material selection, mainly between steel and other metals of lower density. Steel is the main material in the body car structure due to its accessible costs and its capacity to absorb energy in a crash impact and its ability to become stronger when it is deformed. Other advantages of steel components include the capacity of being easily recycled, affordable repairs and long durability.

On average, the total mass of a typical passenger car is 1,260 kg where approximately 71% consists of steel. The mass of the body structure and components for high strength and energy absorption is around 360 kg. AHSS can lead to mass savings in the components of the body structure up to 39% by replacing conventional steels without adding too much cost. This corresponds to 9% of the total vehicle weight. The mass savings achieved due to the use of AHSS has resulted in the lifetime savings from 3 to 4.5 tonnes of greenhouse gasses per vehicle and an

increase in fuel efficiency in the range of 2% to 8%. These savings in emissions can be more than the total amount of CO<sub>2</sub> emitted during the production of all the steel in the vehicle [6, 7].

Advanced High Strength steels (AHSS) have been introduced in the automotive industry due to their particularly good combination of strength and ductility. AHSS are characterized by their microstructures and metallurgical properties that meet the requirements of the automotive industry. One distinct benefit of using AHSS in vehicle components is to improve the impact resistance without increasing the weight of the vehicle [8].

Complex Phase Steels (CP) are a subcategory of the first generation of AHSS. CP steels are characterized by their refined microstructure, which consists of a combination of ferrite, bainite and martensite, but also in certain conditions, retained austenite and/or pearlite may be present in relatively small amounts [9]. CP steels are generally produced by controlling the thermomechanical processing (TMP) from the reheating of the slab to the coiling on hot rolled products [10]. The TMP applied to the steel will define the volume fraction of phases and hence the mechanical properties.

Deformation during TMP has two main purposes: to reduce the thickness of the steel plate to give the desired shape and to refine the microstructure by recrystallization to increase the strength of the steel eliminating the as-cast structure. TMP can also alter the nucleation sites for phase transformation by strain accumulation. This would depend on the TMP parameters during deformation such as deformation temperature, strain, strain rates and interpass time.

Critical processing temperatures, i.e. recrystallization-stop temperature or  $T_{5\%}$ , and phase transformation temperatures,  $A_1$  and  $A_3$ , need to be well defined to design a successful TMP route. Controlled rolling during the finishing passes should take place at temperatures in between  $T_{5\%}$ , to avoid recrystallization of the austenite, and  $A_{r3}$  to avoid deformation of the ferrite.

All parameters used during thermomechanical processing (TMC) have a direct influence on the final mechanical properties of the material. In this thesis, the critical processing temperatures of the material with a composition related to a CP steel have been established by different methods. These temperatures were used to design and perform different TMP routes, which leads to develop a balance in the microstructure and the mechanical properties characteristic of a CP steel. CP steel specimens after the TMP routes were subjected to an extensive characterisation, including but not limited to quantitative metallography by optical and electron microscopy, electron backscattered

diffraction, and tensile tests. Microstructure evolution through TMP, mechanical properties and volume fraction of phases were also evaluated.

Phase transformation temperatures were measured by dilatometry experiments which detect the length change of the samples during specified heat treatment. The phase transformation from ferrite ( $\alpha$ ) to austenite ( $\gamma$ ) or vice versa has a significant change in length due to re-arrangement of atoms. JMatPro® simulation software was also used to compare the continuous cooling transformation (CCT) diagram with the experimental dilatometry results for  $A_{r1}$  and  $A_{r3}$ . Flow stress from double hit deformations under plane strain compression (PSC) conditions were useful to calculate the softening parameter when the material is deformed twice at the same temperature. This softening parameter has been correlated to the recrystallization-stop temperature (~20% softening) and the full recrystallization temperature (~60% softening).

## **2.1. Statement of Objectives**

Research on the TMP of AHSS in a laboratory environment becomes essential as an important stage before industrial rolling production. Laboratory-level replication of hot rolling enables the optimal design of TMP conditions through precise control of temperature, strain, strain rate, heat treatment, and cooling parameters at relatively low cost.

This thesis evaluated different TMP routes designed for CP steel by laboratory simulations to later be implemented on an industrial scale in the hot rolling mill located in the facilities of the company Ternium-Mexico in Monterrey city.

The general objective of this work is:

- 1.- To develop and suggest modifications to the TMP schedule of steel with a CP800 chemical composition. This aims to develop a microstructure which leads to improve the final mechanical properties.

This chemical composition has the potential to increase the metallurgical properties through TMP due to the additions of microalloying elements such as Nb and Ti. These additions have a direct impact on the recrystallization process and promote the formation of hard precipitates. The steel used in this research has less carbon content than common composition of CP steels.

The proposed methodology to achieve this objective can be summarized as:

- The characterisation of the critical processing temperatures associated with a CP steel composition. This includes the determination of transformation temperatures, recrystallization-stop ( $T_{5\%}$ ) temperature and the critical cooling rate.
- To evaluate the microstructure evolution during finishing rolling and the subsequent transformed products with different cooling strategies.
- To establish a relationship between the volume fraction of phases with the final mechanical properties.



# CHAPTER 3

## BACKGROUND

### 3.1. Advanced High Strength Steels (AHSS)

Steels can be classified into two main groups according to their mechanical properties such as tensile strength and elongation as shown in Figure 3.1. The difference between these two families of steels that make one stronger than the other is the microstructure. The conventional steels group includes interstitial free steels, or mild steels, which have a low tensile strength (maximum 600 MPa) but high elongation, around 50 or 60%. The category of Advanced High Strength steels (AHSS) has a very good combination of strength and ductility. AHSS family are characterized by having at least 300 MPa of yield strength, and a minimum of 600 MPa on the ultimate tensile strength (UTS) [11].

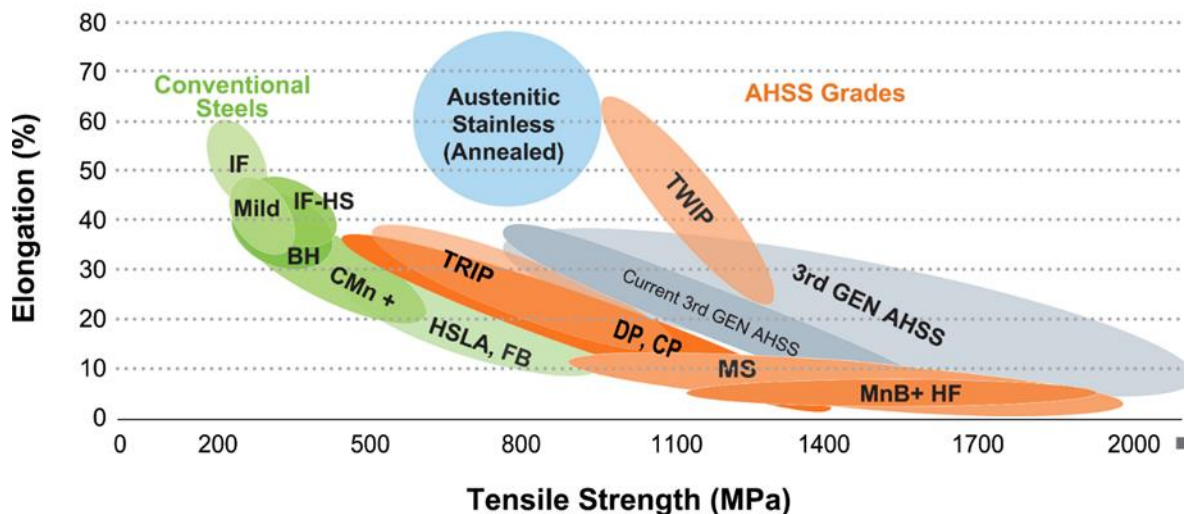
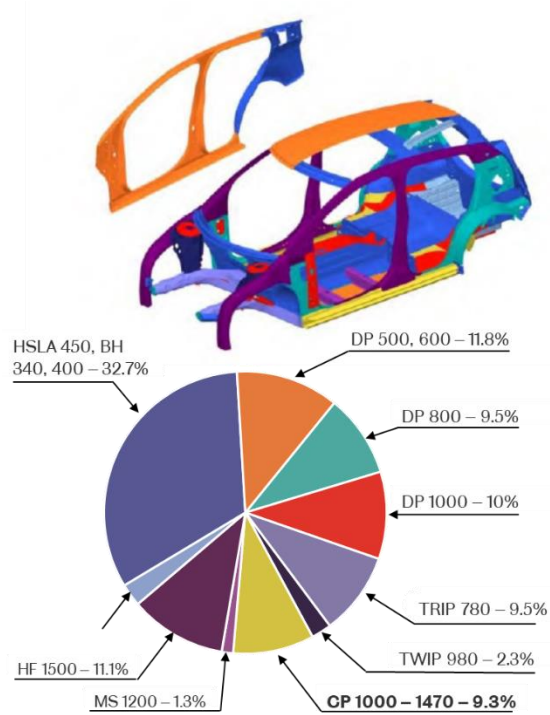


Figure 3.1 Global Formability Diagram for AHSS Grades [10]

Over time, AHSS have been catalogued in different generations. The first generation of AHSS aimed to increase the strength but preventing reduction in ductility, this generation includes the high strength low alloy steels (HSLA), transformation induced plasticity (TRIP), dual phase steels (DP) and complex phase steels (CP). The second generation of AHSS are steels with a higher amount of alloying elements. Thus, they can easily increase both strength and ductility. The disadvantage of this generation of steels is their high cost, making them not affordable for some applications. Some examples of this generation are the twinning induce plasticity (TWIP) steels and the austenitic stainless steels. The third generation is the latest development of AHSS, their characteristic is higher strength and ductility compared to the first generation, but at a lower cost of production than the second generation. The approach to achieve this is through the combination of alloying elements with a fine microstructure. These steels had complex microstructure with a variety of constituents, present a narrow range of chemical compositions, and are produced throughout a thermomechanical controlled process [12].

AHSS were introduced some years ago in the automotive industry [13, 14] gaining attention due to their better mechanical properties compared with conventional steels. The benefit of using AHSS in components of a vehicle is to improve the impact resistance without increasing the mass of the vehicle. Figure 3.2 shows the distribution and percentage amount of AHSS usage on a body car structure.



**Figure 3.2** Future steel vehicle material usage [15]

The main properties to evaluate in AHSS are the microstructural constituents, strength, strain hardening, formability and fracture resistance. Figure 3.3 shows the mechanical properties requirement depending on the AHSS component in the body car structure. Steels that are used for critical parts on the automobile need high strength resistance to maintain a passenger survival space in case of an accident. All AHSS are produced by controlling the chemical composition, the heating and cooling processes, which lead to their final microstructure [9, 10].

Studies have been conducted on various steel compositions and methodologies which focus on the potential of developing a high strength/ductility ratio. Speer et al. [16] used the Q&P method which consists of quenching the full austenite microstructure to the desired temperature between  $M_s$  and  $M_f$  to control to martensite volume fraction. The steel is held at that temperature to allow carbon diffusion and enrichment of the remaining solute in the austenite to increase austenite stability. This results in higher austenite fractions, i.e. higher ductility, at room temperature due to its crystal structure. They suggest the Q&P methodology may be a viable process to generate better

steel grades. The key is to define the balance of two phases, martensite provides resistance while the ductility is given by the austenite.

Wakita et al. [17] studied a low carbon but high Mn steel composition, with the aim to stabilize austenite at low temperatures. They have managed to increase mechanical properties through TMP. Their work shows that high strain passes on austenite led to fine-grained ferrite and a considerable amount of retained austenite. They stated that ultrafine-grained ferrite, adjusting the Mn content in the composition and control of TMP succeed to produce tensile strength of 1080 MPa and 26.9% of total elongation. However, the microstructure consisted of only two microconstituents avoiding bainite formation. It has been reported that the combination of bainite and martensite can be more resistant than pure single phase microstructure and a considerable amount of bainite can increase the yield strength of the steel [18-20]. Hence, it has been considered to develop the complex phase steels microstructures.

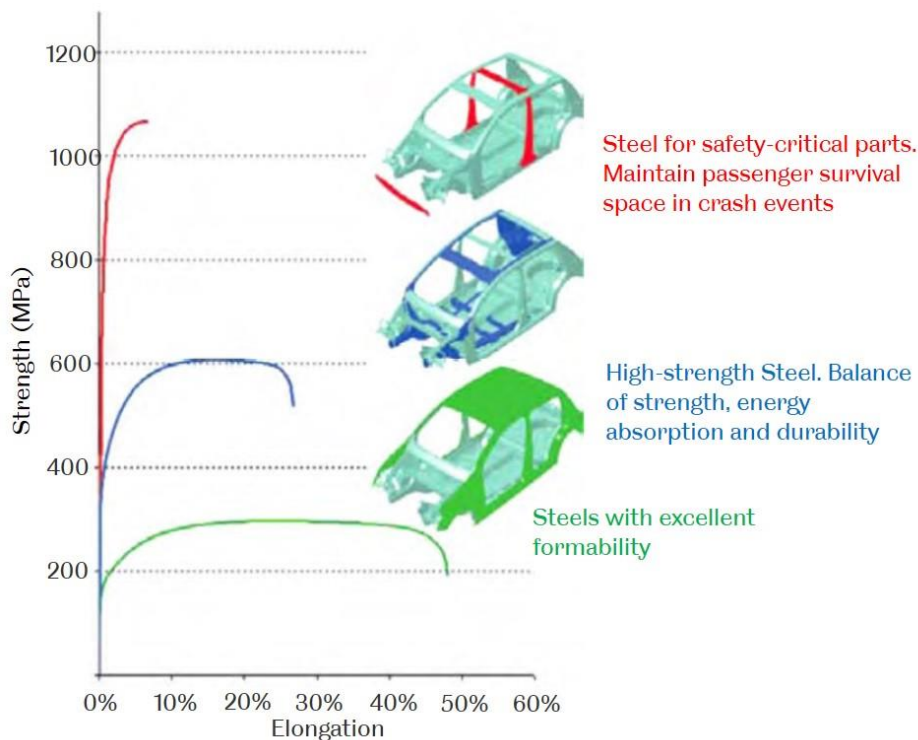


**Figure 3.3** Stress vs elongation diagram for different steel types and their applications on body car structure [15]

### 3.1.1. Complex Phase (CP) steels

Complex phase (CP) steels are within the category of the AHSS family and are commonly used to produce automotive components due to their superior relation of formability and strength. Nowadays, around 10% of the total body car structure is made of CP steels. This includes the parts of the safety cage, B-pillars reinforcements, bumper beams, rocker panels, chassis components or other parts where high energy absorption is required [9, 21, 22]. Complex phase microstructure is generally achieved by a special thermomechanical process for a designated chemical composition. The characteristic microstructure of this type of steels consists of a combination of ferrite, bainite and martensite but also, in certain conditions, retained austenite and/or pearlite may be present in relatively small amounts. A schematic microstructure of a CP steel is shown in Figure 3.4. The volume fraction of these phases will depend on the cooling strategies from austenite in the run-out-table after finishing rolling for hot rolled products. The matrix of a CP steel is commonly composed of soft ferrite and bainite. The ferrite is the soft phase giving the ductility to the steel, while bainite and martensite are hard phases, which provides strength to the steel. In addition, alloying elements such as Niobium, Titanium and Vanadium are added to the CP steels to create precipitates. Fine precipitates prevent the movement of austenite grain boundaries during TMP, which effectively retard the recrystallization process [23-25]. This would increase the steel strength due to the strain accumulation and work-hardened structure. The effect of each of these microalloying elements on the recrystallization-stop temperature is presented later in this chapter.

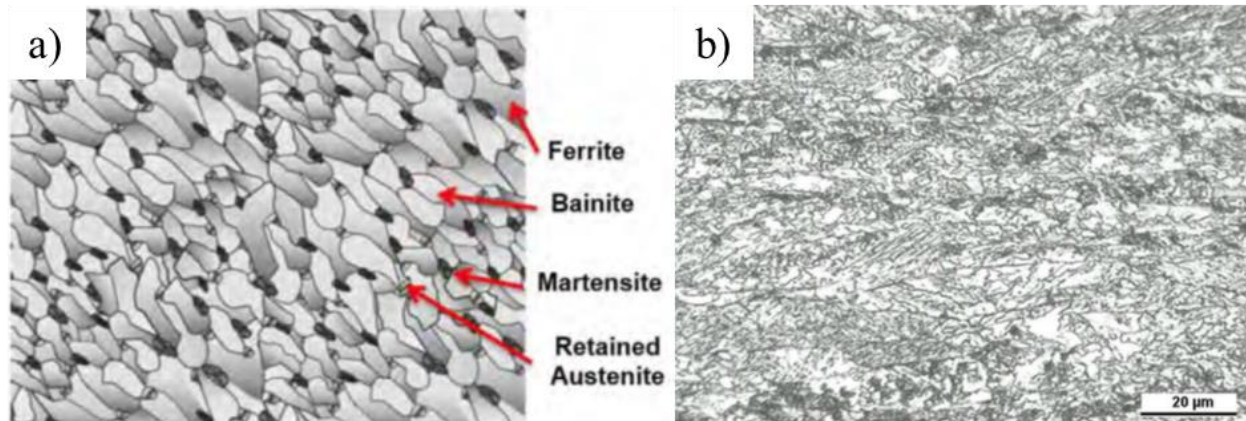


**Figure 3.4** a) Schematic CP steel microstructure [15] b) Microstructure of a CP steel with a bainite/martensite matrix [25]

The grade designation nomenclature of complex phase steels is based on mechanical properties, specifically on ultimate tensile strength (UTS), all units are stated in the International System of Units (SI), i.e., megapascal (MPa). In some cases, a second number is shown after a forward slash (/), where the first number represents the minimum yield strength value and the second number is the UTS value [26]. CP steels can achieve tensile strength levels from 590 MPa to 1000 MPa, and elongations between 15 and 30%. Figure 3.5 shows various engineering stress vs engineering strain curves corresponding to different grades of CP steels and how their mechanical properties can be compared with a conventional steel.

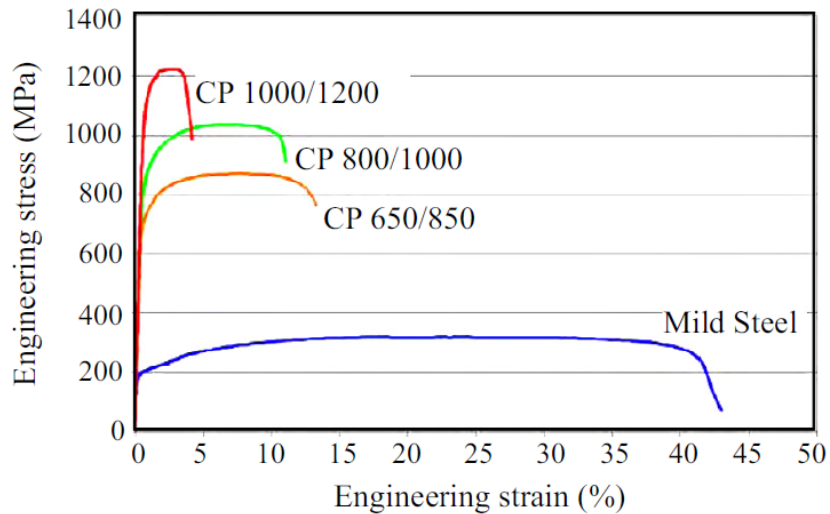


**Figure 3.5** Engineering flow stress curves for different CP steel grades and a conventional steel [24]

The CP steels are similar to DP, but normally CP contains elements such as Nb, Ti and V for grain refinement through the formation of precipitates that do not allow the grain coarsening by limiting the movement of grain boundaries. This enables better control of the recrystallization prior to phase transformation. CP microstructure in steels offers some advantageous features over DP steels, for example, higher yield strength to tensile strength ratio; higher work hardening capability at low strain; better roll-forming, bending and hole-expansion behaviour for high strength level, indicating an exceptional stretch flangeability; higher energy absorption capability and fatigue strength; better spot weldability [11].

CP steels can also be comparable to TRIP steels in chemical composition, but the volume fraction of remaining austenite is quite less for CP. CP microstructure has fine precipitates which enable precipitation hardening resulting in very high strength [27].

There are different ways to get the CP microstructure through TMP. One is by austenitisation to the intercritical region temperature between  $A_1$  and  $A_3$ . This temperature is set depending on the ferrite fraction desired and it is followed by slow cooling to room temperature at a controlled rate depending on the volume fraction of phases required.

The TMP for a CP mostly used in the industry is to reheat the steel above the  $A_3$  temperature, thus reaching on fully austenite phase. Afterwards, steel is deformed in the austenite phase and

rapidly cooled to reach the ferrite or bainite window in the CCT diagram. Then, it is held at that temperature to transform the required amount of ferrite/bainite. Bainite and martensite are essential for the CP microstructure so that, after the holding period, the steel should carry out another fast cooling to transform the remaining austenite [28]. The key point is to ensure that the desired amount of bainite can be transformed in the period when the steel sheet is on the run-out table.

The continuous cooling transformation (CCT) diagrams are used to denote which phase transformation will occur in steel depending on the cooling rate from the austenite phase. CCT diagrams are derived from the Time Temperature Transformation (TTT) diagrams. There is a specific CCT diagram for each steel based on the chemical composition, grain size and austenitisation temperature.

As mentioned before, CP steels are classified by the mechanical properties UTS and elongation, and therefore, there is no specific chemical composition for each grade of CP. This means that different chemical compositions can be transformed into CP steel by controlling the thermal processing. However, for commercial CP steels, there is a chemical requirement according to the CP grade designation standard [26]. Table 3.1 shows the maximum content in weight per cent of the different chemical elements for commercial CP steels.

**Table 3.1** Maximum amount (wt%) of chemical elements in commercial CP steels [26]

<b>Steel grade</b>	<b>C</b>	<b>Mn + Al + Si</b>	<b>P</b>	<b>S</b>	<b>Cu</b>	<b>Ni</b>	<b>Cr + Mo</b>	<b>V + Nb + Ti</b>
CP600	0.18	5.30	0.80	0.015	0.20	0.50	1.00	0.35
CP800	0.18	5.50	0.80	0.015	0.20	0.50	1.00	0.35
CP980	0.25	5.20	0.80	0.015	0.20	0.50	1.00	0.35

One of the functions of adding alloying elements to the steel is the alteration of the thermodynamic phase diagram. The desired microstructure can be produced easier by changing the phase transformation temperature or phase transformation kinetics. Carbon (C) is an essential element in steels, it increases the stability of austenite and is indispensable for the formation of carbides to



enable precipitation hardening. The addition of Mn to CP steels, in range of 1.5wt%, retards the pearlite and bainite transformations and therefore, the martensite transformation does not need very high cooling rates. Silicon is a ferrite former, but high Si content is not favourable because it might produce oxides in the slab surface during hot rolling. P, Cr and Al are ferrite formers, these elements raise  $A_{r3}$  temperature, but the phase transformation kinetics is slower due to the reduced diffusivity of C in austenite. Ni and Cu play as austenite stabilizers and maintain a balance by lowering  $A_{r3}$ . Molybdenum (Mo) delays ferrite transformation, resulting in limited ferrite volume fraction on the run-out table after the hot rolling process [29]. The main alloying elements in CP steels include Nb, Ti and V. Those elements have been reported to have a pronounced effect on the grain refinement, and a retardation of the recrystallization process [29-32]. Nb is likely to form fine and stable dispersed carbides, which prevent dislocation movement, promoting precipitation hardening. V is often used to reduce austenite grain growth, resulting in a fine microstructure to increase the strength. The advantage of Ti, like V, is the formation of nitrides and carbides to inhibit grain growth, but Ti also reinforces corrosion resistance in different environments. TiN precipitates are thermodynamically stable at temperatures as high as 1300°C, and therefore they are very effective for high temperature control and preventing austenite grain from coarsening. The addition of microalloying elements influences the recrystallization-stop temperature ( $T_{5\%}$ ). Increasing microalloying elements shows an increase in the  $T_{5\%}$  temperature. This is because a larger solute supersaturation is generated, increasing the driving force for precipitation that may form a larger volume fraction of second phase particles which effectively retard the austenite recrystallization, increasing the  $T_{5\%}$ . Each of the microalloying elements has a different effect on the formation of precipitates. Nb has the greatest effect in altering  $T_{5\%}$ , as shown in Figure 3.6 compared to Ti, V and Al [33].

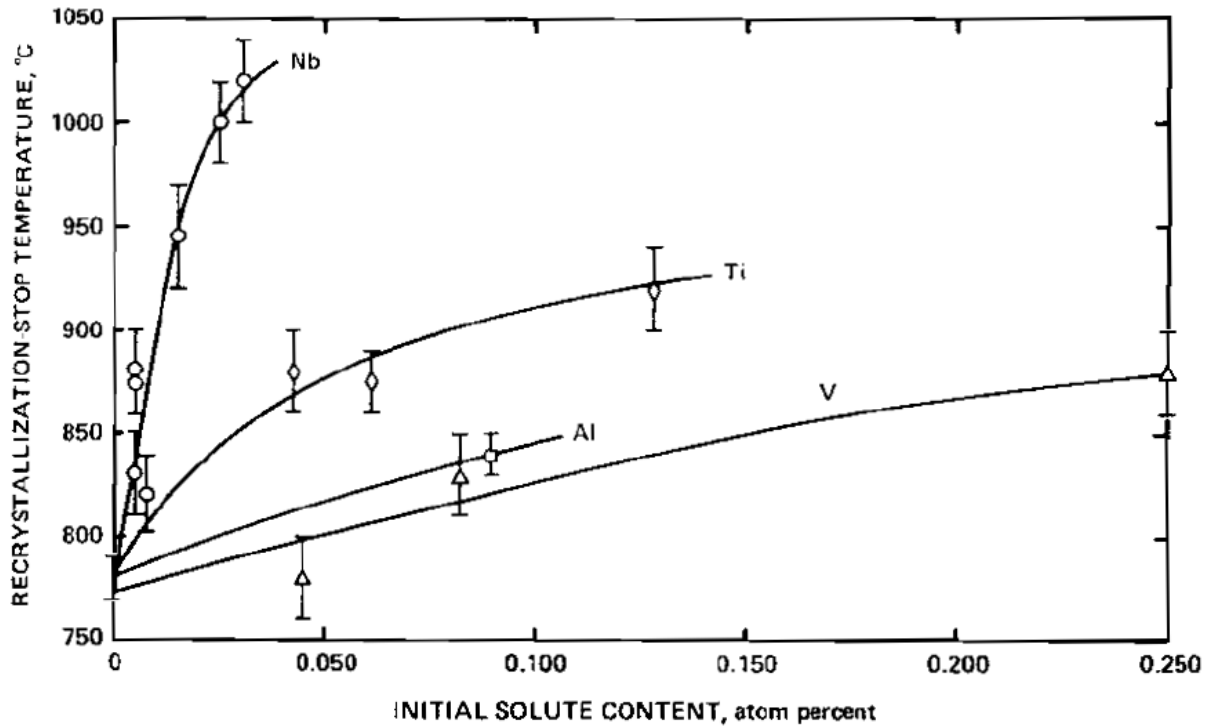


**Figure 3.6** The increase in  $T_{5\%}$  temperature with an increase in the level of microalloying solutes in a 0.07C, 1.40Mn, 0.25Si steel [33]

The mechanical property requirement for CP steel grades specified by the ASTM standard is shown in Table 3.2.

**Table 3.2** Mechanical Property Requirement for CP steel grades [26]

Steel grade	Yield Strength (MPa)	Tensile Strength (MPa)	Elongation (%)
CP600	350	600	16
CP800	500	800	10
CP980	700	980	7

### **3.1.2. Challenge of CP steels today**

Vehicles today are predominantly steel structures. Since CP steels have proven to be excellent materials for various components in a body car, the steel industry has decided to invest in their development to improve the performance in crashworthiness, overall cost and fuel consumption. Automakers are looking for materials with higher strength/weight ratio to reduce CO<sub>2</sub> emissions and to enable safe and environmentally friendly vehicles. The challenge of CP steels is to expand the microstructure and mechanical properties corresponding to the third generation of AHSS, maintaining or reducing the quantities of alloying elements added to CP steel production to keep market prices.

According to the centre for automotive research [34], the body-in-white of a vehicle consists of 75% of different steel grades, where 15% of it is made of advanced and ultra-high strength steels. The study estimates that an optimized vehicle in 2040 would contain between 30 to 35% of AHSS and UHSS of the body car. This leads to exhaustive research and development of the AHSS and more specific the CP steels to increase their strength/ductility ratio, meet the standard and safety specifications foreseen in the future.

The challenge focuses on developing the optimal TMP route to make the most of the alloying elements on the mechanical performance of these steels. The crucial stage in concept is the influence of the processing parameters on the homogeneity of microstructure through the strip during TMP. But also, the design of a realistic and successful cooling strategy for the proper microstructure evolution on the runout table [35]. The possibility to achieve thinner thickness sheets as hot rolled product and thus, minimize the further processing in cold rolling mills has also been considered.

## **3.2. Thermomechanical Processing (TMP)**

Controlled thermomechanical processing (TMP) is a technique designed to improve the mechanical properties of materials by controlling the deformation and thermal processes, from the reheating of the material to quenching [36]. TMP expands the benefits of the alloying elements in

the steel [31], improving the microstructural features, thus allowing the production of automotive AHSS components which meet the requirements imposed by the modern mechanical and structural engineering. Controlled TMP can increase the mechanical properties not only in steels but also in various non-ferrous alloys.

The conditioning of austenite after deformation, the restoration mechanisms, the formation of precipitates and the phase transformation during cooling are some of the metallurgical and mechanical processes that take place and are critical to control during the TMP.

TMP during hot rolling implies control of different parameters such as temperatures, strain rate, rolling reductions and cooling rates, which must be carefully selected to produce the target austenite microstructure for the phase transformations [37]. TMP is an essential tool for the development of multiphase steels. TMP should be designed to ensure a controlled type and extent of transformation on the run-out table by precise control of strip temperature and rolling speeds.

TMP means the control of all processing parameters for beneficial product development. This includes from the reheating temperature, the deformation schedule and the cooling rate to achieve a defined phase distribution and fine microstructures. The purpose of applying a deformation schedule is to obtain an optimum austenite grain refinement. Therefore, the area of austenite grain boundaries per unit volume increases to encourage the onset of phase transformations.

TMP consists of two sequential stages: controlled hot rolling and a subsequent accelerated cooling [38]. The general process of TMP hot rolling (Figure 3.7) starts with slabs, which normally come from continuous casting. These slabs are reheated in a gas furnace to a temperature that the microalloying elements are dissolved, typically between 1200-1300°C. This also reduces the loads required to deform the slab on the rolling mill. As a result of high temperature, iron oxides form on the slab surface. The next step is to remove the oxide layer in a scale breaker to start the rough rolling deformation, which may be in either reversing or a tandem mill. During this stage, the austenite grain is refined multiple times by recrystallization. Later, the temperature decreases, and plates are processed in the finishing rolling, commonly in a tandem mill, where dimensions such as thickness and width are strictly controlled. In this step, microalloying elements form precipitates, which effectively retards recovery and recrystallization, and the austenite is deformed below the recrystallization-stop temperature ( $T_{5\%}$ ) and the grain shape become pancake-like. Finally, the steel is controlled cooled to carry out the phase transformation. The important variables

to control during TMP are austenite grain size, deformation temperature, strain, strain rate, and cooling rates [39].

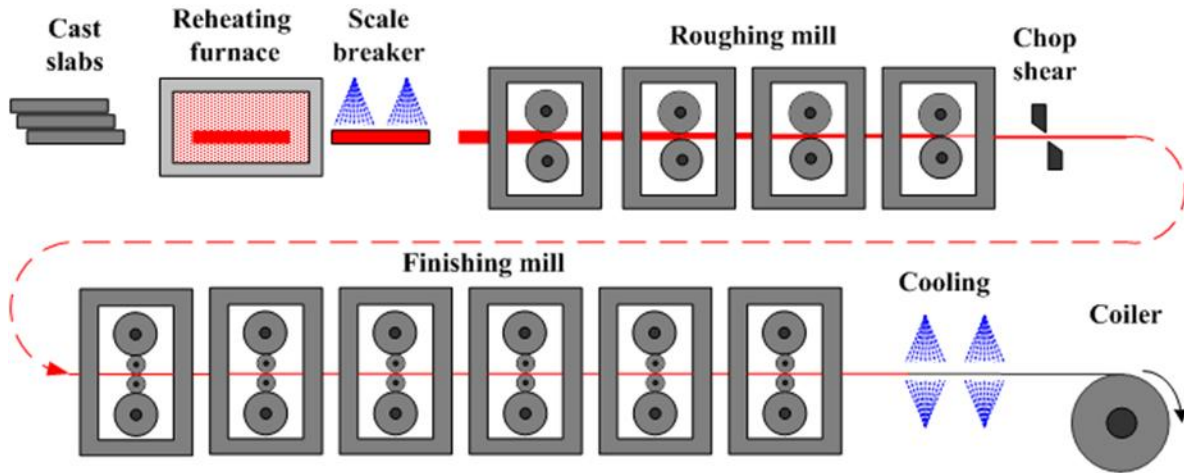


**Figure 3.7** Hot Rolling processing of steel slabs [40]

Every parameter during TMP, i.e. austenitisation temperature, isothermal holding temperature and time, cooling rates but also microalloying elements have a significant influence in the transformation products and volume fractions which control the final microstructure and thus the mechanical properties of the steel.

The controlled TMP can generate favourable microstructures for CP steels, deformation-induced ferrite transformation could take place by varying the processing route working at high temperatures when ferrite is not stable. This results in finer grain size with better final mechanical properties [41].

The initial microstructure of the steel before being subjected to the controlled TMP also influences on the final mechanical properties. According to Schemmann et al. [42] and Zuo et al.[43], an initial microstructure consisted of a combination of bainite and martensite may have better final properties than the mixed initial microstructure of pearlite and ferrite following the same TMP route. This is attributed to the microsegregation of the substitutional elements in each of the phases, which changes the austenitisation temperature, and delays the austenite to ferrite phase transformation. Consequently, the steel with an initial microstructure of bainite and

martensite is more resistant than the pearlite and ferrite as it transforms a greater amount of martensite.

### **3.2.1. Prior Austenite Grain**

One of the factors influencing the mechanical properties of steels is the grain size. The finer the grain size, the higher yield strength of the steel [44-46]. This is due to the higher number of grain boundaries per area which obstruct dislocations displacement [47]. The grain size can be controlled by the different heat treatments as well as TMP. The austenitic grain size before deformation depends on the reheating temperature and the holding time at that temperature [48-50]. These parameters together with the slab deformation can lead to the recrystallization process that refines the austenite grain size [51] but also minimizes the microstructure heterogeneity throughout the slab thickness [52].

The advantage of TMP in the industry is to refine the grain size with the intention of getting high yield strength and high ductility in steels through a cost effective way. This is achieved by controlling the austenite grain size during slab reheating.

The temperature of the strip before cooling from austenite phase has an influence on the final grain size of ferrite. A fine ferrite grain can be produced at high undercooling of austenite since a great number of nucleation sites are developed due to the high temperature gradient during cooling [53].

The final grain size depends on the static and dynamic recrystallization, which in turn depends on the initial microstructure, chemical composition and deformation conditions like temperature, strain and strain rate. A parameter “ $S_v$ ” has been used to quantify the total effective interfacial area for nucleation per unit volume in the deformed austenite [54]. Generally, the ferrite grain size depends inversely on the number of nucleation sites, which include both austenite grain boundaries and intragranular defects, such as twinning and deformation bands [55].  $S_v$  has units of  $\text{mm}^{-1}$  or equivalently area ( $\text{mm}^2$ ) per unit volume ( $\text{mm}^3$ ). Therefore, achieving a large  $S_v$  in the austenite microstructure prior transformation is the goal for controlled TMP rolling.

The strength of a 0.20 C (wt %) steel can be doubled with only a slight reduction in the tensile ductility by simply reducing the grain size to 3–5 microns. This can be achieved by proper control of the austenitizing temperature, i. e., the initial deformation temperature [56].

### **3.2.2. Deformation: strain, temperature and strain rate**

Deformation serves for different purposes during the controlled TMP. The most important reason is to reduce the thickness of the steel plate and give it the desired shape. Secondly, during rough rolling, both, deformation and high temperature lead to refine the microstructure by recrystallization to improve the mechanical properties, rough rolling is also useful to close all defects coming from casting, such as pores. Lastly, at the tandem mill stage, deformation is used to produce the desired final thickness, this would also increase the stored energy and generate more nucleation sites to simplify subsequent phase transformations. During this stage, the dislocation density increases, thus, the strength of the strip too [57].

The typical processing parameters in TMP hot rolling of steels are, for rough rolling, the temperature range is between 950°C and 1200°C, the strain per pass is 0.30-0.60 at strain rates of 5 to 30 s<sup>-1</sup>. The finishing rolling normally takes place at temperatures between 700°C and 950°C, with strain per pass from 0.30 to 0.01 at strain rates of 30 to 300 s<sup>-1</sup>.

There are some critical temperatures during the controlled TMP which need to be well defined to design a successful route. After a deformation pass, depending on the processing parameters and chemical composition, the steel might stop recrystallizing below a certain temperature. This temperature is known as the non-recrystallization temperature ( $T_{5\%}$ ). During deformation passes below  $T_{5\%}$ , the recrystallization is delayed or omitted because of the preference of formation of precipitates or second phase particles. More than 5% of the deformed austenite is recrystallized if deformation occurs at temperatures above  $T_{5\%}$ . On the other hand, the minimum deformation temperature required for the complete recrystallization of austenite structure after a deformation pass is called the full-recrystallization temperature ( $T_{95\%}$ ) [58].

Most of the mechanical energy in a metal that has been plastically deformed is dissipated as heat, and only a very small amount (1 to 10%) is stored mainly in the form of dislocations [59,

60]. Dislocations and high grain boundary area increase the free energy of the steel and have the influence to keep a large  $S_v$  parameter.

The deformation on hot rolling plates can be classified into three stages depending on the temperature it takes place [61]. Figure 3.8 shows the representative microstructure for each of the stages.

1.- The deformation at recrystallization temperature range (above  $T_{95\%}$ ). The austenite grain is refined several times by static recrystallization between each rolling pass reduction. After heavy deformations following recrystallization, the austenite grain size become smaller, until a limit is reached.

2.- The deformation at the un-recrystallized temperature range. When deformation takes place below recrystallization temperature ( $T_{5\%}$ ), the  $\gamma$  grains are elongated in the rolling direction resulting in a “pancake” austenite grain shape. Deformation bands are formed in the rolling direction. Austenite remains un-recrystallized, so that the deformation is considered “cold worked”, and strain is accumulated through all rolling passes. The high dislocation density in the grain boundaries is produced when austenite undergoes heavy deformation below  $T_{5\%}$ . These lattice defects increase the strength of the material, and the process is called work hardening. These sites increase the nucleation rate for acicular ferrite. If a critical strain is exceeded during one pass deformation, the strain can induce dynamic recrystallization [29]. In this region, during cooling, ferrite nucleates on the deformation bands and austenite grain boundaries [62].

3.- The deformation in the  $(\alpha+\gamma)$  two-phase region. The ferrite is work-hardened, and substructures are formed in ferrite. During cooling, the deformed austenite is transformed into equiaxed ferrite grains while deformed ferrite may change into sub-grains.



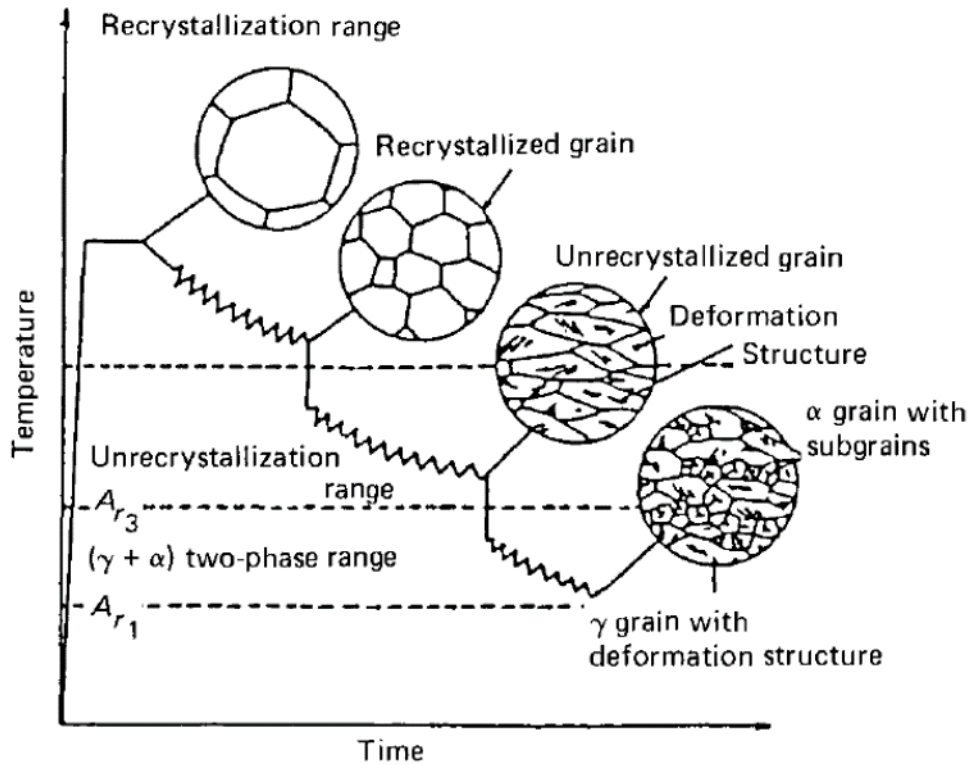


**Figure 3.8** Three stages of the controlled rolling process and the change in microstructure [63]

Finishing rolling passes should take place at temperatures outside the range between  $T_{5\%}$  and  $T_{95\%}$  to have a homogeneous microstructure [62].

The flow stress in hot deformation is a function of some deformation parameters such as temperature and strain rate and can be incorporated into the Zener-Hollomon parameter ( $Z$ ), which effectively is a temperature compensated strain rate. Dynamic restoration mechanisms are altered by  $Z$ . Deformation-induced grain refinement is enhanced at higher  $Z$ .  $Z$  is expressed by Eq.1 :

$$Z = \dot{\epsilon} \exp \frac{-Q}{RT} \quad (1)$$

where  $\dot{\epsilon}$  is the strain rate ( $s^{-1}$ ),  $Q$  is the activation energy for deformation in joules per mole,  $R$  is the gas constant in joules per mole and  $T$  is the absolute temperature [64-66].

According to Cabibbo et al. [67], the deformation in non-recrystallization temperature increases the impact toughness compared with the deformation at fully recrystallization temperature.

### **3.2.3. Controlled cooling**

The key challenge in the fabrication of CP microstructure is to design a good cooling strategy [68]. Continuous Cooling Transformation (CCT) diagrams are useful tools to know the changes in microstructure that can be obtained through different cooling rates. CCT diagrams define the stability of phases, and normally indicate the time and temperature of start and finish phase transformation from austenite to ferrite, pearlite, bainite or martensite. A characteristic of the CCT diagram is that it forms a curve commonly known as a “nose”, which typically indicates the start of the phase transformation to bainite or ferrite, the tip of the nose is an important point in the CCT as this indicates the minimum cooling rate to transform to a full martensite microstructure and this cooling rate is commonly referred as the critical cooling rate. A representative CCT diagram is shown in Figure 3.9.

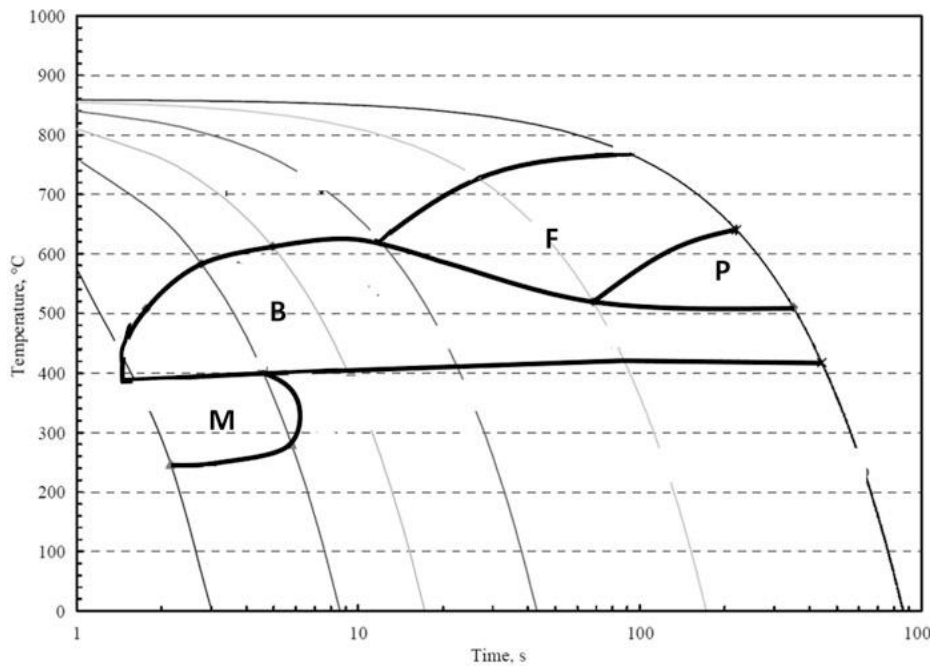


**Figure 3.9** CCT diagram indicating the ranges of cooling rates for producing different microstructures. M = martensite; B = bainite; F = ferrite; P = pearlite [10]

When steel is cooled faster than its critical cooling rate, martensite transformation occurs. The steel plate should be rapidly cooled in a relatively short time. The cooling strategy is designed depending on the dimensions and capacity of the run-out table after finishing rolling. It is appropriate to have a homogeneous cooling on the plate to avoid differences in microstructure throughout the steel plate. The common practice is to cool from the top and bottom sides of the plate [69].

Another factor influencing the mechanical properties of CP steels is the volumetric fraction of the phases. Higher content of martensite (hard phase) increases the tensile strength, while a high-volume fraction of ferrite (soft phase) results in greater elongation [70]. Bainite in CP steels provides a good balance in toughness and ductility. Bainite can also develop greater overall yield stress due to the higher dislocation density [71]. This microstructure should be accompanied by grain refinement to strengthen the steel. A low quantity of interstitial elements in ferrite should not negatively affect the ductility [72].

### **3.3. Restoration mechanisms on microstructural evolution**

The stored energy due to the accumulated dislocations and grain boundaries during hot deformation can be lowered by different processes [73]. The principal mechanisms of restoration on a hot worked metal are the recovery, recrystallization and grain growth. Figure 3.10 shows a diagram of the restoration mechanism process from the deformed metal. When austenite is deformed, recovery is the first softening mechanism to appear. Basically, recovery is a rearrangement of dislocations that make the flow stress to drop. Classical recrystallization needs higher specific strain levels and holding time at high temperature to take place. Recrystallization is the principal mechanism of restoration that affects the flow stress. Recrystallization is the formation of “new” grains in the structure. Grain growth mechanism starts after the recrystallization finish. This mechanism is characterized by the movement of grain boundaries, resulting in a reduction of grain boundary area per volume unit or a smaller  $S_v$ . These 3 mechanisms also affect the performance of phase transformation [74-76].

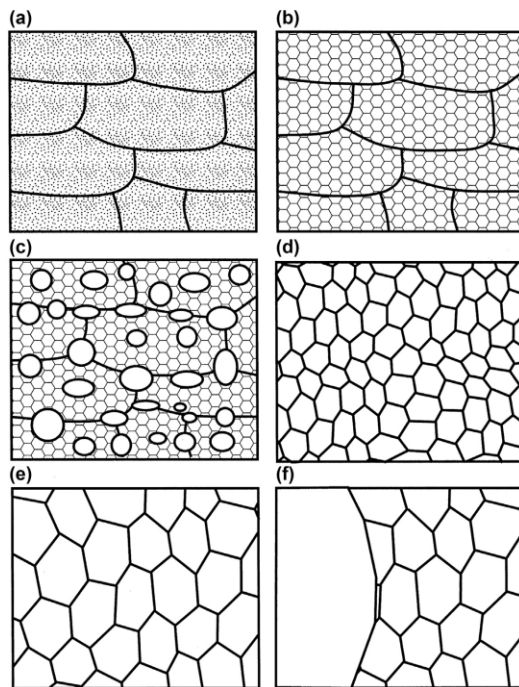


**Figure 3.10** Schematic diagram of the restoration mechanism from deformed metal. a) Deformed state, b) Recovered, c) Partially recrystallized, d) Fully recrystallized, e) Grain growth and f) Abnormal grain growth [60]

Recovery and recrystallization can take place during and after deformation. If a restoration mechanism occurs while the load is still being applied to the metal, it is called dynamic. Static recovery or static recrystallization refers to when the process was carried out after the deformation. If the recrystallization immediately following after deformation is preceded by dynamic recrystallization, it is called metadynamic [77]. Static restoration processes normally take place at elevated temperatures after hot deformation before transformation or during interpass time on the TMP. The stacking fault energy (SFE) of the metal is an important parameter to determine the kinetics of dislocations movements which determines the extent of the restoration mechanisms. The austenite phase with an FCC crystal structure will have a lower SFE than BCC ferrite phase. This means that dislocations climb and cross-slip in austenite are limited and the recovery process is less favourable than in ferrite.

There is plenty of literature on the explanation of restoration mechanisms during TMP of metals, even several works have modelled the conditions of these processes in different materials

and compositions [11, 46, 66, 73-76, 78-88]. The basic concepts and main characteristics of each restoration mechanism are described in this section.

### 3.3.1. Recovery

Recovery, dynamic and static, is a process characterised by the reduction of internal energy through the rearrangement of dislocations into low energy configurations in the deformed material. Figure 3.11 shows the stages of the microstructure evolution during the recovery process where the plastically deformed metal forms cells due to the dislocation rearrangement and then, subgrains are formed and grow because of the annihilation of dislocations. Since recovery reduces the dislocation density, the strength of the metal decreases, but the ductility improves [46]. Although this effect is more drastically observed during the recrystallization process [89].

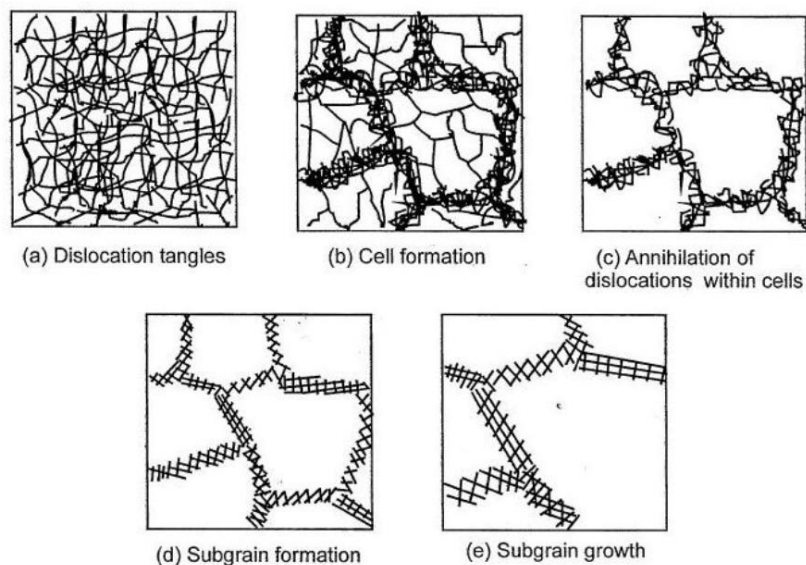


**Figure 3.11** Stages of microstructure evolution during the recovery process [60]

Dynamic recovery could occur to balance continuous work hardening and the accommodation of dislocations leading to a steady state on the macroscopic flow stress. Figure 3.12 shows a representative flow stress curve when the dynamic recovery started during the deformation and is

the only softening process after the work hardening. The constant flow stress after reaching a particular strain level indicates the stabilization of dislocation substructures.

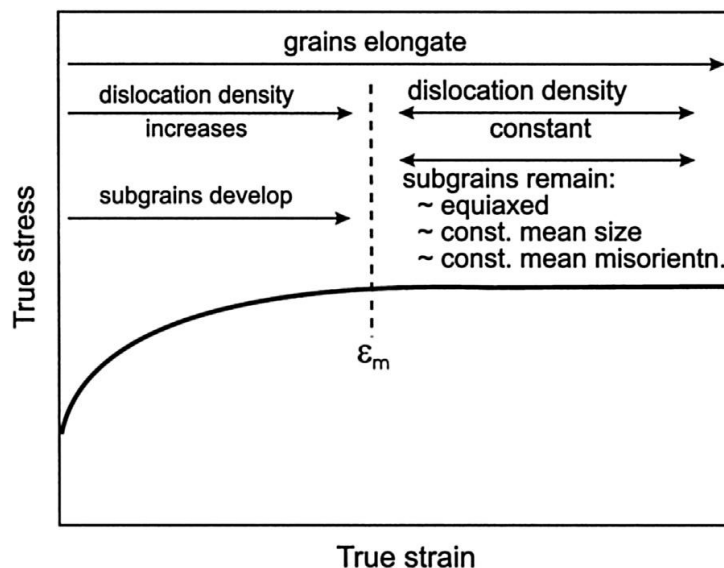


**Figure 3.12** The characteristics of flow stress and microstructural changes when dynamic recovery is the only restoration mechanism [90]

### 3.3.2. Recrystallization

Recrystallization is a restoration process that changes the grain structure of a metal, which is produced by the combination of high temperature and deformation. Recrystallization is characterised by the formation of new smaller grains with low dislocation density and is used to decrease the stored energy in a previously deformed material. The nucleation sites for the new grains are mainly in the grain boundaries of the previous grains. This mechanism process is shown in Figure 3.13. Recrystallization usually reduces the strength and hardness of the material but at the same time the ductility increases.

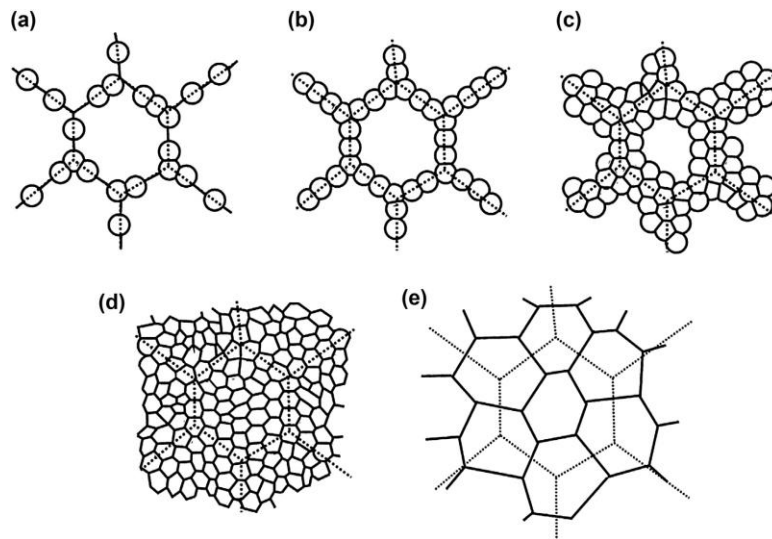


**Figure 3.13** A schematic diagram of the recrystallization process. Dotted lines represent previous grain boundaries and the solid lines are the new recrystallized grains [60]

Dynamic recrystallization is commonly observed in metals and alloys with low SFE. This is attributed to the difficulty of dislocations to cross-slip and climb. Hence, the recrystallization is favoured rather than recovery in metals with low SFE. The flow stress behaviour of austenite during hot deformation is influenced by this mechanism. Dynamic recrystallization is promoted by low  $Z$ , i.e. low strain rate and high temperature. The initial work hardening and slow dynamic recovery lead to dynamic recrystallization. One of the main characteristics to detect when dynamic recrystallization starts, is that the flow stress reaches a peak at a critical strain and the strain hardening decreases. There is a subsequent drop in flow stress after the peak corresponding to the softening process of grain boundary migration due to dynamic recrystallization. This stress drop in the stress-strain curve is more noticeable than that caused by dynamic recovery. Figure 3.14 shows the typical flow stress curves behaviour for work hardening, dynamic recovery and dynamic recrystallization. In part b) of the same figure, the characteristic microstructure evolution through the deformation of deformed and dynamically recrystallized grains.



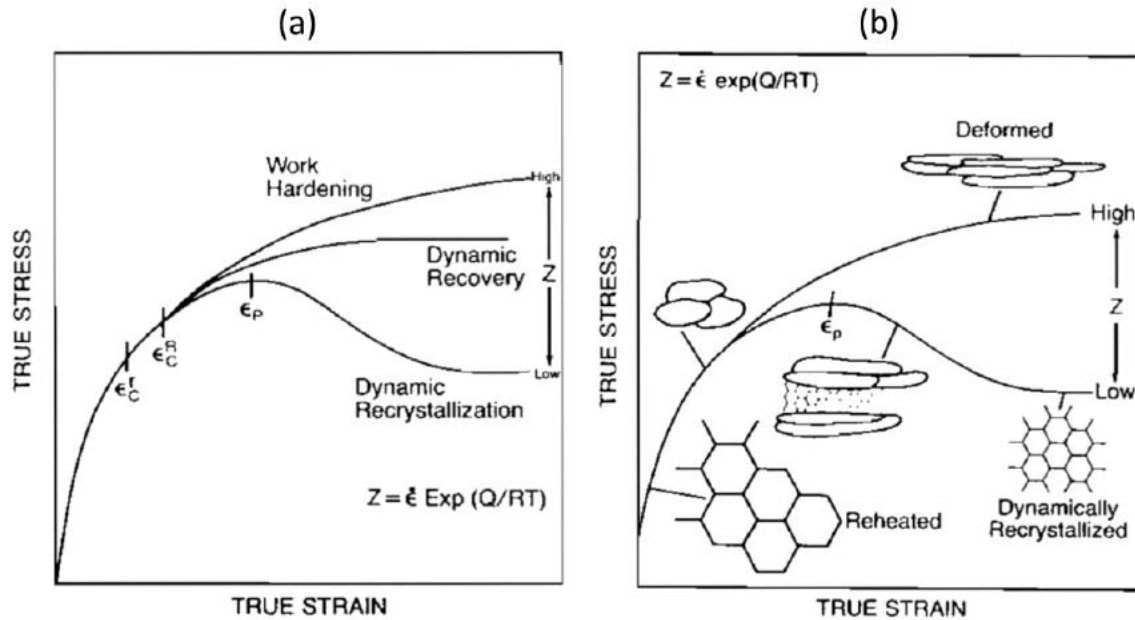


**Figure 3.14** Schematic diagrams of flow stress a) due to different metallurgical phenomena. b) Microstructure evolution through deformation depending on the processing parameters [33, 91]

Unlike dynamic recrystallization, the static recrystallization is carried out during holding time at high temperature after the deformation. From a practical point of view in hot processing, this time can be represented by the time between each deformation pass. There are different processing parameters influencing the static recrystallization conditions to take place. These parameters include the deformation temperature, strain and strain rate of deformation pass, the holding time at temperature after deformation, and the chemical composition due to the interaction with competing process such as precipitation. The effect of these parameters on the recrystallization will be discussed later in Section 6.2.1.

The recrystallization is a thermally activated process and the kinetics depend also on the processing parameters but generally needs an incubation period to nucleate subgrains with high-angle boundaries, then, a rapid growth of the new grains due to the high mobility of the high-angle boundaries. Later, the rate of recrystallization decreases toward completion as a concurrent recovery of the matrix occurs. The nucleation of the new grains is formed preferably at the original grain boundaries [92].

The importance of determining the recrystallization conditions falls in the austenite microstructure during hot working. The nucleation sites for the transformed products are mainly at the grain boundaries or zones of high strain. It is preferably to maintain the strain accumulation and fine austenite grains during deformation to create a large number of nucleation sites. This can be achieved by retarding or avoiding recrystallization through the control of the deformation parameters.

### **3.3.3. Grain growth**

When the recrystallization process is complete, the grain may start to grow if the material is kept at high temperature. This further reduces the stored energy in the material and the  $S_v$  is also lowered. If the temperature in the material decreases, the movement of grain boundaries is limited and thus, there is a slower growth rate of the recrystallized grains which results in finer recrystallized grains [93]. In microalloyed steels, grain growth is inhibited by precipitates or second-phase particles that pin the grain boundaries. Austenite grain growth is not a significant metallurgical phenomenon in strip rolling because the austenite grain size is determined by the recrystallized grains since interpass time in finishing rolling does not allow grain growth. However, the transition between roughing and finishing rolling deformations may offer the ideal conditions in terms of enough time and high temperature for grain coarsening [94].

## **3.4. Summary**

The literature review for this project focuses on the features and challenges to improve the mechanical performance of AHSS during the TMP, more specific of complex phase steels for automotive applications.

The control of the TMP parameters plays as a key role in the microstructure evolution. The competition between the different softening mechanisms and the formation of precipitates is

mainly influenced by these TMP parameters. On the other hand, the microalloying elements in the steel, together with the appropriate processing conditions, favour to better control in the microstructure evolution.

The recrystallization mechanism can be manipulated by the formation of fine precipitates in austenite, along with the control of the processing parameters. This is of vital importance during finishing rolling to accumulate the strain of the last deformation passes and to obtain a heavily work-hardened microstructure with a high  $S_v$ . A heavily deformed structure with high  $S_v$  increases the nucleation sites for ferritic phase transformations. This allows phase transformations to take place on the runout table in a short time and at high cooling rates, which is advantageous for industrial processing.

A strategic TMP route design for specific chemical composition, and the good control of the processing, especially during the runout table simulation, will develop the microstructure and mechanical properties aimed for a CP steel. The CP microstructure consists of a matrix composed of ferrite and bainite. Furthermore, there should be a considerable amount of martensite which provides the strength to the steel and, in some cases, retained austenite can also be present in relatively small amounts. The TMP route, as well as the volumetric fraction of these constituents, defines the mechanical properties of the material.

The present thesis focuses on the design and subsequent analysis of the microstructure evolution during TMP. This leads to the production of the corresponding microstructure and mechanical properties of a CP steel in particular chemical composition to make the most of the microalloying elements and the effect of processing parameters during TMP.

# CHAPTER 4

## EXPERIMENTAL PROCEDURE

### 4.1. As-received material: Phases and Microstructure Characterization

A CP800 steel plate was received coming from the company Ternium S.A. in Monterrey, Mexico. This plate was cut off from the strip after rough rolling in a reversible mill as a transfer bar condition (Figure 4.1). The as-received transfer bar had dimensions of 500x260x36 mm approximately, where the 260 mm length was the rolling direction (RD) and the 36 mm was the thickness.

The chemical composition of the transfer bar was reported to be within the range specified by the ASTM standard for a Complex Phase steel [26]. The transfer bar was sectioned by saw band (using a standard coolant and lubricant) into 3 segments after removing around 50 mm (2 inches) from the edge to discard the effects of the cutting torch. The first segment, of about 3 inches wide, was used for the initial characterization of the material and the other two sections served to machine specimens for plane strain compression and dilatometer tests, respectively.

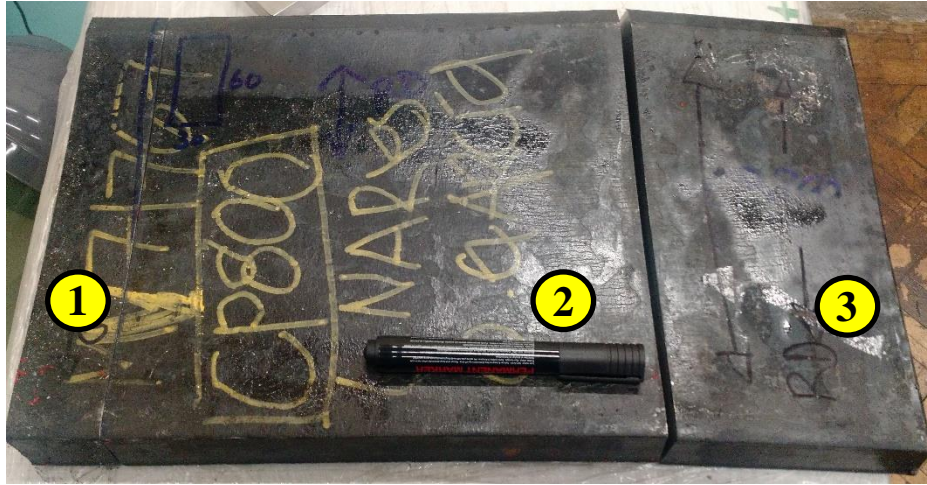


**Figure 4.1** Sectioned as-received CP800 transfer bar.

The first segment was sectioned with an abrasive disc cutter machine to obtain cubic samples of smaller dimensions of around 10 mm per side ( $1000 \text{ mm}^3$ ) so that they can fit in the different equipment used for the initial characterization.

#### **4.1.1. Quantitative Metallography**

The as-received material was characterized by different techniques to identify the initial microstructure and chemical composition.

##### *4.1.1.1. Optical Microscopy*

The Nikon Eclipse LV150 optical microscope was used to observe the microstructure at different magnifications. This microscope is equipped with objective lenses from 5X to 100X. For this technique, the sample is required to have a flat surface, so that, a special preparation was carried out and consists of the following steps:

1. Mounting the sample in conductive Bakelite to standardize the specimen dimensions to 32 mm of diameter. This with the objective that the arm of the automatic polisher can hold each of the specimens. This step is not compulsory, but it will aid and save a lot of time for subsequent steps. Conductive Bakelite was selected due to the specimen requirement for

later analysis via the Scanning Electron Microscopy where it has to easily allow the flow of electrons.

2. Surface grinding with silicon carbide (SiC) abrasive papers, which were placed on an automatic polish machine starting with grit number of 120, 220, 320, 500, 600 to 1000 cooling by water jet. Then, a mechanical polishing with cloths and diamond water-based suspension of 3 and 1 microns were used to remove all the stripes left on the surface by the grit papers. The polishing is completed until the mirror-like surface is obtained with no scratches on it. The parameters selected on the automatic polish machine during grinding (while using SiC abrasive paper) were 2 minutes per each grade of abrasive paper with a force of the specimen on the paper of 30 N. The head and platen keep rotating in the same direction at a speed of 60 and 300 revolutions per minute respectively. During polishing, the same force was used on the cloths. The rotating speed of the head was 40 rpm and for the platen was 110 rpm in opposite directions to avoid the comet tails effect. Polishing was carried out for 10 minutes each grade of diamond suspension, or until the specimen surface had a mirror-like finish. The water jet for cooling was not required during polishing.
3. Etching the sample reveals the microstructure and consists of covering the surface of the polished face with a reagent for a specific time. For this steel, two different solutions were used for the characterization.

The first solution was 2% nital, made by mixing 2 mL of nitric acid and 98 mL of ethanol at room temperature. The samples were sunk into the solution until a clear contrast change is observed in the freshly polished surface, this normally occurs in between 5 to 20 seconds of etching. This etchant is normally used in the field of steels to reveal the general microstructure.

The second etchant is called saturated aqueous picric acid solution and it allows to reveal the prior austenite grain boundaries for grain size analysis [95-98]. As its name implies, the solution is based on distilled water, and the main component is picric acid, also hydrochloric acid (HCl) and a wetting agent should be added to the solution. The amount of the substances to prepare this solution will depend on the chemical composition of the steel. An acceptable etching procedure for the CP800 was found based on several trials varying the amount of the different components and parameters. The preparation of the solution is described as follows: weigh 4.5 g of picric acid crystals at room temperature and pour into 100 mL of distilled water, stir for 3-4 min or until the

picric acid crystals are no longer dissolved, indicating the solution is saturated. After that, the wetting agent is added, in this case, 1 mg of sodium dodecyl sulfate was selected, at this time, a foam is formed on the surface of the solution, so it should be kept stirring until the foam settles down. The mix then is heated to a temperature between 80 to 90 °C, the remaining crystals and sulfate should be completely dissolved at around 60 °C. Then, carefully and aided by a pipette, 5 drops of HCl are added to the warm solution. It was noticed that the freshly made solution is too aggressive to the steel, so that, it needs to be matured by first etching 3 dummy samples for 5 min each. The solution is ready for etching when the colour has changed from bright yellow to dark yellow/orange, as shown in Figure 4.2. Prior austenite grain boundaries of CP800 steel are revealed after etching 60-70 s into the saturated picric acid solution.



**Figure 4.2** Saturated picric acid solution. Before (left) and after (right) maturing

After etching with any of the two solutions mentioned above, the sample must be rinsed with abundant water flow, then wash it with isopropanol and blow air to dry it. Once the sample is clean and dry, it is ready to be observed through the microscope.

#### 4.1.1.1.1. Prior Austenite Grain size – Linear Intercept Method

The prior austenite grain size (PAGS) is an important parameter to consider at the moment of designing a thermomechanical processing route. Once the austenite grain boundaries are successfully revealed following the methodology described in Section 4.1.1.1 using the aqueous picric acid solution as the etchant, the PAGS was determined according to the ASTM E112 standard [99].

PAGS were measured under the linear intercept method, which involves an actual count of the number of grains intercepted by a test line. The precision of grain size estimation by this method is a function of the number of grains counted.

In this study, a total of 8 tests lines were drawn in the metallography, 4 parallel and 4 perpendiculars to the rolling direction to measure the aspect ratio. The lines were drawn at a distance so that those parallels did not cross the same grain. In addition, for statistical analysis, at least 100 grain boundaries were counted in each metallography. The statistical analysis includes the results of the standard deviation for a 95% confidence interval. The aspect ratio was calculated as the average of PAGS measured parallel to the rolling direction divided by the average of PAGS measured perpendicularly to the rolling direction. Statistical analysis was followed as described in the ASTM E112 standard.

#### 4.1.1.2. Scanning Electron Microscope (SEM)

This characterization technique can give information such as the chemical composition, the size and the morphology of the phases that are present in the sample and have a relation with the properties. This microscope allows the observation of the surface and microstructure of the steel with greater detail compared with the optical microscope. The main advantage of SEM is the achievement of a higher amplification and resolution of the image than the optical microscope.

For the initial characterization, the sample used in SEM was the same observed by the optical microscope. The sample was prepared following the same procedure mentioned in 4.1.1.1. The images were obtained from the secondary electron detector (SEI) and backscattered electron



detector (BES). The FEI Inspect F50 SEM was operated in vacuum at a voltage of 30 kV, a spot size of 3 and a working distance between 9 and 11 mm.

Backscattered electrons are those that are scattered from the surface and can be collected as the primary beam scans the specimen surface. In the BSE image, the elements with a higher atomic number appear brighter than the elements with low atomic numbers.

On the other hand, secondary electrons are the result of the interaction of the primary beam with the electrons in the atoms of the specimen. SE have less energy compared with BSE and because of that, SE can only give information about the surface of the specimen. SE is useful to reveal surface topography [100].

Regarding the selection of acceleration voltage during SEM image acquisition, it is noted that a higher kV value was selected than is accustomed in the literature. This experimental decision was based upon a preference for images of higher resolution than those obtained at 15 and 20 kV. Although those kV values usually result in enough secondary electrons being generated on the surface to produce adequate sample topography, the objectives of the present work were better served by such settings. In other words, it was considered that the loss of secondary electrons was outweighed by the better resolution of higher kV values. In fact, the observation of the sample during acquisition informed the selection of the settings, including the working distance and acceleration voltage. In most cases, experimental decisions are based upon the objectives of the characterisation, as opposed to the customary operation settings of the equipment [101].

#### *4.1.1.3. Transmission Electron Microscopy (TEM)*

TEM analysis has been done in a Philips FEI Tecnai T20 whose features and capabilities are described in Table 4.1. The advantage of looking at the steel through TEM is the high magnification and good resolution of this kind of microscopes to obtain information from the material. The microscope was operated under the maximum capacity of accelerated voltage. Bright and Dark Field images were taken with a Gatan 782 ES500W Erlangshen camera. The camera consists of a retractable electron scintillator and a lens coupled CCD camera. The images were recorded via Digital Micrograph software.

**Table 4.1** Specification and Capabilities of Philips FEI Tecnai T20

Source	Thermionic (LaB <sub>6</sub> )
Acceleration voltage	200 kV
Point resolution	0.12 nm
Tilt	±40°
Magnification	50 to 730,000 X
Elemental analysis	N/A

#### 4.1.1.3.1. TEM sample preparation

The main requirement of the samples called “thin foil” for TEM analysis is that it must be as thin enough so that an electron beam of energy used in the microscope can pass through it. Because of this, the preparation of the sample is complex and laborious. The process to obtain a standard steel thin foil for the Philips FEI Tecnai T20 sample holder is explained in detail below.

First, a thin sheet of about 1 mm from the area of interest of CP800 was extracted using either an abrasive or a precision cutting disc. Then, the sheet needs to be ground to a thickness less than 0.5 mm. The easiest way to get that thickness was to stick the sheet on a base to be able to grind it manually on the grinding machine, this step can be done using the roughest SiC abrasive paper. A cylindrical aluminium base of 32 mm in diameter, the same dimension as mounted Bakelite, was heated on a plate up to a temperature that wax can be melted on it. The steel sheet was then put on the wax so it can be firmly held once the wax was cooled. When the thickness of the sheet was less than 0.5 mm, it was perforated into discs of 3 mm of diameter using a hole punch. After that, those discs were attached to a stainless steel 3 mm diameter sample holder to continue grinding with the finest SiC abrasive paper to a thickness range in between 0.08 to 0.12 mm. This step needed extra care because the disc can be easily damaged, fold or broken. This sample preparation technique is detailed in [102].

Finally, the discs needed to be electropolished to remove metal from the surface. The electropolishing automatically stopped when a hole was formed at the centre of the sample. This means the area near the edges of the hole is thin enough to transmit the electrons through it. The electrolyte selected for electropolishing the CP800 steel consisted of 60% of methanol, 35% of butoxyethanol and 5% of perchloric acid (HClO<sub>4</sub> 60%). The parameters to control in the twin-jet

electropolisher are 25 V, a flow rate of 16 at a temperature of -41°C and the current should range from 35 to 50 mA.

#### *4.1.1.4. Optical Emission Spectroscopy*

A piece with dimensions of around 25 x 25 x 10 mm cut from segment 1 of the as-received transfer bar was sent to an external company to analyse the chemical composition of the steel. Optical Emission Spectroscopy, or OES analysis, helps to determine the chemical composition of metal alloys. This method uses a sparking process, which involves applying an electrical charge to the sample and vaporizing a small amount of material. Once this spark occurs, a discharge plasma with a distinct chemical signature is created, allowing the determination of the elemental breakdown of the sample. Results of the analysis are given as a percentage breakdown of the constituent elements [103].

Gas Chromatography Mass Spectrometry, or GC/MS analysis, is a method used to determine trace and single elements in complex chemical mixtures. Rather than giving a full elemental breakdown, GC/MS focuses on one element or compound in a substance. GC/MS analysis was done in the CP800 to measure more precisely the amount of C.

GC/MS is a beneficial method for materials where a very small amount of the compound under test is suspected, or when 100% certainty of an element is required. Because of its singular elemental focus, GC/MS is considered one of the most accurate analyses for quantitative chemical composition [104].

#### **4.1.2. X-Ray Diffraction**

The X-ray diffraction is the technique that allows the identification of crystalline structures based on the diffraction Bragg's Law. This technique uses an X-ray beam of a certain wavelength to fall on the sample. The crystalline structure can be determined by the X-ray diffraction pattern since each crystalline phase are produced at a characteristic diffracted angle. The output data generated

by X-ray tests is a diffractogram of intensity (Y-axis) as a function of the diffraction angle ( $2\theta$ ). The diffractogram normally contains a series of peaks at different angles.

The sample for X-ray analysis was extracted by an abrasive cutter machine from the first segment mentioned above. The requirements of the sample for this technique are a flat and smooth surface and that the thickness is less than 5 mm. To meet these requirements, one of the faces was refined using a 320 grid paper.

For this technique, a Bruker D2 Phaser X-ray diffractometer was used. This machine is equipped with a copper source with a wavelength of 1.5418 Angstroms. For this analysis, the machine was operated with a voltage of 30 kV and a current of 10 mA. The data were collected in a range of  $2\theta$  from 20 to  $100^\circ$  every  $0.02^\circ$  with an analysis time of 30 minutes. The sample was kept rotating at a speed of 15 revolutions per minute to minimize the effects of preferential orientation and get a random orientation of the crystals. DIFFRACT.SUITE EVA software was used for the qualitative analysis of the pattern and the identification of the main peaks.

## 4.2. Critical Processing Temperatures

In order to meet the general objective of this study, it was necessary to define critical processing temperatures. These temperatures were considered critical due to the sensibility they have to alter the final microstructure of the strip after processing, which directly affects the mechanical properties. For example, phase transformation temperatures,  $A_1$  and  $A_3$  in equilibrium, but more important for processing purposes are the phase transformation temperatures during cooling, from austenite to ferrite,  $A_{r1}$  and  $A_{r3}$ . These temperatures will mainly depend on the chemical composition, grain size and cooling rates. Another critical temperature is the recrystallization-stop temperature or  $T_{5\%}$  which indicates when no recrystallization occurs. This temperature will depend on the chemical composition of the steel and the deformation parameters such as the amount of strain, the strain rate and the interpass time. Next, it will be explained how these critical processing temperatures were measured and calculated.

#### **4.2.1. Thermodynamic Analysis**

JMatPro<sup>®</sup> software [105, 106] (Java-based material properties) was used to model the CCT diagram and phase transformation temperatures of the CP800 steel. It also calculates the properties and the volume fraction of phases of the alloy. JMatPro<sup>®</sup> can calculate thermophysical and physical properties for a very large range of temperatures. It has the sensitivity to calculate properties in each phase of the alloy such as the volume fraction, thermal conductivity, Young's modulus and the Poisson's coefficient [107, 108]. The input data for properties calculation was the chemical composition, the range of temperatures to be analysed and the estimated grain size. The CCT diagram was obtained with chemical composition, austenitization temperature, and austenite grain size.

Thermo-Calc [109] was also used for comparison. Thermo-Calc is a simulation software where thermodynamic calculations can be performed. This software is useful for complex homogeneous and heterogeneous phase equilibria [110]. The input data for a calculation of phase diagram and volume fraction of phases was the chemical composition of the alloy and the range of temperatures to be analysed. For CP800 steel calculations, the databases used were TCFE8 v8.1 and MOBFE3 v3.0.[111].

#### **4.2.2. Determination of Phase Transformation Temperatures**

One method to measure phase transformation temperatures of steels is by dilatometry tests [112]. The technique consists of heating a specimen to a high temperature and then cool it back to room temperature. There are different types of commercial dilatometers. All of them should be able to heat and cool a specimen in a controlled atmosphere, program thermal cycles, inject inert gas or liquid for fast cooling and continuously measure the specimen dimension and temperature. The differences are in the heating method of the specimen, which can be either by induction or using resistance. In addition, the dilatometers can also differ in the design or dimensions of the specimens. A schematic representation of the configuration of the different heating methods for dilatometry tests can be seen in Figure 4.3. Dilatometry technique helps to identify length changes in the function of temperature due to the volume expansion or contraction of a given steel

geometry. Steel, like many other metals, dilates when is heated due to the thermal expansion effect, which normally has a linear trend. However, when a phase transformation occurs, there is a significant change in volume because of the rearrangement of atoms in the crystal lattice. During the phase transformation while heating, from ferrite (bcc) to austenite (fcc), there is noticeable shrinkage for the dilatometer measurements because the fcc structure has a larger packing factor than bcc. Thus, the first change in the displacement slope indicates that the phase transformation begins ( $A_{c1}$ ). For carbon steels, at equilibrium conditions, this should take place at approx.  $723^{\circ}\text{C}$ . These temperatures are characteristic of phase transformation due to the rearrangement of atoms in the crystal structure [113].

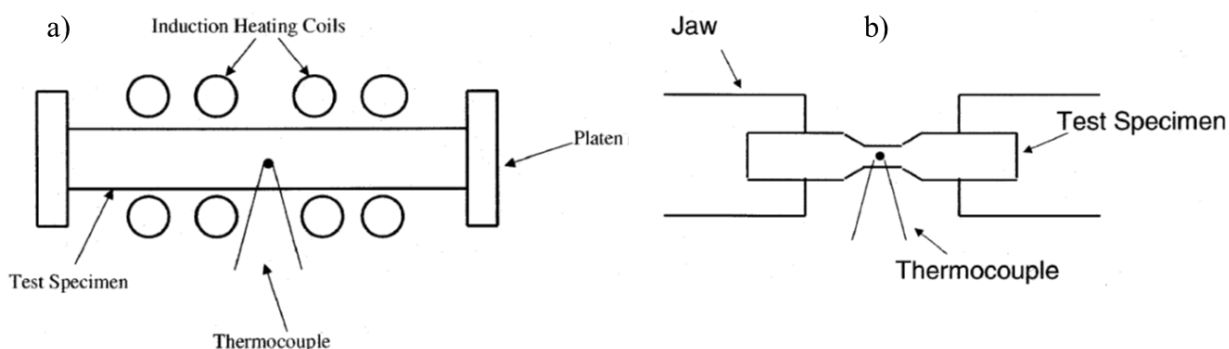


**Figure 4.3** Schematic configuration of heating methods for classical dilatometry testing using a) Induction heating and b) Resistance heating [112]

The dilatometer equipment for this analysis has an induction coil to heat the specimen (Figure 4.4). A PID controller which follows the set point previously loaded into the machine for heating and cooling. A displacement sensor is used during the test to measure the changes in length across the longitudinal direction of the specimen. The cooling rate can be controlled by a cooling system in the machine which is able to cool down by water jet (quench), air blowing (slow cooling) or a combination of both (mist) for intermediate cooling rates. This dilatometer has two options to measure the temperature to follow the set point; by a K-Type thermocouple and by a pyrometer. For this analysis, the K-type thermocouple was selected to follow the set point due to it measured the temperature at the centre of the specimen. Pyrometer was also monitored for a reference during the tests.

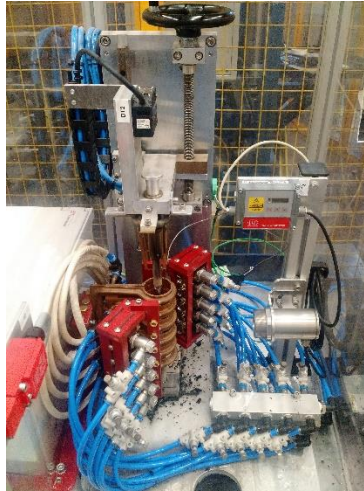


**Figure 4.4** Dilatometer used to measure the length change of the samples.

Cylindrical bars were sent to machine from segment 3 of the as-received transfer bar. The dimensions of the bars were 12 mm in diameter by 155 mm in length and with a hole of 1.6 mm to go to the centre of the bar to place the thermocouple (Figure 4.5). The 155 mm length is parallel to the rolling direction. Then, these bars were drilled on the centre of both faces using a 7 mm drill bit by 5 mm depth approx. This is to be able to hand by the dilatometer holder sample. The K-type thermocouple, 310 stainless steel sheath, 1.5 mm in diameter, was placed inside the bar and plug to the dilatometer to measure the temperature for every test.

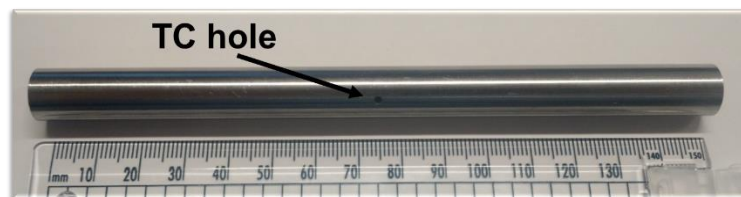


**Figure 4.5** Dilatometer sample of CP800 after machining. Length is parallel to the rolling direction. The scale showed is in mm

The test design for this technique was the austenitization of the steel, so the bars were heated up to 1000°C, at a heating rate of 10°C/s, hold for 3 minutes to homogenize the temperature through

the bar, and then cool down to room temperature at different cooling rates of 0.1, 1, 10 and 20°C/s. The heating parameters were selected to ensure the austenite transformation by heating above the  $A_3$  temperature. The holding time at 1000°C tries to homogenize the temperature of the specimen and at the same time to limit the likely austenite grain coarsening at high temperature. A schematic representation of the heat treatment is shown in Figure 4.6.

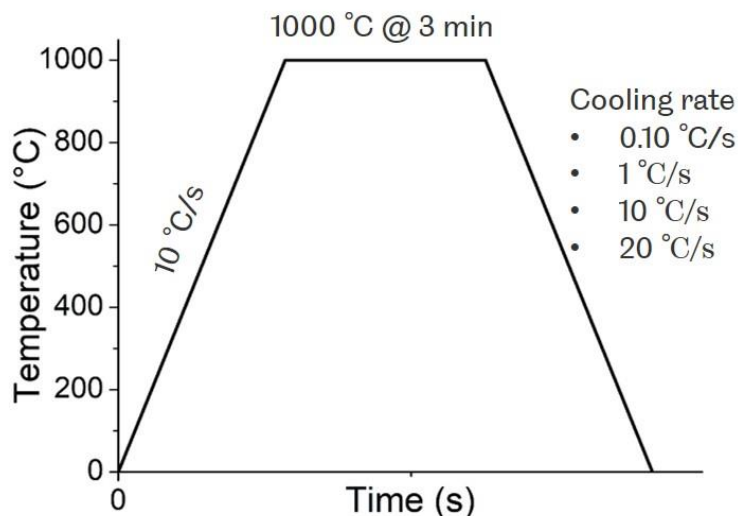


**Figure 4.6** Schematic heat treatment for dilatometer tests.

The output information from every dilatometry test was recorded for every second and includes the time, set point temperature, recorded K-type thermocouple temperatures and displacement. One method to measure  $A_1$  and  $A_3$  is to plot the displacement vs time or temperature. During heating, the dilatation of the bar should increase the displacement over time, and the initial phase transformation is obvious when the slope becomes negative due to the shrinkage. At that point, the corresponding temperature is indicative of  $A_{c1}$ . After that, the graph becomes non-linear. The end of the phase transformation during heating ( $A_{c3}$ ), i.e. when there is fully austenitic microstructure, is the corresponding temperature when the plot turns linear again and has a positive slope with a clear trend. On the other hand, the opposite effect should occur during cooling, finding  $A_{r3}$  first and then  $A_{r1}$ . These temperatures have a strong dependence on the cooling rate. Figure 4.7 shows an example of the data obtained from a dilatometry test. The changes in the slope are indicated



and represent the start and finish phase transformation temperatures for both during heating and cooling of the specimen.

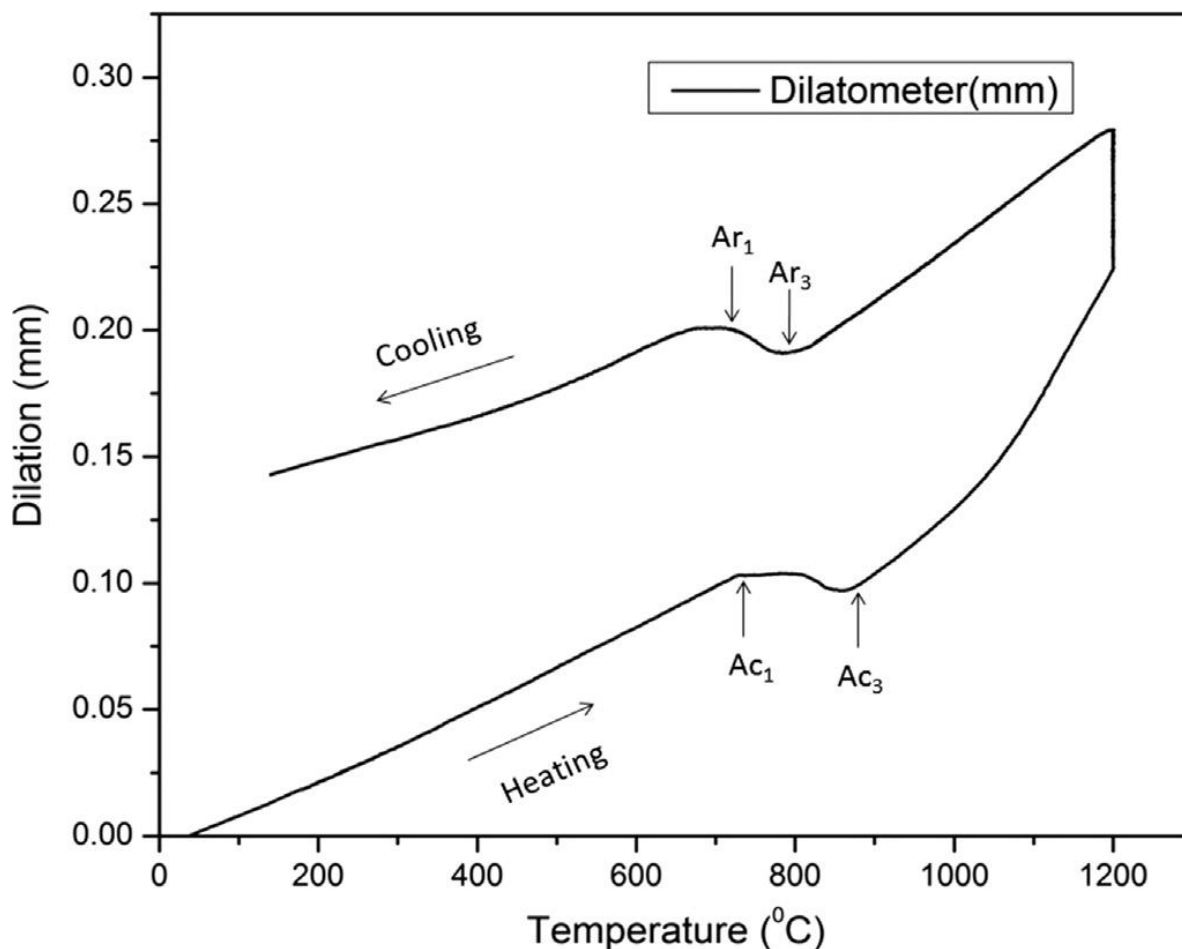


**Figure 4.7** Dilatometry curve for a microalloyed steel obtained through thermomechanical simulator Gleeble 3800 [114]

Also, there are empirical formulas written by several authors to make a quick calculation of these critical transformation temperatures. These formulas are commonly based on the chemical composition of the steel, and some others include parameters such as cooling rate and austenitic grain size. The empirical formulas applied in this study for the calculation of  $A_{R3}$ , the initiation of ferrite transformation, are described in Table 4.2.

**Table 4.2** Equations of  $A_{r3}$  described by different authors. Alloy content is specified in weight %

Author	Equation	Notes
Choquet [115]	$A_{r3} = 902 - 527 C - 62 Mn + 60 Si$	
Mintz [116]	$A_{r3} = 833.6 - 190.6 C - 67.4 Mn + 1522 S - 2296 N_{ti} - 1532 Nb + 7.91 d_{\gamma}^{-\frac{1}{2}} - 0.117 CR$	$N_{ti} = N_t - \frac{Ti}{3.5}$ where $N_t$ = total Nitrogen content $d_{\gamma}$ = Austenite grain diameter (mm) CR = Cooling rate(°C/min)
Mintz 2 [116]	$A_{r3} = 868 - 181 C - 75.8 Mn + 1086 S - 3799 N_{ti} - 1767 Nb - 0.0933 CR$	
Sekine [63]	$A_{r3} = 868 - 396 C - 68.1 Mn + 24.6 Si - 36.1 Ni - 24.8 Cr - 20.7 Cu$	
Shiga [117]	$A_{r3} = 910 - 273 C - 74 Mn - 56 Ni - 16 Cr - 9 Mo - 5 Cu$	
Yuan non-deformed [118]	$A_{r3} = 370 \exp\left(-\frac{\sqrt{D_{\gamma}}}{6.7}\right) - 325 CR^{0.1} - 5649 Nb + 78194 Nb^2 + 1019$	$D_{\gamma}$ = Austenite grain diameter ( $\mu\text{m}$ ) CR = Cooling rate (°C/s)
Ouchi [119]	$A_{r3} = 910 - 310 C - 80 Mn - 20 Cu - 15 Cr - 55 Ni - 80 Mo + 0.35(h-8)$	h = Plate thickness in mm

#### 4.2.3. Recrystallization-Stop Temperature ( $T_{5\%}$ )

The recrystallization-stop temperature,  $T_{5\%}$ , should be firstly defined to design a complete thermomechanical route for the microstructural evolution studies in the CP800. A proper method to calculate and measure  $T_{5\%}$  is through double hit tests. Double hit tests results can be used to calculate the softening percentage between the two passes. The softening of the material is directly related to  $T_{5\%}$  [120].

A double hit test consists of deforming a plane strain compression (PSC) specimen in two passes at the same temperature and the same amount of strain and strain rate at a known interpass time. For CP800, double hit tests were performed as follow: reheat the specimen to 1200°C into the

FTTU (Fast Thermal Treatment Unit) at a heating rate of 10°C/s, hold at 1200°C for 2 min, then the samples were air-cooled to different testing temperatures from 920°C to 1000°C. Afterwards, the specimen was smashed twice at the same temperature, controlling the time between the passes. After the second pass, the specimen was immediately water quench to room temperature.  $T_{5\%}$  was evaluated for different deformation parameters through double hit test by varying the strain per pass and interpass time as specified in Table 4.3. The strain per pass varies from 0.25 to 0.40, and the interpass time from 4 s to 20 s while the strain rate remained constant at 10 s<sup>-1</sup> in every pass. The schematic thermomechanical route for double hit tests is shown in Figure 4.8.

**Table 4.3** Deformation parameters to evaluate  $T_{5\%}$  on double hit tests

	<b>Deformation Temperature (°C)</b>	<b>Strain per pass</b>	<b>Interpass time</b>	<b>Strain rate</b>
<b>Set 1</b>	920, 950, 980, 1000	0.25	20 s	10 s <sup>-1</sup>
<b>Set 2</b>	980, 1000, 1020	0.25	4 s	10 s <sup>-1</sup>
<b>Set 3</b>	950, 980	0.40	4 s	10 s <sup>-1</sup>

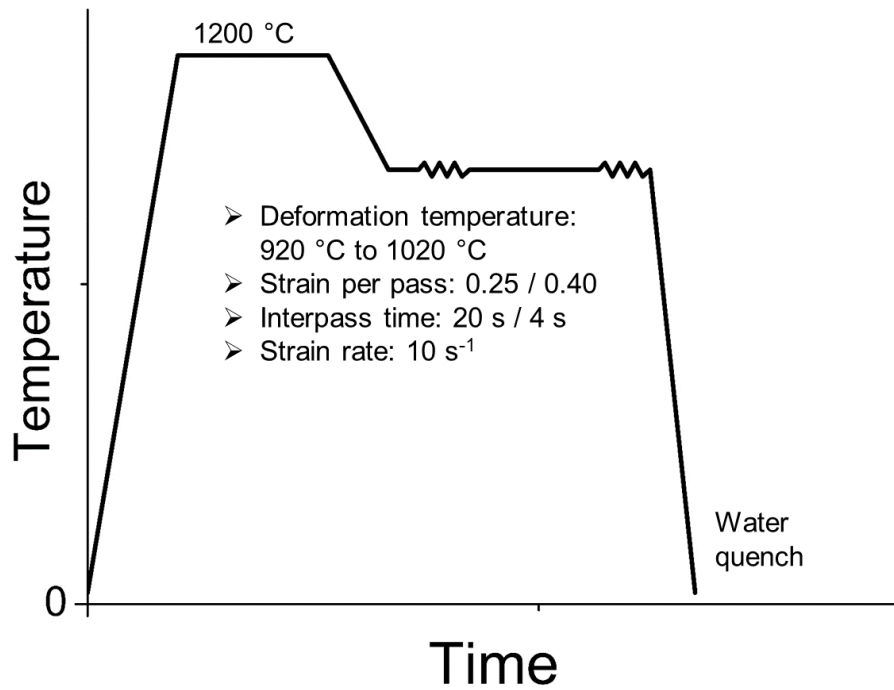


**Figure 4.8** Thermomechanical route of the Double hit tests

The thermomechanical compression (TMC) machine (Figure 4.9) from Servotest Ltd was utilized to carry on the simulation of the hot rolling process and double hit tests. This servo-hydraulic machine has outstanding control of the processing parameters such as deformation temperature, strain, strain rate and interpass time. TMC is useful to replicate almost any thermomechanical route. TMC is equipped with an FTTU which is used for the heat treatment of the specimen. The FTTU has induction coils to heat the sample and the cooling could be done by forced air, water jet or a combination of both.



**Figure 4.9** Thermomechanical compression machine for plane strain compression (PSC test)

The specifications of the TMC machine are given in Table 4.4.

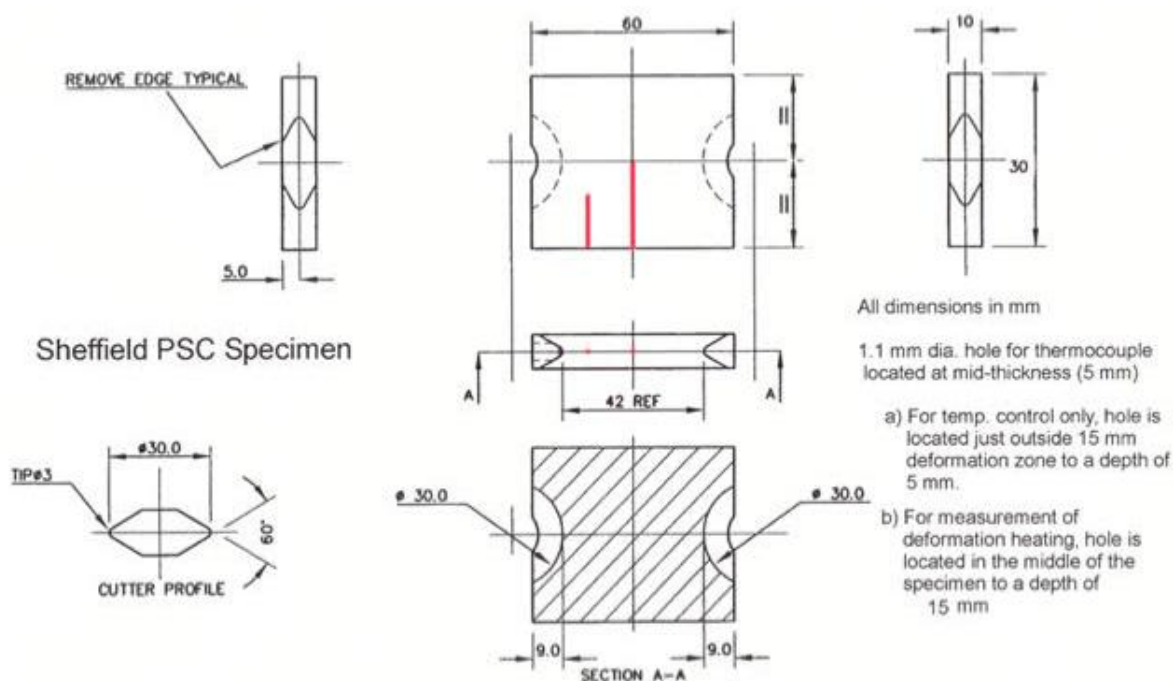
**Table 4.4** TMC general specifications

<b>TMC Specifications</b>	
Actuators	Servo-hydraulic
Maximum Strain	2
Maximum Strain rate	200 s <sup>-1</sup>
Maximum Temperature	1200 °C
Maximum Load	500 kN
Cooling methods	Forced air/water jet/mist
Temperature Control	Up to 3 thermocouples

More detail of the capabilities and operation of the thermomechanical machine used for plane strain compression at the University of Sheffield can be found in the following sources [121-124].

The specimens for the PSC testing were machined from segment 2 of the as-received transfer bar following the sketch in Figure 4.10. For the purposes of this work, the 60 mm length needed to be parallel to the rolling direction of the transfer bar. The hole for the thermocouple was done in the centre of the sample to take into account the deformation heating.

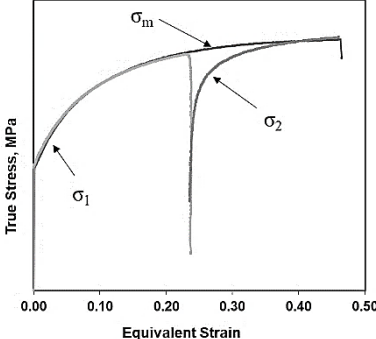
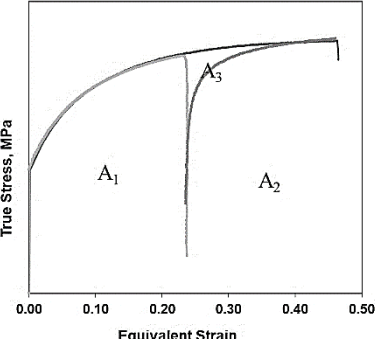
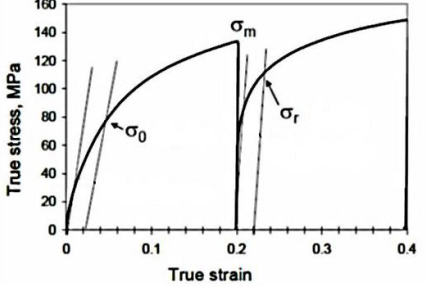
The selected data to record for each test include time, temperature, load, displacement and velocity. These data were then analysed to make corrections following the best practice developed by Loveday et al [125-127] and get the flow stress behaviour during the deformation.



**Figure 4.10** Geometry of the PSC samples

There are different approaches to evaluate the softening after the double hit, a summary of the methods applied in this work is described in Table 4.5.

**Table 4.5** Different methods to calculate the fraction softening of a double hit test.

<p>A<sub>1</sub>) 2% Strain Method [128, 129]                      A<sub>2</sub>) 5% Strain Method [58]</p> $\%Soft = \frac{\sigma_m - \sigma_2}{\sigma_m - \sigma_1}$ <p><math>\sigma_m</math> = Stress at the equivalent 2%/5% strain of the second deformation on the single pass tests.  <math>\sigma_1</math> = Stress at 2%/5% strain of the first deformation  <math>\sigma_2</math> = Stress at 2%/5% strain of the second deformation</p>	
<p>B) Area under the flow stress curve [128]</p> $\%Soft = \frac{A_3 - A_2}{A_3 - A_1}$ <p><math>A_1</math> = Common area under the flow stress curve of the first deformation in double hit test and the part in the single pass test to the same strain level.  <math>A_2</math> = Area under the flow stress curve of the second deformation in double hit test.  <math>A_3</math> = Area under the flow stress curve of the single pass test equivalent to the strained region of the second deformation of double hit test.</p>	
<p>C) Offset Method 2% [58]</p> $\%Soft = \frac{\sigma_m - \sigma_r}{\sigma_m - \sigma_0}$ <p><math>\sigma_m</math> = Max stress of the first deformation  <math>\sigma_1</math> = stress at 2% plastic strain of the first deformation  <math>\sigma_2</math> = stress at 2% plastic strain of the second deformation</p>	

There are also empirical formulas which give a hint of what the  $T_{5\%}$  is. Some of these formulas are described in Table 4.6.

**Table 4.6** Empirical equations to estimate  $T_{5\%}$ . Alloy content is specified in weight %

Author	Equation	Notes
Boratto et al. [130]	$T_{5\%} = 887 + 464C + (6445Nb - 644\sqrt{Nb}) + (723V - 230\sqrt{V}) + 890Ti + 363Al - 357Si$	
Bai [131]	$T_{5\%} = \left\{ 174 \log \left[ Nb \left( C + \frac{12}{14} N_{eff} \right) \right] + 1444 \right\} - 75$	$N_{eff} = N - \frac{14}{48} Ti$
Fletcher [132]	$T_{5\%} = 849 - 349C + 676\sqrt{Nb} + 337V$	
Militzer [133]	$T_{5\%} = 893 + 910Nb$	
Dutta & Palmiere [120]	$T_{5\%} = 936\varepsilon^{-0.014}$	$\varepsilon = \text{true strain}$

#### 4.2.3.1. Recrystallized Fraction – Point Count Method

$T_{5\%}$  was also validated through the observation of the prior austenite grain microstructure at the centre of the deformed specimen. The process to get metallographies from a representative area of deformation in the PSC specimen will be described in Section 4.4.

The metallography is divided into two areas: austenite recrystallized grains and austenite deformed/elongated or non-recrystallized grains. The point count method is based on counting the points that fall in the area of interest in a random array of points.

For the recrystallized fraction of the PSC specimens, a grid consisting of 9 perpendicular lines to the rolling direction and 7 parallel lines to the rolling direction were drawn into the metallography. The parallel lines to rolling direction were placed at a distance so that they did not cross the same grains. The points to count are the intersection of the grid, so each metallography has 67 points to decide how many fall in the austenite recrystallized area. Those points in the recrystallized austenite area counted as 1, those in the non-recrystallized area as 0. Points lying on the grain boundary of a recrystallized grain were counted as 0.5. An example of the grid array in a PSC metallography is shown in Figure 4.11. The austenite recrystallized fraction with the 95% confidence interval is measured following the ASTM E562 standard procedure [134].



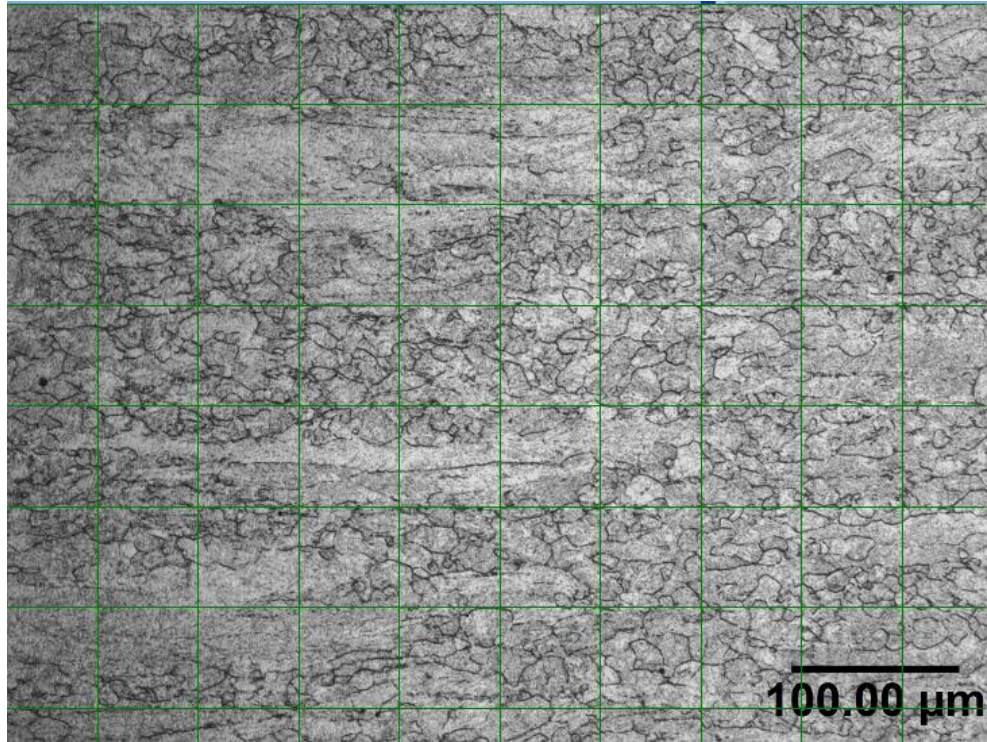


**Figure 4.11** PSC metallography to measure the recrystallized fraction by point count method. Metallography showing 50% of austenite recrystallized area.

### **4.3. Hot Rolling Simulation**

The complex phase microstructure is commonly developed after a thermomechanical treatment of the steel. In order to optimize material and time that an industrial practice could take, hot rolling simulations with plane strain compression method were carried out at a laboratory scale using a world-leading TMC machine already described in Section 4.2.3.

### 4.3.1. Plane Strain Compression (PSC) Testing

Plane strain compression testing is a technique to replicate similar conditions of deformation to a plate or strip rolling. PSC testing can generate data to analyse the mechanical properties of the CP800. PSC testing consists in deforming a specimen at a controlled temperature, defined amount of strain and strain rate to measure the hot flow stress. A schematic representation of PSC testing is shown in Figure 4.12. The PSC specimen geometry was identical to the specimens used for the determination of  $T_{5\%}$ , the dimensions were described in Figure 4.10.

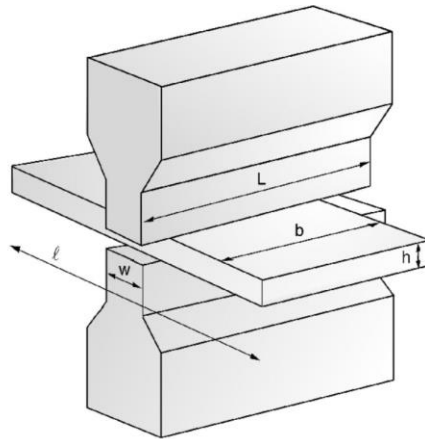


**Figure 4.12** Representative diagram of plane strain compression testing.

The experimental design for PSC tests includes the finishing rolling and the runout table or controlled cooling. This is because the as-received transfer bar had been already processed through the rough rolling mill.

Finishing passes should be carried out at temperatures below  $T_{5\%}$  to develop high mechanical properties [67]. Strain accumulation and high dislocation density increase the nuclei sites for the phase transformation to either ferrite or bainite.

The thermomechanical route for the finishing rolling must be designed in a range of temperatures. At an industrial scale, if the deformation temperature is too high, it would be

complex to maintain the strip at that temperature, in contrary, if the deformation temperature is too low, it would be complicated to deform the slab due to the required excessive force in the mill.

A thermomechanical route was designed of 4 passes for the evaluation of microstructural evolution. This consists of reheating the PSC specimens up to 1150 °C at a rate of 10 °C/s. This temperature was chosen because 1150 °C is a typical value at the end of the rough rolling. After that, the specimen was left for 2 minutes at 1150 °C for homogenization. Then, specimens were air-cooled at 20 °C/s to the first pass temperature,  $T_{5\%}$ . Before the first pass deformation, the sample was held for 5 seconds at  $T_{5\%}$  to stabilize the temperature.

The strain rate for all passes was  $10 \text{ s}^{-1}$ . The time between each pass was 4 seconds to be closer to the industrial practice. The temperature difference between the first pass and the last pass was around 100°C. The total strain, i.e. the accumulation of 4 passes, would be 1.1 as maximum due to dimensional restrictions of the PSC specimens. The strain per pass was planned as follow, 0.4, 0.3, 0.2 and 0.2. A representative sample (water quench) was taken at different stages of the TMP route to observe the austenite microstructure evolution. The schematic TMP route is represented in Figure 4.13. During the deformation, PSC specimens may stick to the tools of the TMC, to avoid this, Boron Nitride spray was applied as a lubricant on all PSC specimens before each test.

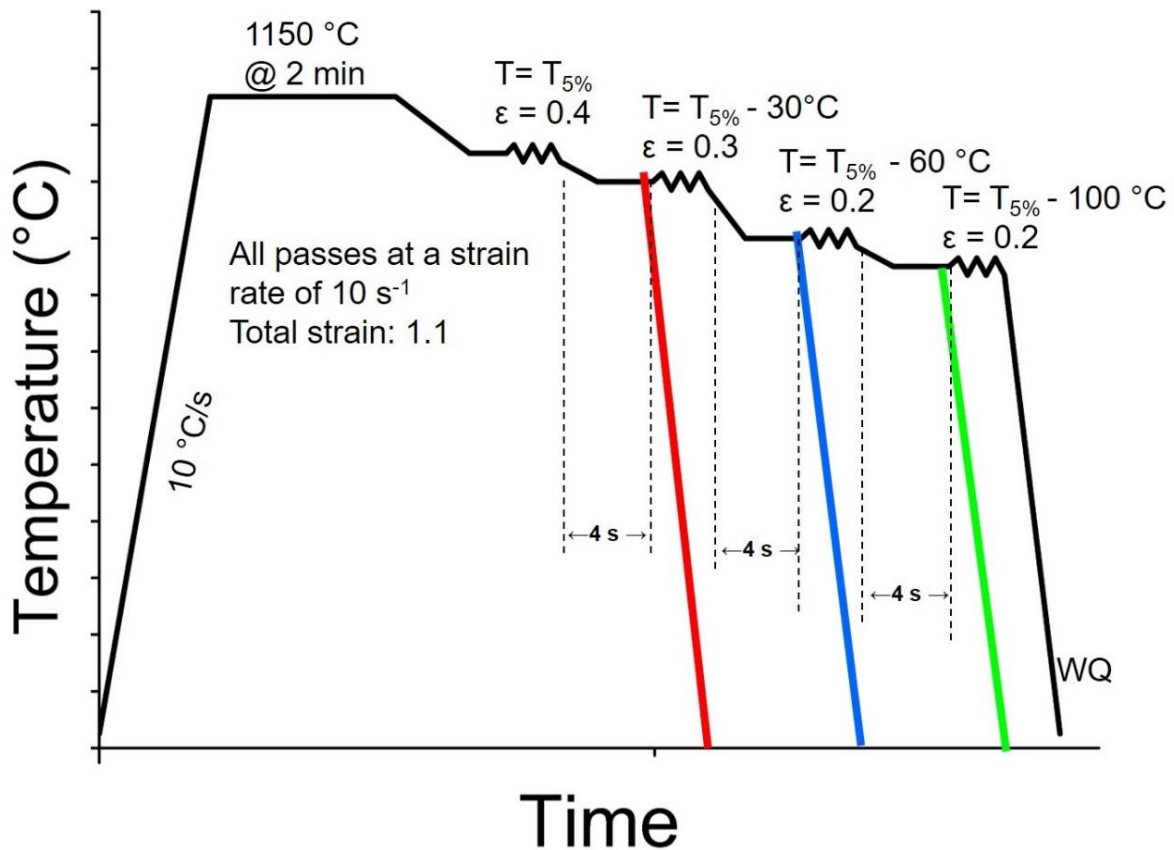


**Figure 4.13** Schematic TMP route for CP800. Coloured lines represent water quench specimens for the evaluation of austenite microstructure evolution

Different controlled cooling strategies after the fourth pass were planned to obtain the microstructure of a CP steel. The simulation of the runout table comprises a stepped cooling after the last pass, first cooling at  $100\text{ }^\circ\text{C/s}$  until temperatures related to bainitic transformation. Then, the specimen was held at that temperature for 13 seconds with the intention of transform bainite. This was followed by a water quench to room temperature to transform the remaining austenite into martensite. The summary of the different tested conditions is better described in Table 4.7.

**Table 4.7** Strategies to obtain CP microstructure during thermomechanical processing.

Specimen	Description
SC1	Last deformation pass at $T_{5\%} - 100\text{ }^{\circ}\text{C}$ , step cooling at $550\text{ }^{\circ}\text{C}$ for 13 seconds
SC2	Last deformation pass at $T_{5\%} - 100\text{ }^{\circ}\text{C}$ , step cooling at $500\text{ }^{\circ}\text{C}$ for 13 seconds
SC3	Last deformation pass at $A_3$ , step cooling at $550\text{ }^{\circ}\text{C}$ for 13 seconds
SC4	Last deformation pass at $A_3$ , step cooling at $500\text{ }^{\circ}\text{C}$ for 13 seconds
SC5	Last deformation pass at $A_3$ , step cooling at $500\text{ }^{\circ}\text{C}$ for 60 seconds

#### 4.4. Characterization after PSC Testing

As PSC specimens were too large for a metallographic investigation, they were sectioned by abrasive disc after the deformations as shown in Figure 4.14 to analyse a representative area of deformation.

The representative area of deformation was chosen to be at the centre of the specimen in the longitudinal section of the rolling direction. This section is helpful to measure the degree of grain deformation, the aspect ratio of grains from the hot-rolled product.

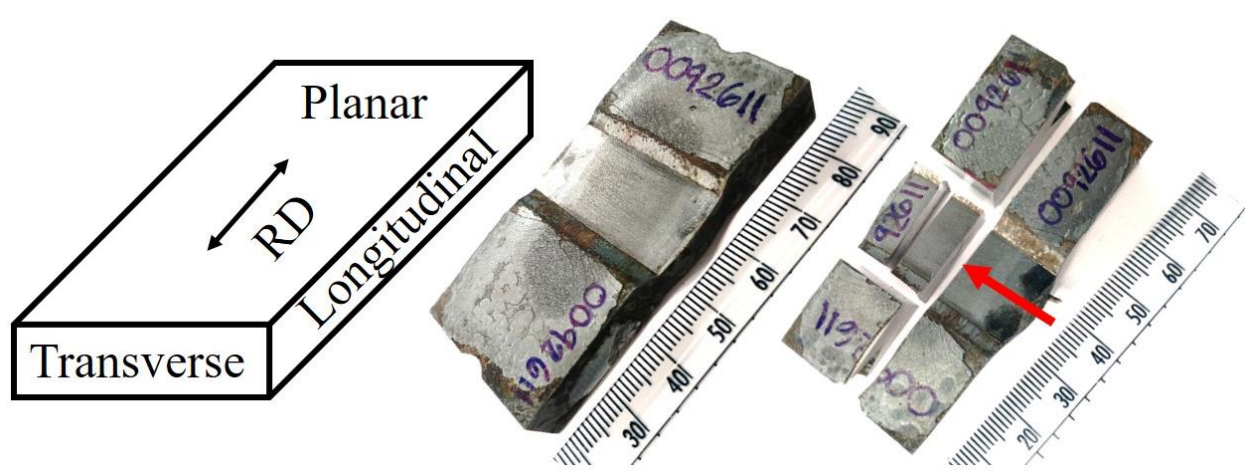


**Figure 4.14** The three planes in a rolled product. Rolling direction is indicated with the double-headed arrow. PSC specimen after deformation and all sectioning steps to mount the longitudinal face indicated by the red arrow. Bar scales are in mm.

Characterization after PSC testing includes the techniques of optical microscopy, SEM and TEM already explained in 4.1.1 but also hardness evaluation and EBSD analysis which will be described later in this chapter.

#### **4.4.1. Microstructure Evolution through TMP**

Representative PSC samples were taken through TMP to observe the evolution of austenite as shown in Figure 4.13. This includes 5 different samples: one sample after the 2 minutes at 1150°C, one sample after each pass (first, second, and third pass) including the interpass time to the next deformation, and one sample immediately water quenched after the fourth pass. All deformation passes were carried out in the austenite phase. For the austenite microstructural evolution analysis, the PSC specimens were sectioned as explained in Section 4.4 to obtain a representative area of the deformation. The specimens followed the metallographic preparation mentioned in Section 4.1.1.1 and the aqueous picric acid solution was used as an etchant. PAGB were analysed by optical microscope and SEM. PAGES was measured in the parallel and perpendicular to rolling direction following the linear intercept method already described in Section 4.1.1.1. Phase transformation behaviour is directly influenced by the distance between the PAGB thus, altering the CCT diagram of the CP800 steel.

Additionally, PSC samples of the complete TMP route were also analysed. Complete TMP route includes the samples with total strain accumulation of 1.1 in 4 passes and different controlled cooling strategies as described in Table 4.7. The metallographic preparation of these specimens was the same except that the etching procedure was done with 2% nital solution to reveal the microstructure. In addition to optical microscopy and SEM, specimens with the complete TMP route were also analysed by EBSD, TEM, and also went through an evaluation of mechanical properties by tensile and hardness tests.

#### **4.4.2. Analysis of Crystallographic texture and deformation by Electron Backscattered Diffraction (EBSD)**

More detail of the microstructure developed during the TMP was studied by EBSD analysis. EBSD consists of the acquisition of diffraction patterns [135]. The EBSD data was collected using an FEI Inspect F50 SEM microscope operated at 20 kV. Due to the dimensional limitations of the EBSD specimen because of its holder, it was necessary to do extra cuts of the PSC specimen using a precision cutter. The EBSD specimen must not exceed 10 mm by 5 mm in the longitudinal face and the thickness must be less than 5 mm. The specimen was mounted in Bakelite for easier metallographic preparation, as an extra step to the standard procedure, the EBSD specimens were polished with colloidal silica during 30 minutes after the last polishing step. Then, the Bakelite was carefully broken in a manual press to avoid scratches on the specimen. Finally, the specimens were ultrasonic cleaned for a period from 10 to 15 min in isopropanol.

The specimen was introduced into the microscope as the normal operation of the SEM but then, it was tilted to 70° where additional backscattered electron detectors are required to produce a significant diffraction pattern. The specimen should be correctly attached to the EBSD holder to avoid movement of the specimen while tilting. Once tilted, the working distance of the microscope should be calibrated with the EBSD detector.

Flamenco software from Channel 5 was used for EBSD collection data. BCC old and FCC phases were chosen for indexing. The step size, i.e. the pixel size of the digitised microstructure, for all specimens was 0.2 µm. Finer microstructure detail is acquired decreasing the step size, but this would significantly increase the operation time. The data was post-processed using the HKL Channel 5 software package.

#### **4.4.3. Evaluation of Mechanical Properties**

##### *4.4.3.1. Hardness*

Hardness is an indicator of the resistance of a material to plastic deformation induced by applied forces. Two different methods for hardness evaluation were considered, the Vickers microhardness

to get an overall measurement of the specimen, and the nanoindentation hardness for identification of smaller phases.

Vickers microhardness measurements were conducted via Durascan 70 G5. The selected force to make the indentations was 0.01 kgf, equivalent to 0.098 N or HV0.01. The diagonal lengths of the indentation are measured to calculate the Vickers hardness. These measurements are converted to HV under Eq. 2 as explained in the ISO 6507 standard for Vickers hardness test [136].

The sample condition for Vickers microhardness measurements was polished and 2% nital etched.

$$HV = \frac{\text{Tests force (kgf)}}{\text{Surface area of deformation (mm}^2\text{)}} \quad (2)$$

Nanoindentation test is a technique to determine the mechanical properties of small features from load-displacement measurements. The nanohardness values are calculated similar than the Vickers microhardness test, from the penetration depth of the indentation. For nanoindentation, the applied loads and the geometry of the indenter changes. This provides an indirect measure of the area of contact at full load [137, 138].

The Berkovich indenter was chosen for CP800 nanoindenter measurements. Specimens were subjected to a maximum load of 500  $\mu$ N for 5 seconds. Surface morphologies of the specimens were observed by atomic force microscopy, allowing to select the area of interest for the indentation.

The roughness of the surface specimen is an important factor for nanoindentation tests, so a special surface specimen preparation was carried out before each test. Specimens followed the preparation procedure mentioned in Section 4.1.1.1, with an extra polishing step using colloidal silica for 10 to 15 min. Afterwards, specimens must be ultrasonically cleaned for at least 15 min followed by an electrochemical polishing. The electrolyte selected for electropolishing was the I-1 from the ASM Handbook V9 and consists of 200 mL of ethanol, 35 mL of distilled H<sub>2</sub>O and 15 mL of HClO<sub>4</sub> (60%) [139], specimens were subjected to 10 V.



#### 4.4.3.2. Tensile tests

The tension test is used to evaluate the mechanical properties of materials. The tensile test is about applying tensile force on a specimen and measure the elongation up to the eventual fracture. The tensile test specimens are gripped from opposite ends within the load frame of a test machine.

Tensile specimens come from the remaining half of the deformed PSC specimens (refer to Figure 4.14). Slides of 2 mm thickness at the centre of the deformation were machined by Electric Discharge machining (EDM) to provide stress-free cut. The axis in tension was parallel to the rolling direction.

Tensile tests were performed in a Zwick Roell Z050 kN, with a load cell of 21 kN limit for the grippers (Figure 4.15). The gauge was manually placed on the specimens using a pair of solid wires glued at the centre of the PSC deformation with a distance of  $10 \pm 1$  mm from each other as shown in Figure 4.16. The gauge length was monitored and recorded during the tests by a non-contact video extensometer camera attached to the tensile machine. As the CP800 tensile specimens have smaller dimensions than those specified in the ASTM E8 standard for sub size specimens, the crosshead speed was adjusted in the machine so that the strain rate met the requirement in the ASTM E8 standard [140]. Because of that, the crosshead speed for every test of the CP800 was set to 0.00375 mm/s. Initial and final cross-section measurements were got by a digital Vernier.



**Figure 4.15** Tension machine Zwick Roell Z050

The output data from the tensile tests include the load vs extension of the gauge. These parameters are used to get the engineering stress ( $\sigma$ ) and engineering strain ( $\epsilon$ ) (Eq.3 and Eq.4.)

$$\sigma = \frac{P}{A_0} \quad (3)$$

Where P is the axial tensile load in Newton, and  $A_0$  is the initial cross-section area of the specimen.

$$\epsilon = \frac{L_f - L_0}{L_0} = \frac{\Delta L}{L_0} \quad (4)$$

Where  $L_f$  and  $L_0$  are the final and initial gauge length.

Four main properties were calculated from the flow stress engineering curve. The yield strength ( $YS_{0.2\%}$ ) was determined by drawing an offset line at 0.2% strain of the elastic part of the flow stress curve. The  $YS_{0.2\%}$  value is the stress at which the offset intersects the flow stress curve. The Young's modulus (E), which is the slope at the elastic part of the curve and follows the Hook's Law behaviour (Eq.5).

$$E = \frac{\sigma}{\epsilon} \quad (5)$$

The ultimate tensile strength (UTS), which is the maximum value of  $\sigma$  in the curve, from this point, the specimen starts to necking. The total  $\epsilon$  to the fracture of the specimen is considered as the ductility of the specimen. The ductility of the specimen is reported as % elongation of the gauge length (%EL) or % reduction in the cross-section area (%RA) (Eq.6 and Eq.7).

$$\%El = \frac{\Delta L}{L_0} \times 100 \quad (6)$$

$$\%RA = \frac{A_0 - A_f}{A_0} \times 100 = \frac{\Delta A}{A_0} \times 100 \quad (7)$$

Where  $A_f$  is the cross-section area of the specimen at fracture.

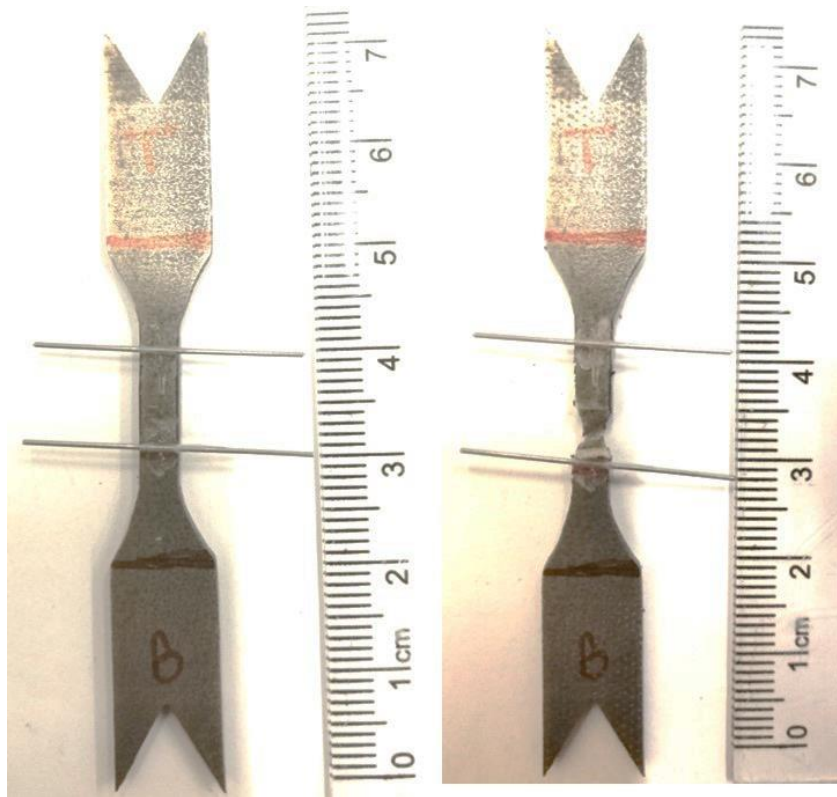


**Figure 4.16** Tensile specimen from PSC specimen before and after the tensile test. Pins are attached at the centre for extension measurements. Scale bar is in centimetres

# CHAPTER 5

## RESULTS

### 5.1. Initial Characterization

The as-received CP800 transfer bar was characterized by different techniques in its longitudinal direction. Optical microscopy images using 2% nital and the aqueous picric acid solution etchants are observed in Figure 5.1 and Figure 5.2. The general microstructure shows a complete martensitic structure, which means that the transfer bar was quenched after the rough rolling. The PAGS of the as-received transfer bar is  $46 \pm 5.7 \mu\text{m}$ . The transfer bar has an equiaxed grain structure of aspect ratio near unity. This suggests that rough rolling would have taken place under conditions for full recrystallization of the austenite grains.

SEM and TEM micrographs, in Figure 5.3 and Figure 5.4 respectively, confirmed the martensitic structure showing fine laths and plate structure which is typical of martensite. The laths have their origin and end point at the boundary of either packet of martensite or PAGB. Martensite is formed as a consequence of rapid cooling from austenite. In the industrial process, the strip is cropped after hot roughing and the transfer bar falls into a pit with water and therefore it is quenched.

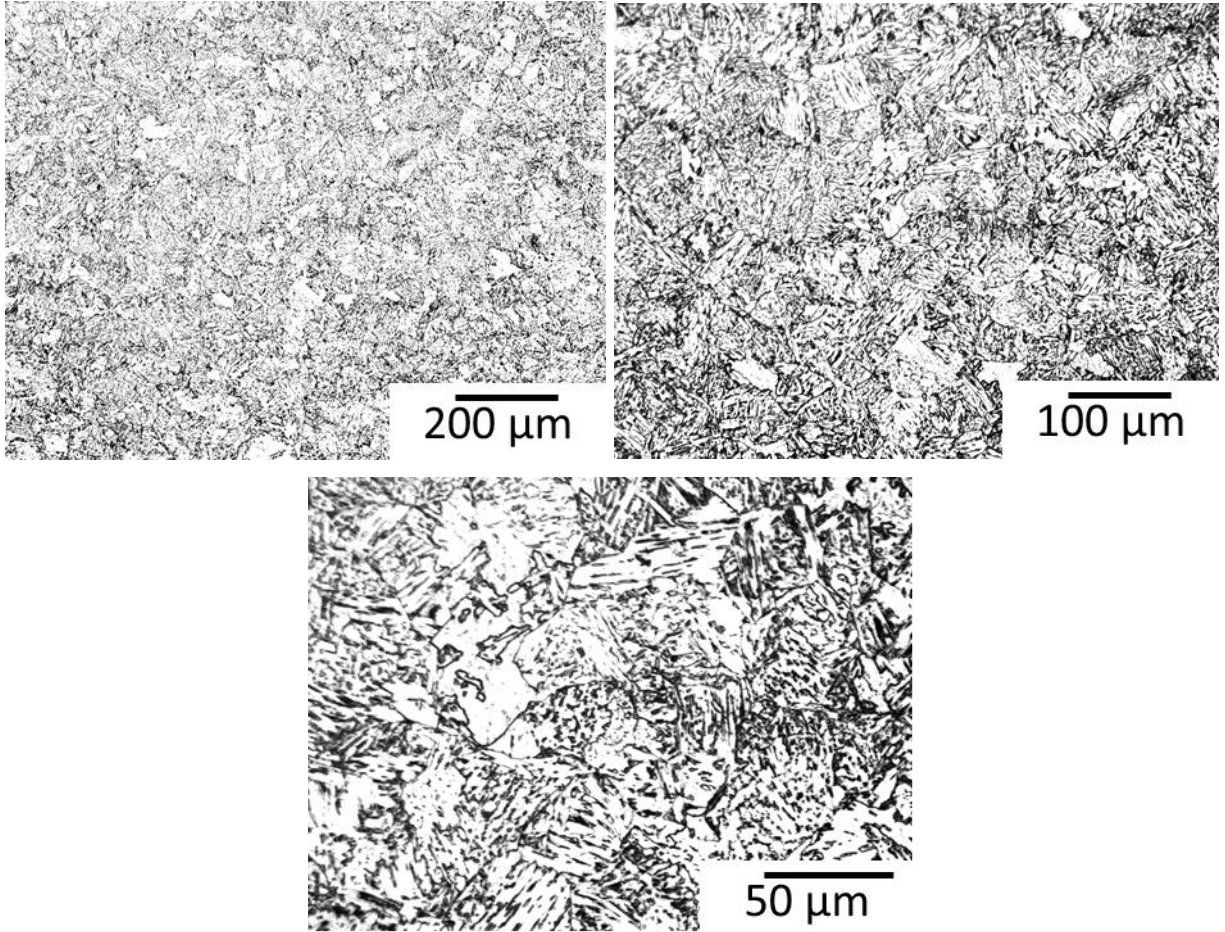


**Figure 5.1** As-received CP800 transfer bar microstructure. Etchant: 2% Nital.

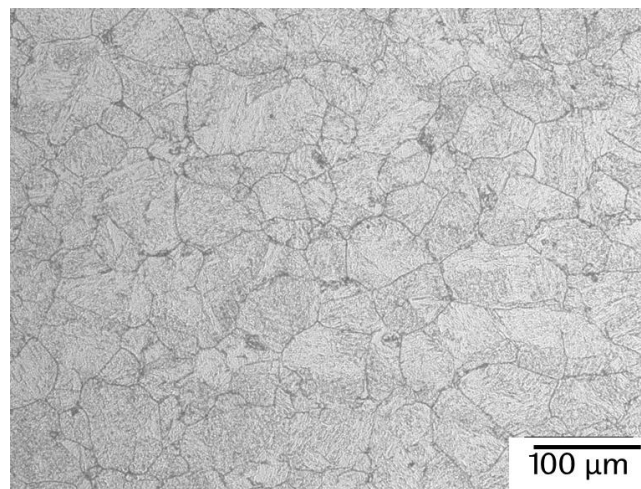


**Figure 5.2** PAGB of CP800 as-received transfer bar. PAGS =  $46 \pm 5.7 \mu\text{m}$ . Etchant: Aqueous picric acid solution.

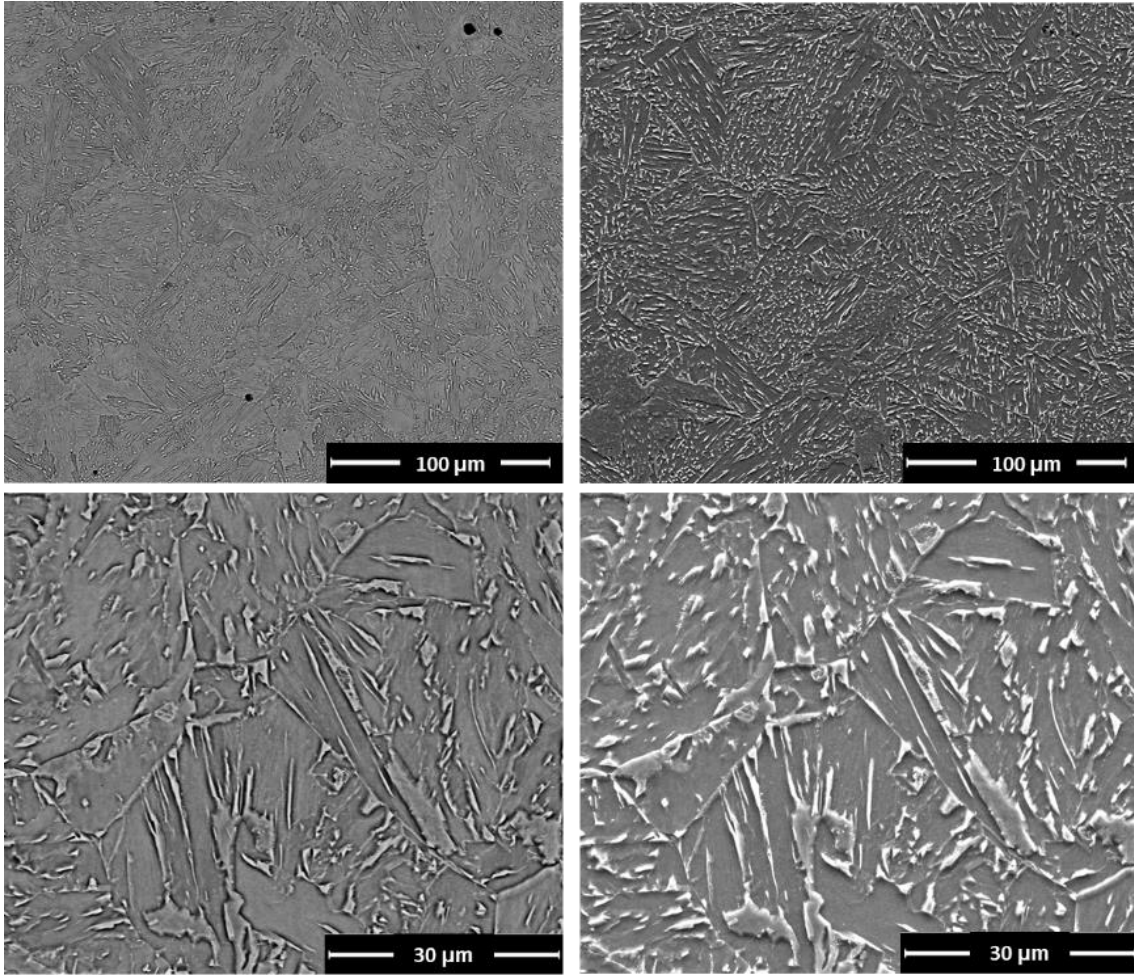


**Figure 5.3** SEM images of the as-received CP800 transfer bar. Backscattered electrons (left) and secondary electrons (right).

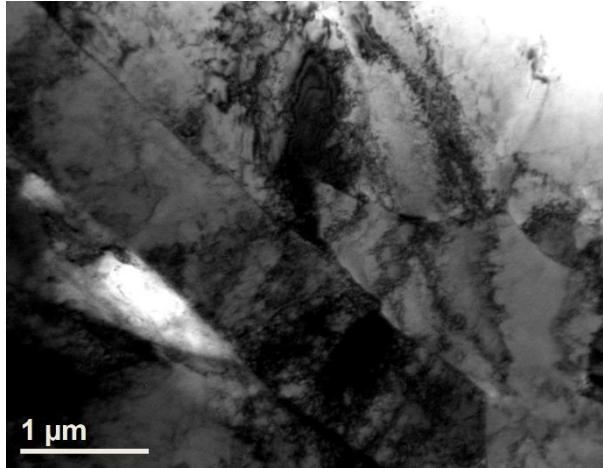


**Figure 5.4** TEM bright field image of lath martensite of the as-received CP800 transfer bar.

The X-ray diffractogram showed in Figure 5.5 reveals peaks at different angles of diffraction. The main peaks were observed at  $2\Theta$  angles of 44.6, 65, 82.3 and a small peak at 99 approximately. These peaks are characteristic of Fe crystal structures. Microstructures and XRD diffraction pattern show that there is no precipitation in the as-received condition of the CP800. This might be due to the high processing temperatures where all alloying elements were in solution.

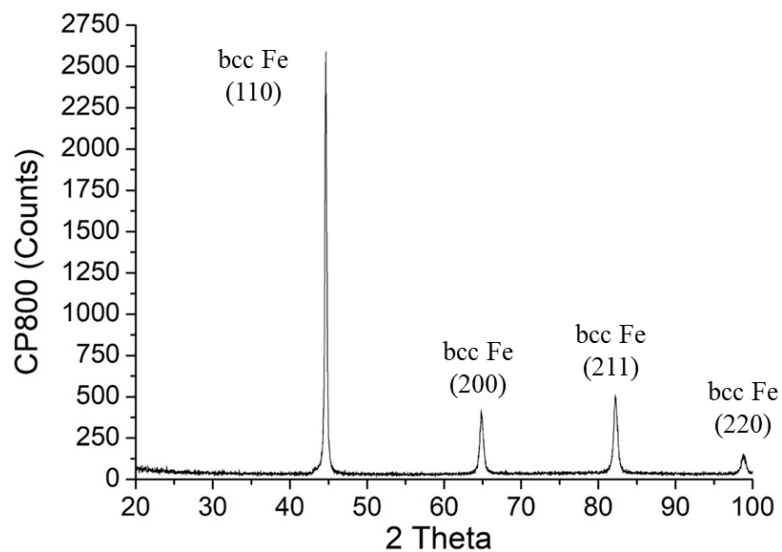


**Figure 5.5** X-ray diffraction pattern of the as-received CP800 transfer bar.

The chemical composition analysis by optical emission spectroscopy and GC/MS is shown in Table 5.1, and it is specified in weight per cent. Alloying elements are added to steels to improve the strength and ductility. Manganese is an austenite stabilizer and may decrease the phase transformation temperature. Mo and Cr are commonly added to increase steel hardenability. Niobium, Titanium and Vanadium microalloying elements are prone to form carbides. Those microalloying elements will retard the recrystallization and grain growth processes.

**Table 5.1** Chemical composition of as-received CP800 transfer bar.

<b>Element</b>	<b>C</b>	<b>Si</b>	<b>Mn</b>	<b>P</b>	<b>Cr</b>	<b>Mo</b>	<b>Ni</b>	<b>Ti</b>	<b>Nb</b>	<b>V</b>	<b>N</b>
<b>%Wt</b>	0.07	0.14	1.83	0.012	0.21	0.13	0.02	0.02	0.06	0.01	0.0035

## 5.2. Phase Transformation Temperatures

Temperature and displacement measurements in the dilatometer were plotted over time for every test. Figure 5.6 shows the test results for the dilatometry specimen cooled at 10 °C/s. It was noticed that during the heating at low temperatures, the thermocouple measurements follow perfectly to the set point, but at around 700 °C, the heating rate slightly drops. This could be explained by different reasons, one of them is because the coils need more energy to continue raising the temperature. Also, this could be due to the latent heat that the steel utilizes for the phase transformation since the phase transformation from martensite to austenite is an endothermic reaction. Another reason could be because of the magnetic field affecting the induction coils when the specimens reach the Curie point temperature. The real cooling rate was measured as the temperature slope in the cooling region. At the end of the test, during cooling, at around 200 °C, there is a fluctuant behaviour on the length change. This was due to the bad reading measurements of the thermocouple at this stage. As no phase transformation is expected below this temperature, that region was discarded for the cooling rate calculation. The summary of the dilatometry results and the measured phase transformation temperatures are shown in Table 5.2. As the heating rate on every test was set to 10 °C/s, there is no significant change in  $A_{c1}$  and  $A_{c3}$  for all tests being around 780°C and 840°C, respectively. The temperature during heating on the specimen cooled at



20 °C/s was not recorded correctly, however,  $A_{r3}$  and  $A_{r1}$  would be measured during the cooling. The slower the cooling rate the higher the phase transformation start temperature during cooling. This is because, at slow cooling rates, the steel tends to reach a thermodynamically stable equilibrium condition and the supercooling effect decreases the atomic diffusion velocity [141].

**Table 5.2** Summary of dilatometry tests for the CP800.

<b>Specimen</b>	<b><math>A_{c1}</math> (°C)</b>	<b><math>A_{c3}</math> (°C)</b>	<b><math>A_{r1}</math> (°C)</b>	<b><math>A_{r3}</math> (°C)</b>	<b>Real cooling rate (°C/s)</b>
0.1 °C/s	782	841	674	755	0.1
1 °C/s	781	838	604	710	1
10 °C/s	805	848	480	672	9.88
20 °C/s	N/A	N/A	496	641	14.12

The  $A_{r3}$  calculations based on the equations described in Table 4.2 are summarized in Table 5.3, where the Yuan's is the most accurate approach for the cooling rates of 10 °C/s and 20 °C/s compared with the dilatometry results, even though Yuan's equation is limited to steels with less amount of Nb than the CP800 has.  $A_{r3}$  measurements of the test with a cooling rate of 1 °C/s is within a range comparable to the predictions of Sekine. Choquet and Shiga, who does not consider the cooling rate in their empirical formula, are the closest to the  $A_{r3}$  temperature measured by the dilatometer at the slowest cooling rate of 0.1 °C/s. The initial phase transformation temperatures predicted by Mintz at cooling rates of 10 °C/s and 20 °C/s are in the temperature range that can be related to a bainite transformation instead of ferrite. It is important to mention that some of these formulae have different restrictions to be applied to the CP800 steel studied in this work. For example, some of them do not consider the cooling rate or are restricted to a defined range of cooling rates. Dilatometry tests have demonstrated that this parameter is crucial for the measurements of phase transformation temperatures. Other considerations for the formula imply that they can only be applied to steels with a certain range in chemical composition or certain PAGS. These are some of the reasons the  $A_{r3}$  estimation is imprecise from the  $A_{r3}$  measured by dilatometry.

The calculation of phase transformation temperatures by software simulations is shown in Figure 5.7 a) and b) for JMatPro® and Thermo-Calc packages, respectively. Both software shows very similar results on the phase transformation temperatures at thermodynamic conditions.  $A_3$  was defined as 832°C by JMatPro® and 835°C by Thermo-Calc, whilst  $A_1$  is predicted to be 665°C for both software. In addition, it was observed that most of the alloying elements are in solution at temperatures above 1220°C except for the MN compound that remains stable in a quantity less than 0.02%. It is important to remark these temperatures are established for thermodynamic steady conditions.

The CCT diagram for the CP800 steel (Figure 5.8) was calculated with the JMatPro software under the conditions of the dilatometry experiments, i.e., austenitization temperature of 1000 °C and PAGS of 45 µm. As dilatometry tests showed, the cooling rate has a direct effect on the  $\gamma \rightarrow \alpha$  transformation temperature. Dilatometry data was added to the CCT diagram and are marked as red asterisks. The  $A_{r3}$  temperatures obtained in the dilatometer are in the range of those calculated by JMatPro for the different cooling rates.

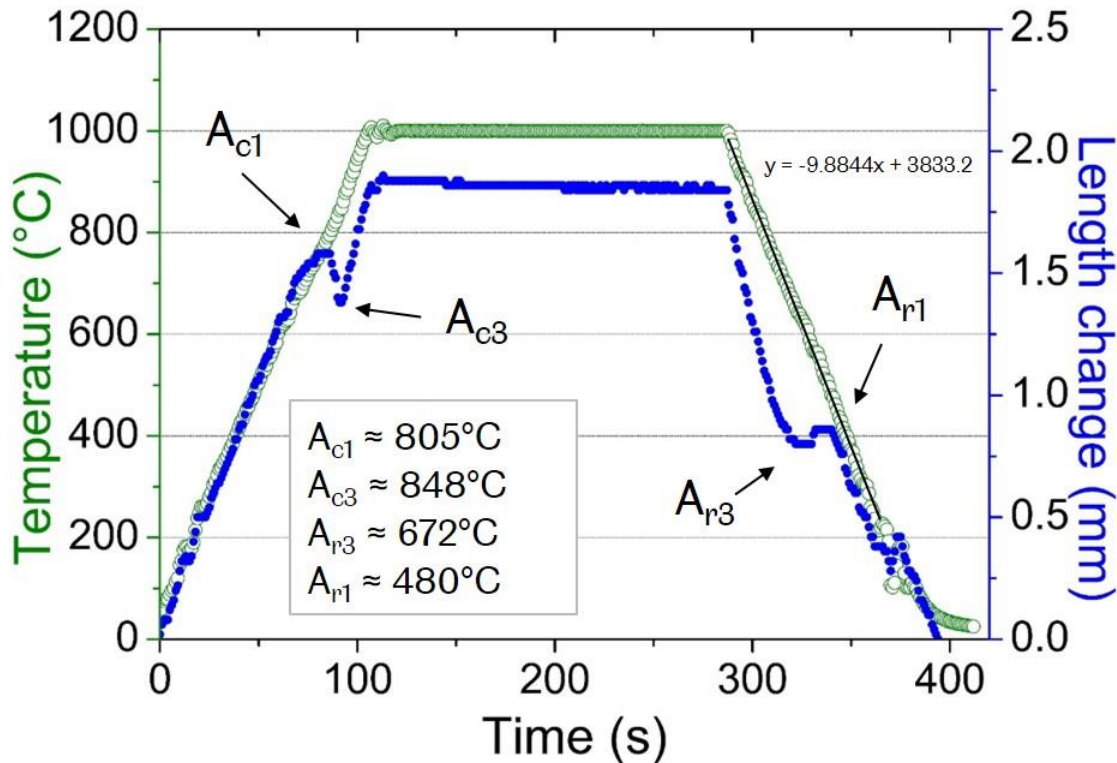


**Figure 5.6** Phase transformation measured by dilatometry for CP800 cooled at 10 °C/s.

**Table 5.3** Estimation of  $A_{F3}$  for the CP800 chemical composition and initial PAGS of 46  $\mu\text{m}$ .

Author	Cooling rate ( $^{\circ}\text{C/s}$ )				Notes / Useful ranges
	0.1	1	10	20	
Choquet [115]	760 $^{\circ}\text{C}$				Do not consider cooling rate
Mintz [116]	653 $^{\circ}\text{C}$	647 $^{\circ}\text{C}$	584 $^{\circ}\text{C}$	514 $^{\circ}\text{C}$	Mn (0.3 – 1.6 %), grain size (70 – 950 $\mu\text{m}$ ), and cooling rate (0.4 – 3 $^{\circ}\text{C/s}$ )
Mintz 2 [116]	623 $^{\circ}\text{C}$	618 $^{\circ}\text{C}$	568 $^{\circ}\text{C}$	512 $^{\circ}\text{C}$	Nb (0 – 0.042 %) and cooling rate (0.1 – 3 $^{\circ}\text{C/s}$ )
Sekine [63]	713 $^{\circ}\text{C}$				Do not consider cooling rate
Shiga [117]	749 $^{\circ}\text{C}$				Do not consider cooling rate
Yuan non-deformed [118]	837 $^{\circ}\text{C}$	771 $^{\circ}\text{C}$	686 $^{\circ}\text{C}$	657 $^{\circ}\text{C}$	Nb (0 – 0.038 %) and cooling rate (0.5 – 30 $^{\circ}\text{C/s}$ )
Ouchi [119]	725 $^{\circ}\text{C}$				Plate thickness = 3 mm

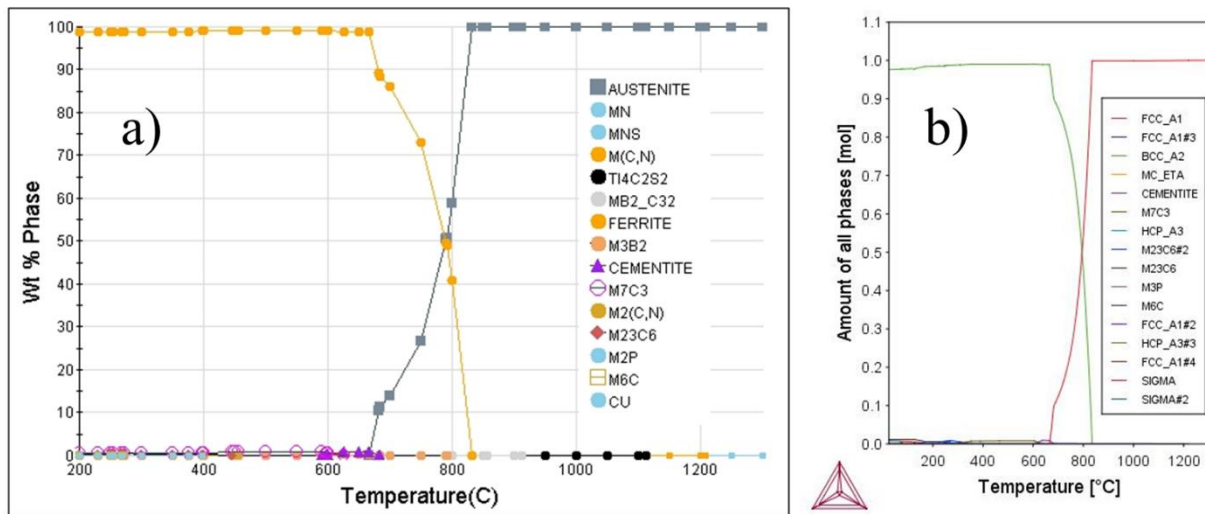


**Figure 5.7** Thermodynamic equilibrium diagrams calculated by a) JMatPro and b) Thermocalc for CP800 chemical composition.

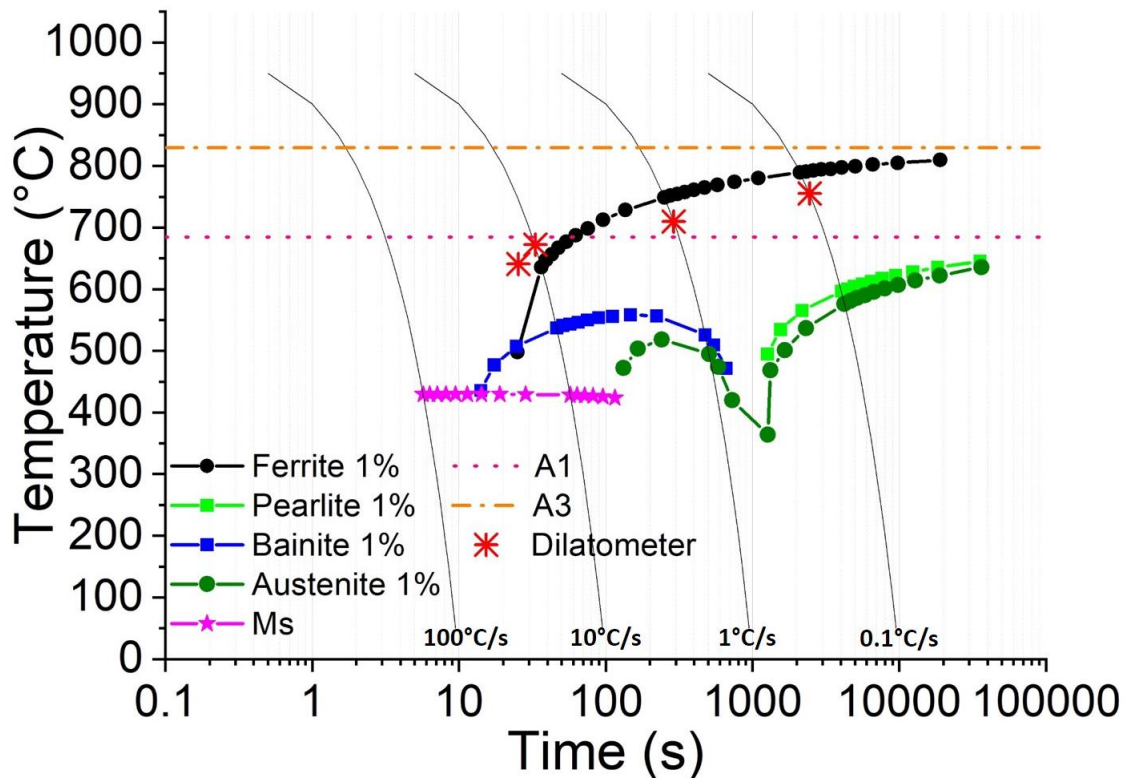


**Figure 5.8** Continuous Cooling Transformation diagram from JMatPro® for the CP800. Austenitisation temperature: 1000 °C, PAGS: 45 µm. Red asterisks represent actual dilatometry measurements.

### 5.3. Recrystallization-Stop Temperature ( $T_{5\%}$ )

As defined before, the recrystallization-stop temperature ( $T_{5\%}$ ) is the maximum temperature at which no more than 5% of recrystallization is observed in austenite grains at certain deformation conditions.

$T_{5\%}$  was determined through the evaluation of two different methodologies: Double hit tests to measure the fraction softening and the observation of the PAGB on the microstructure.

### **5.3.1. Flow Stress of Double and Single Hit Tests**

Flow stress curves of single and double hit tests corresponding to deformation parameters of set 1 are shown in Figure 5.9 for the temperatures 920°C, 950°C, 980°C and 1000°C. The initial stress value in each of the tests is an indicator of the yield stress at that specific temperature. At higher temperatures, less load is required to deform the material [142]. At 1000°C the maximum stress is about 200 MPa whereas at 920°C the maximum stress in the curve is up to 250 MPa. The 950°C single and double hit tests show a discrepancy at the start of the curve i.e. the strain of the first pass. This difference could be minimized by adjusting the friction coefficient but, since all tests were analysed with a friction coefficient of 0.25 (used for the Boron Nitride [143]), the softening analyses were done using this value although the amount of lubricant applied on the specimens could have been considerably different in both tests.

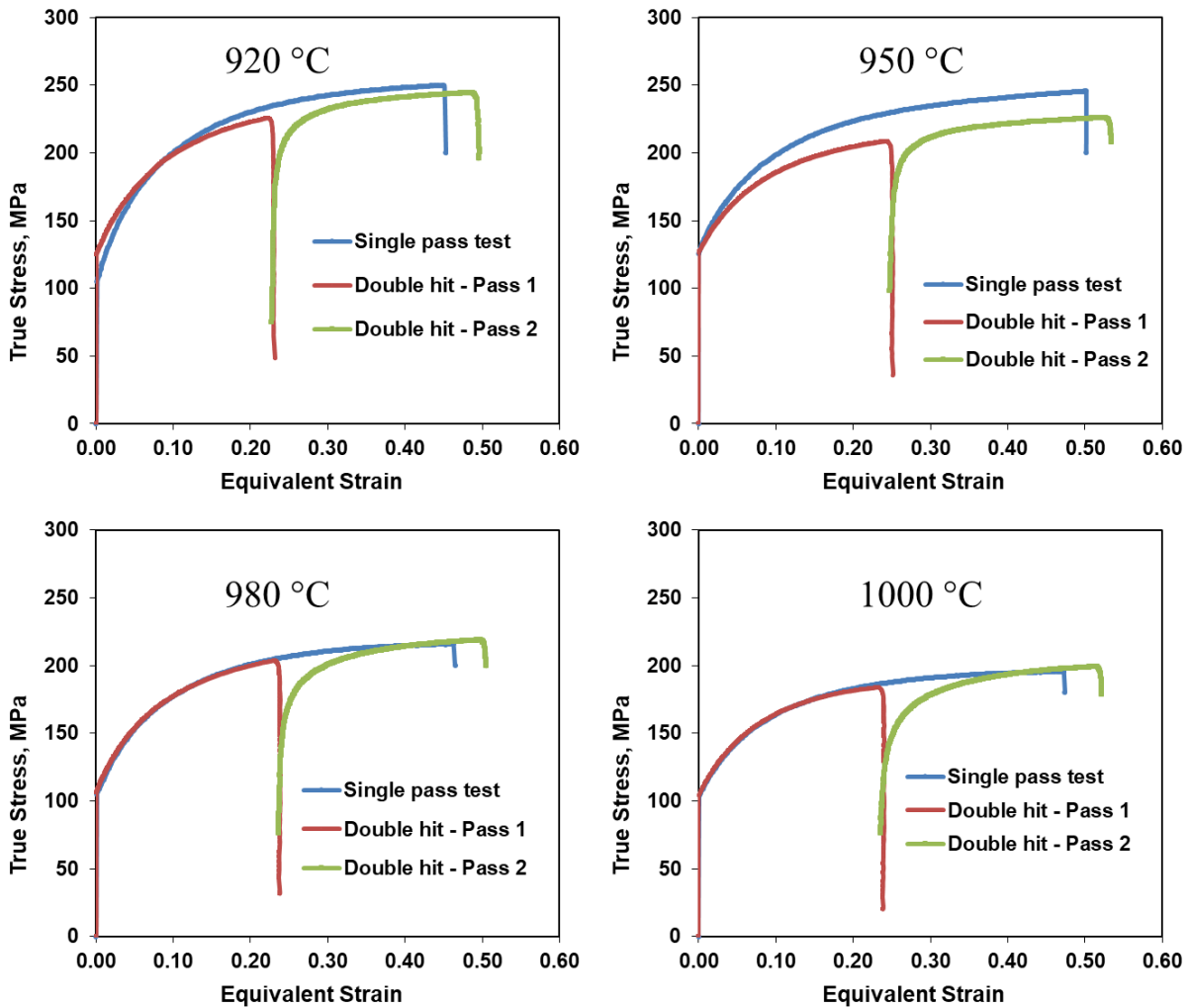


**Figure 5.9** Flow stress curves of single and double hit tests at 920 °C, 950 °C, 980 °C and 1000 °C. Deformation parameters of set 1: total strain 0.5, interpass time 20 s, strain rate 10 s<sup>-1</sup>

T<sub>5%</sub> was also calculated with different deformation parameters to consider the effects of interpass time and the total strain. The interpass time changed from 20 s to 4 s for the deformation parameters of set 2, keeping all other parameters constant. Double hit tests were performed at 980°C, 1000°C and 1020°C, the measured flow stress is plotted in Figure 5.10. For the single pass at 980°C and 1000°C, the data was taken from the single pass tests of set 1, whilst on the 1020°C, the single pass was extrapolated from the first pass of the double hit test. In set 2, none of the double hit tests

reached the strain of 0.25 in the first pass, however, the actual strain was considered for the softening analysis.

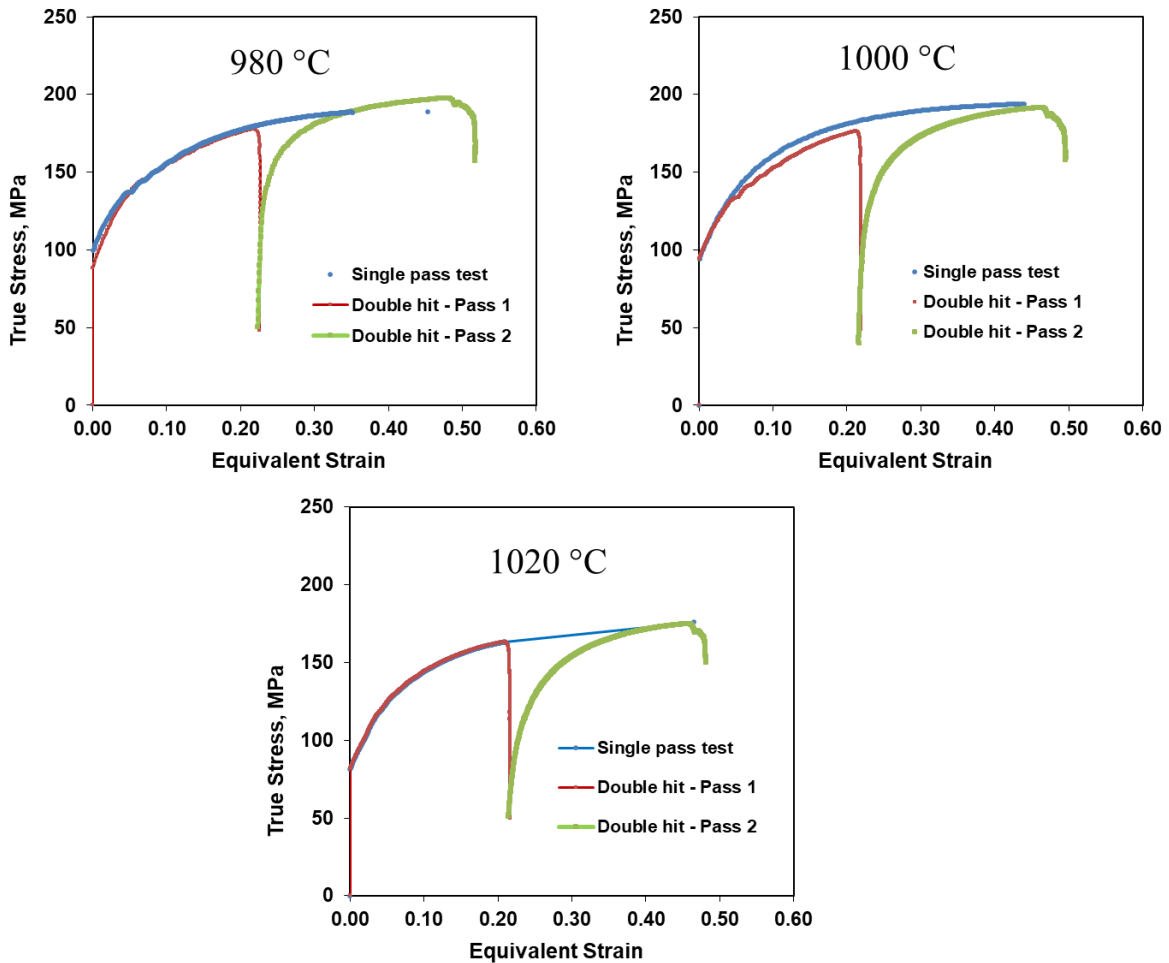


**Figure 5.10** Flow stress curves of single and double hit tests at 980°C, 1000°C and 1020°C. Deformation parameters of set 2: total strain 0.5, interpass time 4 s, strain rate  $10 \text{ s}^{-1}$

Then, double hit tests were done with the deformation conditions of set 3, i.e., interpass time of 4 seconds and an increasing in the strain per pass to 0.4 setting a total strain of 0.8. The strain rate remained constant at  $10 \text{ s}^{-1}$  and the deformation temperature was set to 980°C and 950°C. These parameters are closer to the conditions used in industrial practice. Flow stress curves of deformations corresponding to set 3 are plotted in Figure 5.11. There were no single pass tests

done for set 3 with a total strain of 0.80. For the 980°C, the first pass on the double hit test was extrapolated to calculate the softening. In the case of the 950°C, the single pass was done with a strain of 0.40 and then it was extrapolated to measure the % softening.

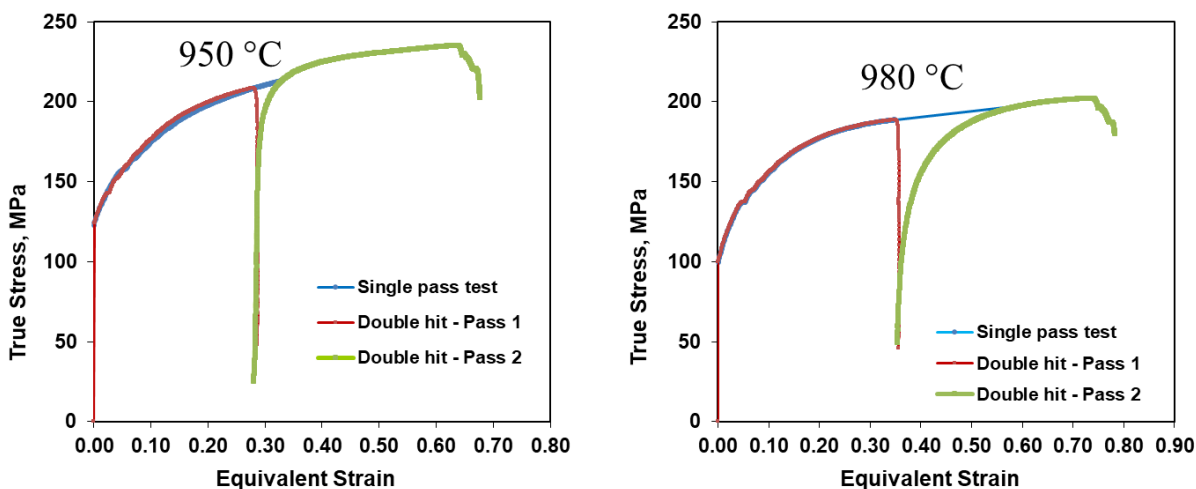


**Figure 5.11** Flow stress curves of double hit tests at 950°C and 980°C. Deformation parameters of set 3: total strain 0.8, interpass time 4 s, strain rate  $10 \text{ s}^{-1}$

### 5.3.2. Fraction Softening calculations

The softening percentage on double hit tests for the deformation conditions of set 1, set 2 and set 3 were calculated with the methods mentioned in Table 4.5 and are summarized in Figure 5.12. In some tests, such as the double hit at 920°C of set 1, the deformation of the first pass does not reach the strain of 0.25 that had been set in the machine. Thus, the total strain was not 0.5 as planned. However, the softening analysis by the method of the area under the flow curve, only consider the same deformation for both passes. For example, in the case of the double hit test at 980°C of set 2, where the first pass only reaches a strain of 0.23 instead of 0.25, the area under the flow curve considered for the first pass was from 0 to 0.23, and for the second pass from 0.23 to 0.46 in strain.

Sometimes tests were not executed as programmed on the TMC machine. This can be attributed to different factors such as the alignment of the tools, lubricant thickness, or oxide layer on the



tools. As there were limited PSC specimens of CP800 for  $T_{5\%}$  double hit calculations, softening analysis were carried out with the actual values of the deformation parameters during the tests. Some tests diverse from the established strain per pass, as can be observed on the flow stress curves. And more rarely, and as the temperature range of tests is narrow, recorded temperature by thermocouple during the deformations was slightly off of the target causing inconsistency on the overall analysis of the softening calculations.

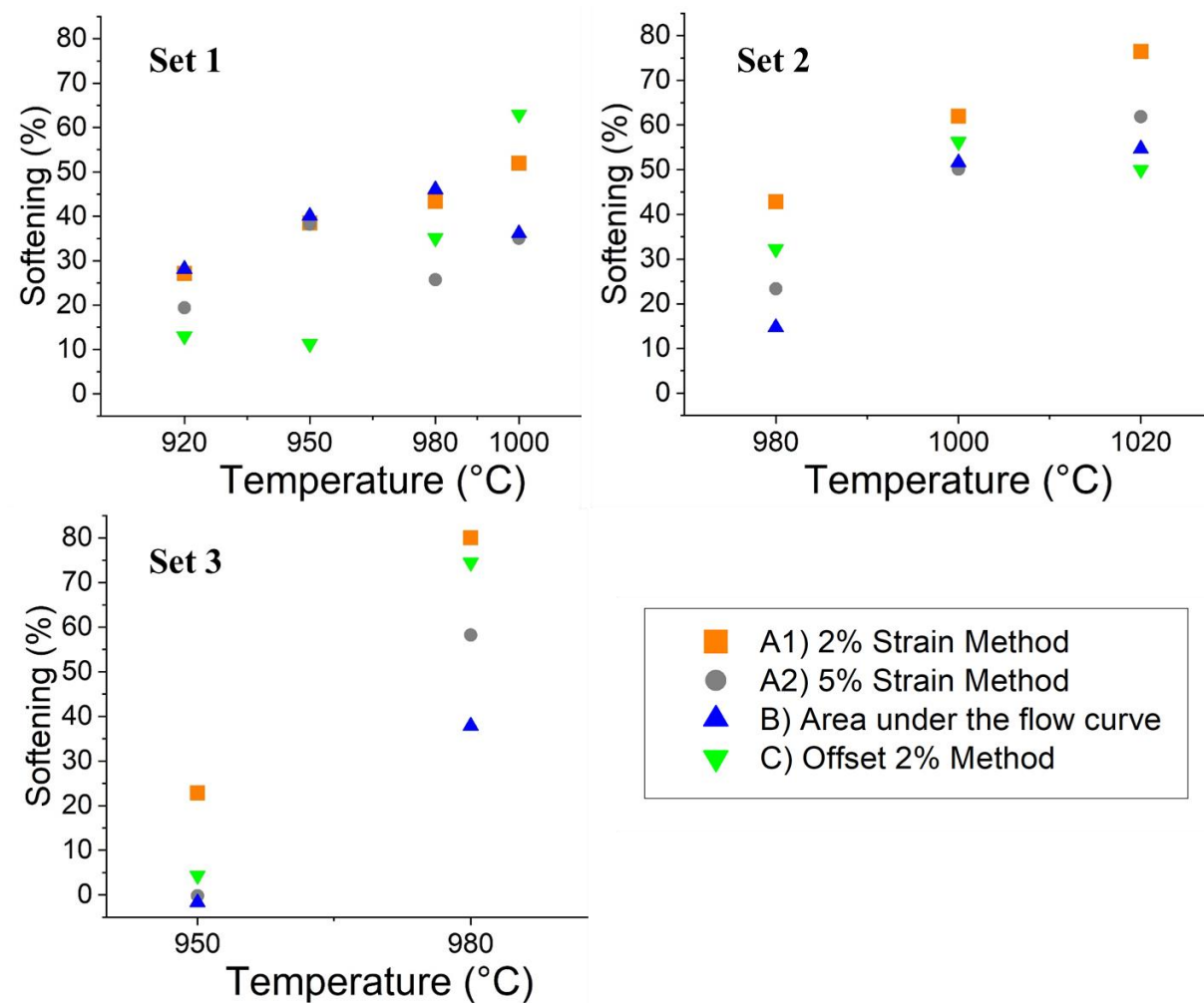


**Figure 5.12** Softening % of double hit tests at different deformation temperatures. Set 1:  $\epsilon=0.25$ ; Interpass time = 20 s. Set 2:  $\epsilon=0.25$ ; Interpass time = 4 s. Set 3:  $\epsilon=0.40$ ; Interpass time = 4 s

### 5.3.3. Microstructure evaluation of Double and Single Hit Tests

The characterization of the prior austenite grain was done in each of the deformed samples. This would also validate the recrystallization-stop temperature as determined by the fractional softening behaviour previously described. Figure 5.13 shows the microstructures of the deformed specimens for single and double hit tests for deformations parameters of set 1. The specimens deformed at 920°C, 950°C and the double hit test at 980°C show completely elongated austenite grains. Partial recrystallization structure begins to be detected in the single pass tests at 980°C and 1000°C, as well as the double hit test at 1000°C.

The microstructure details, shape and size of the grains, of the single and double hit tests are summarized in Table 5.4 and Table 5.5. Table 5.5 only shows measurements from the non-recrystallized structure and fully recrystallized austenite. Single pass tests of set 3 were done for a total strain of 0.40 and, after the deformation, the specimens were held at the deformation temperature for 4 seconds followed by water quench.

The average distance in between the PAGB caused by an accumulated strain of 0.5 in the non-recrystallized conditions is 20  $\mu\text{m}$  in the direction perpendicular to the rolling and 80  $\mu\text{m}$  parallel to the rolling direction, resulting in a grain aspect ratio of 4. The double hit test at 950°C of set 1 has a slightly shorter distance in between PAGB perpendicularly to the rolling direction. This is explained by the strain accumulation which, specifically in this test, was 0.53, a little higher than expected. The microstructures of PAGB corresponding to double hit tests of set 2 are shown in Figure 5.14, fully recrystallized structure is present in temperatures above 1000°C with PAGS of 14  $\mu\text{m}$  and aspect ratio of 1.2, even though the strain on the first pass reached only 0.21 on 1000°C and 1020°C tests. There is partial recrystallization of 19% on the double hit at 980°C when the maximum strain in the first pass was 0.22. In deformation conditions of set 3 (Figure 5.15), deformations taking place at 980°C shows completely recrystallized austenite, the double hit tests measured a strain of 0.36 on the first pass and 0.78 accumulated strain whilst on the single pass test the maximum strain was 0.36. The partial recrystallization of 17% is present at 950°C in single pass test with a strain of 0.36 and in the double hit test, there is 8% recrystallized fraction with only a strain of 0.29 on the first pass and 0.67 total strain. These values were much lower than the expected.

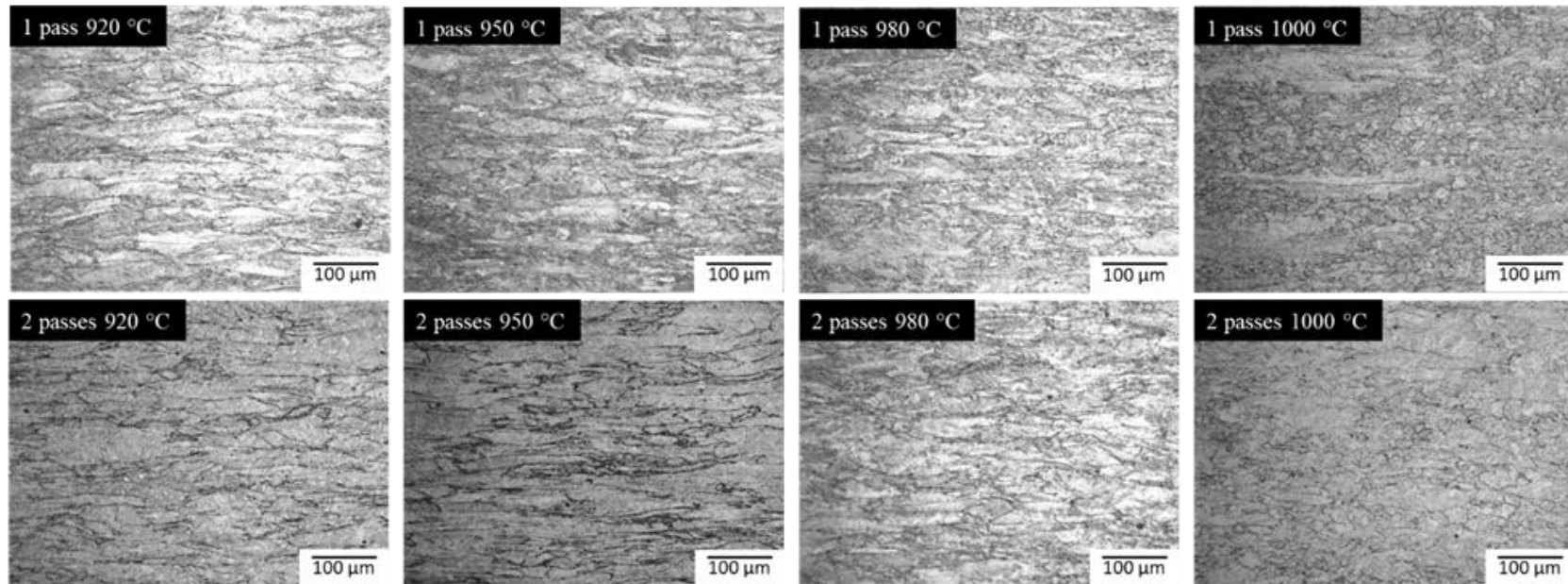


**Figure 5.13** Prior Austenite Grain Boundaries of single and double hit deformed specimens at different temperatures. Deformation parameters of set 1: total strain 0.5, interpass time 20 s, strain rate  $10 \text{ s}^{-1}$

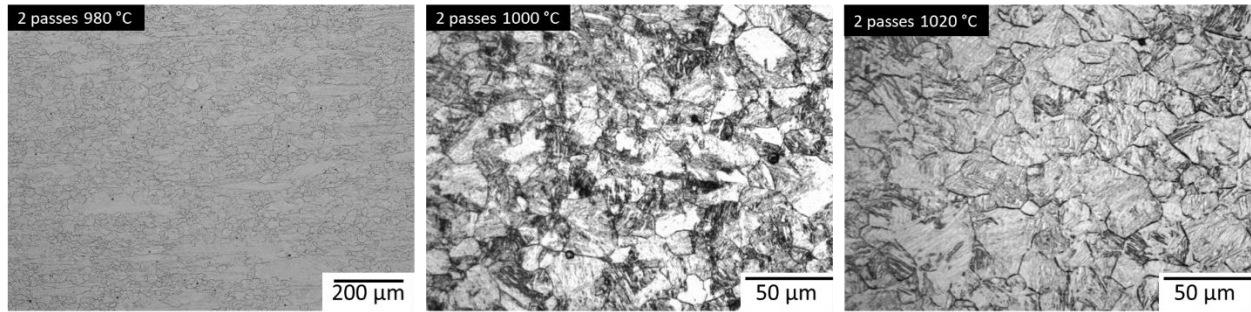


**Figure 5.14** Prior Austenite Grain Boundaries of double hit tests at different temperatures. Deformation parameters of set 2: total strain 0.5, interpass time 4 s, strain rate  $10 \text{ s}^{-1}$

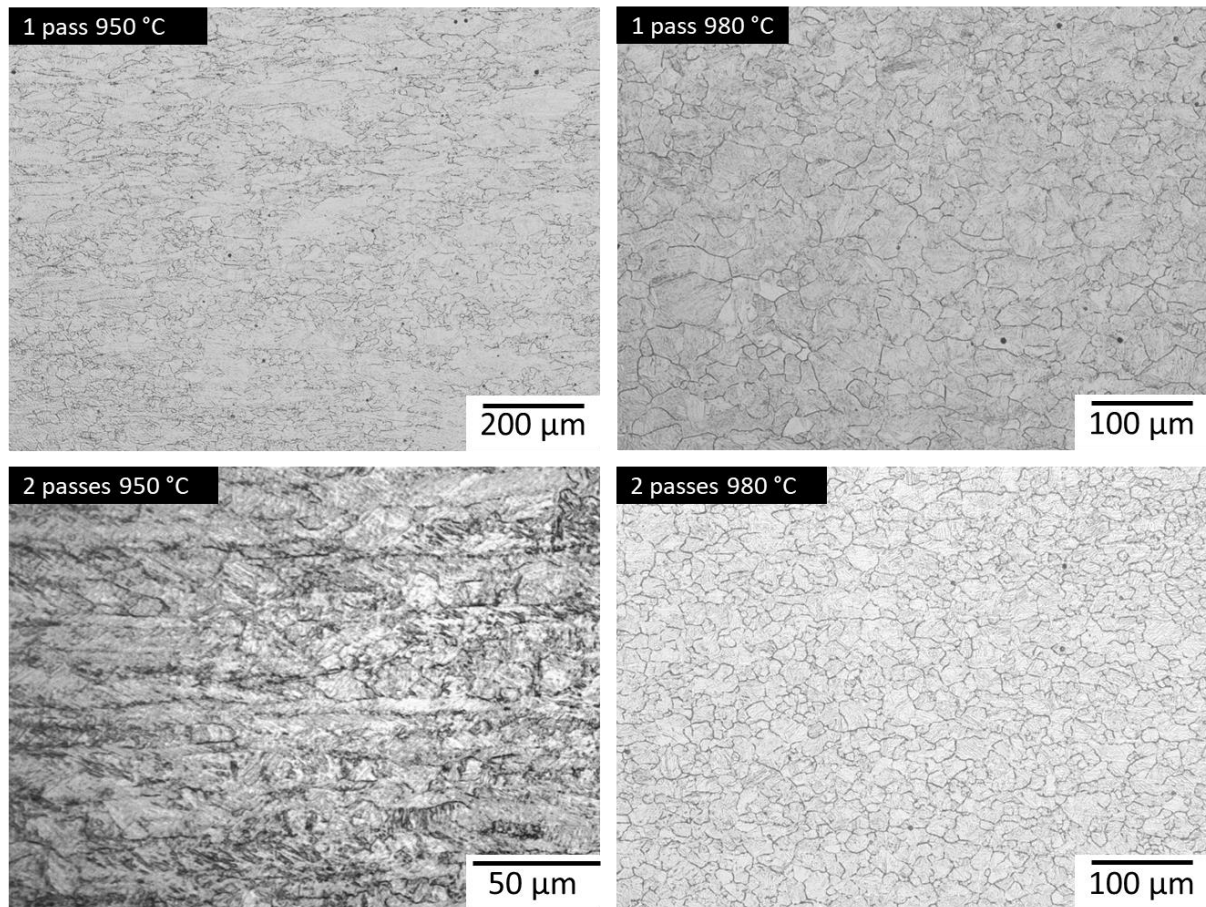


**Figure 5.15** Prior Austenite Grain Boundaries of single and double hit tests at different temperatures. Deformation parameters of set 3: strain per pass 0.4, interpass time 4 s, strain rate  $10 \text{ s}^{-1}$

**Table 5.4** Prior Austenite Grains microstructure of single and double hit tests

Deformation parameters	Deformation Temperature	Single pass test	Double hit test
Set 1	1000 °C	Partial recrystallization (50%)	Partial recrystallization (33%)
	980 °C	Partial recrystallization (22%)	Non-recrystallized
	950 °C	Non-recrystallized	Non-recrystallized
	920 °C	Non-recrystallized	Non-recrystallized
Set 2	1020 °C	-	Fully recrystallized
	1000 °C	-	Fully recrystallized
	980 °C	-	Partial recrystallization (19%)
Set 3	980 °C	Fully recrystallized	Fully recrystallized
	950 °C	Partial recrystallization (17%)	Partial recrystallization (8%)

**Table 5.5** Grain size measurements of the deformed specimens.

Test	Temperature	Grain size ( $\mu\text{m}$ )	ASTM	Aspect ratio	Grain size RD ( $\mu\text{m}$ )	Grain size $\perp$ to RD ( $\mu\text{m}$ )
Set 1 - Single Pass	920°C	53 $\pm$ 36	6 $\pm$ 2	4.5	86 $\pm$ 60	19 $\pm$ 3
	950°C	53 $\pm$ 32	6 $\pm$ 2	4.4	86 $\pm$ 50	19 $\pm$ 3
Set 1 - Double Hit test	920°C	46 $\pm$ 27	6 $\pm$ 2	3.6	71 $\pm$ 42	20 $\pm$ 3
	950°C	47 $\pm$ 22	6 $\pm$ 2	4.1	76 $\pm$ 6	18 $\pm$ 3
	980°C	43 $\pm$ 18	6 $\pm$ 1	2.9	65 $\pm$ 22	22 $\pm$ 3
Set 2 - Double Hit	1000°C	14 $\pm$ 3	9 $\pm$ 0.5	1.2	-	-
	1020°C	15 $\pm$ 2	9 $\pm$ 0.4	1.2	-	-
Set 3 – Single Pass	980°C	25 $\pm$ 3	7 $\pm$ 0.3	1.1	-	-
Set 3 - Double Hit	980°C	18 $\pm$ 3	8 $\pm$ 0.5	1.4	-	-

$T_{5\%}$  was also calculated for CP800 from the equations of different authors (Table 4.6) to compare with the experimental results [144]. These estimations are presented in Table 5.6. Bai, Militzer and Dutta calculations are in the same range. Boratto's prediction has a gap of around 150°C in comparison with the others. All equations show the effect of the alloying elements on the recrystallization-stop temperature except Dutta & Palmiere, which only consider the amount of the applied true strain.

**Table 5.6**  $T_{5\%}$  estimation for the CP800.

<b>Author</b>	<b><math>T_{5\%}</math> CP800</b>	
Boratto et al. [130]	1100 °C	
Bai [131]	943 °C	
Fletcher [132]	993 °C	
Militzer [133]	947 °C	
Dutta & Palmiere [120]	$\epsilon=0.25$ 954 °C	$\epsilon=0.40$ 948 °C

#### 5.4. Hot Rolling Simulation

Hot rolling simulation was performed on the TMC machine for the CP800 according to the thermomechanical processing route designed in Figure 4.13.  $T_{5\%}$  was defined as 950°C following the softening percentage analysis, double hit test microstructures and the empirical equations for deformation conditions of set 3.  $A_3$  was set to be 830°C as specified by the steady state conditions of simulation software, although it is expected that  $A_{r3}$  is lower due to the cooling rates applied during the TMP.

#### 5.4.1. Microstructure Evolution of Deformed Austenite

The evolution of austenite during thermomechanical treatment is observed in Figure 5.16. TMP consisted of reheating the PSC specimen up to 1150°C at a heating rate of 10 °C/s, holding at 1150°C for two minutes and then cooling at 20 °C/s to the first pass deformation temperature, which is 950°C (Figure 5.16 A). The PSC specimens were quenched after 4 seconds of each deformation pass, i.e., just before the consecutive pass. The first deformation pass took place, with a total strain of 0.4 and a constant strain rate of 10 s<sup>-1</sup>, to lower the temperature to the next deformation pass, 920°C, over a period of 4 seconds (Figure 5.16 B). After the second pass of 0.3 strain, the specimen was cooled to the next deformation temperature, 890°C, in 4 seconds (Figure 5.16 C). Consequently, after 4 seconds from the third pass of 0.2 strain at 890°C, another specimen was quenched (Figure 5.16 D). Finally, Figure 5.16 E) shows an immediately quenched specimen after the fourth pass of the TMC schedule.

Condition A) shows an equiaxed austenite grain structure with an average grain size of 38 µm. This condition has a PAGS slightly smaller than the as-received transfer bar condition. This is indicative of the austenite grain refinement due to thermal cycling even when it had one cycle [145, 146]. The condition B) shows a partial recrystallized structure of 19% which is in accordance with the results of single hit tests of set 3 at 950°C. It is important to recall T<sub>5%</sub> was derived from the softening calculations of double hit tests. The microstructure of condition C) clearly shows a decrease in recrystallized fraction but there are still some equiaxed grains in the centre and the elongated grains have a higher aspect ratio than in the previous condition. From the third pass, or condition D) onwards, there is no longer evidence of recrystallization in the microstructures, the austenite grains are completely elongated. The areas that look darker in the microstructure are because the distance between grain boundaries is too short. In the condition E), with the strain accumulation of 1.1, the distance between PAGB perpendicular to the rolling direction reaches values of 3 µm.

The deformation passes had an expected behaviour since in each of them was observed work hardening because the deformation temperature was decreasing in each pass. The first pass finished with the stress of around 200 MPa, the second pass at 920°C had maximum true stress of 235 MPa, third and fourth passes had 255 MPa and 280 MPa, respectively.

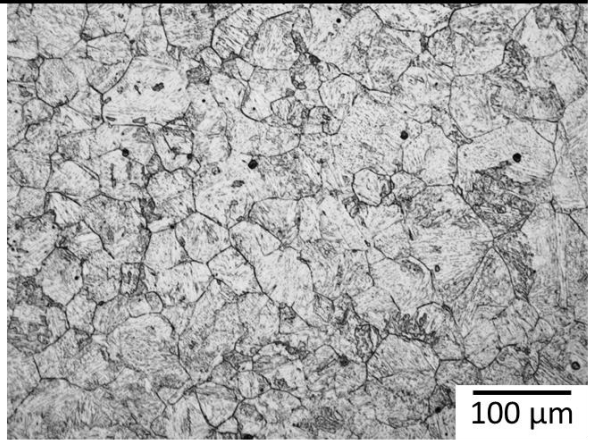


A) Reheated 2 min at 1150 °C, cool to 950 °C and then quench

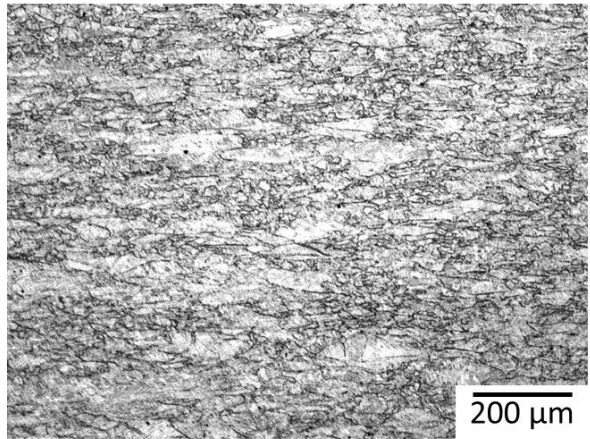
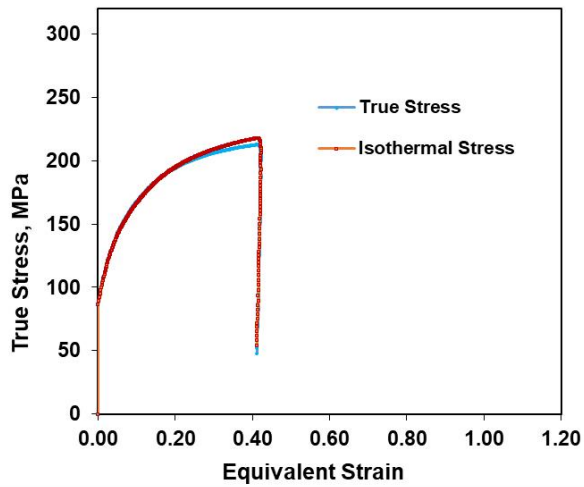
# No Deformation

Grain size =  $37.8 \pm 6.1 \mu\text{m}$

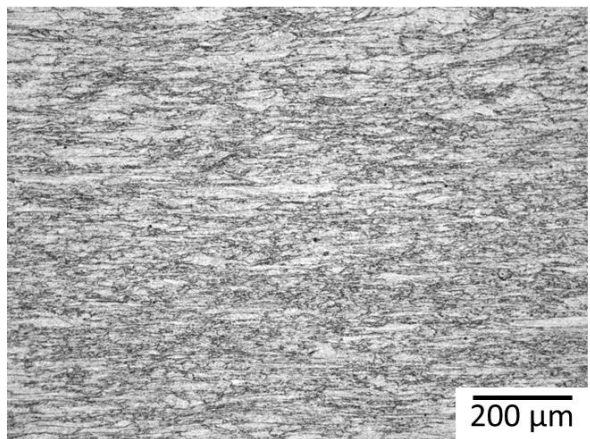
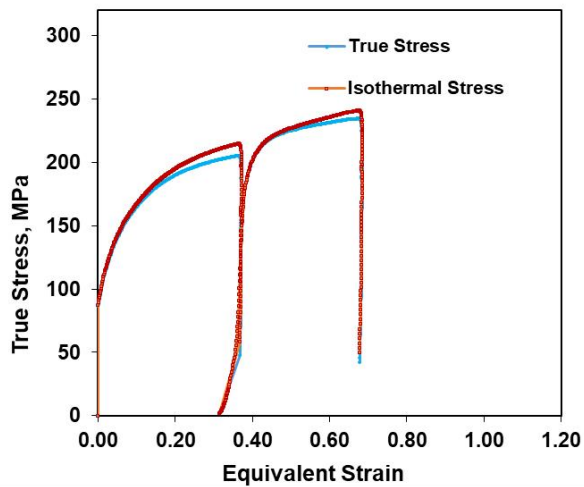
Aspect ratio = 1.4



B) 1 Pass of 0.40 at 950 °C, cool to 920 °C in 4 s then quench. Strain accumulation = 0.4

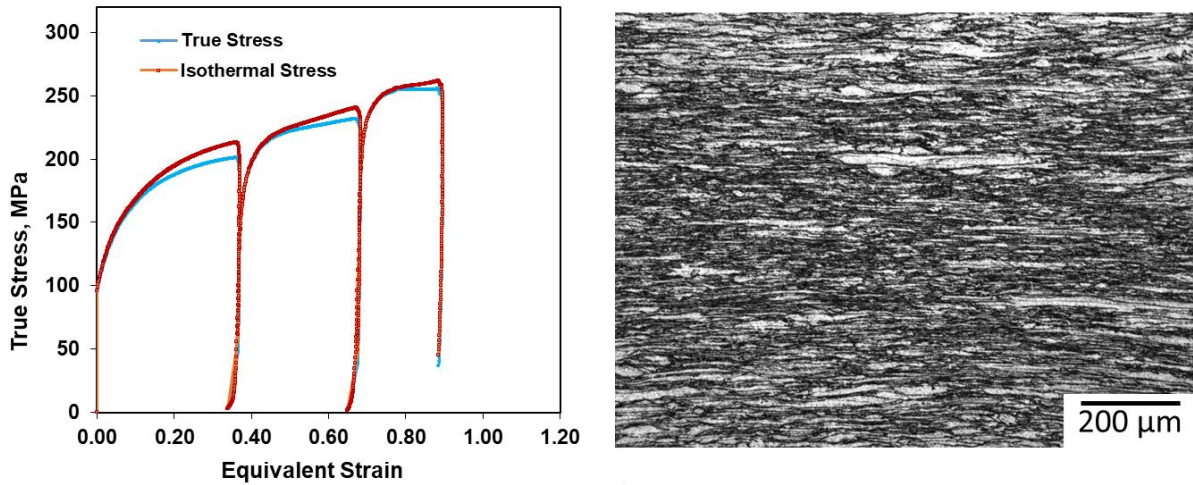


C) Quench just before third pass. Strain accumulation = 0.7





D) Quench just before fourth pass. Strain accumulation = 0.9



E) Quench immediately after fourth pass. Strain accumulation = 1.1

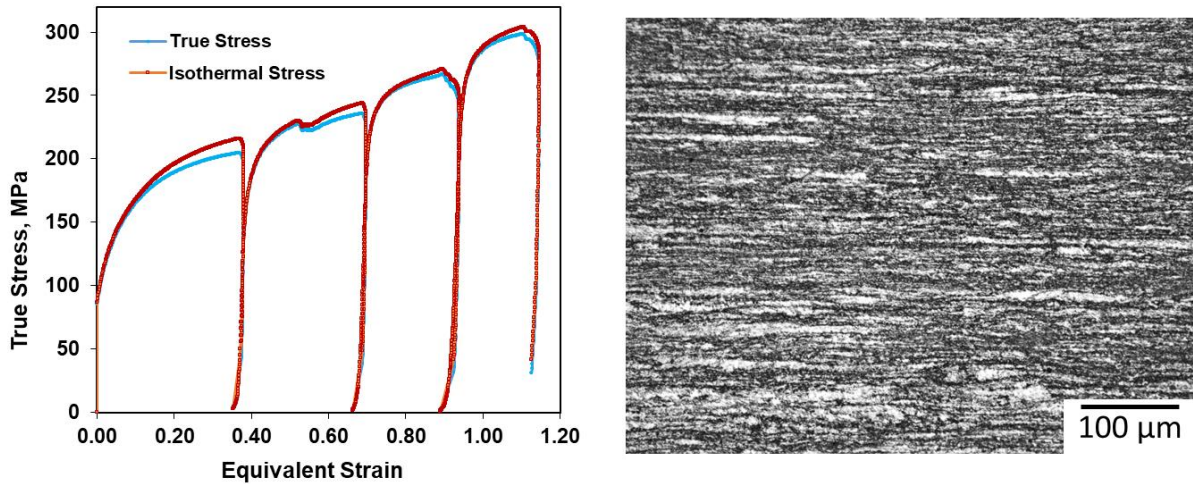


**Figure 5.16** Flow stress curves and microstructure evolution of austenite during TMP

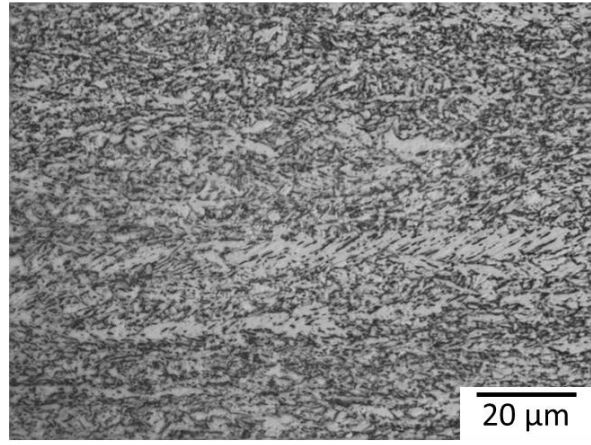
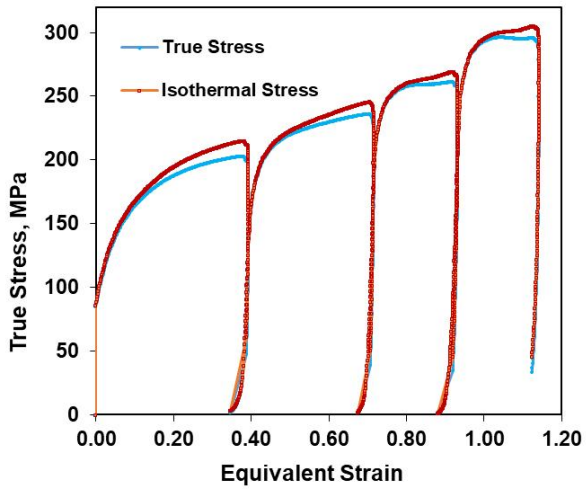
#### 5.4.2. Finishing Rolling + Runout table simulation

Once the steel strip goes out from the finishing mill, it needs to follow a controlled cooling strategy to obtain the appropriate microstructure for the desired mechanical properties. The initial microstructure on the runout table would be the final microstructure on the finishing mill. As revealed in the previous section, the microstructure after the 4-pass schedule has elongated

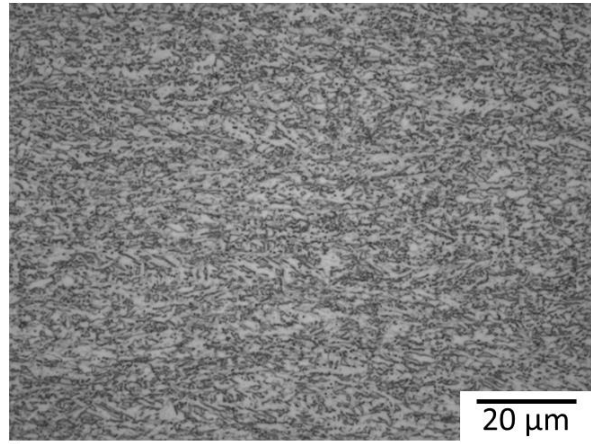
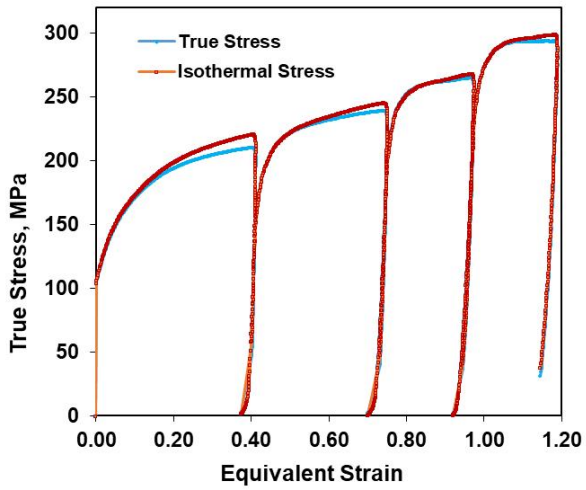
austenite grains. In this work, the controlled cooling simulations includes an isothermal step at a specific temperature during cooling as was already described in Table 4.7. The flow stress curves along with their corresponding microstructure of the controlled step cooling conditions are shown in Figure 5.17. Flow stress behaviour should not be different in these tests since the deformation passes in each of them are the same. However, controlled cooling will define the final microstructure. Actual measurements during the TMP schedule and the run-out table simulation are specified in Table 5.7 and Table 5.8, respectively. The optical microscope was not suitable to get the detail of the product phases. Strain accumulation was observed at the centre of the specimen, while near the surface, where the tools were in contact during the deformation, seems that there is no strain due to the equiaxial shape of the grains. Generally, at the higher strain zone, microstructures show deformation bands oriented in the rolling direction. These microstructures were observed at higher magnifications by SEM and TEM, which will be shown and explained in Section 5.5.

There is an atypical behaviour observed in the flow stress of the fourth pass of tests SC3 and SC5. This variation is due to the instability of the strain rate during this pass. This is a consequence of the higher friction during this pass as the lubrication between the specimen and the tools get worn after each pass.

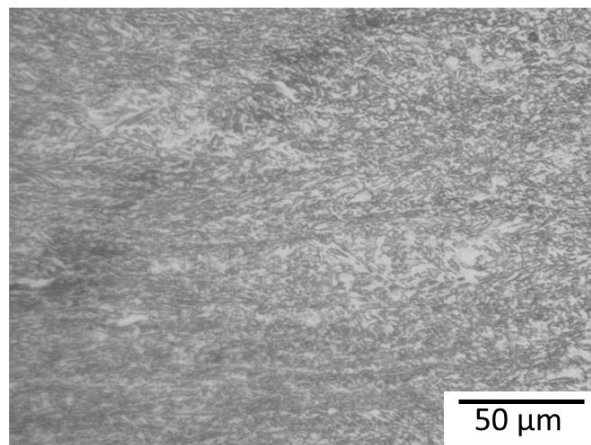
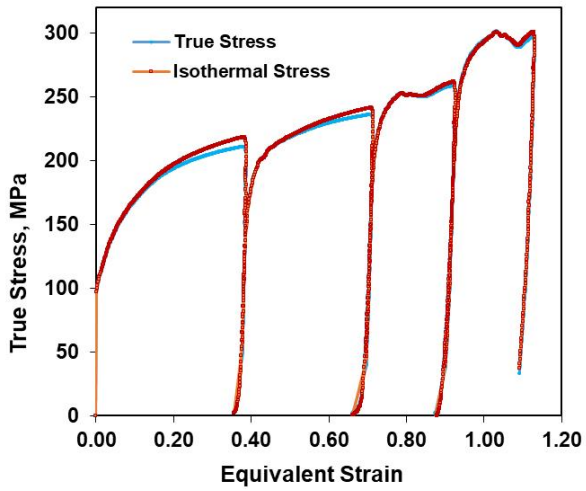
SC1



SC2

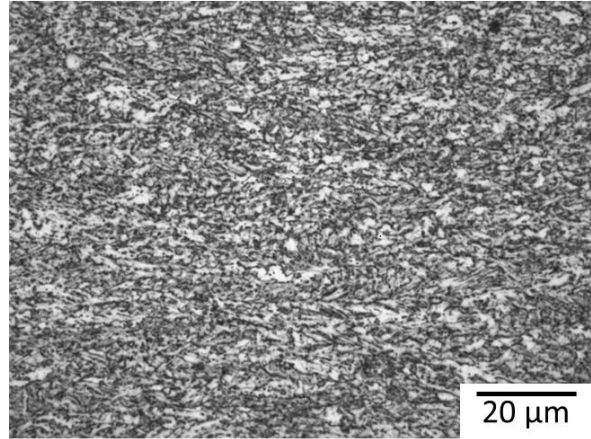
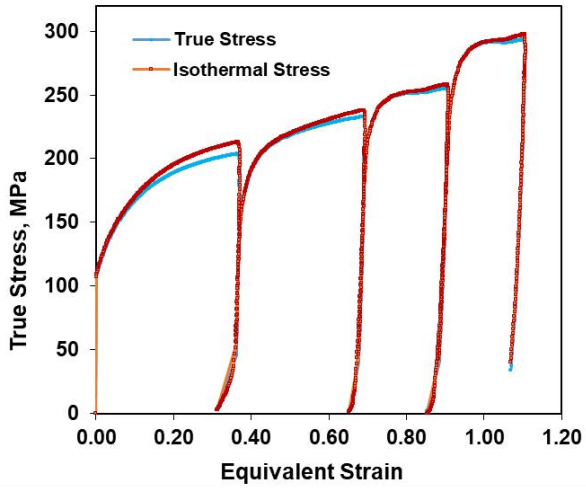


SC3





SC4



SC5

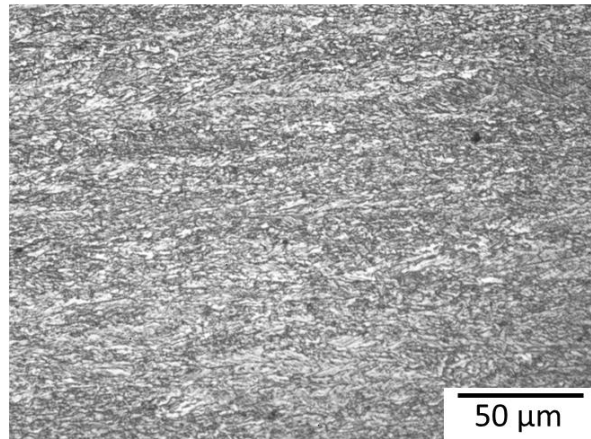
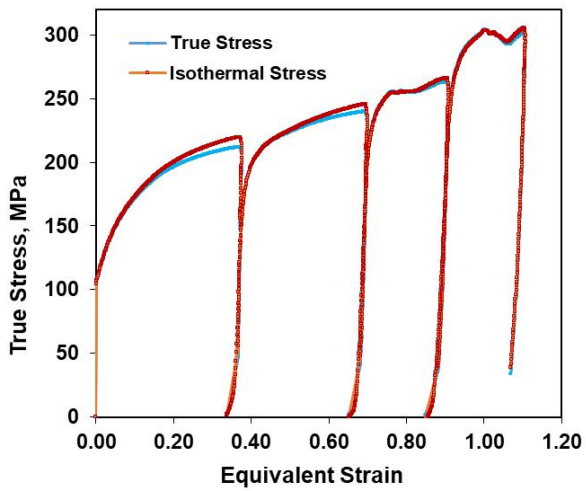


**Figure 5.17** Flow stress and corresponding microstructure of specimens that follow the full TMP schedule with controlled cooling

**Table 5.7** Actual measurements of strain and temperature per deformation pass of the specimens with the full TMP schedule

Test	1 <sup>st</sup> pass		2 <sup>nd</sup> pass		3 <sup>rd</sup> pass		4 <sup>th</sup> pass	
	Strain	Temp (°C)	Strain	Temp (°C)	Strain	Temp (°C)	Strain	Temp (°C)
SC1	0.39	963	0.71	922	0.93	890	1.14	848
SC2	0.41	957	0.75	918	0.97	885	1.19	847
SC3	0.38	953	0.71	918	0.92	885	1.13	823
SC4	0.37	958	0.69	920	0.90	888	1.1	826
SC5	0.37	952	0.69	917	0.90	885	1.1	823

**Table 5.8** Actual measurements during cooling on specimens of full TMP schedule. Cooling rate 1 consider from the last deformation pass until the holding temperature. Cooling rate 2 includes after the holding temperature until room temperature

Test	Cooling rate 1 (°C/s)	Step temperature	Holding time (s)	Cooling rate 2 (°C/s)
SC1	92	550°C	13	348
SC2	98	500°C	13	334
SC3	158	555°C	13	270
SC4	87	493°C	13	263
SC5	-	500°C	≈ 60	-

## 5.5. Identification and Quantification of Transformation Products

The mechanical properties of steels are related to its microstructure. Thus, it is of vital importance to be able to identify and quantify the phases that are present in the microstructure. The final microstructure of a hot-rolled steel sheet is developed considering different factors, mainly its chemical composition and the thermomechanical processing schedule to which it was subjected.

As mentioned earlier, complex phase steels generally consist of a combination of ferrite, bainite, and martensite, and under certain conditions, relatively small amounts of retained austenite may be present in the steel.

The microstructures of specimens that followed the full TMP schedule and controlled cooling were observed under SEM and TEM. SEM microstructures are shown in Figure 5.18, the rolling direction is parallel to the horizontal axis. The deformation bands are clearly revealed in some of these microstructures, such as in SC3 and SC5. The dark equiaxial grains, more predominantly seen in SC4, are considered as polygonal ferrite grains by their morphology and size. Bright spots, which are observed in the grain boundaries in SC1, SC4 and SC5 could be an indicator of the presence of MA constituents, while in SC2, the bright zones have different internal morphology, like needle shape, which is characteristic of martensite and are not necessarily located on the grain boundaries. SC3 shows a lamellar structure in the deformation bands. This microstructure is mainly composed of bainite and martensite.

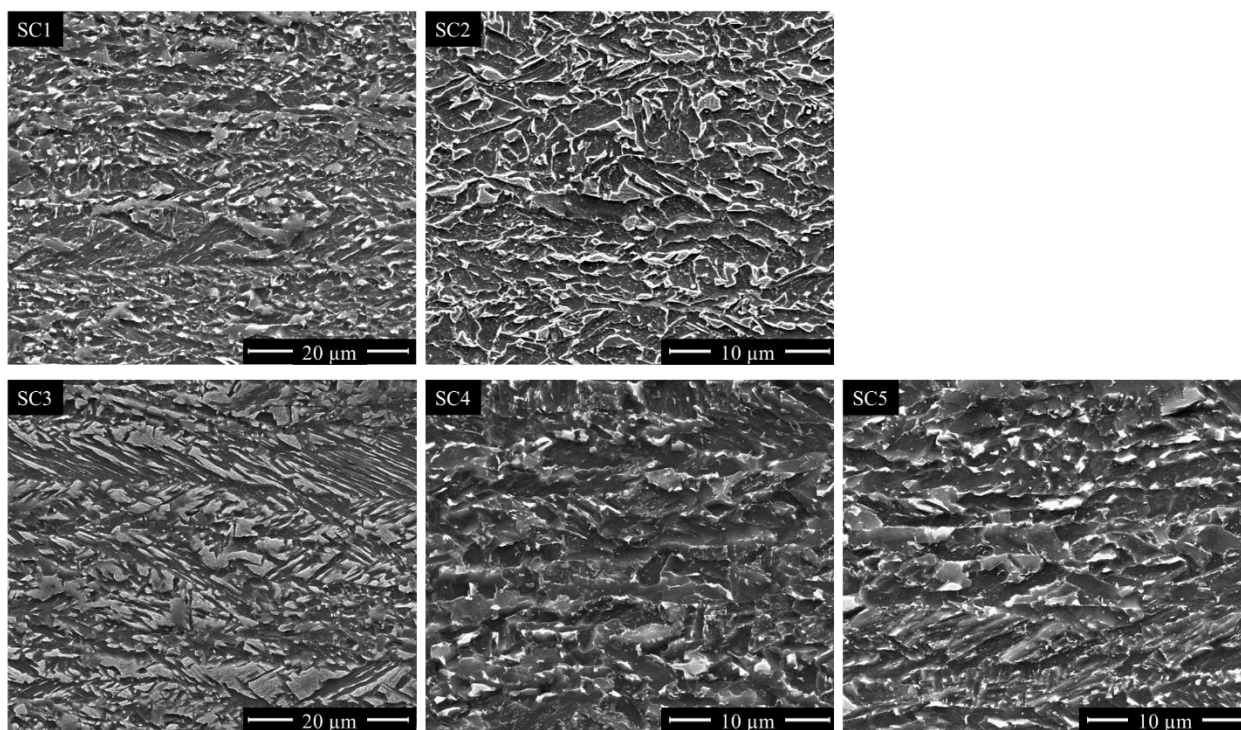


**Figure 5.18** SEM SE micrographs of specimens after full TMP schedule and controlled cooling

Quantification of phases by TEM is complex and limited due to the small volume observed in the thin foil. However, the thin foils observed by TEM can confirm the presence of the expected phases. Features of bainitic ferrite can be found in SC2 (Figure 5.19). This microstructure consists of a parallel lath-like shape free from carbides in the ferrite with a considerable amount of dislocations between the laths. Some lath boundaries look darker, which indicates a higher carbon concentration in the remained austenite during the transformation, a characteristic of upper bainite [147, 148]. SC3 shows a complex structure, with some plate shape but also equiaxial grains (Figure 5.20). Figure 5.21, corresponding to SC4, clearly shows martensite areas and accumulation of dislocations at the grain boundaries. All specimens had dislocations, but the SC5, in Figure 5.22, seems to be the specimen with the highest dislocation density, within and at the grain boundaries.

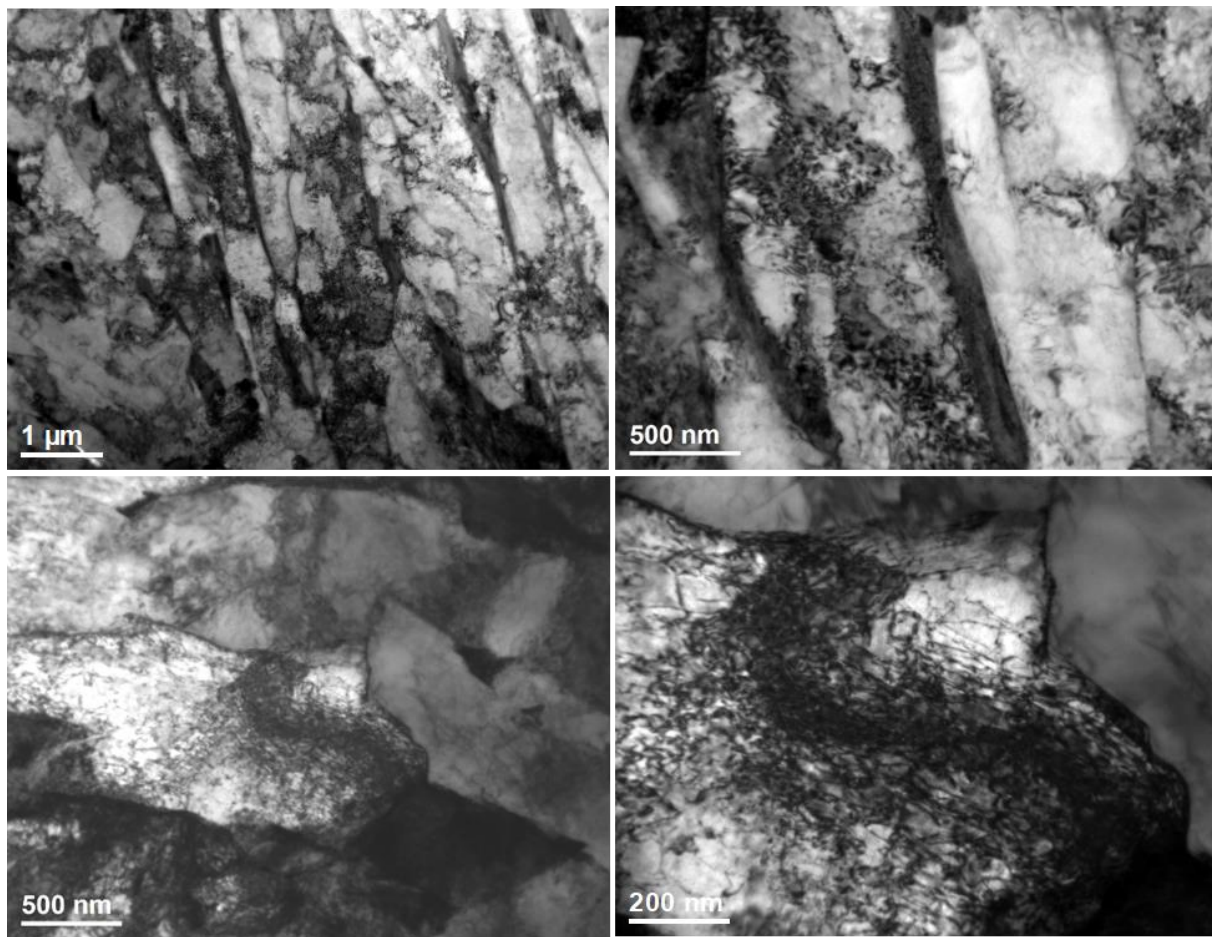


**Figure 5.19** TEM images of SC2



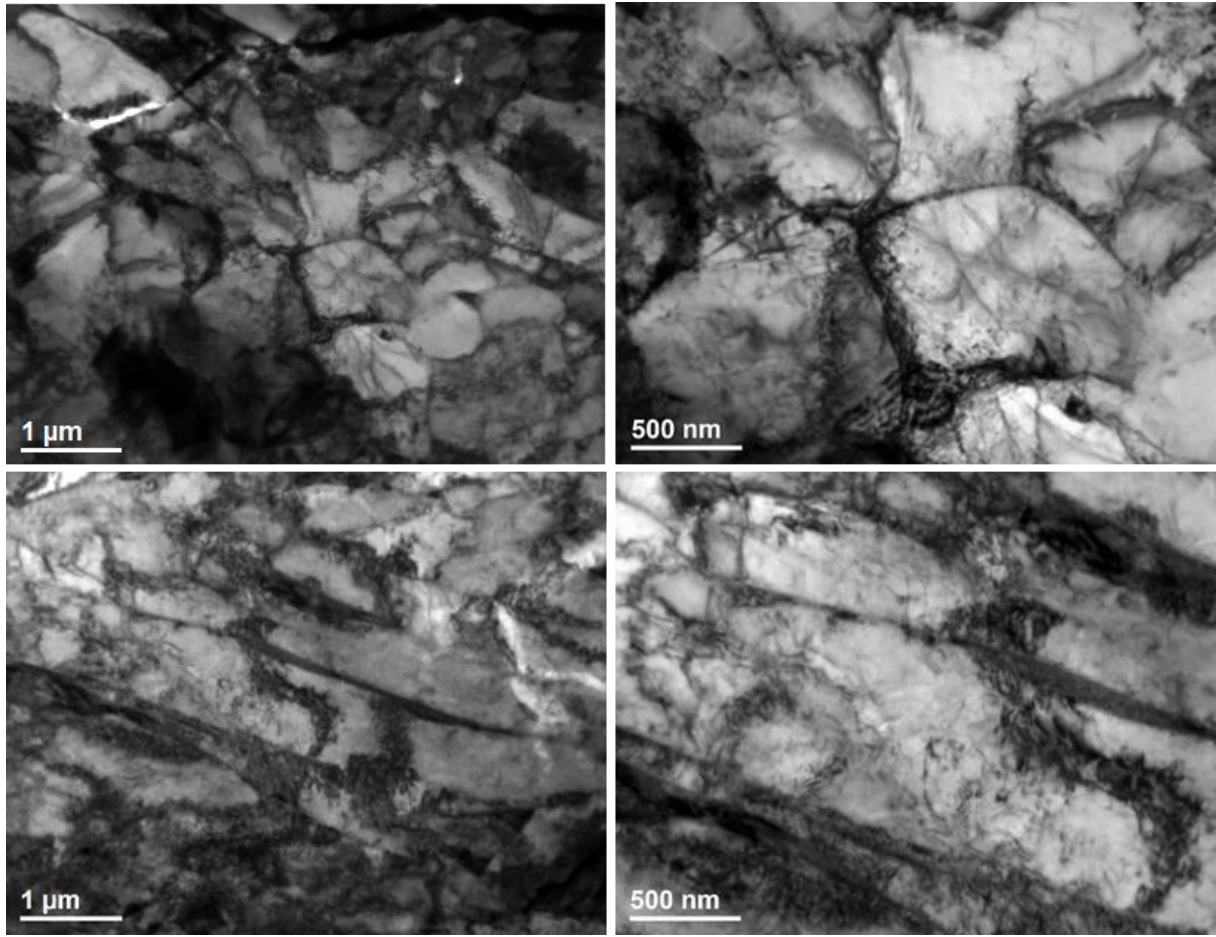


**Figure 5.20** TEM images of SC3



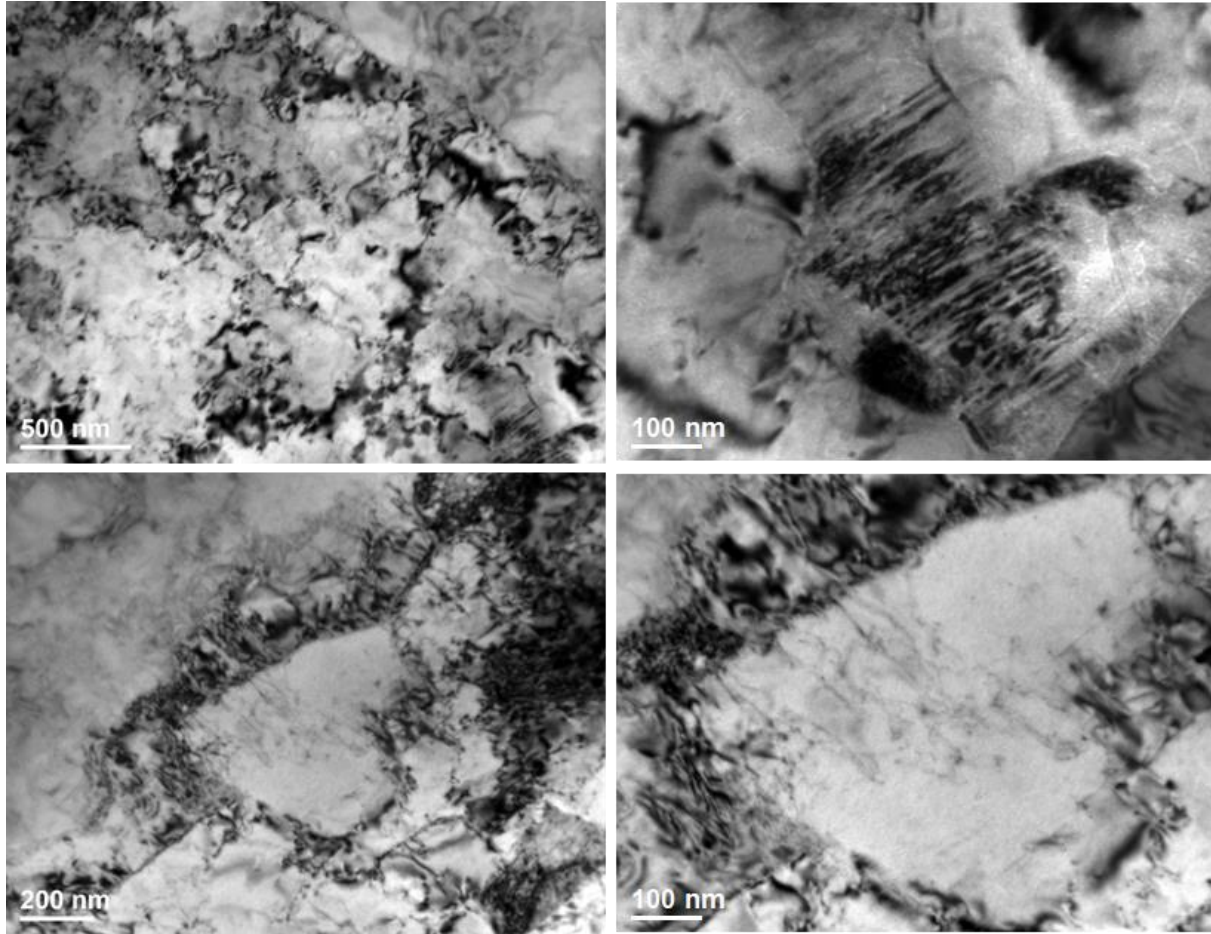


**Figure 5.21** TEM images of SC4

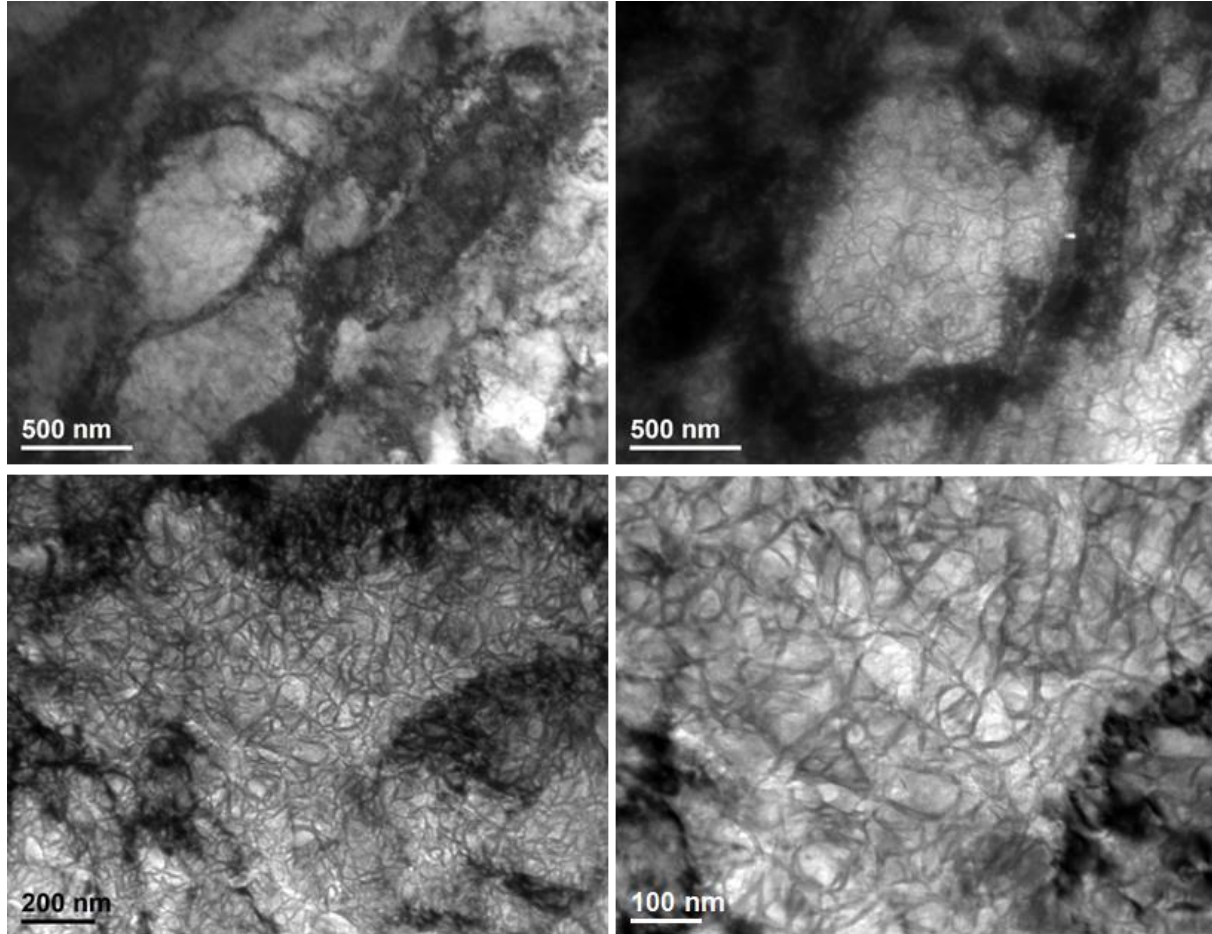


**Figure 5.22** TEM images of SC5

Extra SEM and TEM images of the step cooling specimens can be found in Appendix I.

Same specimens were analysed by EBSD to define the phases and measure their volume fraction. It should be mentioned that for the EBSD analysis, all collected data had a minimum of 85% of indexing rate. Subsets were created for every sample to focus on a specific area to avoid pixels with scratches or obvious defects with many mis-indexed points. Before constructing the maps, the noise reduction function was performed on every subset. There are two types of noise reduction: the wild spikes and the zero solutions. Initially, wild spikes function was applied to the subsets. This function will identify and correct indexed pixels that do not correspond to their environment. For example, when there is a single pixel that does not match with their surroundings, this function changes this pixel for one that fits with its neighbours. After that, noise reduction

with the zero solutions command can be applied at different levels. This command identifies non-indexed pixels and converts them into indexed pixels according to their environment. The lowest level of noise reduction of the zero-solution filter consists on converting the non-indexed pixels that have the most indexed pixels around them, the maximum surrounded indexed pixels is 8. The determination of those non-indexed pixels is the result of the average of their surrounding indexed pixels. This filter was applied from the lowest level until the non-indexed pixels reach values below 0.5%. This was commonly got with the 5 neighbours level.

The maps types constructed for the analysis were Band Slope (BS), Band Contrast (BC) also referred as Image Quality (IQ) and the Inverse Pole Figure (IPF). Filters of Grain Orientation Spread (GOS), and grain characteristics as grain boundaries, grain size and aspect ratio were applied to these maps to identify different phases in the specimens. The maps constructed for the analysis of SC3 are shown below, along with the criterion used for the detection of phases. The EBSD maps corresponding to the rest of the specimens that followed the full TMP schedule can be found in Appendix II. All specimens followed the same criteria for phases segmentation.

BS and BC are parameters related to the quality of the Kikuchi pattern [149]. BS is the maximum intensity gradient between the Kikuchi band and the background, while the BC or IQ is the average intensity of the Kikuchi band with respect to the intensity within the pattern [149, 150]. Tango software in Channel 5 package creates these two maps on a black and white scale that goes from 0 (white) to 255 (black), assigning a colour to each pixel depending on the value of BS or BC. BS and BC maps for SC3 are shown in Figure 5.23. The lower the value of BS or BC means that the pattern is similar to the solution defined by the software. In this case, the software was only looking for BCC and FCC crystal structures. On the other hand, when BS or BC value is high (darker pixels) indicates that the structure detected does not fit exactly to the solution within the software. As most of the indexed pixels were indexed as BCC structure, darker pixels in BS or BC maps refers to an imperfect BCC structure or a structure with defects.

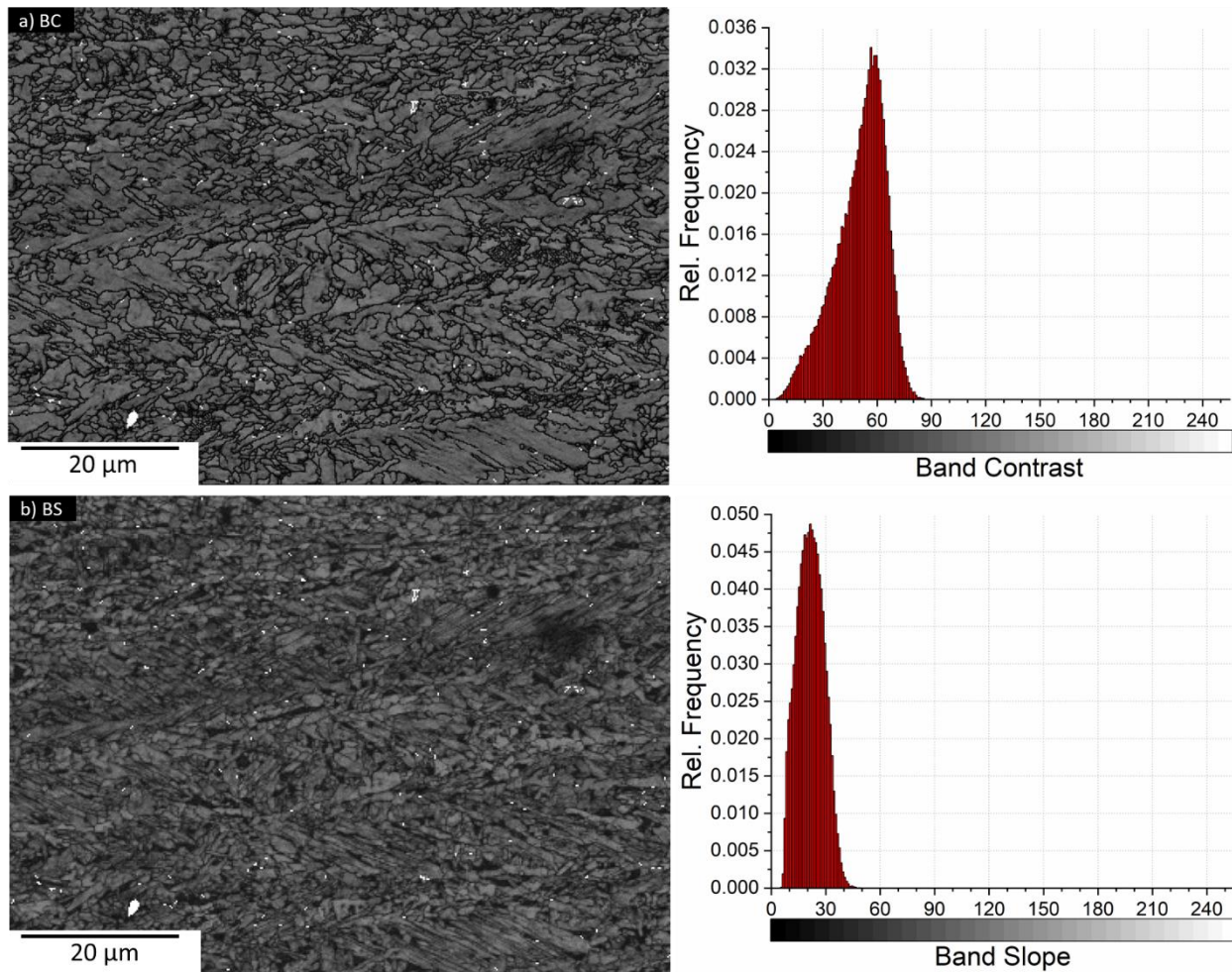


**Figure 5.23** a) BC map,  $GB = 5^\circ$  and b) BS map of SC3 and their distribution of pixels

EBSD analysis can be performed based on pixel or grain detection. In this work, the detection of grains was performed by the delimitation of a selected misorientation angle, once all the grains have been detected, they were classified depending on their corresponding phase. The criteria to define a grain was a misorientation angle greater than or equal to  $5^\circ$  and that the minimum area of a grain must be higher than 10 pixels or  $0.4 \mu\text{m}^2$ .

The phase discrimination was carried out as follows. Initially, retained austenite was simply identified by its FCC crystal structure which was automatically detected by the EBSD system.

It is known that martensite has a body-centered tetragonal (BCT) crystal structure and the lattice parameter  $a/c$  ratio depends on the carbon content. However, the detection of structures in the



EBSD system will index BCT structure as a distorted BCC and, consequently, with poor quality of the pattern. Therefore, a threshold value is applied to the BS or BC map to differentiate martensite from the rest of the BCC structures. Since BS and BC values are assigned per pixel, meaning that there is a range of BS or BC values within a grain, all the pixels inside a grain are averaged to define the BS or BC value of the grain. According to the above, in a BS or BC map, the darker grains tend to be martensite and the brighter grains could be classified as ferrite [151]. Grain averaged BC is used to separate martensite from ferrite [152, 153]. The threshold value of the averaged BC grain chosen for the separation of martensite depends on the BC distribution in each of the subsets. Figure 5.24 shows the grain averaged band contrast map and its distribution of SC3. Pixels in red colour are filtered as indexed FCC structure, i.e. retained austenite.

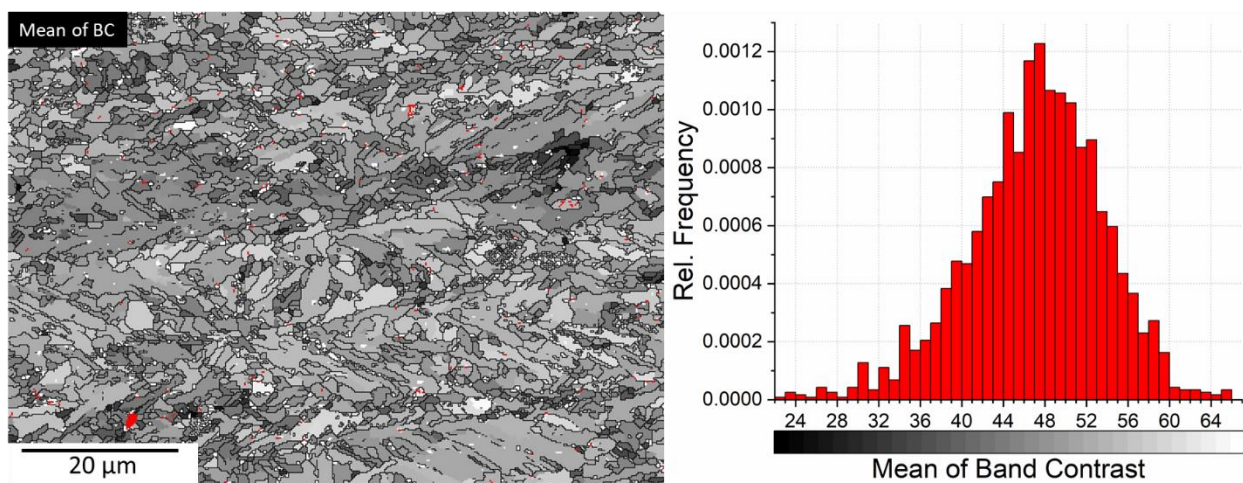


**Figure 5.24** Grain averaged Band Contrast map of SC3. GB = 5° and its distribution

One of the differences between the bainitic ferrite and polygonal ferrite is the dislocation density or defects within the grains. One method to distinguish the bainitic ferrite from polygonal ferrite in EBSD maps is through the Grain Orientation Spread (GOS) component. GOS refers to the degree of orientation change between every pixel in the grain and the average misorientation within a grain [154]. GOS map and the distribution for the SC3 is represented in Figure 5.25. Thus, when a grain has a high GOS value means that there is a great level of misorientation within that grain. This could be indicative of a phase that has many defects or a product of a displacive phase

transformation, such as bainitic ferrite. Opposite, a low GOS indicates there is no internal misorientation in that grain, which is characteristic of a clean and well-arranged phase like polygonal ferrite. This can be better observed by drawing the low angle grain boundaries with minimum misorientation of  $2^\circ$  as shown by the blue lines in Figure 5.26. These low angle grain boundaries can be related to substructures in the bainitic grains [155, 156], which also coincides with the grains with higher GOS values. The threshold GOS value to separate bainitic ferrite from polygonal ferrite will depend on the distribution of GOS value in the subset of each specimen but for deformed specimens it has to be in the range from 1 to 1.25 [157, 158]. Furthermore, another characteristic of the polygonal ferrite is the low aspect ratio compared to bainitic ferrite and martensite [159]. Besides from GOS, an aspect ratio constraint was applied to the grains, so that polygonal ferrite grains should not have an aspect ratio greater than 1.7. The grains with low GOS values (in blue) coincides to have an equiaxial shape or very low aspect ratio and also have relatively small grain size.

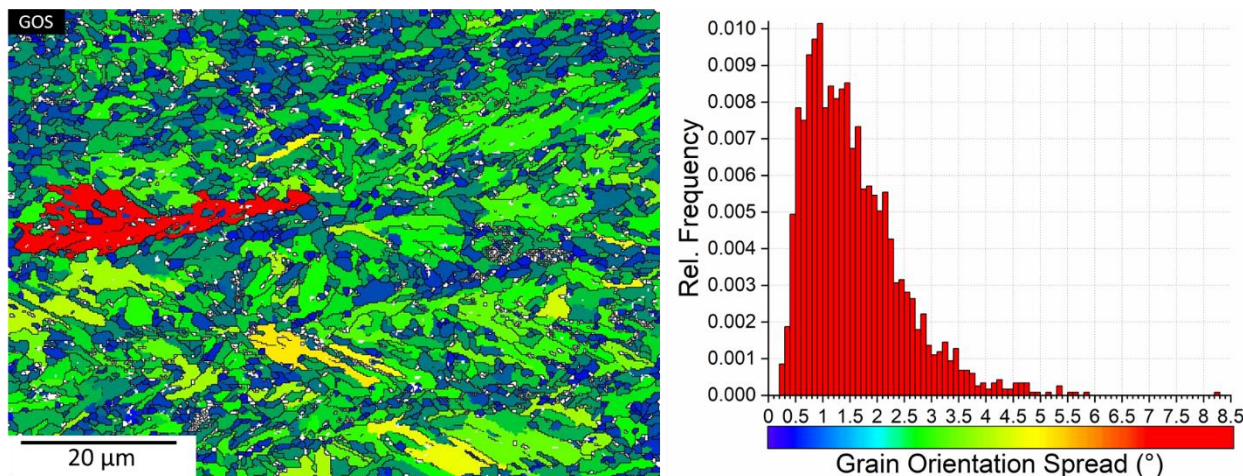


**Figure 5.25** Grain Orientation Spread map of SC3 and its distribution histogram

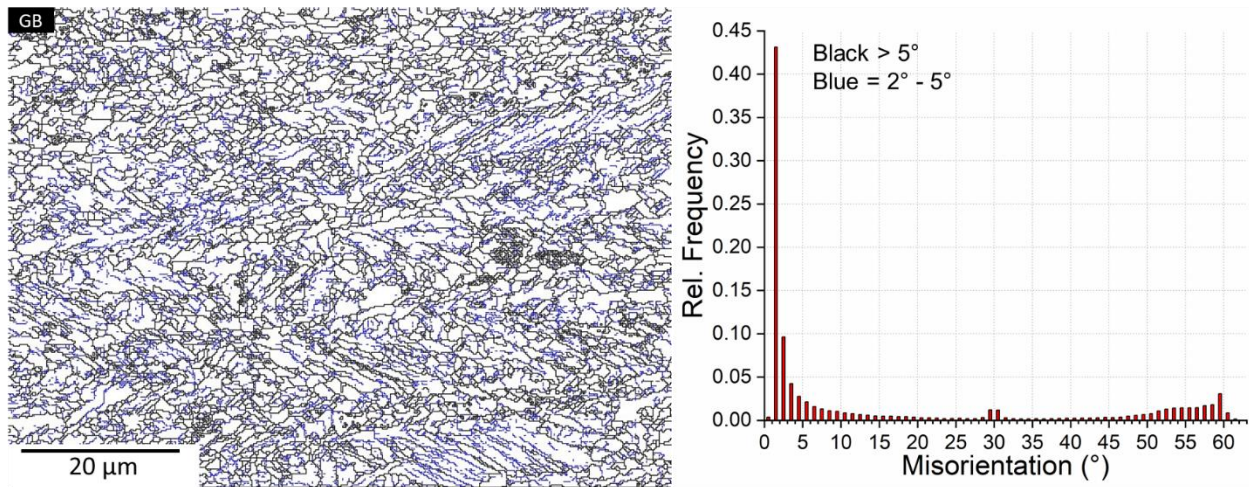


**Figure 5.26** Grain Boundaries Misorientation map of SC3 and the misorientation distribution. Black lines represent misorientation higher than 5° and blue lines from 2° to 5°

The IPF map (Figure 5.27) of the deformed specimen under non-recrystallization conditions of austenite following a controlled cooling shows that the longitudinal plane describes a texturing in the [111] direction of the BCC. The deformation bands that correspond to the same orientation on the IPF map coincide with the low angle grain boundaries, which is also an indicator of a displacive phase transformation [160]. It can also be observed that within the deformation bands, the low angle grain boundaries are aligned at about 45° with respect to the rolling direction.



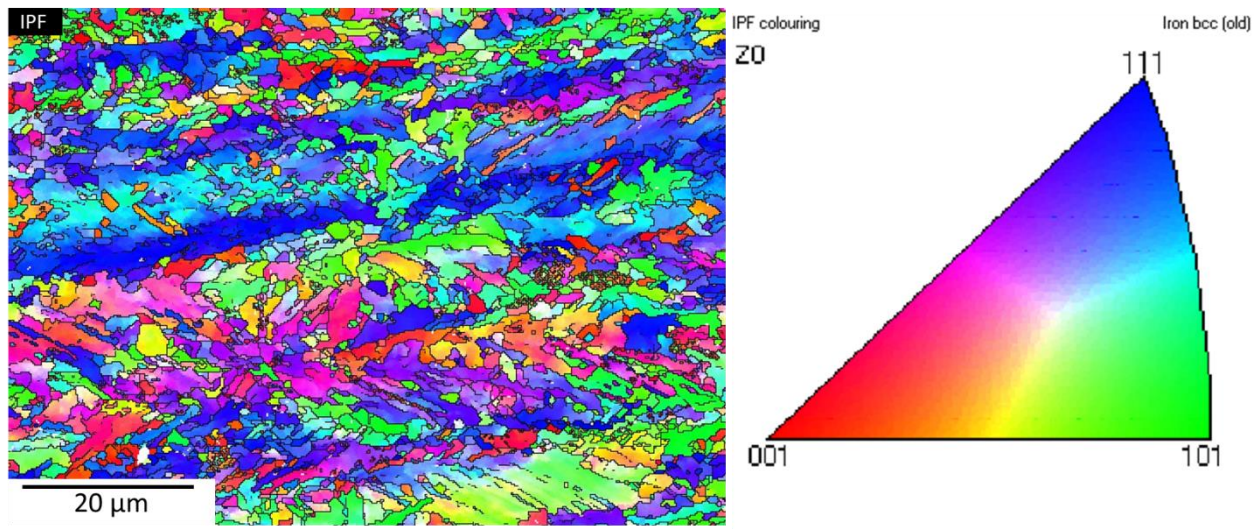


**Figure 5.27** Inverse Pole Figure map of SC3 and the orientation code

The maps with the segmented phases using the criteria already described for all the specimens that followed the complete TMP schedule are shown in Figure 5.28. The red phase represents retained austenite, black grains represent martensite while blue grains denote bainitic ferrite and lastly, grains coloured in yellow represent polygonal ferrite. The phases were quantified based on the area of the grains and the results are shown as phase percentages in Table 5.9. The white spots in the maps of phases were not classified as any of the phases. One of the reasons is that these spots do not meet the designated criteria to define a grain, which is to have a misorientation higher than or equal to  $5^\circ$  and to have an area of at least 10 pixels. Sometimes these data points are classified as pseudosymmetries, which are considered as errors in the indexing data points. Pseudosymmetry quantification was obtained from the misorientation profile of each specimen. Pseudosymmetries are reported to have a misorientation of  $30^\circ$  and  $60^\circ$  and can be related to the quality of the specimen preparation or the quantity of Kikuchi bands used for the indexing procedure [161]. The specimen that was immediately quenched after the last pass presented the higher amount of martensite, as expected.



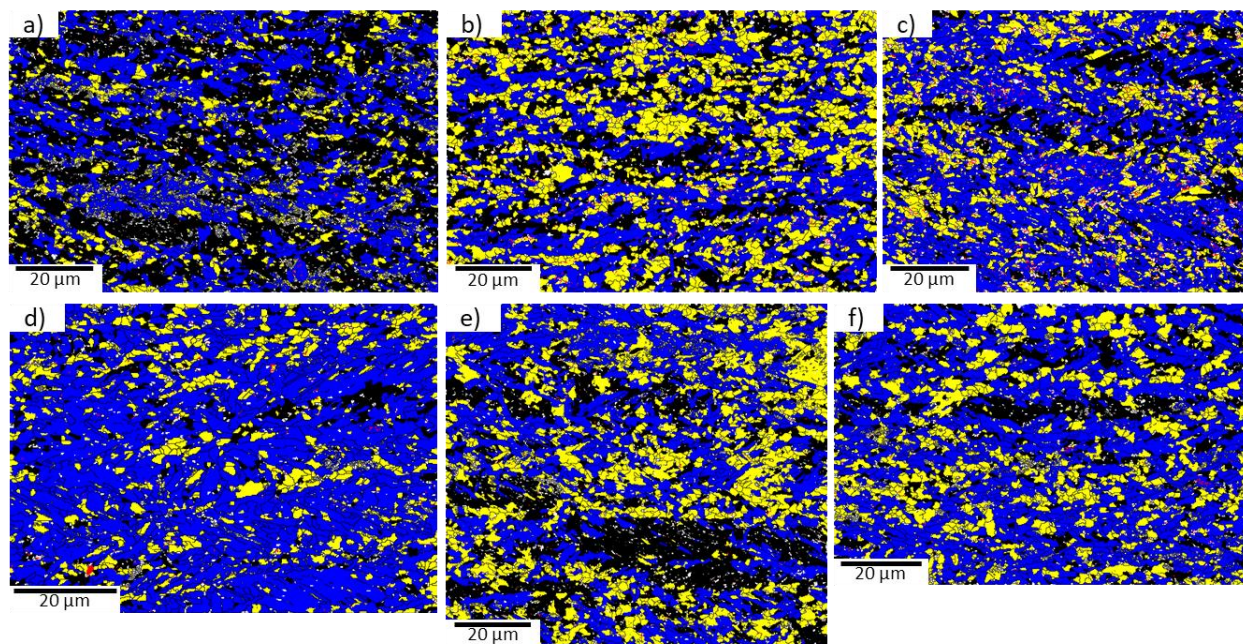


**Figure 5.28** Maps of phases segmentation of a) Quench after 4<sup>th</sup> pass, b) SC1, c) SC2, d) SC3, e) SC4 and f) SC5. Colour representation: Red = Retained Austenite, Black = Martensite, Blue = Bainitic Ferrite and Yellow = Polygonal Ferrite

**Table 5.9** Phase percentages in different specimens analysed by EBSD.

Specimen	Martensite	Bainitic Ferrite	Polygonal Ferrite	Retained Austenite	Pseudosymmetry
Quench	53.0	32.8	8.6	0.3	5.4
SC1	33.8	35.8	27.1	1.3	0.5
SC2	28.1	48.7	15.7	2.4	0.4
SC3	22.6	61.4	12.4	0.3	2.4
SC4	39.0	34.4	22.3	0.3	3.1
SC5	29.8	46.3	19.8	0.3	3.7

## 5.6. Mechanical properties evaluation

Microhardness Vickers test was only evaluated on SC3 with 13 measurements which varies from 277 to 451 HV/0.01 with an average of  $353 \pm 44$  HV/0.01. This variation is because the indentation left on the specimen is larger than the grains of the phases in the microstructure. Therefore, different phases were considered in a single microhardness measurement. This is better explained in Figure 5.29, an SEM image showing one of the indenter marks covering bright and dark areas corresponding to different phases on the microstructure where the microhardness was measured. The tensile strength of the material cannot be properly estimated due to the low load applied during the tests [162]. Nevertheless, if a greater load (1 kgf) had been applied in this test, the Vickers hardness value got for this specimen would suggest a tensile strength of 1146 MPa [163, 164].

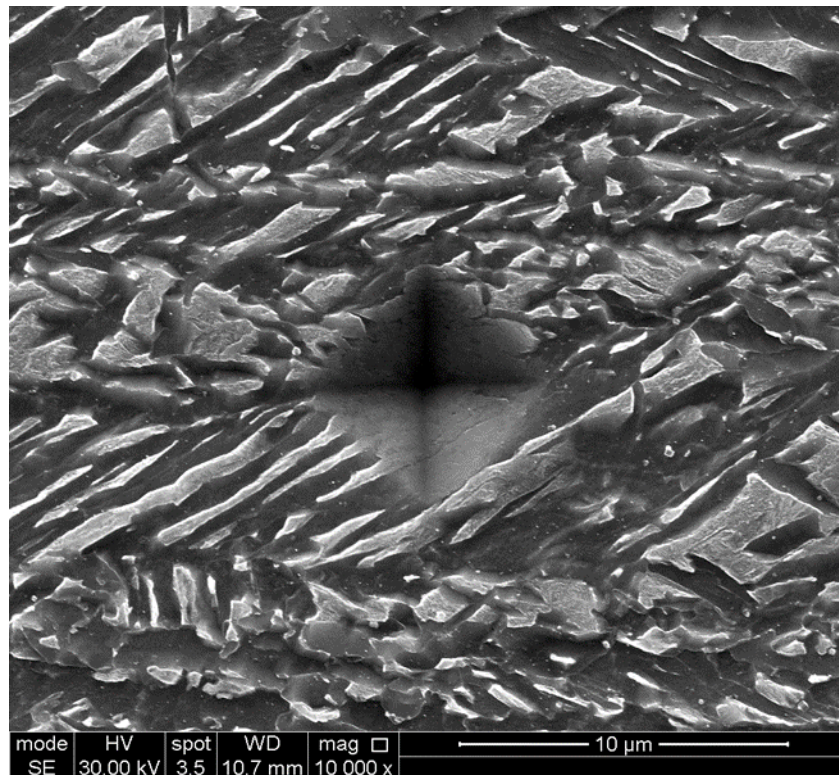


**Figure 5.29** SEM SE image of SC3 showing the indentation left for the Vickers hardness measurement

The evaluation of mechanical properties for each of the phases needed lower loads applied into the specimen, so the indentations can fit in a single phase on the microstructure. Nanoindentation analysis was carried out in SC3 and SC5. Topography images together with nanohardness measurements are shown in Figure 5.30 for SC3 and in Figure 5.31 for SC5. The analysed area of SC3 was  $100 \mu\text{m}^2$  while in SC5 was  $225 \mu\text{m}^2$ . The contrast in the images indicates the depth in the surface of the specimen, the darker area means the cantilever went deeper, and the brighter areas indicate heights of up to 200 nm. Different features in the microstructure were named as a dark matrix, light block smooth, light block rough and light lamellar. According to the hardness values and morphology of the features, the dark matrix can be considered as ferrite as it is the feature with the lowest hardness values.

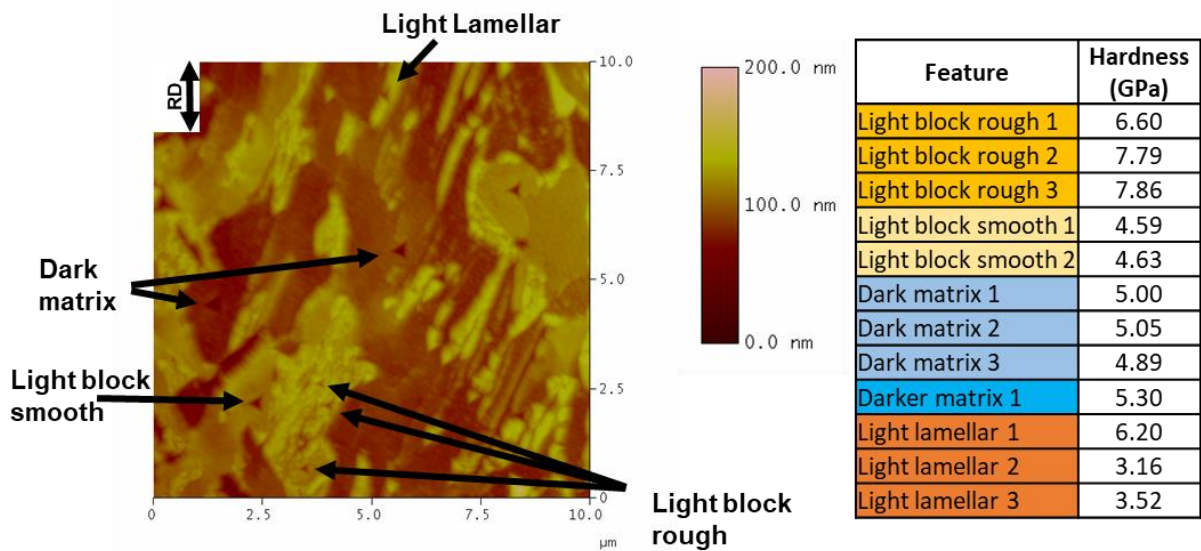


**Figure 5.30** AFM image of SC3 along with the nanohardness measurements for different features in microstructure



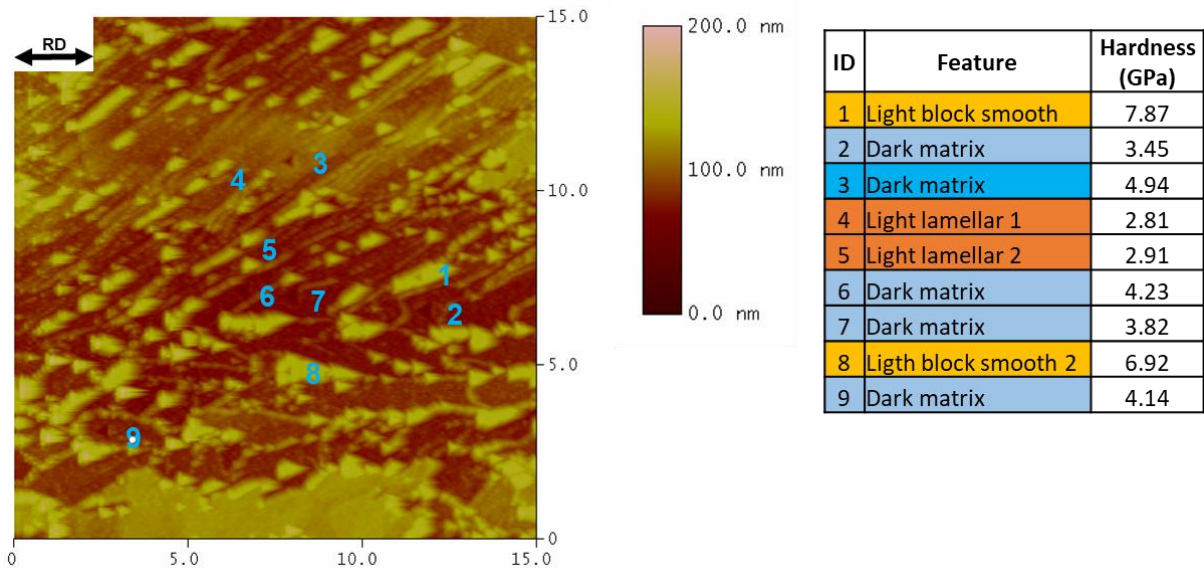


**Figure 5.31** AFM image of SC5 along with the nanohardness measurements for different features in microstructure

Since the bright areas indicate height, they can be considered as displacive phases as they form a relief on the surface after the transformation [165, 166]. The differences in height can also be attributed to the chemical reaction during the electropolishing in the sample preparation. This reaction preferentially attacks the ferrite structure, causing the lower heights with respect to other phases [167, 168]. Another characteristic of the displacive phases, such as martensite and bainite, is their higher hardness compared to the reconstructive phases, which coincides with the reported nano-hardness values. In the case of the SC3, the light-block smooth areas have low hardness values and are normally located next to the lightest rough areas, which are considered as martensite due to the height and hardness. Martensite, a displacive transformation, can influence the height of its surrounding phases, for example, ferrite. The hardness of the light lamellar structures has a considerable gradient in their values. Since the lamellar structure is high, one of the thoughts is that the thickness of the structure is narrower than the indenter and the indenter may not have had solid contact with the structure affecting the hardness measurement.

The tensile flow stress of controlled step-cooling specimens is shown in Figure 5.32. Table 5.10 indicates the mechanical properties of each specimen. Since last deformation pass on SC3 was

carried out at a lower temperature, this is the strongest specimen but at the same time is the less ductile. SC5 could not reach 800 MPa in UTS but it had the best elongation behaviour. This is because of the longer holding time during the step cooling. All specimens present their maximum stress at around 0.05 of strain. The Young's modulus is in the correct range of 200 GPa corresponding to steel. Ductility in all specimens presented elongations from 19 to 25% while the reduction of area is between 44 and 64%.

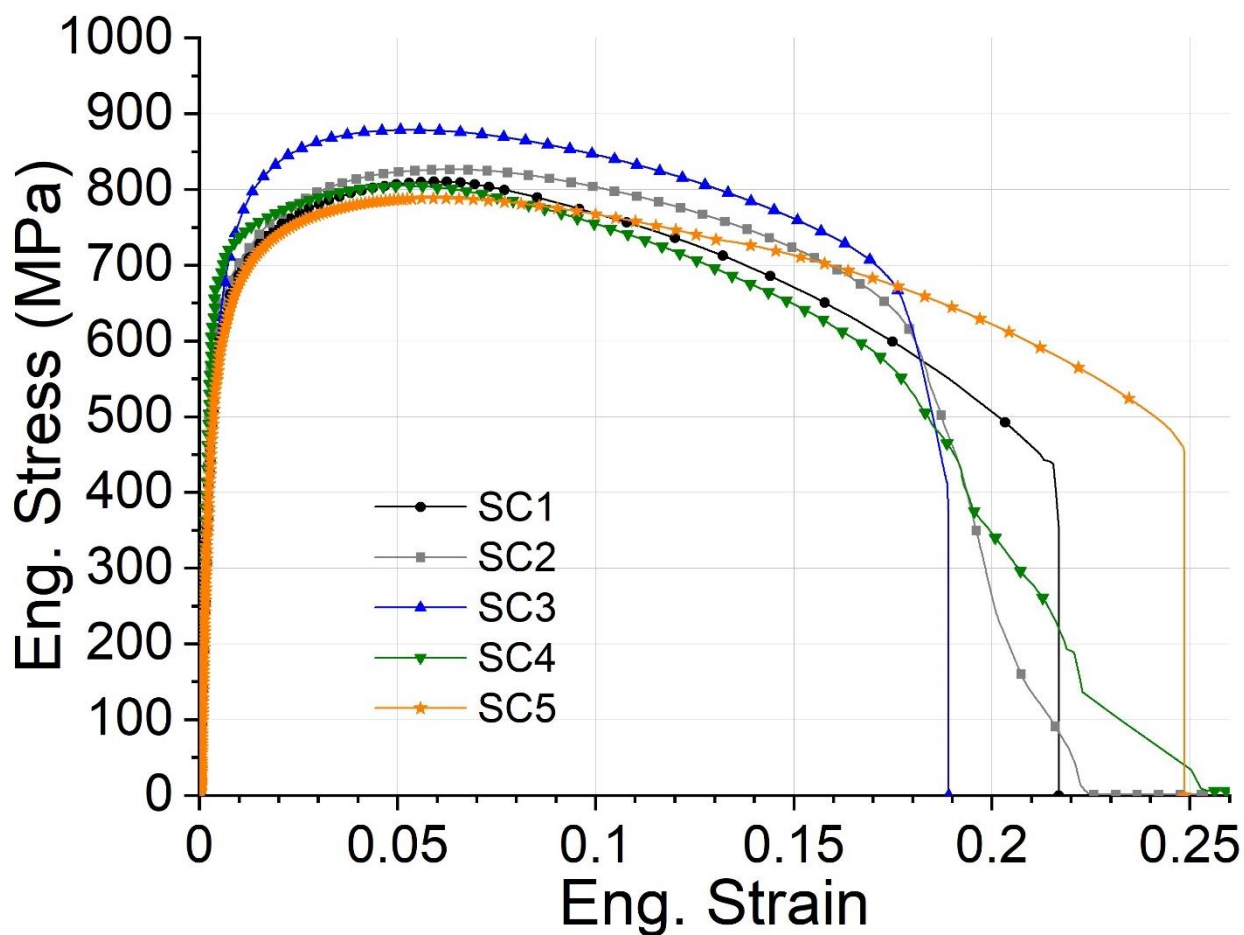


**Figure 5.32** Tensile engineering flow stress at room temperature of specimens with full TMP schedule

**Table 5.10** Mechanical properties calculated from the tensile tests

<b>Specimen</b>	<b>UTS (MPa)</b>	<b>YS<sub>(0.2%)</sub> (MPa)</b>	<b>E (GPa)</b>	<b>% EL</b>	<b>% RA</b>
SC1	810.3	626.8	203.3	21.7	64.4
SC2	826.4	643.0	208.9	22.5	49.7
SC3	878.5	665.3	196.4	18.9	44.1
SC4	804.7	684.3	204.6	25.3	51.6
SC5	788.3	572.0	196.8	24.9	60.7

According to the tensile tests and volume fraction of phases, bainite is the microconstituent that has the greatest influence in the mechanical properties of the CP800.

# CHAPTER 6

## DISCUSSION

### 6.1. Effect of Prior Austenite Grain on Final Product

The initial microstructure is an important factor to predict the final structure after a certain thermomechanical process [43]. The thermomechanical processing of steel plates is divided into several stages. The deformation stages are the roughing and finishing. The roughing is carried out at high temperatures and normally a high degree of strain is applied per pass causing ideal conditions for recrystallization of the austenite grains. In this research, the condition of the as-received material was quench after roughing, so only the effect of austenitic grain during finishing rolling was considered.

Microstructures and XRD indicate that the as-received condition for the CP transfer bar has a homogeneous structure with no presence of large precipitates. The prior austenite grain size confirms that the rough rolling took place at conditions where fully recrystallization occurs due to the equiaxed shape and size of the austenite grains. It is known that the austenite grain refinement will increase the final mechanical properties due to the finer product [56, 57, 72] so that the austenite grain size is an important factor to control during the thermomechanical processing [145].

Austenitic grain size directly influences the critical processing temperatures. In the case of the  $A_{r3}$  temperature, the smaller the grain, or higher density of austenite grain boundaries, the CCT curve shifts to the left due to the increasing number of nucleation sites for a transformation product. Thus, a greater supercooling is required to quench the material. Both, the initial austenite grain size and the amount of strain accumulation in the slab impact to the extent of the  $S_v$  parameter.

Finishing passes should be carried out at temperatures below  $T_{5\%}$  to have better mechanical properties [67]. The purpose of this is to generate strain accumulation without recrystallization of austenite and a greater dislocation density. This will produce larger  $S_v$ , which is the ratio of grain

boundary area per unit volume, causing high driving force and increasing the nucleation sites for recrystallization or phase transformation to either ferrite or bainite [54, 169].

The importance of deformation in the non-recrystallization region lies in the division of the austenite grains into several blocks as a result of the introduction of dislocations and deformation bands into the grains. The nucleation sites for new phases are generally areas with a high density of defects, such as grain boundaries. Therefore, a greater amount of grain boundaries, or high  $S_v$ , combined with high-energy sites such as dislocations, is beneficial to facilitate the desired phase transformation at controlled cooling rates. In addition, the fine austenite microstructure will limit the grain size of the transformed products, which gives an additional advantage since the finer grains increase the strength of the material.

#### **6.1.1. Defining $T_{5\%}$**

The recrystallization-stop temperature ( $T_{5\%}$ ) is the maximum temperature at which no more than 5% of recrystallization in austenite grains is observed at certain deformation conditions.  $T_{5\%}$  varies with the chemical composition and the TMP parameters. The main TMP parameters affecting  $T_{5\%}$  include the strain per pass and the interpass time, but also the strain rate can influence on the determination of  $T_{5\%}$ .

For deformation parameters corresponding to set 1, the signs of recrystallization start to be observed in the single pass test at 980°C, the structure consists of a combination of recrystallized and elongated grains (see Figure 5.13). It is thought that the recrystallized grains were formed after the deformation but before quenching, this period is about 1 second. This statement comes from the flow stress curve, where no dynamic recrystallization behaviour is observed, the same situation is presented in the specimen deformed in the single pass at 1000°C.

On the other hand, on the double hit test at 1000°C of set 1, some grains recrystallized during the 20 seconds of interpass time. Although the single and double hit tests at 1000°C have the same total strain of 0.5, the recrystallized fraction differs. The recrystallized fraction in double hit test at 1000°C is less than the single pass at the same temperature because the static recovery process started during the 20 seconds of interpass time, where there was a rearrangement of dislocations which causes no further recrystallization to happen. This analogy also applies for the tests of set



3, with the difference that there should be a higher recrystallized fraction in set 3 tests at the same temperature as set 1 because set 3 tests were subjected to a higher amount of strain per pass.

In set 2, it is until double hit deformations at 980°C that a partially recrystallized structure is observed. By comparing the double hit tests at 980°C of set 1 and 2, it is observed that for a shorter interpass time, there is a higher percentage of recrystallized fraction, this is because there is not enough time for the dislocations rearrangement that makes that the static recovery process to not complete. This causes a higher driving force for the second pass which encourages recrystallization to take place.

The overall softening between passes is attributed to both recovery and recrystallisation, which are the main restoration mechanisms during TMP. None of the methods described in Table 4.5 to calculate the softening in double hit tests followed as expected. The softening must increase when the deformation temperature is higher. In each of the methods, there is one temperature that does not comply with this. This could be explained because of the slight difference between the total strain at the first and second pass on each of the tests, as was explained in Section 5.3.2. Nevertheless, offset 2% method (Method C) was the closest to the expected behaviour so that this method was chosen for a better reference. The softening calculations with the 2% offset method have been plotted in Figure 6.1 for all sets at different temperatures, where  $T_{5\%}$  and  $T_{95\%}$  are also designated as 20 and 60% softening, respectively.

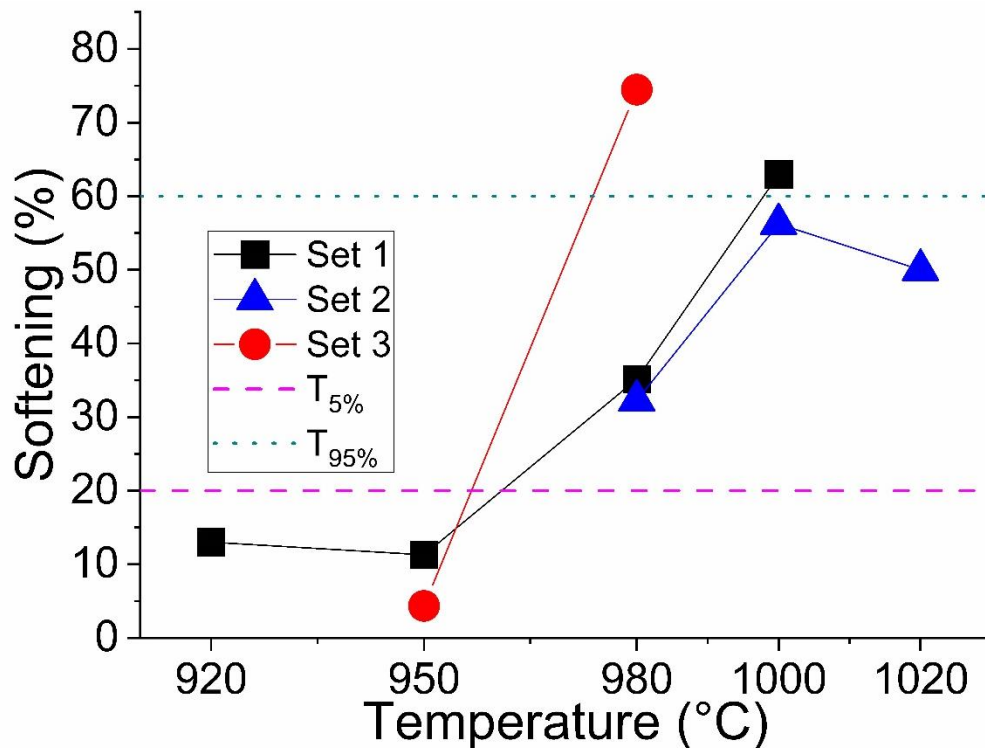


**Figure 6.1** Softening percentage calculated by method C for the 3 sets of double hit tests.  $T_{5\%}$  and  $T_{95\%}$  are represented as 20 and 60% softening

Even though the softening on the 1000°C of set 1 was around 63%, a bit higher than the softening established for fully recrystallized structure, the microstructure still shows some elongated grains. The non-recrystallized fraction in this condition does not exceed 50%. Similar situation with the double hit at 980°C, the softening fraction indicates partial recrystallization in the structure but in fact, the microstructure of this conditions shows completely elongated grains.

The softening percentage calculated for set 2 at temperatures of 1000°C and 1020°C suggests that the morphology of the austenitic grain should be partially recrystallized, the microstructures show a completely equiaxed grain shape with PAGS of 14  $\mu\text{m}$  and aspect ratio of 1.2. Aspect ratio close to 1, along with the small grain size, suggest that the austenite experienced complete recrystallization in the structure.

Although  $T_{5\%}$  can be calculated for different deformation conditions, the critical temperature to focus in is going to be with the processing parameters of set 3, which is the most representative of hot rolling in industrial practice. According to the overall softening of double hit analysis and the PAGB microstructures,  $T_{5\%}$  for set 3 can be defined as 950°C. The austenite structure of this condition has only 8% of recrystallized grains, while at 980°C, the austenite is completely recrystallized. A gradient in deformation temperatures of 30°C at a high amount of strain is more than enough to drastically change the microstructure. This is not exclusive for this type of steels as Dutta and Palmiere [120] showed that the temperature gradient between  $T_{5\%}$  and  $T_{95\%}$  becomes smaller when increasing the strain, as schematically shown in Figure 6.2.

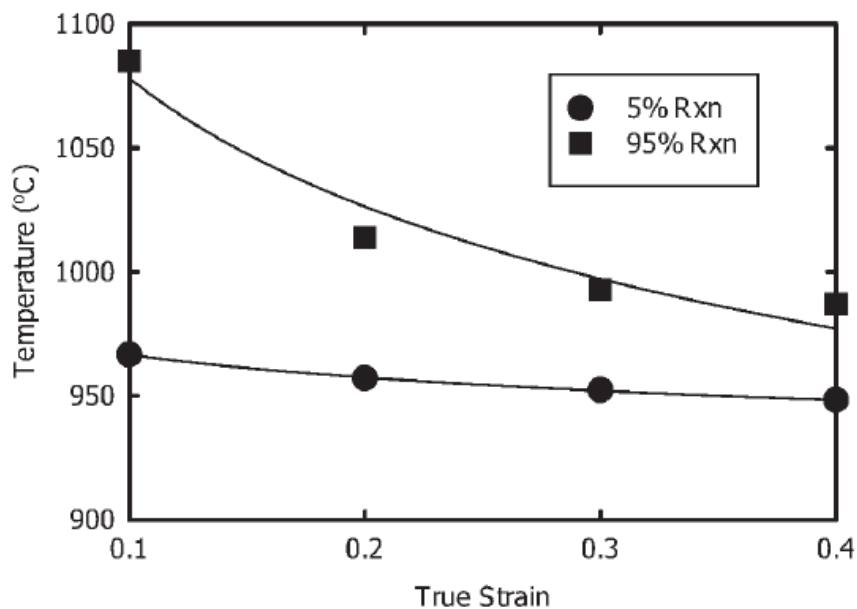


**Figure 6.2** Temperature gradient between  $T_{5\%}$  and  $T_{95\%}$  as a function of strain per pass [120]

The observation of PAGB is the most trustful method to detect the presence of recrystallization, leaving the overall softening calculations and the analysis of flow stress just to get a hint of the shape of the austenite structure without having to crop the strip to characterize a sample.

### 6.1.2. Precipitation vs Recrystallization

Precipitation of niobium carbonitrides Nb(CN) alters the recrystallization conditions in the austenite during hot rolling processing. Precipitation and recrystallization are competing processes. The first process to appear will depend on the processing conditions. As explained earlier, the recrystallization will take place when the driving force or stored energy of deformation is high enough for the restoration mechanism, this is favoured with high temperature and high deformation. By the opposite, there is a lower limit on the processing temperature where the driving force for precipitation encourages the formation of niobium carbonitrides before the start of recrystallization. It has been reported [170] that a high concentration of Nb leads to an increase in the volume fraction of lath bainite and (Nb,Ti)C particles, both are beneficial to improve the strength by microstructure refinement and phase strengthening.

The time for the start of precipitation and recrystallization mechanisms after a deformation pass can be simulated with the empirical model shown below and explained in [128, 171-173]. This model predicts which phenomena will occur first during the interpass time between deformations at specified conditions. The time for 5% of precipitation can be estimated by Eq.8

$$t_{0.05} = 3 \times 10^{-6} [Nb]^{-1} \varepsilon^{-1} Z^{-0.5} \times \exp \frac{-270\,000}{RT} \exp \frac{2.5 \times 10^{10}}{T^3 (\ln k_s)^2} \quad (8)$$

Where  $t_{0.05}$  is the time for 5% of precipitation in seconds, [Nb] is the concentration of niobium in wt%,  $\varepsilon$  is the strain of the deformation pass,  $Z$  is the Zener-Hollomon parameter already described in Section 3.2.2, Eq. 1,  $R$  is the gas constant in joules per K·mole,  $T$  is the absolute temperature and  $K_s$  is the Nb(C,N) supersaturation ratio, which is defined as the ratio of the actual amount of Nb in solid solution to the equilibrium amount and can be calculated with the Eq. 9. Figure 6.3 shows the required time for 5% of precipitation after different strain levels for the CP steel.

$$k_s = \frac{\log[Nb][C + \frac{12}{14}N]}{2.06 - \left(\frac{6700}{T}\right)} \quad (9)$$

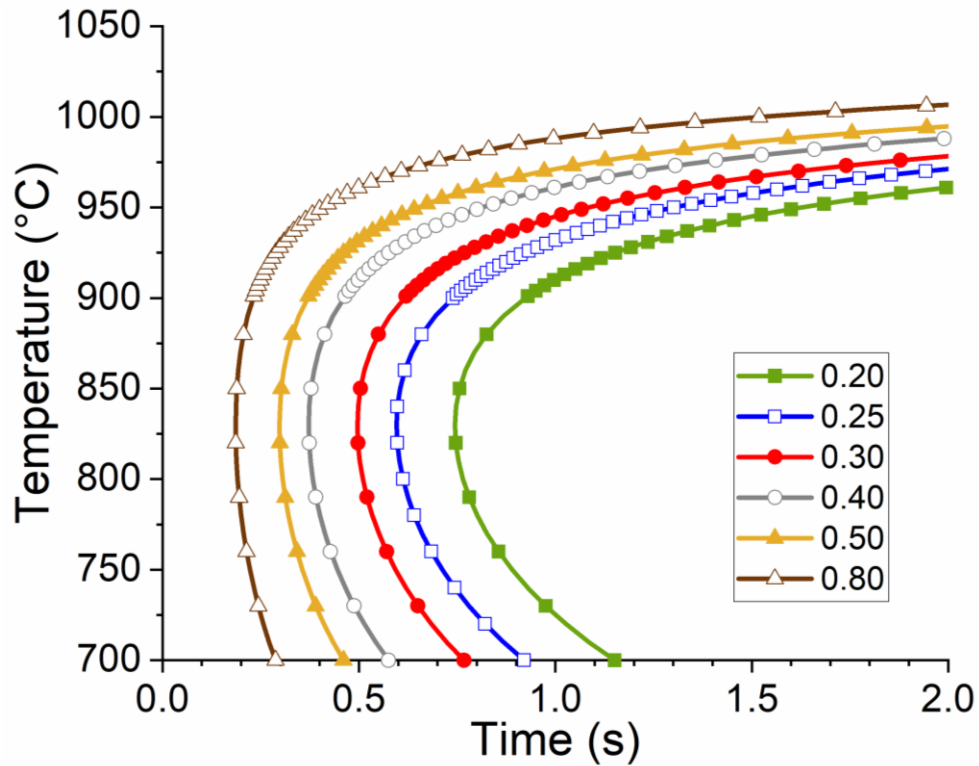


**Figure 6.3** Precipitation start time-temperature curves for different amounts of strain from 0.20 to 0.80

The time for 5% static recrystallization,  $t_{0.05x}$ , can be expressed by the Eq. 10 as:

$$t_{0.05x} = 6.75 \times 10^{-20} d_0^2 \varepsilon^{-4} \times \exp \frac{-300\,000}{RT} \exp \left\{ \left( \frac{2.75 \times 10^5}{T} - 185 \right) [Nb] \right\} \quad (10)$$

where  $d_0$  is the initial austenite grain size before deformation. Finally, the time to get 95% of static recrystallization ( $t_{0.95x}$ ) in the structure can be calculated from the Johnson model for the volume fraction of recrystallization that is given by Eq. 11, where X represents the recrystallized fraction,

$t$  is the time in seconds to achieve the  $X$  recrystallized fraction. By substituting  $X$  for 0.95 in Eq 11, corresponding to the 95% of recrystallization,  $t_{0.95x}$  can be simplified as a function of  $t_{0.05x}$  as shown in Eq. 12:

$$X = 1 - \exp\left(-\ln(0.95)\left(\frac{t}{t_{0.05x}}\right)^2\right) \quad (11)$$

$$t_{0.95x} = 7.66 \times t_{0.05x} \quad (12)$$

The time for the start and complete recrystallization will change depending on the amount of strain applied in a deformation pass. This can be better observed in Figure 6.4 a) and b).

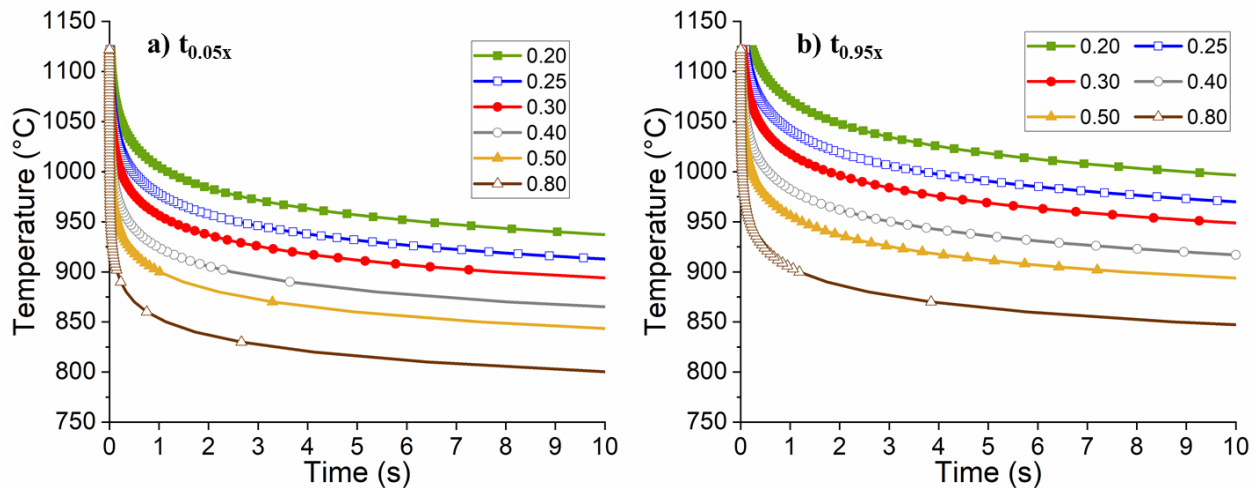


**Figure 6.4** Recrystallization time-temperature curves for a) start 5% of recrystallization and b) complete 95% of recrystallization varying the amount of strain from 0.20 to 0.80

The precipitation vs recrystallisation diagrams for the 0.25 strain, corresponding to deformation conditions of set 1 and 2, as well as the diagram for 0.40 strain per pass, considering for set 3 in double hit test are shown in Figure 6.5. The temperature at the intersection point of  $t_{0.05}$  and  $t_{0.05x}$  can be considered the  $T_{5\%}$  because if the deformation temperature decreases, the precipitation of Nb(C,N) would start first. These precipitates pin the movement of dislocations and grain

boundaries producing that the restoration mechanism of recrystallization to be more difficult to take place. The same can be assumed for the complete recrystallization temperature,  $T_{95\%}$ , which corresponds to the temperature at the intersection of  $t_{0.05}$  and  $t_{0.95x}$ .

An increase in the amount of strain per deformation pass also increases the driving force for recrystallization. This is the reason that at higher strain levels, the lower  $T_{5\%}$ , it can also be noticed that the recrystallization starts earlier when high strain is applied at certain deformation temperature as this mechanism is a thermally activated process.

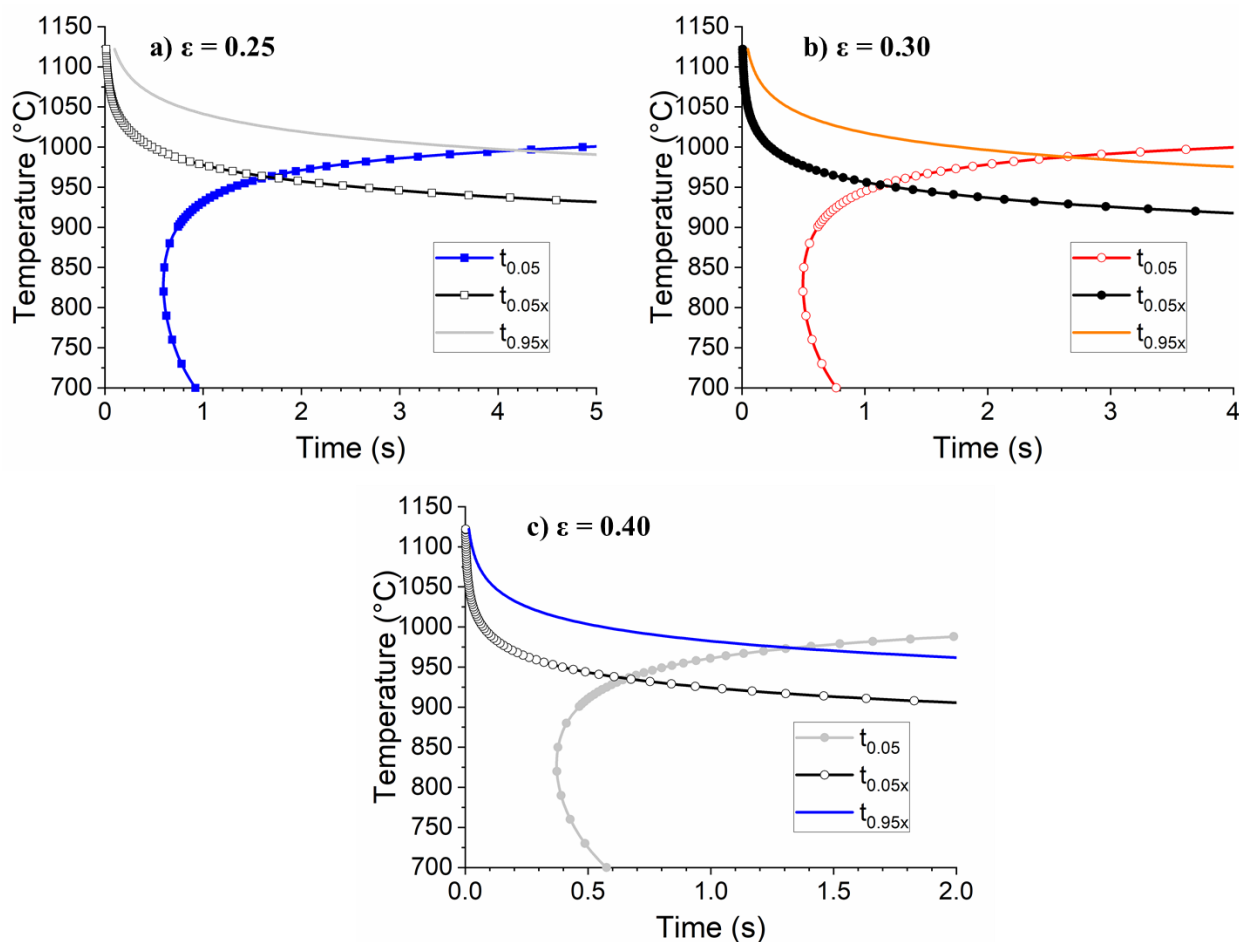


**Figure 6.5** Interaction of the precipitation-recrystallization curves calculated by the model for a) Set 1&2  $\epsilon = 0.25$ , b)  $\epsilon = 0.30$  and c) Set 3  $\epsilon = 0.40$

Figure 6.6 shows the  $T_{5\%}$  and  $T_{95\%}$  for different strain levels calculated with the empirical model. The temperature gradient for these two critical parameters, in the case of the steel evaluated in this

research, is around 35°C. This was first confirmed by the microstructural analysis of the double hit test, particularly on set 3, where the test that was done at 950°C shows elongated austenite grains with only 8% of recrystallization, while the test at deformation temperature of 980°C confirmed that the microstructure was completely recrystallized.

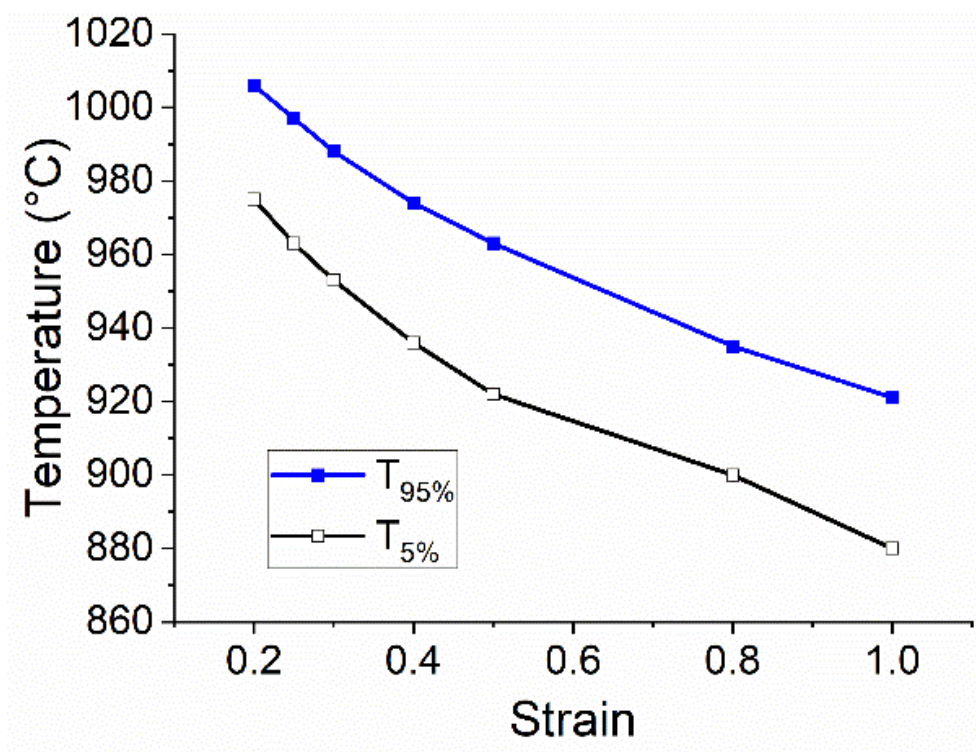


**Figure 6.6** Modelled  $T_{5\%}$  and  $T_{95\%}$  as a function of strain for the CP composition

The empirical model is in good agreement with the experimentally measured recrystallisation fractions for single pass tests for the different sets of deformation conditions. According to the microstructure analysis, and recalling that set 1 and set 2 have the same amount of strain per deformation pass,  $T_{5\%}$  should be between 980°C and 950°C and the model predicts a temperature of 963°C. In case of set 3, the  $T_{5\%}$  for a single pass should be just below 950°C since, at this temperature, partial recrystallization of 17% was observed in the microstructure, for this set conditions, the model predicts 936°C. The effect of interpass time or holding time at deformation temperature after the deformation will be discussed in Section 6.2.1.



## 6.2. Designing a Thermomechanical Schedule for CP800

The combination of a fine-grained and recrystallized austenite after the rough rolling process, following by further deformation of austenite below  $T_{5\%}$  during finishing rolling produce a large ratio of the area of austenite grain boundaries per unit volume, or large  $S_v$ . A large  $S_v$  indicates a suitable amount of nucleation sites for the subsequent phase transformation products, which also encourage the formation of fine transformed grains.

As explained earlier, the TMP route for the CP transfer bar was designed from the entrance of the finishing mill. Once all critical processing temperatures were well defined, the first temperature to select in the TMP schedule is for the first pass on the finishing mill.

The TMP route that makes the most of the chemical composition on mechanical properties would be by refining the austenite grain and also that the deformation in the finishing mill takes place in between  $T_{5\%}$ , to avoid austenite recrystallization [174], and  $A_{r3}$  to avoid deformation of ferrite [67] or a phase different from austenite. Austenite has an FCC crystal structure and is more ductile than ferrite which has a BCC structure due to the close-packed lattice.

There should be a balance of temperature when designing a TMP route for AHSS. If the designed temperature at the beginning of the finishing mill is too high, it would be complex to maintain the strip at high temperature without increasing the processing costs. The metallurgical disadvantage is that the austenite might recrystallize at higher temperatures. In contrary, if the deformation temperature in the first stand of finishing mill is too low, the demanded force in the mill to deform the slab will be higher, increasing the operational costs. Since there is a decrease in temperature in every deformation pass, the strip might start phase transformation by the last deformation pass in the finishing mill. This is not adequate because when the strip is deformed in the intercritical region temperature, the combination of phases in the microstructure causes diverse mechanical properties in different zones of the strip.

The reheating temperature of the PSC specimens was 1150°C. This temperature was estimated from the transfer bar temperature when it was removed and quenched from the rolling mill. The deformation conditions of set 3 of double hit tests are representative of the first pass of the finishing mill in the industrial practice. For this reason, the first pass on the simulation of finishing rolling had the deformation conditions of the set 3.

It is expected that during the interpass time, the temperature of the strip decreases along with the driving force for recrystallization for the following passes. Besides, it is recommended that for the subsequent deformation passes, the equivalent strain applied per pass is reducing, and in consequence, the driving force for recrystallization also decreases. This would prevent the recrystallization process and the microstructure maintains the strain accumulation of each pass. The temperature in the last pass of the rolling mill should be higher than  $A_{r3}$  to ensure austenite deformation. However, last pass temperature needs to be low enough to avoid static recrystallization before entering the runout table, although the mill force increases [175].

$A_{r3}$  is the temperature at which austenite starts to transform into ferrite during cooling. Although the dilatometer results suggest the temperature at the exit of the finishing mill should be at least the higher  $A_{r3}$  found at a slow cooling rate, 755°C. This was verified by the simulation software and the empirical formulas, where Yuan's [118] was the closest to the dilatometer results. However, the temperature of the last pass on the TMP design was selected to be in a range of 850-830°C for different reasons. First, it is strongly recommended to deform the strip at the highest temperature possible to minimize the demanded force in the mill, and in turn, to reduce wear on the rolls. But at the same time, this temperature should be within the range to keep the metallurgical advantages of deformation. Then, in a tandem mill, the temperature difference in the strip from the entrance to the exit of the finishing mill rarely exceeds 150°C in a typical 6-stand configuration. This would also reassure that the deformation takes place in the austenite region.

Even though the PAG microstructure is not completely elongated after the interpass time of the first pass of the finishing rolling (refer to Figure 5.16 B), the microstructure forms a full pancake-like structure after the fourth pass of the TMP schedule. This is produced because the deformation temperature decreases after every pass. Complete non recrystallized structure is essential to obtain fine transformed products and homogeneous mechanical properties on the strip. The static restoration process happening during the 4 seconds between each rolling pass has an effect on the softening for the successive deformation pass. This is also an indicator that a considerable amount of Nb(C,N) precipitates are formed after the second deformation pass on. These precipitates prevent the restoration mechanisms to be completed during the interpass time, thus, the strain and work hardening are accumulated in the following passes.

The key challenge in the fabrication of CP microstructure is to design a worthy cooling strategy [35]. The cooling strategy is designed depending on the dimensions and capacity of the run-out table after finishing rolling. In this case, dilatometer and software simulations are useful to design the cooling strategy [113, 176].

The desired phase volume fractions in the AHSS is obtained by designing a cooling strategy on the run-out table. Since a large  $S_v$  resulted after the deformation passes, the CCT curve would shift to the left, which enable the phase transformation to ferrite even while cooling at high cooling rates. This shift can be also related to the increase of the transformation start temperatures at equivalent cooling rates of deformed and non-deformed specimens [177, 178] and the increment in Gibbs energy of the austenite phase due to plastic deformation [179]. In order to get a considerable amount of bainite, which is a strong phase with greater ductility than martensite, it is recommended to hold the temperature for a short time at bainite transformation temperatures. It is worthy to point out that the CCT diagram showed in Figure 5.8 is no longer representative of the conditions got at the exit of the last deformation pass (refer to Figure 5.16 E). Therefore, a new CCT diagram needs to be calculated due to the smaller grain size as a consequence of the large  $S_v$  or the austenite pancake structure. The austenitisation temperature was 850°C as it is the temperature after the last deformation pass or the beginning of the cooling design, the grain size was estimated based on the distance between grain boundaries of the heavily deformed austenite, the average shortest distance corresponds to the perpendicular of the rolling direction. The estimation of the grain size for the calculation of the CCT diagram does not mean that the average austenitic grain size in the microstructure is 3 $\mu$ m. However, this value was measured as the average distance in the minor axis of the elongated austenite grains. The grain boundaries together with the high dislocation density and strain accumulation generate a large number of nucleation sites for new phases. The CCT diagram for the conditions after the last deformation pass is shown in Figure 6.7, where the bainite region lies around 450-550°C. This CCT diagram predicts the austenite transformation to ferrite even at cooling rates as high as 100°C/s and that the martensite is only formed at cooling rates no lower than 90°C/s.

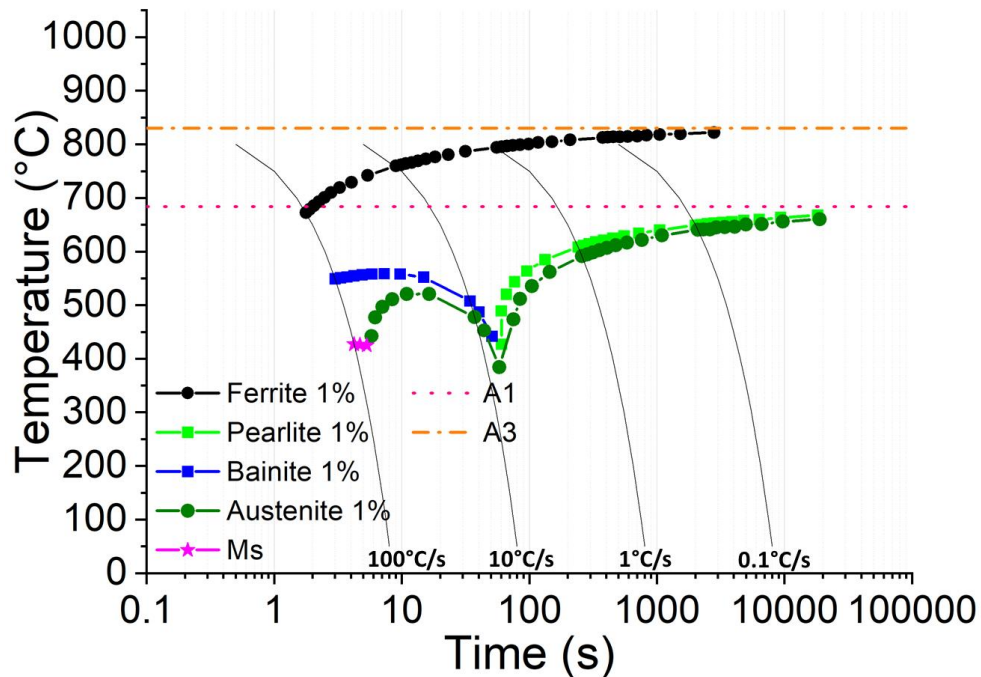


**Figure 6.7** CCT diagram from JMatPro® for CP steel using the conditions after the last pass of the TMP schedule. Austenitisation temperature: 850°C, PAGS: 3  $\mu$ m

Zhou et al [180] designed a TMP schedule of the steel with composition 0.08C-1.8Mn-0.3Si-0.2Ni-0.16Mo where the cooling strategies after deformation were a direct cooling after deformation and another was air cool to 600°C following by water quench. The later route presents better resistance performance but lower yield/UTS ratio, the matrix microstructure after this route consists of polygonal ferrite combined with lath bainite. Since the air cool from the exit of the mill to 600°C is not reasonable in the actual runout table due to the time required to reach that temperature, other cooling strategies were analysed that involves a rapid cool to bainite range temperatures, holding for a period at that temperature followed by quenching. Different studies have investigated the isothermal holding at bainite temperatures, Karellova et al [181] and Zi Yong et al [182] included the effect of the isothermal temperature, they found that the mechanical properties such as yield strength, tensile strength and hole expansion ratio are improved by lowering the isothermal holding temperature. This is in agreement with the SC1 and SC2 specimens (550°C and 500°C isothermal temperatures, respectively) but differs from the SC3 and SC4. This can be explained since the measured cooling rate 1 in SC4 was lower (refer to Table

5.8) and favoured the ferrite transformation. The volume fraction of phases confirmed a higher amount of ferrite in SC4, which is also reflected in the mechanical properties in a greater elongation compared to SC3.

### **6.2.1. Effect of TMP parameters on microstructure evolution**

The microstructural evolution in AHSS is affected by different factors such as the chemical composition, the initial microstructure and every parameter during TMP, such as the deformation temperature, strain, strain rates, interpass time, and the accelerated cooling process. The microstructural evolution analysis is beneficial to achieve the target on mechanical properties. Poor control of the TMP parameters implies considerable changes on the microstructure of steels and therefore, on the mechanical properties [183].

Although the cooling strategy from austenite defines the final microstructure of the steel. The previous process, i.e., the controlled deformation schedule, together with the chemical composition, define the CCT diagram of the steel, allowing an appropriate design of the cooling strategy. The control of the microstructure evolution during TMP involves the strain accumulation, and depending on the selected parameters, can be followed by the recovery or rearrangement and annihilation of dislocations, recrystallization and grain growth [184].

As explained earlier for the  $T_{5\%}$  evaluation, the deformation temperature and the applied strain have a strong influence on the austenite microstructure evolution. One way to decrease  $T_{5\%}$  is by increasing the strain per pass, as can be observed by comparing the double hit tests of set 2 and set 3. This is because more energy is being supplied to the material and the conditions become preferable to start the process of any restoration mechanism or recrystallization. The range temperature between  $T_{5\%}$  and  $T_{95\%}$  becomes narrow and can be as close as  $30^{\circ}\text{C}$  for the deformation conditions of set 3 [120]. Figure 6.8 shows schematically the effect of the deformation temperature together with the amount of strain at different interpass times on the austenite grain shape. Dash lines represent the sets of double hit deformation conditions. When the deformation takes place at low temperature and a small amount of strain, the austenite grains show a completely non-recrystallized structure and the shape of grains becomes elongated or pancake-like. As energy

is added to the steel, either thermal or mechanical, the driving force for recrystallization increases. Naturally, the complete suppression of recrystallization is reached, where new grains begin to form. The microstructure by then, evolve with the new grains and consists of a combined microstructure of recrystallized and elongated austenite grains, also described as partial recrystallization structure. Finally, when the austenite microstructure evolution contains fully recrystallized grains after a deformation pass, indicates that the deformation parameters exceeded the initial suppression of recrystallization and that the deformation took place at high temperature and/or high amount of strain.

This analogy not only applies for the estimation of  $T_{5\%}$ , but it can also be employed on the different stages of the TMP schedule where deformation is applied.

The equivalent diagram corresponding to the steel composition and deformation conditions evaluated in this study was presented in Figure 6.6, which was calculated with the simulation model and validated by the microstructure observations.

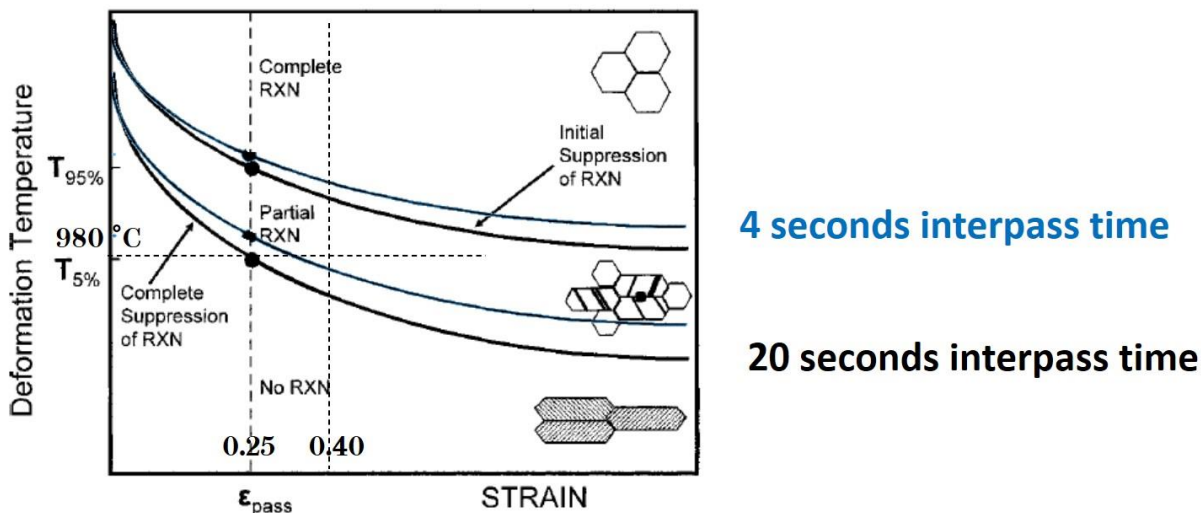


**Figure 6.8** Schematic austenite microstructures as a function of the processing parameters such as deformation temperature, amount of strain and the interpass time. Figure adapted from [31]

$T_{5\%}$  can vary from different chemical compositions in steels, but also  $T_{5\%}$  is dependant of the processing parameters, the higher the strain, the lower the temperature required to initiate the

recrystallization. The interpass time between the passes will also affect  $T_{5\%}$ . As mentioned above, recrystallization and precipitation are competing mechanisms which might nucleate when the steel is subjected to thermomechanical processing. The predominant mechanism or the first mechanism to arise is defined by the processing parameters. Although the present thesis studied a single steel chemical composition, the alloying elements also interact with this critical temperature, especially the carbide formation elements such as Niobium. The higher content of Nb, the higher  $T_{5\%}$  [185].

With such short interpass times, where the nucleation of precipitates was not achievable, there would be no mechanism to prevent the recrystallization to start [186]. This leads to a decrease of  $T_{5\%}$  for short interpass time. On the contrary, if the interpass time is long enough for the nucleation and formation of fine precipitates, these precipitates would pin the austenite grain boundaries retarding the recrystallization mechanism to start. This conducts to an increase of  $T_{5\%}$  for interpass time longer than the precipitation start time. After the nucleation and formation of fine precipitates,  $T_{5\%}$  remains practically constant until the precipitates coarse and weaken the grain boundaries movement, meaning that recrystallization is favoured and  $T_{5\%}$  decreases [187-189].

The calculated precipitation start time for the deformation conditions after the first pass on the TMP schedule is in the order of 0.8 seconds as can be observed in Figure 6.5c). However, the interpass time designed was 4 seconds, which is representative of the actual interpass time in a finishing tandem mill. This means that there was more than enough time before the second deformation pass for the fine precipitates to form. As an example, if the interpass time between the first and the second pass is increased to 20 seconds, maintaining at the deformation temperature, the dominant mechanism in the microstructure evolution might change since the longer interpass time allows the dislocations to move and initiate the static recovery followed by static recrystallization. Furthermore, as explained in the previous paragraph, the precipitates would limit their function of retarding recrystallization by the possible coarsening during this longer period after the deformation. This would cause that the austenite microstructure just before the second pass on the TMP schedule consists of partial recrystallization, which is not recommended for the development of AHSS microstructure.

Another analogy of the effect of interpass time on  $T_{5\%}$  is that when the interpass time of a double hit test is shortened, that is the case of deformation conditions of set 3, the flow stress behaviour on the second pass would have a trend similar to the single pass test at the equivalent strain. Hence,

the overall softening percentage decreases for the second pass and the driving force for recrystallization would not be enough for the restoration process to take place [30, 31, 190]. Therefore,  $T_{5\%}$  increases by shortening the interpass time.

Although the effect of the strain rate was not evaluated in the present thesis, it is well reported that at higher strain rates, the flow stress increases [191]. Consequently, at higher strain rates, the chances for dynamic recovery are reduced since the time during deformation is less. Also, the austenite is more likely to present a work-hardened behaviour, indicating that for those deformation conditions the driving force for static recrystallization increases for the subsequent pass. Because of this, the static recrystallization does not require additional energy to carry on, and thus, it can be considered that  $T_{5\%}$  has decreased [188, 192].

Dilatometry testing reveals that cooling rate has a strong influence on  $A_{r3}$  during the austenite to ferrite transformation. The results indicate that a higher cooling rates the lower the  $A_{r3}$  temperature, and that at slower cooling rates, the  $A_{r3}$  approaches to the equilibrium  $A_3$  temperature. This parameter can determine whether ferrite is able to form during the microstructural evolution on the TMP.

The cooling rate applied during the runout table in a thermomechanical processed steel impacts in the mechanical behaviour and volumetric fraction of phases [193]. As the cooling rate increases, martensite is more likely to form. Due to martensite is a hard and brittle phase, the higher amount of martensite increases the overall strength, but the ductility is reduced. This trend is associated with the generation of local dislocations introduced by the shear deformation during martensitic transformation, together with the carbon supersaturation in martensite [194].

Increasing the strength by higher cooling rates suggests that higher energy is required for dislocation movement. Therefore, the first fast cooling on the runout table after the last pass on the finishing rolling prevents the recovery mechanism to take place, resulting in a high dislocation density in the final microstructure [195, 196].

The condition of the strip at the exit of the finishing mill exhibits a heavily deformed austenite microstructure with a high  $S_v$ . At this stage, there are several nucleation sites for ferrite, thus, this phase is capable to nucleate even at fast cooling rates as can be observed in the CCT diagram in Figure 6.7. High cooling rates are advantageous for increasing the strength since the interstitial elements have less time for diffusion and limit the ferrite grain size. In addition, the high cooling



rates reduce the time that the strip stays on the cooling table, which makes a more efficient process. The step cooling in the runout table intends to transform a higher amount of bainite which also provides strength to the steel. Figure 6.9 shows a simulation of the volume fraction and mechanical properties according to JMatPro® software using the actual temperature measurements in the TMP machine during the cooling strategy of SC3. This simulation is based on the conditions described for the CCT diagram in Figure 6.7. During cooling, ferrite starts to form at around 755°C, while less than 0.5% of the bainite volume fraction starts at 580°C, but then, during the isothermal holding time at bainite region temperature (550°C), the remaining austenite in the microstructure is transformed into bainite. It can also be observed that the tensile strength significantly increases when increasing the amount of bainite. The different cooling strategies evaluated at the exit of the finishing mill were also simulated in the JMatPro® software, and the prediction of volumetric fraction of phases with the expected mechanical properties is shown in Table 6.1. According to the software, none of the cooling patterns led to a martensitic transformation. This might be because the isothermal holding time is long enough to transform all the remaining austenite into bainite. The prediction of mechanical properties by JMatPro® does not agree with the measured values of UTS in the tensile tests. JMatPro® foresees the mechanical properties based on the holding isothermal temperature of the step cooling since SC2, SC4 and SC5 expect the same mechanical properties despite their differences in the TMP route. Regarding SC1 and SC3, lower stresses are expected due to the higher temperature in the isothermal holding time. The small variation in tensile stress in SC1 and SC3 may be due to the difference in the cooling rate. Furthermore, the computed phase distribution and mechanical properties for SC4 and SC5 is identical, which is not reliable due to their differences in the isothermal holding time. As it was previously presented, in the actual tensile tests of SC4 and SC5, there is a great difference in the YS caused by the longer isothermal holding time in SC5 despite having the same deformation route.

Hairer et al [197] studied the microstructure development of a CP800 by varying the cooling rates on the runout table after the finishing rolling mill. They conclude that the hardness increases due to the higher ratio of bainite/ferrite at higher cooling rates showing a 361 HV1 for a 120°K/s.

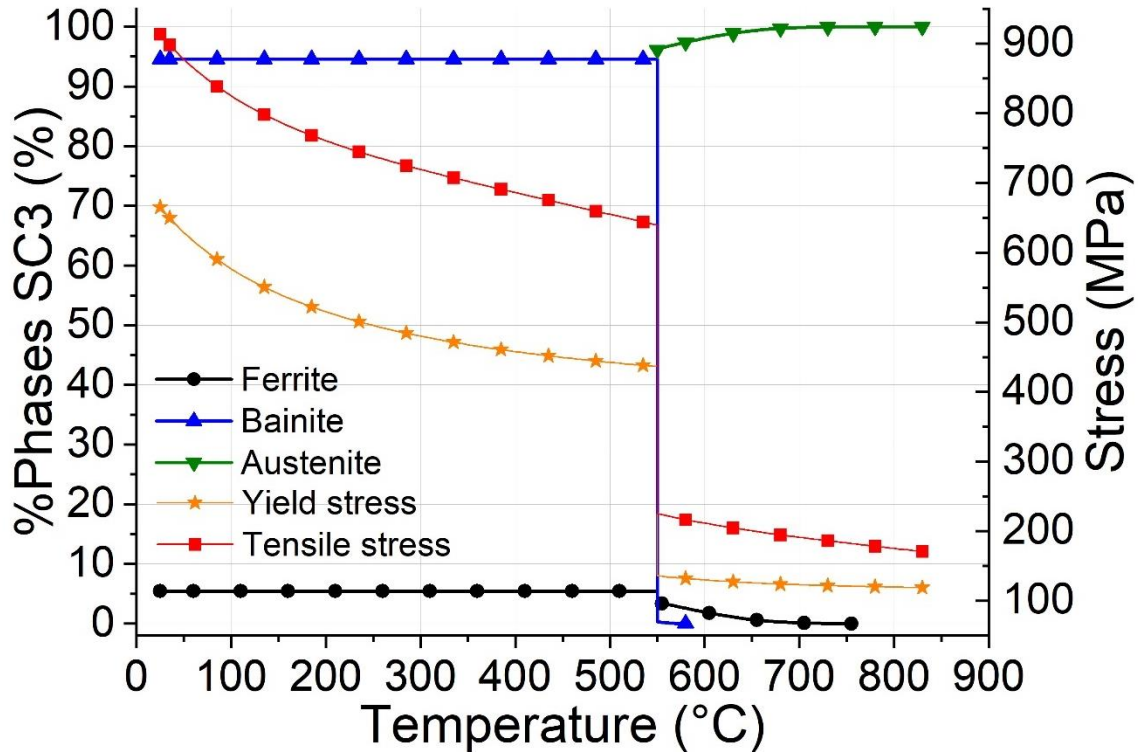


**Figure 6.9** JMatPro® simulation of the evolution of austenite decomposition and mechanical properties following the cooling strategy of SC3

**Table 6.1** Volume fraction and mechanical properties prediction based on the different cooling strategies after the finishing rolling. Calculations made by JMatPro® software

Cooling strategy	Volume fraction (%)				Mechanical properties (MPa)	
	Martensite	Bainite	Ferrite	Austenite	Yield stress	Tensile stress
SC1	0	85.4	15.5	0	667	910
SC2	0	87.7	12.3	0	672	921
SC3	0	94.6	5.4	0	665	913
SC4	0	85	15	0	672	921
SC5	0	85	15	0	672	921

Since the tensile specimens were obtained from the PSC specimens to evaluate the mechanical properties developed by the different TMP schedules, the measured percentage of elongation

cannot be comparable with the ASTM standard for tensile tests due to the variances in the gauge length and cross-sectional dimensions of the specimens, even for the sub-size standard. However, for this analysis, the percentage of reduction of area (%RA) is more relevant since the ductility measured by this parameter is not dependant on the dimensions of the specimen [198]. Since the %RA is not considered as a property of the material but only a characterization of the conditions of the tests, there is no specific range of %RA for the different CP steel grades. However, this parameter has been reported by other authors for the CP800 with similar testing conditions and specimen dimensions to this work. Nikky et al [199] reported a reduction of area of 69% in a CP800 tested over the rolling direction in a sub size specimen with 2.9 mm thickness, the UTS reached 810 MPa and a total elongation of 19.6% in a 25 mm gauge length. The microstructure consisted only of ferrite and bainite with a small amount, between 1 and 2%, of martensite. The gauge length used in Nikky's work is longer than the one used in the present thesis, and because of that, the elongation percentage cannot be compared. However, the UTS and %RA correspond to the properties got after the TMP simulation of SC1 route. Another study presented by Singh et al [200] used a CP800 steel sheet for tensile tests specimens with 2 mm thickness and 4 mm width, using a gauge length of 10 mm. These specimen dimensions are very close to the testing in this thesis, which had a theoretical initial cross-sectional area of 6 mm<sup>2</sup>, where the thickness had 3 mm and 2 mm of width. Singh et al [200] and Cadoni et al [201] reported a UTS of 872 MPa, YS of 685 MPa, total elongation of 15.48% and the reduction on the cross-sectional area of 45.53% at a low strain rate tensile test. These mechanical properties totally match with those obtained from the SC3 TMP route design.

It is well known that the final microstructure of steel depends not only on the chemical composition but mainly on the TMP route to which the steel was exposed. The mechanical properties at a macro scale are strongly related to the microstructure, i.e., the shape, size, volume fraction and dispersion of every constituent or phase on the microstructure. Figure 6.10 shows the correlation of the volume fraction of phases with the mechanical properties that were developed according to each evaluated TMP route. This correlation considered that martensite and bainitic ferrite (lower X-axis) are the transformed products that provide strength to the steel (UTS in the left Y-axis), while polygonal ferrite with the slight presence of retained austenite (upper X-axis) increase the ductility (%RA in right Y-axis).

Normally, ductility in AHSS is reduced as strength increases [202]. Such is the case of the SC3 and SC2, which obtained the greatest strength resistance, but at the same time, these specimens obtained the least ductility. On the other hand, samples SC4 and SC5 presented the lowest UTS, which was unexpected since the last pass temperature on the TMP schedule were lower (830°C) than the rest of the specimens. In the case of SC4, the actual cooling rate 1, corresponding to the range from the last pass temperature and the isothermal temperature, was slower compared to the cooling rate 1 of the rest of the specimens. This allowed the generation of a greater amount of ferrite, and consequently, a lower UTS. However, this cooling rate 1 has no effect on the yield stress since SC4 exhibited the highest yield stress of all the specimens due to the last pass was carried out at a lower temperature.

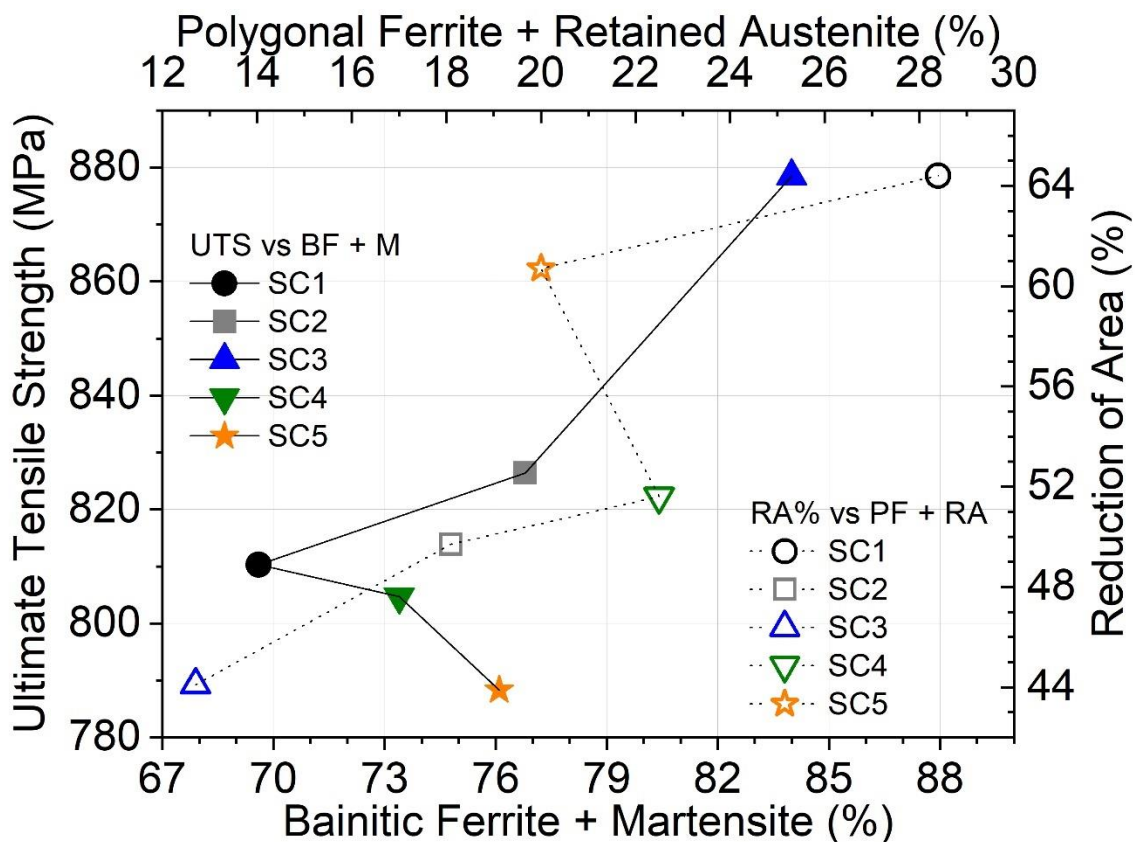


**Figure 6.10** Correlation between volume fraction of phases with the mechanical properties developed in the different TMP schedules

The longer isothermal holding time during cooling not necessarily results in a higher amount of bainitic ferrite, but it clearly acts as tempering heat treatment. The SC5 specimen had the longest isotherm time and have achieved volumetric fractions similar to other routes with a shorter holding time such as the SC2. However, the mechanical properties evidence that there was a decrease in UTS and increase in elongation even though the last deformation pass on SC2 was performed at a higher temperature. This is a consequence of the softening mechanisms and relaxation of residual stresses that were caused by the longer period at high temperature. Respective to the microstructure observation, SC5 specimen shows the cleanest structure in terms of dislocation density and complex substructure in the deformation bands. Despite the same total amount of strain, there are less low angle grain boundaries in the distribution of microstructure. The isothermal temperature in the bainite region can lead to different morphologies of bainite, mainly the lath type bainite for lower isothermal temperature and the granular bainite for higher isothermal temperature [203].

One parameter to evaluate the efficacy of a TMP route on the improvement of mechanical properties in an AHSS is the product of the UTS by %RA. SC1 shows the highest value of 52,183, as shown in Figure 6.11. This specimen has a moderate UTS resistance but the highest ductility due to its high content of polygonal ferrite combined with fine grains. Despite SC3 has the highest UTS resistance, its factors generate the lowest UTS-%RA ratio, which makes it not to be the best candidate for an application where a combination of high strength and formability is needed.

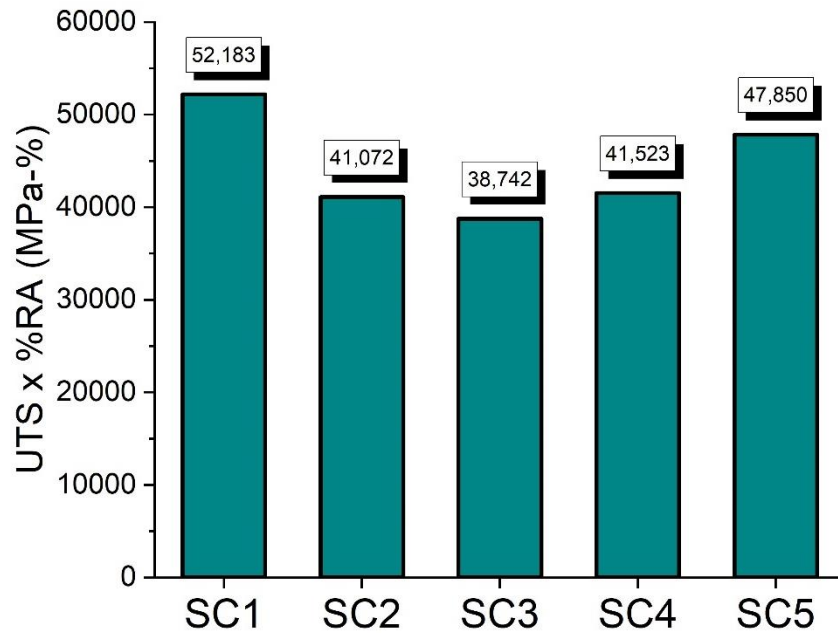


**Figure 6.11** UTS by %RA product of the specimens subjected to the different TMP schedules

### 6.3. Comparison of Laboratory simulation vs Industrial TMP Schedule

Further academic research on TMP for industrial applications is essential for the improvement of technology or the development of new products. This can be achieved by using laboratory techniques capable of replicating the industrial processing conditions in a hot rolling mill [174]. These techniques are indispensable to understand the processing parameters and their effect on the microstructure evolution during specific deformation strategies.

Due to the metallurgical complexity of AHSSs, sometimes it is not viable to roll all AHSS grades in a rolling mill with the same rolling technology due to the capability of the mill.

It has been demonstrated that deformation conditions experienced during plate and strip steel hot rolling can be replicated by the plane strain compression testing [125, 127, 204]. PSC testing is commonly used to generate material property data for the conditions encountered in a hot rolling mill. To investigate the potential microstructure development on the chemical composition in the

present thesis, the selection of processing parameters for laboratory testing slightly differs from the industrial process. Figure 6.12 shows a general schematic representation of a full TMP route at an industrial mill, covering from the reheating of the slab to the coiling of the strip (refer also to Figure 3.7). Figure 4.13 shows the designed deformation passes for laboratory simulation of the finishing rolling mill.

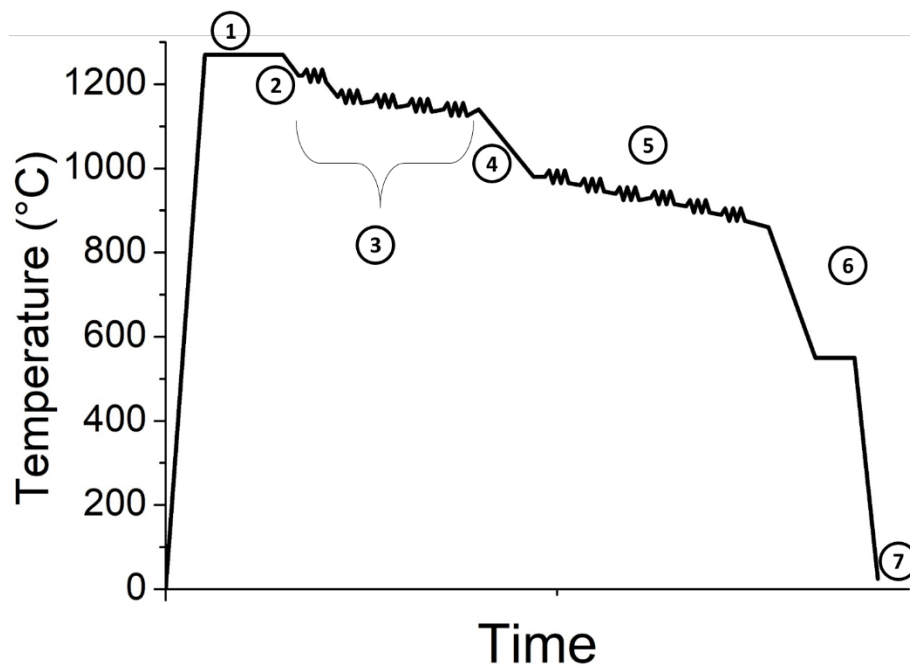


**Figure 6.12** General full TMP processing of steel in an industrial mill

- 1.- Reheating slab at a temperature between 1200°C and 1300°C for 1-2 hours.
- 2.- Scale breaker.
- 3.- Entrance to the reversible mill for 5 passes of rough rolling above  $T_{95\%}$  with long interpass time and a typical total strain from 1.6 to 2.
- 4.- Coil box & crop.
- 5.- Entrance to the finishing tandem mill to carry out 6 passes below  $T_{5\%}$  with short and variable interpass times. Typical total strain from 1.7 to 2.3
- 6.- Entrance to the runout table. Cooling strategies are variable.
7. Coiling of the strip from 300°C to 650°C, followed by a very slow cooling rate.

The main differences in the deformation parameters between the industrial process and the TMP routes evaluated in the laboratory are described below.

First, the total strain was limited by the dimensional restriction of the thickness on PSC specimens. Also, the designed TMP route consisted of fewer deformation passes trying to maintain the ratio of strain accumulation per pass that is normally generated in the industrial mill.

Then, in the simulation of the finishing passes on the laboratory TMP machine, the interpass time between the 4 passes remained constant. This is unreal in the actual mill since the reduction on every stand will enlarge the strip in the longitudinal direction, causing an increasing strip speed in the mill after every deformation pass. Since the distance between each deformation stand of the finishing mill is constant, the interpass time decreases after each subsequent pass. This also affects the strain rate in every pass. In the industrial practice, the strain rate increases after each pass and generally it is in a range from 1 to 40 s<sup>-1</sup>. In the laboratory simulation, the effect of strain rate was not considered, so it remained constant for each pass to simplify the analysis of microstructure evolution. As explained earlier, T<sub>5%</sub> increases when shortening the interpass time, but actually, the deformation temperature decreases after every pass because of the heat transfer to the environment. None of these factors in the processing contributes to increase the driving force for recrystallization. This causes strain accumulation and heavily deformed austenite with great S<sub>v</sub>, which is considered the ideal austenite microstructure at the start of the runout table.

The thickness of the PSC specimen after deformation of the complete TMP schedule is 3 mm, while in strips is normally lower. This concerns that transformation products could be different at the centre and the surface of the specimen, as the centre had completely pancake structure while the equiaxed PAG are present at the surface due to the equivalent strain in the PSC specimens, that is mainly distributed at the centre, as shown in Figure 6.13. The phase transformation product, near the top and bottom of the PSC specimen and out of the deformation zone (where the tools of the TMP machine made contact with the specimen) is more likely to form only martensite at the cooling rates experienced in the simulation of runout table because of the effect of grain shape and size that modifies the CCT diagram. This can be observed in the microstructures in Figure 6.14 taken at the top, centre, and bottom of the PSC specimen. Considering a larger amount of strain during the industrial practice in the finishing rolling, the austenite microstructure would be more



homogeneous throughout the strip thickness and also, there would be a greater  $S_v$ , which might increase the final tensile strength.

The width of the strip is another factor to consider when designing the TMP schedule at industrial scale due to the force required in the motors of the mill to deform the slab. This force is mainly dependant of the deformation temperature of the steel. As has already been proved, this parameter has a strong impact on the development of microstructure evolution during TMP.

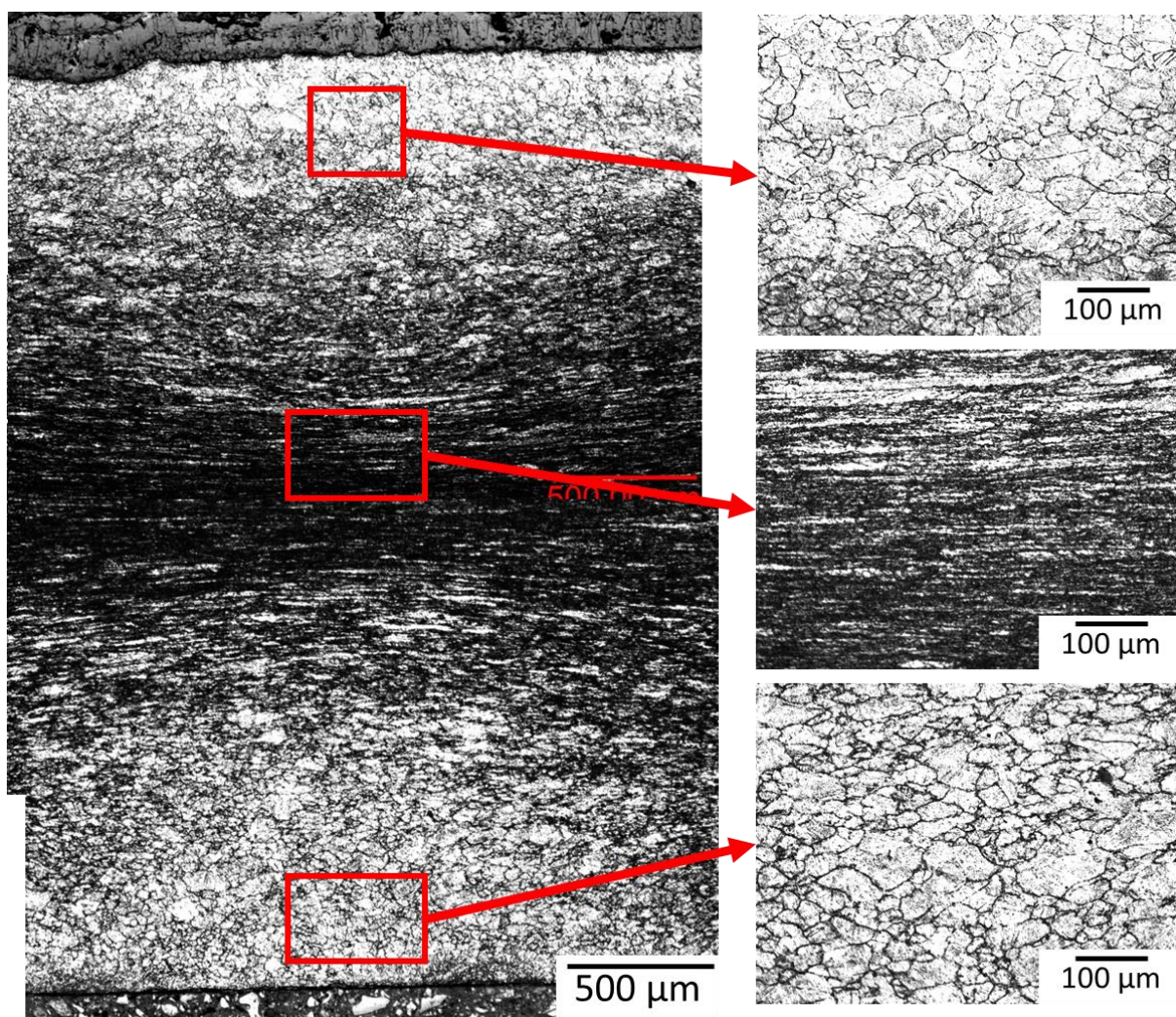


**Figure 6.13** Equivalent strain distribution after the PSC deformation observed in the longitudinal direction. Microstructure near the top and bottom surfaces exhibit more equiaxed austenite grains while at the centre is completely elongated structure. Etchant: saturated picric acid solution

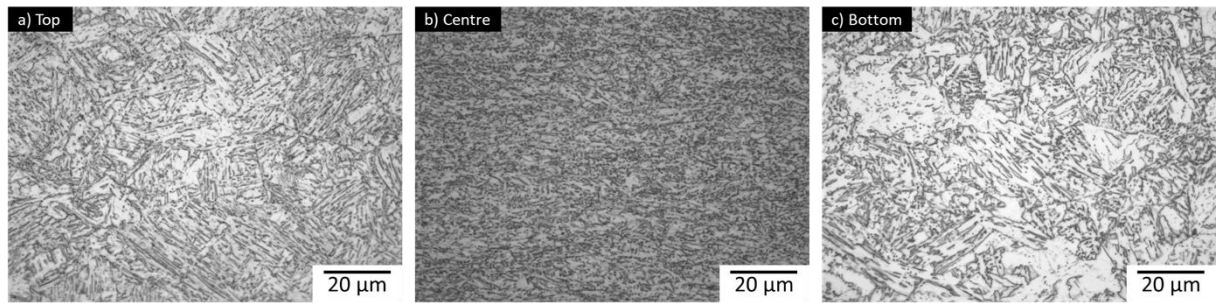


**Figure 6.14** Microstructure observation at a) top and c) bottom near the surface of the PSC specimen and b) at the centre of the specimen. Etchant: 2% nital

# CHAPTER 7

## CONCLUSIONS

The TMP technology enabled to develop features of a CP800 steel grade from the as-received composition and microstructure. This type of steel is classified in the AHSS family, and its main application goes to the automotive industry for components where a great combination of high strength and high ductility is required.

The designed TMP consisted of the finishing rolling simulation to take place at deformation conditions below  $T_{5\%}$ . The austenite microstructure evolution involved strain accumulation from each deformation pass to form deformation bands with high dislocation density before the phase transformation. This was followed by different cooling strategies that varied the volume fraction of phases. In general, this conditioning of austenite implies a heavy deformation at a temperature where there may be a minimum recovery but no recrystallisation, which upon phase transformation produces a fine and homogeneous microstructure. This leads to mechanical properties in tensile tests at room temperature ranging from 780 to 880 MPa in UTS, and 44% to 64% in reduction of area.

1. Laboratory studies demonstrated that the strict control of parameters during the TMP is vital. A slight variation on the TMP schedule implies considerable changes in the final microstructure and therefore, in the mechanical properties. This may cause a downgrade of the alloy or the alloy may be classified in a different category of steels.
2. The chemical composition of a steel is not exclusive for a specific AHSS grade. The TMP route will define the final microstructure. The microalloying elements give the advantage to properly design a TMP route and to encourage the development of the required microstructure using the range of processing parameters available in the actual hot rolling mill facility.

3. According to the TMP analysis, it is not mandatory to avoid the deformation at conditions that lead to a partial recrystallized structure in the first pass of the finishing rolling. This condition can be considered as long as the following passes allow the strain accumulation to develop a completely elongated austenite microstructure at the end of finishing rolling. The advantage of this is that the strip can be deformed at a higher temperature, which considerably reduces the demanded force in the mill. However, this could generate fewer nucleation sites that might change the final microstructure during the controlled cooling process on the runout table.
4. A consistent agreement was found on the characterization techniques for the microstructures after the controlled TMP schedules. The analysis of EBSD for identification of phases was validated by the observation of these constituents in the electron microscopes and their nanohardness values got in the AFM studies.
5. All TMP schedules in this work developed fine microstructures by the effect of the finishing hot rolling below  $T_{5\%}$  and proper cooling strategy design. This resulted, only by TMP, in an improvement in the strength-ductility balance for this steel composition as a hot rolled product, i.e., without the need for cold rolling to achieve the same strength levels.
6. The recrystallization-stop temperature ( $T_{5\%}$ ) is highly influenced by the processing parameters.  $T_{5\%}$  decreases by different factors such as increasing the amount of strain and/or strain rate. It also decreases by maintaining long interpass times. The temperature gradient between  $T_{5\%}$  and  $T_{95\%}$  can be as low as  $30^{\circ}\text{C}$  for high strain deformations.
7. Analysis of PAG microstructures is the most trustful method to detect the presence of recrystallization after a deformation pass. The fraction softening analysis gives a hint of which type of austenite structure is present at certain deformation conditions. This is done without

the need to crop part of the strip to follow the metallographic preparation and analyse the microstructure.

8. The deformation parameters impact on the microstructure at the exit of the finishing mill, which is an important factor to design the cooling strategy. The nucleation sites for ferrite transformation increase with the austenite grain boundaries closer to each other. This allows the formation of the CP microstructure even at high cooling rates, leading to a more efficient cooling process in the runout table due to the relatively short times needed for transformations.
9. The step cooling during the controlled cooling is the most convenient strategy, not only for a metallurgical point of view but also for productivity efficiency. However, the isothermal step temperature and time in the cooling strategy need to be carefully selected as they alter the microstructural evolution. This way, the transformation of an appropriate volume fraction of bainitic ferrite can be achieved by applying fast cooling rates. Otherwise, slow cooling rates cause longer times in the runout table but also, a restoration mechanism is more likely to begin. Therefore, the final tensile strength is adversely affected although the final product would be more ductile.
10. From the evaluated TMP routes, the highest UTS consisted in the last pass deformation at low temperature followed by a fast cooling rate to the isothermal step at 550°C, which is in the upper region of the bainite transformation in the CCT diagram. Though, this specimen had the lowest ductility. By the opposite, the specimen with the highest ductility was subjected to the low last pass temperature and the longest isothermal holding period at 500°C. This specimen presented the lowest UTS of the specimens. However, the greatest combination of strength and ductility were developed by the last pass deformation at 850°C and the isothermal step cooling at 550°C.

# CHAPTER 8

## FUTURE WORK

This chapter discusses some suggestions and considerations for future work in the study of the development of microstructures and mechanical properties of AHSS for automotive applications. After the analysis of the results in this thesis, if my doctoral studies could extend for a longer time, I would have liked to perform tests to simulate the coiling process. This implies a slow and controlled cooling rate after the step cooling on the runout table. I would not expect a radical change in phase volume fraction during this process. However, this heat treatment would play as a tempering process, and consequently, the final mechanical properties of the strip would be altered.

Once the complete process has been simulated in the laboratory with success on the development of desired microstructure and mechanical properties, the need to scale the TMP strategy to an industrial level will be the next challenge. The capacity of the steel plant must be considered and the TMP schedule should be designed with a more flexible range of deformation parameters since, most of the time, it is more difficult to have a homogeneous control of the parameters throughout the entire strip during the TMP.

Another aspect to consider for a future work that has not been considered in this thesis is that some specifications for certain AHSS grades for automotive applications require the hole expansion testing, which could be significantly useful to validate the quality and functionality of the steel grade developed through a specific TMP route.

Finally, as a recommendation for future studies on TMP route designs at laboratory scale for different grades of AHSS is that the entire process, from the reheating of slabs and rough rolling, could be simulated with larger specimens that can support the total strain with a more representative number of passes to the actual process. Although some works have simulated this using torsion instead of plane strain compression, heading to a further study in the comparison of the two techniques, involving the mechanical performance and the development of microstructures. Simulations of the entire TMP can lead to an optimization of the rough rolling

deformation, which according to literature, the ideal roughing condition is to refine the austenitic grain by recrystallization, but at the same time, to nucleate fine niobium precipitates to delay recrystallization in the next stage, i.e., the finishing rolling. Furthermore, the time between roughing and finishing rolling should not be as long to prevent the precipitates to grow, and that their effect on recrystallization delay to be negatively affected. As studied in this work, the finishing rolling should always be carried out below the processing conditions to avoid recrystallization and increase the  $S_v$ . The cooling strategy on the runout table must be designed with a CCT diagram for the conditions at the exit of the finishing rolling.

# CHAPTER 9

## REFERENCES

- [1] "Climate Change & CO<sub>2</sub>." OICA. <http://www.oica.net/category/climate-change-and-co2/> (accessed 2017).
- [2] "Key CO<sub>2</sub> Emissions Trends," International Energy Agency, 2016. [Online]. Available: <http://www.iea.org/publications/freepublications/publication/KeyCO2EmissionsTrends.pdf>
- [3] L. W. Cheah, "Cars on a diet: the material and energy impacts of passenger vehicle weight reduction in the U.S.," Degree of Doctor of Philosophy in Engineering Systems, Engineering Systems Division, Massachusetts Institute of Technology, 2010.
- [4] J. Norman and J. Allwood, "The impact of reducing car weight on global emissions: the future fleet in Great Britain," *Philosophical Transactions. Series A, Mathematical, Physical, and Engineering Sciences*, vol. 375, no. 2095, pp. 20160364-20160364, 2017, doi: 10.1098/rsta.2016.0364.
- [5] W. Gan, S. Babu, N. Kapustka, and R. Wagoner, "Microstructural effects on the springback of advanced high- strength steel," *Metallurgical and Materials Transactions A*, vol. 37, no. 11, pp. 3221-3231, 2006, doi: 10.1007/BF02586157.
- [6] "Steel in automotive." World Steel Association. <http://www.worldsteel.org/steel-by-topic/steel-markets/automotive.html> (accessed 2020).
- [7] (2019) Steel & AHSS in automotive: Prominence and impact. *Efficient Manufacturing*. Available: <https://www.industr.com/en/steel-ahss-in-automotive-prominence-and-impact-2361539>
- [8] T. B. Hilditch, T. de Souza, and P. D. Hodgson, "2 - Properties and automotive applications of advanced high-strength steels (AHSS)," in *Welding and Joining of Advanced High Strength Steels (AHSS)*, M. Shome and M. Tumuluru Eds.: Woodhead Publishing, 2015, pp. 9-28.



- [9] "Complex Phase (CP) Steels | WorldAutoSteel." <https://www.worldautosteel.org/steel-basics/steel-types/complex-phase-cp-steels/> (accessed 2018).
- [10] N. Fonstein, *Advanced High Strength Sheet steels*. Springer International Publishing AG, 2015.
- [11] Z. Jingwei and J. Zhengyi, *Rolling of advanced high strength steels: theory, simulation and practice*. Taylor & Francis Group, 2017.
- [12] D. K. Matlock and J. G. Speer, "Third Generation of AHSS: Microstructure Design Concepts," in *Microstructure and Texture in Steels*: Springer, 2009, ch. 11, pp. 185 - 205.
- [13] D. Múnera, F. Pinard, and L. Lacassin, "Very and Ultra High Strength Steels Based Tailored Welded Blanks: A Step Further Towards Crashworthiness Improvement," Warrendale, PA: SAE International, Warrendale, 0148-7191, 2006.
- [14] B. Hammer, T. Heller, and G. Stich, "Properties and application of multiphase steels with special focus on hot rolled martensitic steels," ThyssenKrupp Steel AG.
- [15] WorldAutoSteel, *Advanced High-Strength Steels Application Guidelines Version 6.0*. 2017.
- [16] J. G. Speer *et al.*, "Quenching and Partitioning: A Fundamentally New Process to Create High Strength Trip Sheet Microstructures," in *Symposium, Austenite formation and decomposition*, Warrendale, Pa., 2003: TMS;, pp. 505-522. [Online]. Available: <https://www.tib.eu/de/suchen/id/BLCP%3ACN050898361>
- [17] M. Wakita, Y. Adachi, and Y. Tomota, "Crystallography and Mechanical Properties of Ultrafine TRIP-Aided Multi-Phase Steels," *Materials Science Forum*, vol. 539-543, pp. 4351-4356, 2007, doi: 10.4028/[www.scientific.net/MSF.539-543.4351](http://www.scientific.net/MSF.539-543.4351).
- [18] K. Abbaszadeh, H. Saghafian, and S. Kheirandish, "Effect of Bainite Morphology on Mechanical Properties of the Mixed Bainite- martensite Microstructure in D6AC Steel," *Journal of Materials Science & Technology*, vol. 28, no. 4, pp. 336-342, 2012, doi: 10.1016/S1005-0302(12)60065-6.
- [19] C. H. Young and H. K. D. H. Bhadeshia, "Strength of mixtures of bainite and martensite," *Materials Science and Technology*, vol. 10, no. 3, pp. 209-214, 1994/03/01 1994, doi: 10.1179/mst.1994.10.3.209.

- [20] Y. Tomita and K. Okabayashi, "Improvement in lower temperature mechanical properties of 0.40 pct C-Ni-Cr-Mo ultrahigh strength steel with the second phase lower bainite," *Metallurgical Transactions A*, vol. 14, no. 2, pp. 485-492, 1983/02/01 1983, doi: 10.1007/BF02644225.
- [21] M. Militzer and W. J. Poole, "A critical comparison of microstructure evolution in hot rolled and cold rolled dual phase steels," presented at the World Congress on Integrated Computational materials engineering, 2004.
- [22] K. Sato, H. Sueyoshi, and K. Yamada, "Characterization of complex phase steel using backscattered electron images with controlled collection angles," *Microscopy*, vol. 64, no. 5, pp. 297-304, 2015, doi: 10.1093/jmicro/dfv022.
- [23] R. Kuziak, R. Kawalla, and S. Waengler, "Advanced high strength steels for automotive industry," *Archives of Civil and Mechanical Engineering*, vol. 8, no. 2, pp. 103-117, 2008, doi: 10.1016/S1644-9665(12)60197-6.
- [24] J. Zhao and Z. Jiang, "Thermomechanical processing of advanced high strength steels," *Progress in Materials Science*, vol. 94, pp. 174-242, 2018, doi: 10.1016/j.pmatsci.2018.01.006.
- [25] C. Mesplont, "Phase transformations and microstructure- mechanical properties relations in Complex Phase high strength steels " PhD, Department of Metallurgy and Materials, University of Lille, 2002.
- [26] *ASTM A1079-17 Standard Specification for Steel Sheet, Complex Phase (CP), Dual Phase (DP) and Transformation Induced Plasticity (TRIP), Zinc-Coated (Galvanized) or Zinc-Iron Alloy-Coated (Galvannealed) by the Hot-Dip Process*, A. International, West Conshohocken, PA, 2017.
- [27] T. Nanda, V. Singh, V. Singh, A. Chakraborty, and S. Sharma, "Third generation of advanced high- strength steels: Processing routes and properties," vol. 233, ed. London, England, 2019, pp. 209-238.
- [28] K. Sugimoto and M. Mukherjee, "Trip aided and complex phase steels," *Automotive steels*, pp. 217-257, 2017, doi: <https://doi.org/10.1016/B978-0-08-100638-2.00008-0>.

- [29] T. Allam, "Direct Hot Rolled Dual Phase Weathering Steel," Doctor of engineering sciences, Faculty of Geo Resources and Materials Engineering, University of Aachen, 2015.
- [30] A. J. Deardo, "Niobium in modern steels," *International Materials Reviews*, vol. 48, no. 6, pp. 371-402, 2003, doi: 10.1179/095066003225008833.
- [31] E. J. Palmiere, C. I. Garcia, and A. J. DeArdo, "The influence of Niobium Supersaturation in Austenite on the Static Recrystallization behavior of Low Carbon Microalloyed steels," *Metallurgical and Materials Transactions A*, vol. Volume 27A, no. April 1996, pp. 951-960, 1996.
- [32] D. Li *et al.*, "Influences of Nb-microalloying on microstructure and mechanical properties of Fe–25Mn–3Si–3Al TWIP steel," *Materials & Design*, vol. 84, pp. 238-244, 2015/11/05/2015, doi: <https://doi.org/10.1016/j.matdes.2015.06.092>.
- [33] E. J. Palmiere, "Suppression of Recrystallization during the Hot Deformation of Microalloyed Austenite," PhD, University of Pittsburgh, 1992.
- [34] Smith, Brett, Adela, Spulber, M. Shashank, and F. Terni. (2017) Technology Roadmaps: Intelligent Mobility Technology, Materials and Manufacturing Processes, and Light Duty Vehicle Propulsion. *Center for Automotive Research*.
- [35] B. Buchmayr, M. Degner, and H. Palkowski, "Future Challenges in the Steel Industry and Consequences for Rolling Plant Technologies," *BHM Berg- und Huttenmannische Monatshefte*, vol. 163, no. 3, pp. 76-83, 2018, doi: 10.1007/s00501-018-0708-x.
- [36] C. Ouchi, "Development of steel plates by intensive use of TMCP and direct quenching processes," *ISIJ Int.*, vol. 41, no. 6, pp. 542-553, 2001, doi: 10.2355/isijinternational.41.542.
- [37] E. I. Poliak, N. S. Pottore, R. M. Skolly, W. P. Umlauf, and J. C. Brannbacka, "Thermomechanical processing of advanced high strength steels in production hot strip rolling " *La metallurgia italiana*, vol. February, 2009.
- [38] K. Nishioka and K. Ichikawa, "Progress in thermomechanical control of steel plates and their commercialization," vol. 13, ed, 2012, p. 023001.
- [39] J. H. Chung, J. K. Park, T. H. Kim, K. H. Kim, and S. Y. Ok, "Study of deformation-induced phase transformation in plain low carbon steel at low strain rate," *Materials*

- Science & Engineering A*, vol. 527, no. 20, pp. 5072-5077, 2010, doi: 10.1016/j.msea.2010.04.095.
- [40] D. Kopeliovich, "Steel strip processing." [http://www.substech.com/dokuwiki/doku.php?id=steel\\_strip\\_processing](http://www.substech.com/dokuwiki/doku.php?id=steel_strip_processing) (accessed 2017).
- [41] P. Gong, E. J. Palmiere, and W. M. Rainforth, "Thermomechanical processing route to achieve ultrafine grains in low carbon microalloyed steels," *Acta Materialia*, vol. 119, pp. 43-54, 2016, doi: 10.1016/j.actamat.2016.08.010.
- [42] L. Schemmann, S. Zaeferrer, D. Raabe, F. Friedel, and D. Mattissen, "Alloying effects on microstructure formation of dual phase steels," *Acta Materialia*, vol. 95, pp. 386-398, 2015, doi: 10.1016/j.actamat.2015.05.005.
- [43] X. Zuo and Z. Zhang, "Effect of Initial Microstructures on the Properties of Ferrite-martensite Dual- phase Pipeline Steels with Strain- based Design," *Materials Research*, vol. 15, no. 2, pp. 317-322, 2012, doi: 10.1590/S1516-14392012005000021.
- [44] E. O. Hall, "The Deformation and Ageing of Mild Steel: II Characteristics of the L ders Deformation," *Proceedings of the Physical Society. Section B*, vol. 64, no. 9, pp. 742-747, 1951/09/01 1951, doi: 10.1088/0370-1301/64/9/302.
- [45] N. J. Petch, "The Cleavage Strength of Polycrystals," *Journal of the Iron and Steel Institute*, vol. 174, pp. 25-28, 1953.
- [46] T. Ishikawa, "Understanding and controlling microstructural evolution in metal forming: an overview," in *Microstructure Evolution in Metal Forming Processes*, J. Lin, D. Balint, and M. Pietrzyk Eds.: Woodhead Publishing, 2012, pp. 3-16.
- [47] "Grain size and material strength," vol. March 2010, ed. Brush Wellman Inc., 2010.
- [48] D. Xu, C. Ji, H. Zhao, D. Ju, and M. Zhu, "A new study on the growth behavior of austenite grains during heating processes," *Scientific Reports*, vol. 7, no. 1, p. 3968, 2017/06/21 2017, doi: 10.1038/s41598-017-04371-8.
- [49] J. Reiter, C. Bernhard, and H. Presslinger, "Austenite grain size in the continuous casting process: Metallographic methods and evaluation," *Materials Characterization*, vol. 59, no. 6, pp. 737-746, 2008/06/01/ 2008, doi: <https://doi.org/10.1016/j.matchar.2007.06.003>.

- [50] S. Illescas, J. Fernández, and J. M. Guilemany, "Estudio del crecimiento de grano de la fase austenítica en un acero HSLA de bajo contenido en carbono," *Revista de Metalurgia*, vol. 44, no. 1, pp. 39-51, 2008-02-28 2008, doi: 10.3989/revmetalm.2008.v44.i1.94.
- [51] A. Kundu, C. L. Davis, and M. Strangwood, "Grain Structure Development during Reheating and Deformation of Niobium-Microalloyed Steels," *Materials and Manufacturing Processes*, vol. 25, no. 1-3, pp. 125-132, 2010/03/22 2010, doi: 10.1080/10426910903153216.
- [52] H. T. Zhang, G. Pang, R. Z. Wang, and C. Liu, "Austenite Grain Size of Thin Slab and Its Influence on Direct Hot Strip Rolling of Nb Microalloyed Steel," *Materials Science Forum*, vol. 500-501, pp. 295-302, 2005, doi: 10.4028/[www.scientific.net/MSF.500-501.295](http://www.scientific.net/MSF.500-501.295).
- [53] Y. Houbaert, R. Colás, F. Castro C, A. Artigas A, and A. Monsalve G, "Caracterización de aceros dual- phase obtenidos por laminación en caliente," *Revista de Metalurgia*, vol. 47, no. 1, pp. 5-14, 2011, doi: 10.3989/revmetalmadrid.0914.
- [54] A. J. DeArdo, C. I. Garcia, and E. J. Palmiere, "Thermomechanical Processing of Steel," vol. 4, 10th ed. Metals Handbook ASM International, 1991, pp. 237-255.
- [55] G. R. Speich, L. J. Cuddy, C. R. Gordon, and A. J. DeArdo, "Formation of Ferrite from Control-Rolled Austenite," in *International Conference on Phase Transformations in Ferrous Alloys*, 1984: The Metallurgical Society of AIME, pp. 341-389.
- [56] Z. Q. Sun, W. Y. Yang, J. J. Qi, and A. M. Hu, "Deformation enhanced transformation and dynamic recrystallization of ferrite in a low carbon steel during multipass hot deformation," *Materials Science & Engineering A*, vol. 334, no. 1, pp. 201-206, 2002, doi: 10.1016/S0921-5093(01)01806-8.
- [57] Neerajagarwal, G. P. Chaudhari, and S. K. Nath, "Fine Grained Dual Phase Steel by Thermomechanical Processing " *International Journal of Applied Research in Mechanical Engineering*, vol. Volume-3, no. Issue-1, pp. 22-25, 2013.
- [58] C. Homsher, "Determination of the non-recrystallization temperature (TNR) in multiple microalloyed steels," C. Tyne, E. De Moor, and J. Speer, Eds., ed: ProQuest Dissertations Publishing, 2013.

- [59] N. Hansen, R. F. Mehl, and A. Medalist, "New discoveries in deformed metals," *Metallurgical and Materials Transactions A*, vol. 32, no. 12, pp. 2917-2935, 2001/12/01 2001, doi: 10.1007/s11661-001-0167-x.
- [60] J. Humphreys, G. S. Rohrer, and A. Rollett, *Recrystallization and related annealing phenomena*, Third Edition ed. Elsevier, 2017.
- [61] J. J. Jonas, "Effect of Quench and Interpass Time on Dynamic and Static Softening during Hot Rolling," *steel research international*, vol. 76, no. 5, pp. 392-398, 2005/05/01 2005, doi: 10.1002/srin.200506027.
- [62] A. Bakkaloğlu, "Effect of processing parameters on the microstructure and properties of an Nb microalloyed steel," *Materials Letters*, vol. 56, no. 3, pp. 263-272, 2002, doi: 10.1016/S0167-577X(02)00453-6.
- [63] Tamura, Sekine, Tanaka, and Ouchi, *Thermomechanical processing of high-strength low-alloy steels*. Butterworth & Co., 1988.
- [64] D. Bombac, M. J. Peet, S. Zenitani, S. Kimura, T. Kurimura, and H. K. D. H. Bhadeshia, "An integrated hot rolling and microstructure model for dual- phase steels," *An integrated hot rolling and microstructure model for dual-phase steels*, vol. 22, no. 4, p. 045005, 2014, doi: 10.1088/0965-0393/22/4/045005.
- [65] C. Sellars, "Modelling Microstructural Development During Hot Rolling," *Materials Science and Technology*, vol. 6, no. 11, pp. 1072-1081, 1990, doi: 10.1179/mst.1990.6.11.1072.
- [66] J. J. Jonas, C. M. Sellars, and W. J. M. Tegart, "Strength and structure under hot-working conditions," *Metallurgical Reviews*, vol. 14, no. 1, pp. 1-24, 1969, doi: 10.1179/mtlr.1969.14.1.1.
- [67] M. Cabibbo, A. Fabrizi, M. Merlin, and G. Garagnani, "Effect of thermo- mechanical treatments on the microstructure of micro- alloyed low- carbon steels," *Full Set - Includes 'Journal of Materials Science Letters'*, vol. 43, no. 21, pp. 6857-6865, 2008, doi: 10.1007/s10853-008-3000-8.
- [68] D. Staddon and K. Lings, "The development of dual phase steels for the manufacture of high strength fasteners without heat treatment," *Wire Journal International*, no. October, pp. 78-81, 2006.

- [69] Y. Zhao, "The cooling of a hot steel plate by an impinging water jet," PhD, School of Mechanical, Materials and Mechatronics, University of Wollongong, 2005. [Online]. Available: <http://ro.uow.edu.au/theses/450>
- [70] A. Saai, O. S. Hopperstad, Y. Granbom, and O. G. Lademo, "Influence of Volume Fraction and Distribution of Martensite Phase on the Strain Localization in Dual Phase Steels," *Procedia Materials Science*, vol. 3, pp. 900-905, 2014, doi: 10.1016/j.mspro.2014.06.146.
- [71] X. Zhang *et al.*, "Mechanical Behavior of Carbide-free Medium Carbon Bainitic Steels," *Metallurgical and Materials Transactions A*, vol. 45, 03/01 2014, doi: 10.1007/s11661-013-2079-y.
- [72] R. G. Davies, "Influence of Martensite Composition and Content on the Properties of Dual Phase Steels," *Metallurgical Transactions A*, vol. 9A, no. May 1978, pp. 671-679, 1978.
- [73] R. D. Doherty *et al.*, "Current issues in recrystallization: a review," *Materials Science and Engineering: A*, vol. 238, no. 2, pp. 219-274, 1997/11/15/ 1997, doi: [https://doi.org/10.1016/S0921-5093\(97\)00424-3](https://doi.org/10.1016/S0921-5093(97)00424-3).
- [74] C. M. Sellars, "Recrystallization of Metals during Hot Deformation," *Philosophical Transactions of the Royal Society of London. Series A, Mathematical and Physical Sciences (1934-1990)*, vol. 288, no. 1350, pp. 147-158, 1978, doi: 10.1098/rsta.1978.0010.
- [75] C. M. Sellars and J. A. Whiteman, "Recrystallization and grain growth in hot rolling," *Metal Science*, vol. 13, no. 3-4, pp. 187-194, 1979, doi: 10.1179/msc.1979.13.3-4.187.
- [76] R. A. Petković, M. J. Luton, and J. J. Jonas, "Recovery and recrystallization of carbon steel between intervals of hot working," *Canadian Metallurgical Quarterly*, vol. 14, no. 2, pp. 137-145, 1975, doi: 10.1179/000844375795050201.
- [77] R. A. Djaic and J. J. Jonas, "Static recrystallization of austenite between intervals of hot working," *Iron and Steel Institute*, vol. 210, no. 4, pp. 256-261, 1972.
- [78] R. Paulo Rangel, S. Fulvio, Jr., S. Hugo Ricardo Zschommler, P. Ronald Lesley, and P. Angelo Fernando, "Nucleation and growth during recrystallization," *Materials Research*, vol. 8, no. 3, pp. 225-238, 2005, doi: 10.1590/S1516-14392005000300002.
- [79] D. Hull and D. J. Bacon, *Introduction to Dislocations*, Fifth ed. (Introduction to Dislocations (Fifth Edition)). Oxford: Butterworth-Heinemann, 2011, p. 257.

- [80] R. Barbosa and H. Braga, "Analysis of the Occurrence of Dynamic Recrystallization in Hot Rolling by Modeling of the Stress-Strain Curve," *ISIJ International*, vol. 32, no. 2, pp. 257-259, 1992, doi: 10.2355/isijinternational.32.257.
- [81] M. Militzer, "Computer Simulation of Microstructure Evolution in Low Carbon Sheet Steels," *ISIJ International*, vol. 47, pp. 1-15, 01/01 2007, doi: 10.2355/isijinternational.47.1.
- [82] S. B. Davenport, N. J. Silk, C. N. Sparks, and C. M. Sellars, "Development of constitutive equations for modelling of hot rolling," *Materials Science and Technology*, vol. 16, no. 5, pp. 539-546, 2000/05/01 2000, doi: 10.1179/026708300101508045.
- [83] C. M. Sellars, "Dynamic Recrystallisation," (in English), *Metalurgia I Odlewnictwo*, vol. 5, no. 3, 1979.
- [84] J. Jonas, "Dynamic recrystallization—scientific curiosity or industrial tool?," *Materials Science and Engineering: A*, vol. 184, no. 2, pp. 155-165, 1994.
- [85] P. L. O. Rossi and C. M. Sellars, "Quantitative metallography of recrystallization," *Acta Materialia*, vol. 45, no. 1, pp. 137-148, 1997/01/01/ 1997, doi: [https://doi.org/10.1016/S1359-6454\(96\)00167-X](https://doi.org/10.1016/S1359-6454(96)00167-X).
- [86] Q. Zhu, C. M. Sellars, and H. K. D. H. Bhadeshia, "Quantitative metallography of deformed grains," *Materials Science and Technology*, vol. 23, no. 7, pp. 757-766, 2007/07/01 2007, doi: 10.1179/174328407X157308.
- [87] J. Burke and D. Turnbull, "Recrystallization and grain growth," *Progress in Metal Physics*, vol. 3, p. 220, January 01, 1952 1952, doi: 10.1016/0502-8205(52)90009-9.
- [88] G. Glover and C. M. Sellars, "Static recrystallization after hot deformation of  $\alpha$  iron," *Metallurgical Transactions*, vol. 3, no. 8, pp. 2271-2280, 1972/08/01 1972, doi: 10.1007/BF02643242.
- [89] R. Honeycombe, *The plastic deformation of metals*. Frome: Butler & Tanner, 1985.
- [90] C. M. Sellars, "From trial and error to computer modelling of thermomechanical processing," *Ironmaking & Steelmaking*, vol. 38, no. 4, pp. 250-257, 2011, doi: 10.1179/030192310X12706305605817.
- [91] A. J. DeArdo, "Fundamental aspects of the physical metallurgy of thermomechanical processing of steel," in *International Conference on Physical Metallurgy of*



- Thermomechanical Processing of Steels and Other Metals. THERMEC-88.*, 1988, vol. 1, pp. 20-29.
- [92] "Recovery, Recrystallization, and Grain-Growth Structures," in *Metalworking: Bulk Forming*, vol. 14A, S. L. Semiatin Ed.: ASM International, 2005, pp. 552-562.
- [93] W. P. Sun, M. Militzer, E. B. Hawbolt, and T. R. Meadowcroft, "Austenite grain refinement and growth during the thermomechanical processing of steels," in *Hot Workability of Steels and Light Alloys-Composites*, Canada, 1996, pp. 285-292.
- [94] H. Fredriksson, "Mechanism of grain growth in metals," *Materials Science and Technology*, vol. 6, no. 9, pp. 811-818, 1990/09/01 1990, doi: 10.1179/mst.1990.6.9.811.
- [95] L. Zhang and D. C. Guo, "A general etchant for revealing prior- austenite grain boundaries in steels," *Materials Characterization*, vol. 30, no. 4, pp. 299-302, 1993, doi: 10.1016/1044-5803(93)90078-A.
- [96] C. García de Andrés, M. J. Bartolomé, C. Capdevila, D. San Martín, F. G. Caballero, and V. López, "Metallographic techniques for the determination of the austenite grain size in medium- carbon microalloyed steels," *Materials Characterization*, vol. 46, no. 5, pp. 389-398, 2001, doi: 10.1016/S1044-5803(01)00142-5.
- [97] G. F. Vander Voort, "Revealing Prior-Austenite Grain Boundaries in Heat Treated Steels (Article)," 2018.
- [98] A. W. Brewer, K. A. Erven, and G. Krauss, "Etching and image analysis of prior austenite grain boundaries in hardened steels," *Materials Characterization*, vol. 27, no. 1, pp. 53-56, 1991/07/01/ 1991, doi: [https://doi.org/10.1016/1044-5803\(91\)90079-J](https://doi.org/10.1016/1044-5803(91)90079-J).
- [99] *ASTM E112 Standard Test Methods for Determining Average Grain Size*, A. International, 2013.
- [100] B. Bruce and B. Arlan, "Metallographer's guide; practices and procedures for irons and steels," vol. 26, ed. Portland: Ringgold Inc, 2002, p. n/a.
- [101] V. M. Dusevich, J. H. Purk, and J. D. Eick, "Choosing the Right Accelerating Voltage for SEM (An Introduction for Beginners)," *Microscopy Today*, vol. 18, no. 1, pp. 48-52, 2010, doi: 10.1017/S1551929510991190.
- [102] D. S. Rao, K. Muraleedharan, and C. Humphreys, "TEM specimen preparation techniques," *Microscopy: Science, Technology, Applications and Education*, 2010.

- [103] "Optical Emission Spectroscopy (OES) Analysis." @ElementTesting. <https://www.element.com/materials-testing-services/chemical-analysis-labs/oes-analysis> (accessed 2019).
- [104] "Gas Chromatography Mass Spectrometry - GC/MS Analysis Laboratories." @ElementTesting. <https://www.element.com/materials-testing-services/chemical-analysis-labs/gcms-analysis-laboratories> (accessed 2019).
- [105] N. Saunders, U. Guo, X. Li, A. Miodownik, and J. Schillé, "Using JMatPro to model materials properties and behavior," *The Journal of The Minerals, Metals & Materials Society (TMS)*, vol. 55, no. 12, pp. 60-65, 2003, doi: 10.1007/s11837-003-0013-2.
- [106] "JMatPro software v9.0 for materials properties." Sente Software. <https://www.sentesoftware.co.uk/> (accessed 2018).
- [107] Z. Guo, N. Saunders, J. P. Schillé, and A. P. Miodownik, "Material properties for process simulation," *Materials Science & Engineering A*, vol. 499, no. 1, pp. 7-13, 2009, doi: 10.1016/j.msea.2007.09.097.
- [108] J.-P. Schillé, Z. Guo, N. Saunders, and A. P. Miodownik, "Modeling Phase Transformations and Material Properties Critical to Processing Simulation of Steels," *Materials and Manufacturing Processes*, vol. 26, no. 1, pp. 137-143, 2011, doi: 10.1080/10426910903153059.
- [109] J. O. Andersson, T. Helander, L. Höglund, P. Shi, and B. Sundman, "Thermo- Calc & DICTRA, computational tools for materials science," *Calphad*, vol. 26, no. 2, pp. 273-312, 2002, doi: 10.1016/S0364-5916(02)00037-8.
- [110] "Thermo-Calc User Guide 2017a," ed, (accessed 21 March 2017).
- [111] "TCFE8 Steels/Fe-alloys database version 8.1," ed: Thermo-Calc Software.
- [112] *ASTM A1033-18, Standard Practice for Quantitative Measurement and Reporting of Hypoeutectoid Carbon and Low-Alloy Steel Phase Transformations*, A. International, West Conshohocken, PA, 2018.
- [113] C. García De Andrés, F. G. Caballero, C. Capdevila, and L. F. Álvarez, "Application of dilatometric analysis to the study of solid- solid phase transformations in steels," *Materials Characterization*, vol. 48, no. 1, pp. 101-111, 2002, doi: 10.1016/S1044-5803(02)00259-0.

- [114] S. Ghosh and S. Mula, "Thermomechanical processing of low carbon Nb–Ti stabilized microalloyed steel: Microstructure and mechanical properties," *Materials Science and Engineering: A*, vol. 646, pp. 218-233, 2015, doi: <https://doi.org/10.1016/j.msea.2015.08.072>.
- [115] P. Choquet, "Mathematical Model for Predictions of Austenite and Ferrite Microstructures in Hot Rolling Processes," St. Germain-en-Laye, 1985.
- [116] B. Mintz, J. R. Banerjee, and K. M. Banks, "Regression equation for Ar<sub>3</sub> temperature for coarse grained as cast steels," *Ironmaking & Steelmaking*, vol. 38, no. 3, pp. 197-203, 2011, doi: 10.1179/030192310X12827375731429.
- [117] C. Shiga, T. Hatomura, J.-i. Kudoh, A. Kamada, K. Hirose, and T. Sekine, "Development of Large Diameter High Strength Line Pipes for low Temperature services," 1981, vol. 4.
- [118] X. Yuan, Z. Liu, S. Jiao, L. Ma, and G. Wang, "The onset temperatures of gamma to alpha phase transformation in hot deformed and non-deformed Nb micro- alloyed steels," *ISIJ International*, vol. 46, no. 4, pp. 579-585, 2006.
- [119] C. Ouchi, T. Sampei, and I. Kozasu, "Effect of Hot Rolling conditions and chemical compositions on the onset temperature of gamma-alpha transformation after hot rolling," *Tetsu-To-Hagane/Journal of the Iron and Steel Institute of Japan*, vol. 67, no. 1, pp. 143-152, 1981, doi: 10.2355/tetsutohagane1955.67.1\_143.
- [120] B. Dutta and E. Palmiere, "Effect of prestrain and deformation temperature on the recrystallization behavior of steels microalloyed with niobium," *Metallurgical and Materials Transactions A*, vol. 34, no. 6, pp. 1237-1247, 2003, doi: 10.1007/s11661-003-0234-6.
- [121] J. S. Hinton, "Laboratory Simulation of Microstructural Evolution in AISI 430 Ferritic Stainless Steel during the Steckel Mill Process," Doctor of Philosophy, Department of Engineering Materials, The University of Sheffield, 2006.
- [122] Z. Cui, "Thermomechanical Processing of Structural Steels with Dilute Niobium Additions," Doctor of Philosophy, Department of Materials Science and Engineering, The University of Sheffield, 2016.
- [123] "Advanced metals processing - Research Centres - Materials Science and Engineering." University of Sheffield.

- <https://www.sheffield.ac.uk/materials/centresandfacilities/metalsprocessing> (accessed 2019).
- [124] H. Zhao, "Effect of Austenite Deformation and Continuous Cooling on the Microstructural Evolution in a Microalloyed Steel," PhD, Materials Science and Engineering, University of Sheffield, 2016.
- [125] M. S. Loveday *et al.*, "Measurement of flow stress in hot plane strain compression tests," *Materials at High Temperatures*, vol. 23, no. 2, pp. 85-118, 2006/01/01 2006, doi: 10.1179/mht.2006.006.
- [126] R. Colas-Ortiz, "High Strain Rate, High Temperature Deformation of Stainless Steel " Doctor of Philosophy, Department of Metallurgy, The University of Sheffield, 1983.
- [127] M. Loveday, G. Mahon, B. Roebuck, C. Sellars, and M. van der Winden, "Measuring flow stress in hot plane strain compression tests," 2002.
- [128] L. Sun, "The effects of strain path reversal on austenite grain subdivision, recrystallisation and phase transformations in microalloyed steel," Doctor of Philosophy, Department of Materials Science and Engineering, University of Sheffield, 2012.
- [129] C. N. Homsher and C. J. Van Tyne, "Comparison of Two Physical Simulation Tests to Determine the No- Recrystallization Temperature in Hot Rolled Steel Plates," *Materials Performance and Characterization*, vol. 4, no. 3, pp. 293-306, 2015, doi: 10.1520/MPC20150002.
- [130] F. Boratto, R. Barbosa, S. Yue, and J. J. Jonas, "Effect of Chemical Composition on Critical Temperatures of Microalloyed Steels.," in *International Conference on Physical Metallurgy of Thermomechanical Processing of Steels and Other Metals THERMEC '88*, Tokyo, 1988, vol. 1, pp. 383-390.
- [131] D. Bai, R. Bodnar, J. Ward, J. Dorricott, and S. Sanders, "Development of discrete X80 line pipe plate at SSAB Americas," in *International Symposium on the Recent Developments in Plate Steels*, 2011, pp. 13-22.
- [132] F. Fletcher, *Meta-analysis of T<sub>nr</sub> measurements: determining new empirical models based on composition and strain*. 2008, pp. 1-14.
- [133] M. Militzer, "Modelling of microstructure evolution and properties of low-carbon steels," *Acta Metallurgica Sinica*, vol. 13, no. April, 2, pp. 574-580, 2000.

- [134] *Standard Test Method for Determining Volume Fraction by Systematic Manual Point Count*, 2011.
- [135] S. Zaefferer, N. N. Elhami, and P. Konijnenberg, "18 - Electron backscatter diffraction (EBSD) techniques for studying phase transformations in steels," in *Phase Transformations in Steels*, vol. 2, E. Pereloma and D. V. Edmonds Eds.: Woodhead Publishing, 2012, pp. 557-587.
- [136] *ISO 6507-1 Metallic materials–Vickers hardness test*, 2018.
- [137] A. C. Fischer-Cripps, *Nanoindentation*, 3rd ed. ed. New York ; London: New York ; London : Springer, 2011, 2011.
- [138] G. Z. Voyiadjis and M. Yaghoobi, "Review of Nanoindentation Size Effect: Experiments and Atomistic Simulation," *Crystals*, vol. 7, no. 10, p. 321, 2017.
- [139] *ASM Handbook, Volume 9: Metallography and Microstructures, Chemical and Electrolytic Polishing*. 2004, pp. 281-293.
- [140] *ASTM E8/E8M-16a Standard Test Methods for Tension Testing of Metallic Materials*, A. International, West Conshohocken, PA, 2016.
- [141] S. Zhao, D. Wei, R. Li, and L. Zhang, "Effect of Cooling Rate on Phase Transformation and Microstructure of Nb-Ti Microalloyed Steel," *Materials Transactions*, vol. 55, no. 8, p. 1274, 2014, doi: 10.2320/matertrans.M2013395.
- [142] G. R. Ebrahimi, A. Momeni, S. Kazemi, and H. Alinejad, "Flow curves, dynamic recrystallization and precipitation in a medium carbon low alloy steel," *Vacuum*, vol. 142, pp. 135-145, 2017, doi: 10.1016/j.vacuum.2017.05.010.
- [143] S. Funahashi, "The effects of friction and lubrication on multipass hot deformation," 2010.
- [144] A. A. Gorni, *Steel forming and heat treating handbook*. 2017.
- [145] J. Hidalgo and M. Santofimia, "Effect of Prior Austenite Grain Size Refinement by Thermal Cycling on the Microstructural Features of As- Quenched Lath Martensite," *Metallurgical and Materials Transactions A*, vol. 47, no. 11, pp. 5288-5301, 2016, doi: 10.1007/s11661-016-3525-4.
- [146] R. A. Grange, "The rapid heat treatment of steel," *Metallurgical Transactions*, vol. 2, no. 1, pp. 65-78, 1971/12/01 1971, doi: 10.1007/BF02662639.

- [147] Z. Ławrynowicz and A. Barbacki, "Features of bainite transformation in steels," *Advances in Materials Science*, vol. 2, 01/01 2002.
- [148] G. Spanos and W. T. Reynolds, "Microstructure of Metals and Alloys," in *Physical Metallurgy (Fifth Edition)*, D. E. Laughlin and K. Hono Eds. Oxford: Elsevier, 2014, pp. 1073-1112.
- [149] J.-Y. Kang, S.-J. Park, and M.-B. Moon, "Phase Analysis on Dual-Phase Steel Using Band Slope of Electron Backscatter Diffraction Pattern," *Microscopy and Microanalysis*, vol. 19, no. S5, pp. 13-16, 2013, doi: 10.1017/S1431927613012233.
- [150] J. Wu, P. J. Wray, C. I. Garcia, M. Hua, and A. J. Deardo, "Image Quality Analysis: A New Method of Characterizing Microstructures," *ISIJ International*, vol. 45, no. 2, pp. 254-262, 2005, doi: 10.2355/isijinternational.45.254.
- [151] A. J. DeArdo, C. I. Garcia, K. Cho, and M. Hua, "New Method of Characterizing and Quantifying Complex Microstructures in Steels," *Materials and Manufacturing Processes*, vol. 25, no. 1-3, pp. 33-40, 2010/03/22 2010, doi: 10.1080/10426910903143415.
- [152] H. Zhao, B. P. Wynne, and E. J. Palmiere, "A phase quantification method based on EBSD data for a continuously cooled microalloyed steel," *Materials Characterization*, vol. 123, pp. 339-348, 2017, doi: 10.1016/j.matchar.2016.11.024.
- [153] J.-Y. Kang *et al.*, "Phase Analysis of Steels by Grain-averaged EBSD Functions," *ISIJ International*, vol. 51, no. 1, pp. 130-136, 2011, doi: 10.2355/isijinternational.51.130.
- [154] *Channel 5 User Guide*. Oxford Instruments, 2014.
- [155] Y. S. Sun Chao, Liu Guoliang, "Evolution of Microstructures of a Low Carbon Bainitic Steel Held at High Service Temperature," *Acta Metallurgica Sinica (English Letters)*, vol. 27, no. 3, pp. 436-443, 2014-06-25 2014, doi: 10.1007/s40195-014-0078-7.
- [156] S. Kang, J. G. Speer, R. W. Regier, H. Nako, S. C. Kennett, and K. O. Findley, "The analysis of bainitic ferrite microstructure in microalloyed plate steels through quantitative characterization of intervariant boundaries," *Materials Science and Engineering: A*, vol. 669, pp. 459-468, 2016/07/04/ 2016, doi: <https://doi.org/10.1016/j.msea.2016.05.111>.
- [157] R. Fialho Tomaz, D. Brandão Santos, K. Camey, R. Barbosa, M. Spangler Andrade, and D. Pérez Escobar, "Complex phase quantification methodology using electron backscatter diffraction ( EBSD) on low manganese high temperature processed steel ( HTP)

- microalloyed steel," *Journal of Materials Research and Technology*, vol. 8, no. 2, pp. 2423-2431, 2019, doi: 10.1016/j.jmrt.2019.01.021.
- [158] X. Li, A. Ramazani, U. Prahl, and W. Bleck, "Quantification of complex- phase steel microstructure by using combined EBSD and EPMA measurements," *Materials Characterization*, vol. 142, pp. 179-186, 2018, doi: 10.1016/j.matchar.2018.05.038.
- [159] S. L. Shrestha, A. J. Breen, P. Trimby, G. Proust, S. P. Ringer, and J. M. Cairney, "An automated method of quantifying ferrite microstructures using electron backscatter diffraction ( EBSD) data," *Ultramicroscopy*, vol. 137, pp. 40-47, 2014, doi: 10.1016/j.ultramic.2013.11.003.
- [160] J. Jonas, "Microstructure and Texture in Steels and Other Materials," 2009: Springer-Verlag London, doi: 10.1007/978-1-84882-454-6.
- [161] L. Ryde, "Application of EBSD to analysis of microstructures in commercial steels," *Materials Science and Technology: Applications of orientation imaging microscopy*, vol. 22, no. 11, pp. 1297-1306, 2006, doi: 10.1179/174328406X130948.
- [162] G. Béres and Z. Weltsch, "Estimation of Strength Properties from Microhardness Results in Dual Phase Steels with Different Martensite Volume Fraction," *Periodica Polytechnica. Transportation Engineering*, vol. 47, no. 3, pp. 206-212, 2019, doi: 10.3311/PPtr.12113.
- [163] BBS. "Hardness conversion table." <https://www.bbshalmstad.se/en/infocenter/hardness-conversion-table> (accessed July 2020).
- [164] Tribonet. "Calculation Hardness vickers indenter." <http://www.tribonet.org/hardness-calculation-vickers-indenter> (accessed July 2020).
- [165] G. Y. P. Medina, E. H. Delgado, A. F. M. Pérez, and H. L. Ferreira, "Phases quantification in DP600 steel welded by GTAW process using SEM and atomic force microscopy," *Materials Research*, vol. 20, pp. 1161-1165, 2017.
- [166] M. J. Peet and H. Bhadeshia, "Surface Relief Due to Bainite Transformation at 473 K (200 °C)," *Metallurgical and Materials Transactions A*, vol. 42, no. 11, p. 3344, 2011/06/16 2011, doi: 10.1007/s11661-011-0755-3.
- [167] T. Ros-Yáñez, Y. Houbaert, and A. Mertens, "Characterization of TRIP-assisted multiphase steel surface topography by atomic force microscopy," *Materials*

- Characterization*, vol. 47, no. 2, pp. 93-104, 2001/08/01/ 2001, doi: [https://doi.org/10.1016/S1044-5803\(01\)00157-7](https://doi.org/10.1016/S1044-5803(01)00157-7).
- [168] W. Handoko, F. Pahlevani, and V. Sahajwalla, "Corrosion Behaviour of Dual-Phase High Carbon Steel—Microstructure Influence," *Journal of Manufacturing and Materials Processing*, vol. 1, no. 2, p. 21, 2017.
- [169] H. Zhao, B. P. Wynne, and E. J. Palmiere, "Conditions for the occurrence of acicular ferrite transformation in HSLA steels," *Journal of Materials Science*, vol. 53, no. 5, pp. 3785-3804, 2018/03/01 2018, doi: 10.1007/s10853-017-1781-3.
- [170] X. Chen, F. Wang, C. Li, and S. Liu, "Effect of Niobium on Microstructure and Mechanical Properties of Nb–Ti Microalloyed Carbide-Free Bainitic Steels," in *TMS 2019 148th Annual Meeting & Exhibition Supplemental Proceedings*, Cham, 2019// 2019: Springer International Publishing, pp. 549-560.
- [171] B. Dutta and C. M. Sellars, "Effect of composition and process variables on Nb(C, N) precipitation in niobium microalloyed austenite," *Materials Science and Technology*, vol. 3, no. 3, pp. 197-206, 1987/03/01 1987, doi: 10.1179/mst.1987.3.3.197.
- [172] B. Dutta, E. J. Palmiere, and C. M. Sellars, "Modelling the kinetics of strain induced precipitation in Nb microalloyed steels," *Acta materialia*, vol. 49, no. 5, pp. 785-794, 2001, doi: 10.1016/s1359-6454(00)00389-x.
- [173] P. Gong, E. J. Palmiere, and W. M. Rainforth, "Characterisation of strain-induced precipitation behaviour in microalloyed steels during thermomechanical controlled processing," *Materials Characterization*, vol. 124, pp. 83-89, 2017/02/01/ 2017, doi: <https://doi.org/10.1016/j.matchar.2016.12.009>.
- [174] E. I. Poliak, "Determining the No-Recrystallization Conditions for Industrial Hot Strip Rolling of Steels Using Laboratory Simulations," *Materials Science Forum*, vol. 715-716, pp. 782-787, 2012, doi: 10.4028/[www.scientific.net/MSF.715-716.782](http://www.scientific.net/MSF.715-716.782).
- [175] A. El-Kawas, M. Abbas, R. Ramadan, and S. Ibrahim, "Effect of Nb Addition on the Hot Deformation Behavior and Microstructure of Low Carbon Steel," *Journal of Petroleum and Mining Engineering*, vol. 20, no. 1, pp. 66-72, 2018, doi: 10.21608/jpme.2018.38800.
- [176] N. Isasti, D. Jorge-Badiola, M. Taheri, and P. Uranga, "Phase Transformation Study in Nb-Mo Microalloyed Steels Using Dilatometry and EBSD Quantification," *Metallurgical and*



- Materials Transactions A*, vol. 44, no. 8, pp. 3552-3563, 2013, doi: 10.1007/s11661-013-1738-3.
- [177] P. Cizek, B. P. Wynne, C. H. J. Davies, B. C. Muddle, and P. D. Hodgson, "Effect of composition and austenite deformation on the transformation characteristics of low-carbon and ultralow-carbon microalloyed steels," *Metallurgical and Materials Transactions A*, vol. 33, no. 5, pp. 1331-1349, 2002/05/01 2002, doi: 10.1007/s11661-002-0059-8.
- [178] A. Grajcar, W. Zalecki, P. Skrzypczyk, A. Kilarski, A. Kowalski, and S. Kołodziej, "Dilatometric study of phase transformations in advanced high-strength bainitic steel," *Journal of Thermal Analysis and Calorimetry*, vol. 118, no. 2, pp. 739-748, 2014/11/01 2014, doi: 10.1007/s10973-014-4054-2.
- [179] S. K. Rajput *et al.*, "Physical simulation of hot deformation and microstructural evolution of AISI 1016 steel using processing maps," *Materials Science and Engineering: A*, vol. 587, pp. 291-300, 2013/12/10/ 2013, doi: <https://doi.org/10.1016/j.msea.2013.08.057>.
- [180] Y. Zhou, X. M. Wang, and X. L. He, "Microstructure and Mechanical Properties of Microalloyed Multiphase Steel," *Materials Science Forum*, vol. 788, pp. 406-413, 2014, doi: 10.4028/[www.scientific.net/MSF.788.406](http://www.scientific.net/MSF.788.406).
- [181] A. Karelova, F. Hairer, C. Kremaszky, E. Werner, T. Hebesberger, and A. Pichler, "Influence of the overaging temperature on microstructure and mechanical properties of complex-phase bainitic steel," 2009.
- [182] Z. Hou, D. Wu, S. Zheng, X. Yang, Z. Li, and Y. Xu, "Effect of Holding Temperature on Microstructure and Mechanical Properties of High-Strength Multiphase Steel," *steel research international*, vol. 87, pp. n/a-n/a, 12/01 2015, doi: 10.1002/srin.201500331.
- [183] D. Belato, W. De Waele, D. Vanderschueren, and S. Hertelé, *Latest developments in mechanical properties and metallurgical features of high strength line pipe steels*. 2013.
- [184] L. Bäcke, "Modeling the Microstructural Evolution during Hot Deformation of Microalloyed Steels," Doctoral thesis, comprehensive summary, KTH, Stockholm, 2009. [Online]. Available: <http://urn.kb.se/resolve?urn=urn:nbn:se:kth:diva-10390>
- [185] R. A. Almatani and A. J. DeArdo, "Rational Alloy Design of Niobium-Bearing HSLA Steels," *Metals*, vol. 10, no. 3, p. 413, 2020.

- [186] T. Sakai, A. Belyakov, R. Kaibyshev, H. Miura, and J. J. Jonas, "Dynamic and post-dynamic recrystallization under hot, cold and severe plastic deformation conditions," *Progress in Materials Science*, vol. 60, pp. 130-207, 2014/03/01/ 2014, doi: <https://doi.org/10.1016/j.pmatsci.2013.09.002>.
- [187] R. Abad, B. López , and J. M. Rodriguez-Ibabe, "The effect of prior austenite microstructure and deformation variables on the recrystallization behaviour of some HSLA steels," in *Journal of Materials Processing Technology*, 2001, vol. 117, no. 3, p. CD ROM section C4.
- [188] B. López and J. M. Rodriguez-Ibabe, "Recrystallisation and grain growth in hot working of steels," in *Microstructure Evolution in Metal Forming Processes*, J. Lin, D. Balint, and M. Pietrzyk Eds.: Woodhead Publishing, 2012, pp. 67-113.
- [189] J. J. Jonas, "Effect of Interpass Time on the Hot Rolling Behaviour of Microalloyed Steels," *Materials Science Forum*, vol. 284-286, pp. 3-14, 1998, doi: 10.4028/[www.scientific.net/MSF.284-286.3](http://www.scientific.net/MSF.284-286.3).
- [190] B. Pereda, B. López, and J. Rodriguez-Ibabe, *Increasing the non-recrystallization temperature of Nb microalloyed steels by Mo addition*. 2007, pp. 151-159.
- [191] M. Opiela and A. Grajcar, "Hot deformation behavior and softening kinetics of Ti–V–B microalloyed steels," *Archives of Civil and Mechanical Engineering*, vol. 12, no. 3, pp. 327-333, 2012/09/01/ 2012, doi: <https://doi.org/10.1016/j.acme.2012.06.003>.
- [192] D. Q. Bai, S. Yue, W. P. Sun, and J. J. Jonas, "Effect of deformation parameters on the non-recrystallization temperature in Nb-bearing steels," *Metallurgical Transactions A*, vol. 24, no. 10, pp. 2151-2159, 1993/10/01 1993, doi: 10.1007/BF02648589.
- [193] X.-H. Wang, J. Kang, Y.-J. Li, G. Yuan, R. D. K. Misra, and G.-D. Wang, "Effect of Cooling Rates in Coiling Process on Microstructures and Mechanical Properties in Al-Bearing Hot-Rolled TRIP Steel," *Acta Metallurgica Sinica (English Letters)*, vol. 32, no. 10, pp. 1207-1218, 2019/10/01 2019, doi: 10.1007/s40195-018-00868-x.
- [194] M. Asadi, *Influence of the hot rolling process on the mechanical behavior of dual phase steels*. Universitätsbibliothek Clausthal, 2010.

- [195] D. Matlock, D. Bruce, and J. Speer, "Strengthening mechanism and their applications in extremely low C steels," in *International Forum for the Properties and Application of IF Steels (IF Steels 2003)[12–14 May, 2003]*, 2003, pp. 118-127.
- [196] D. Wu, Z. Li, and H.-s. LÜ, "Effect of Controlled Cooling After Hot Rolling on Mechanical Properties of Hot Rolled TRIP Steel," *Journal of Iron and Steel Research, International*, vol. 15, no. 2, pp. 65-70, 2008/03/01/ 2008, doi: [https://doi.org/10.1016/S1006-706X\(08\)60034-5](https://doi.org/10.1016/S1006-706X(08)60034-5).
- [197] F. Hairer, A. Karellova, C. Kremaszky, E. Werner, T. Hebesberger, and A. Pichler, "Influence of heat treatment on the microstructure and hardness of a low alloyed complex phase steel," 2009.
- [198] F. A. McClintock and A. S. Argon, *Mechanical behavior of materials*. Reading, Mass.: Addison-Wesley Pub. Co. (in English), 1966.
- [199] N. Pathak, C. Butcher, M. J. Worswick, E. Bellhouse, and J. Gao, "Damage Evolution in Complex-Phase and Dual-Phase Steels during Edge Stretching," *Materials*, vol. 10, no. 4, p. 346, 2017.
- [200] N. K. Singh, E. Cadoni, M. K. Singha, and N. K. Gupta, "Quasi-Static and Dynamic Tensile Behavior of CP800 Steel," *Mechanics of Advanced Materials and Structures*, vol. 21, no. 7, pp. 531-537, 2014/08/09 2014, doi: 10.1080/15376494.2012.699594.
- [201] E. Cadoni, N. K. Singh, M. K. Singha, and N. K. Gupta, "Strain rate behaviour of multiphase and complex-phase steels for automotive applications," *EPJ Web of Conferences*, vol. 26, p. 05003, 2012.
- [202] J. Kliber, G. Plestilova, O. Zacek, and M. C. Somani, "Effects of Thermomechanical Processing on Microstructure and Mechanical Properties Multiphase Steels Exhibiting a TRIP Effect," *Materials Science Forum*, vol. 539-543, pp. 4357-4362, 2007, doi: 10.4028/[www.scientific.net/MSF.539-543.4357](http://www.scientific.net/MSF.539-543.4357).
- [203] V. Javaheri, N. Khodaie, A. Kaijalainen, and D. Porter, "Effect of niobium and phase transformation temperature on the microstructure and texture of a novel 0.40% C thermomechanically processed steel," *Materials Characterization*, vol. 142, pp. 295-308, 2018/08/01/ 2018, doi: <https://doi.org/10.1016/j.matchar.2018.05.056>.

[204] D. Bacon and G. E. Dieter, *Mechanical metallurgy : SI metric edition*. London: McGraw-Hill Book Company (in English), 1988.

# APPENDIX I

## Microstructures by Electron Microscopy

More of the metallography's of the specimens subjected to the simulation of finishing rolling followed by a controlled cooling are presented in this appendix. The conditions of the processing parameters are detailed in Table AI.1. These metallography's were generated with both transmission and scanning electron microscopy equipment and are a complement of Section 5.5 of this thesis.

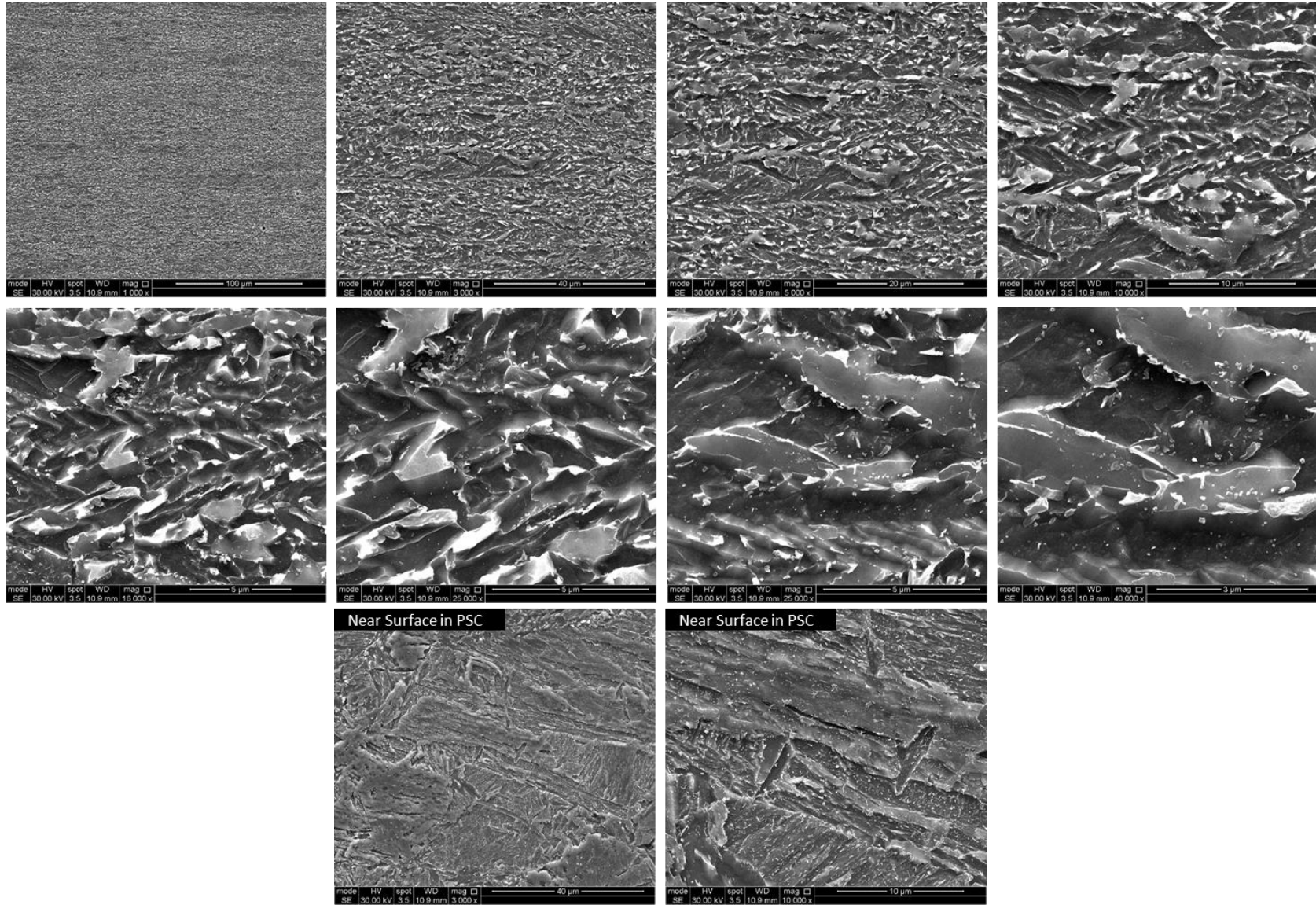
The general microstructure of these CP steels shows a ferrite and bainite matrix, and some martensitic islands can also be observed. The fine grain size in all specimens was the result of the strain accumulation in the deformation passes prior to controlled cooling. These images represent different areas of the specimen, always within the strain zone at different magnifications.

**Table AI.1** Strategies to obtain CP microstructure during the thermomechanical processing

<b>Specimen</b>	<b>Description</b>
Quench	Last deformation pass at 850°C, immediately quench after the fourth pass
SC1	Last deformation pass at 850°C, step cooling at 550 °C for 13 seconds
SC2	Last deformation pass at 850°C, step cooling at 500 °C for 13 seconds
SC3	Last deformation pass at 830°C, step cooling at 550 °C for 13 seconds
SC4	Last deformation pass at 830°C, step cooling at 500 °C for 13 seconds
SC5	Last deformation pass at 830°C, step cooling at 500 °C for 60 seconds

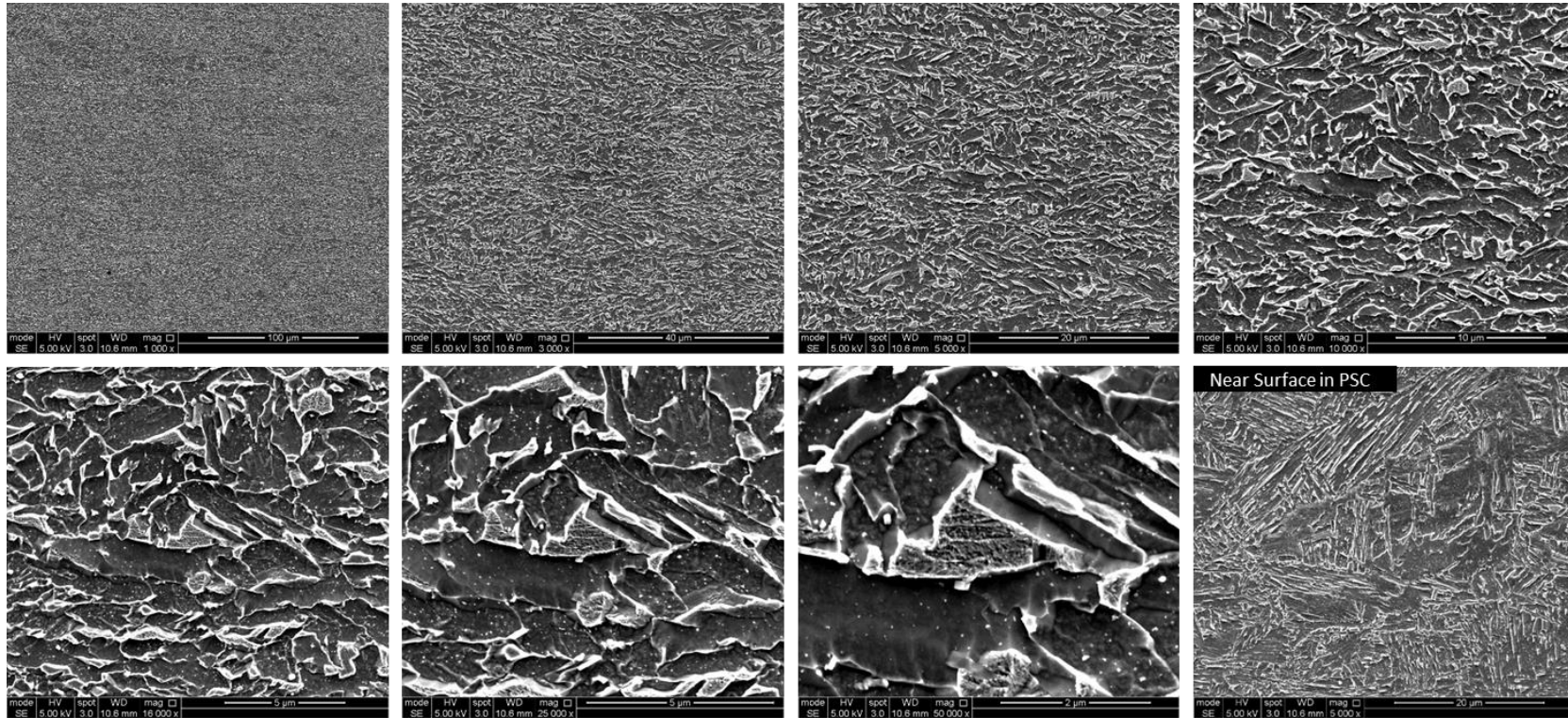
# AI.1. SC1

## AI.1a. SC1 Secondary electrons



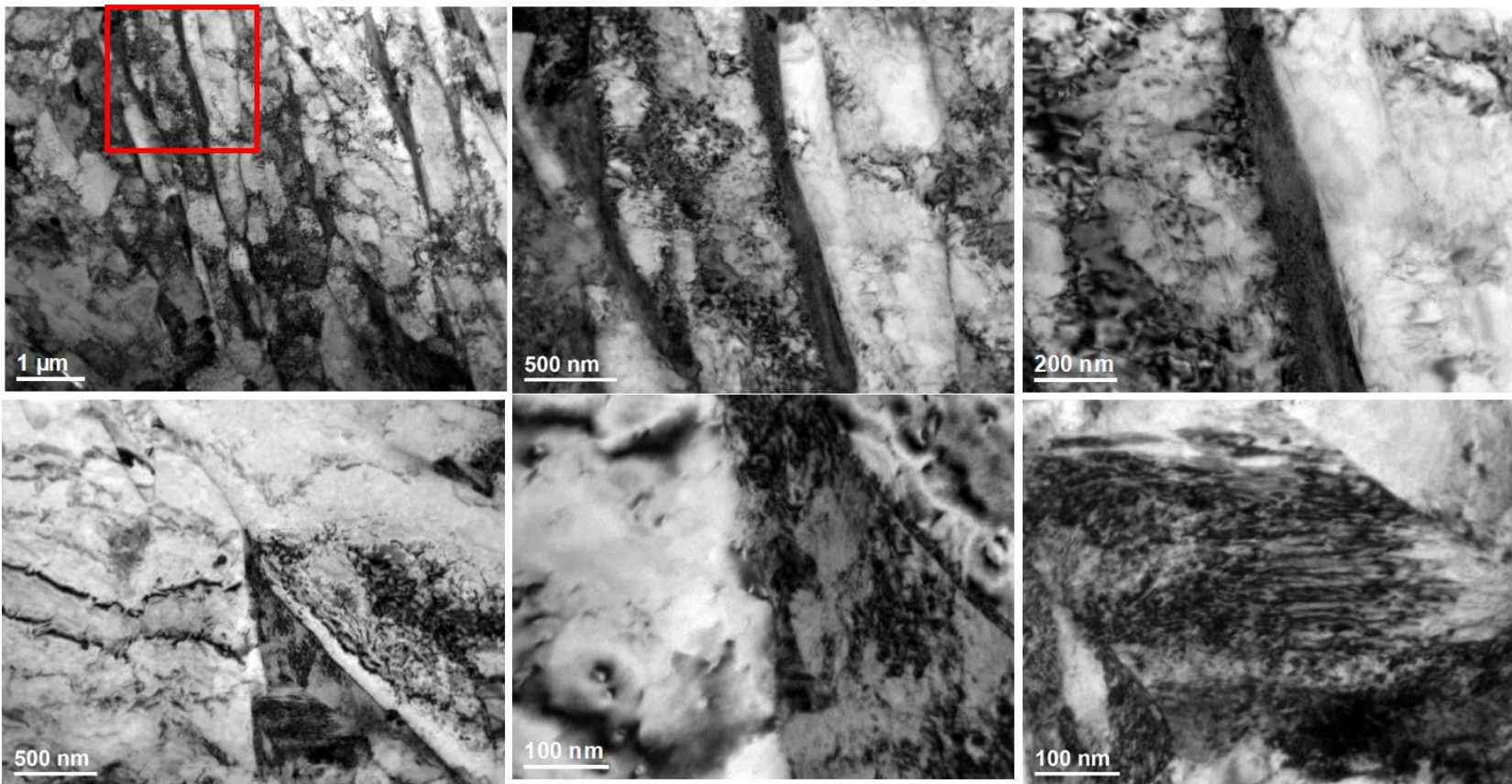
## AI.2 SC2

### AI.2a. SC2 Secondary electrons

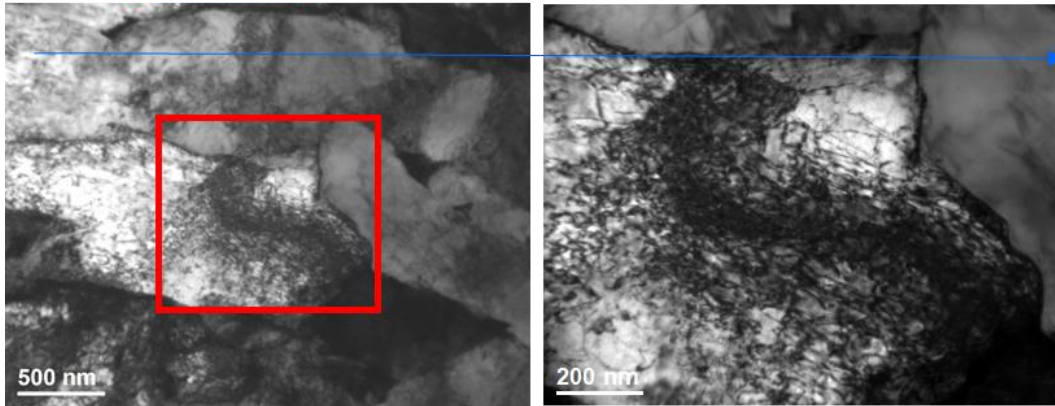
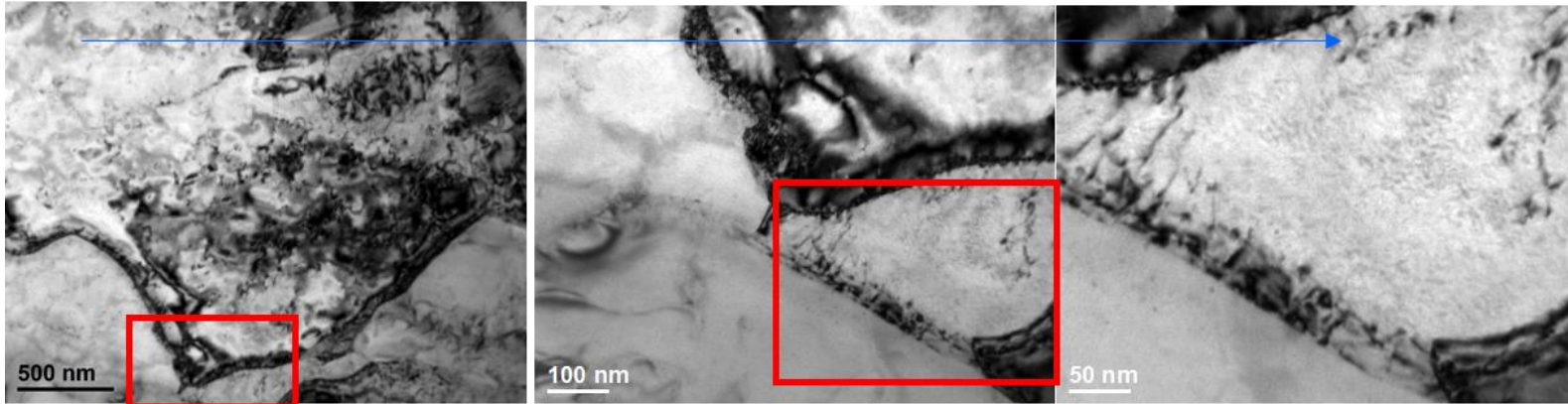
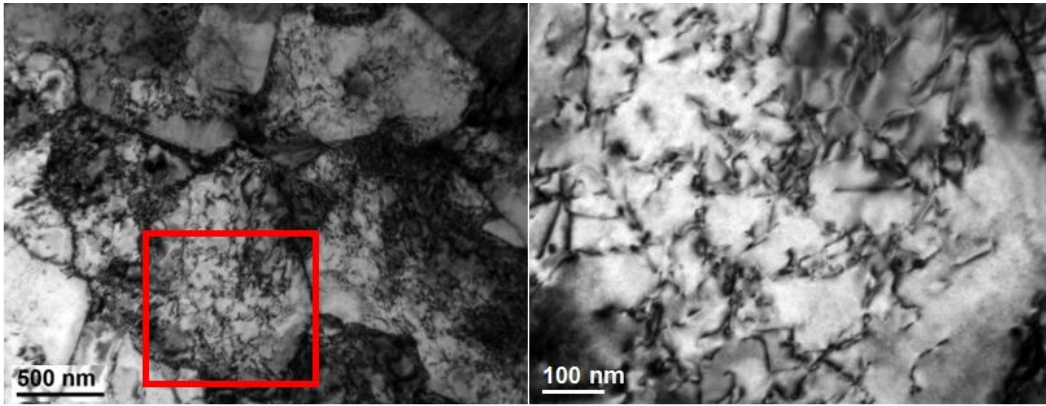




AI.2b. SC2 TEM thin foil

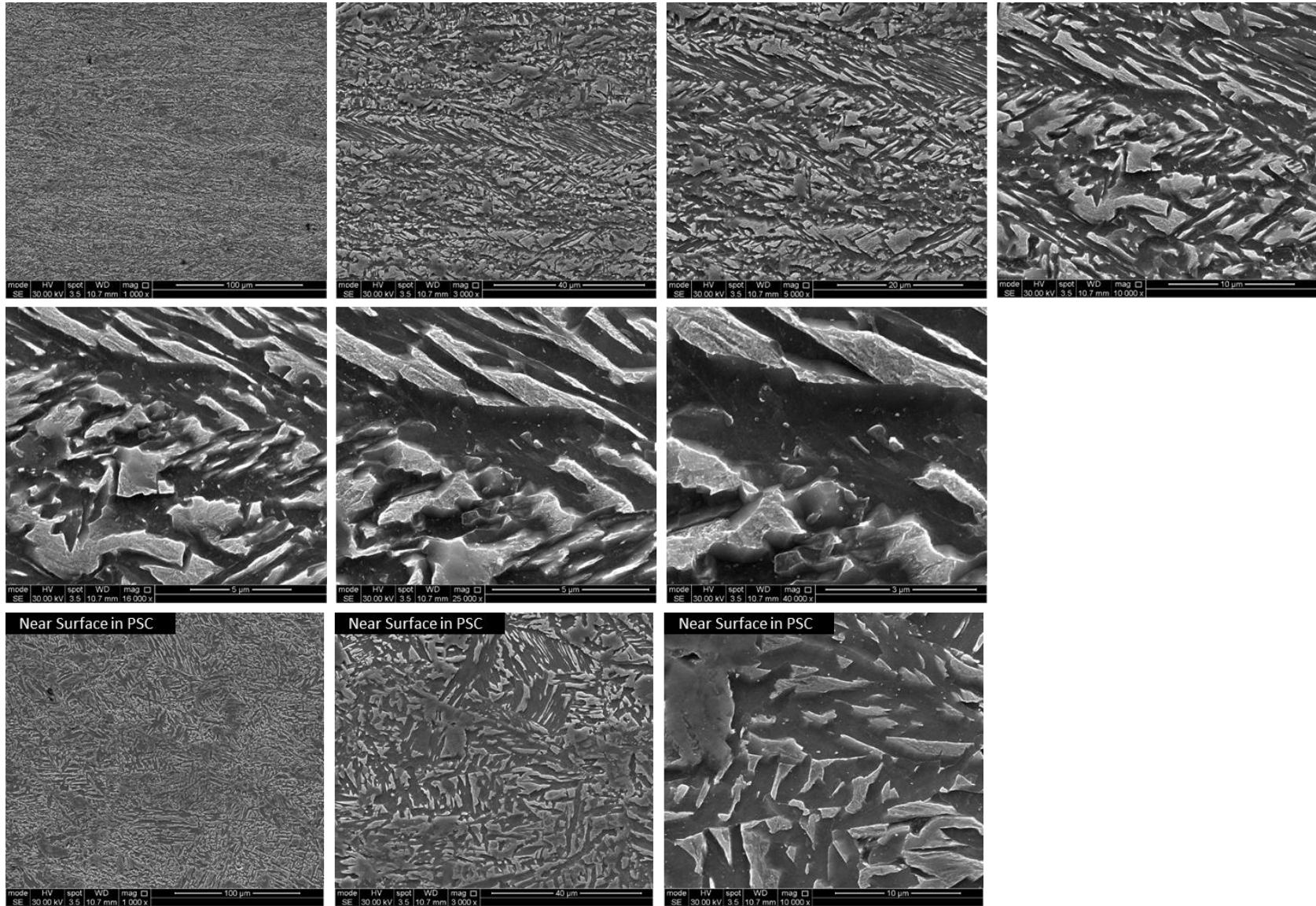




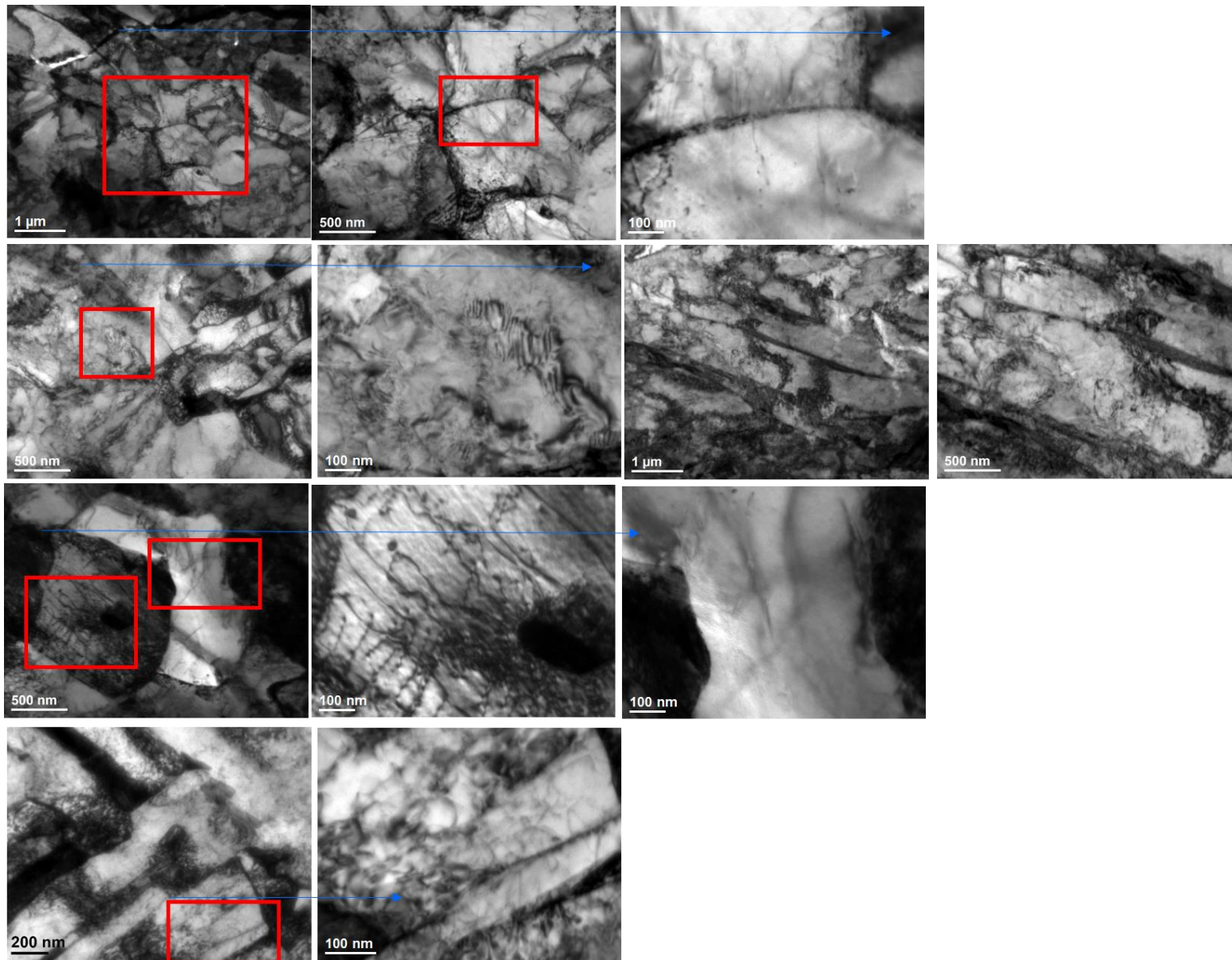


# Al.3 SC3

## Al.3a. SC3 Secondary electrons



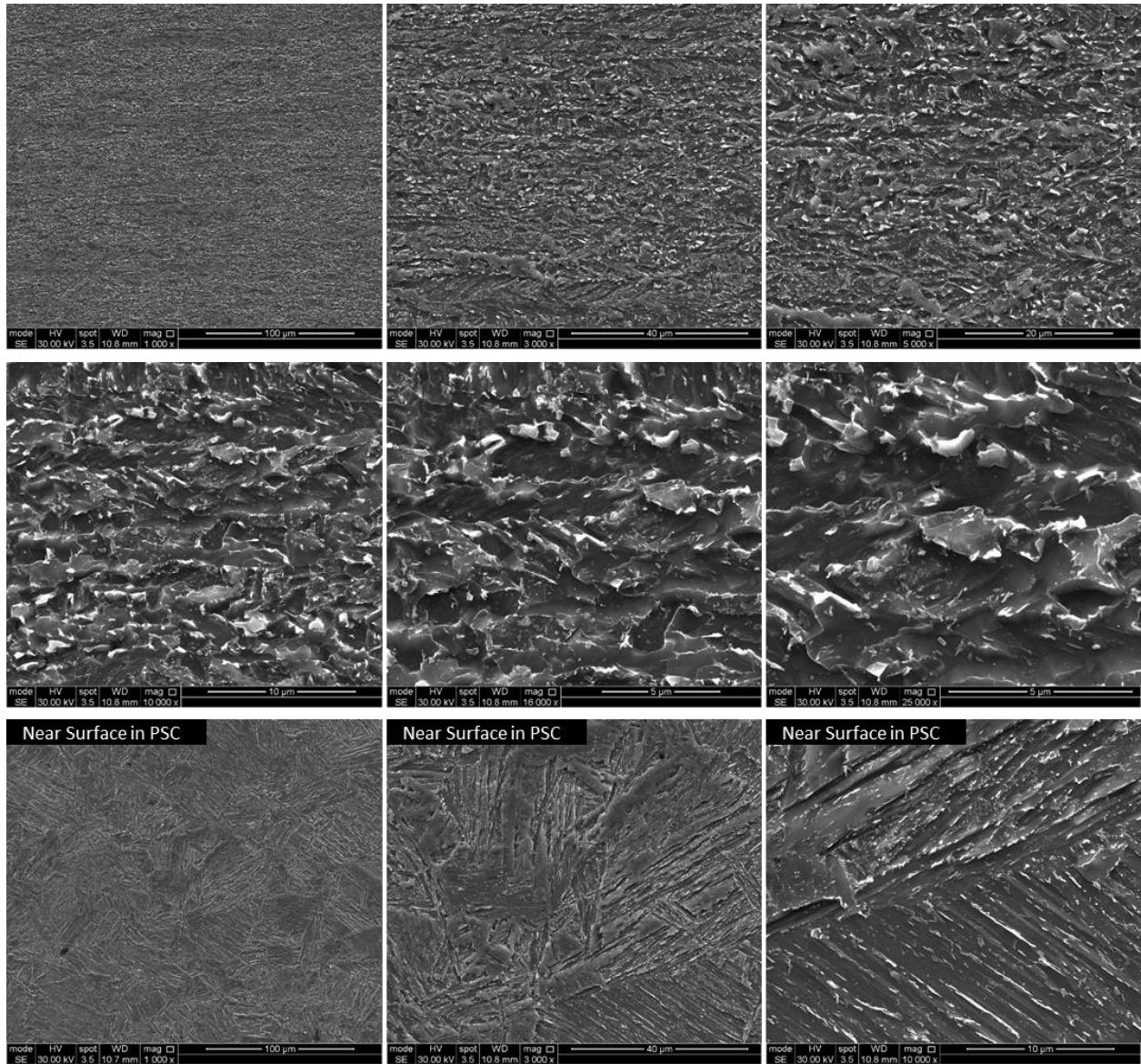
Al.3b. SC3 TEM thin foil



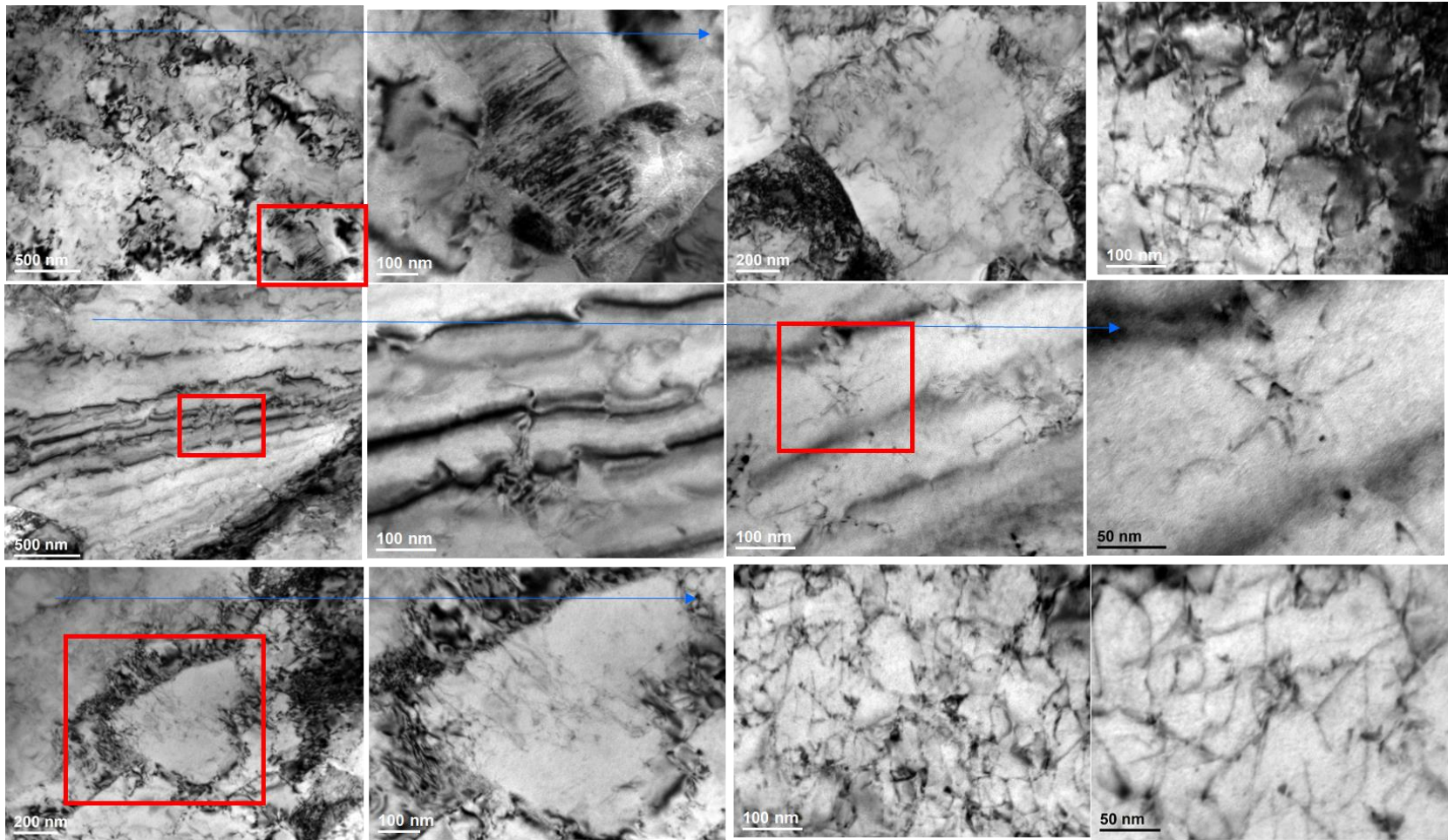


# AI.4 SC4

## AI.4a. SC4 Secondary electrons

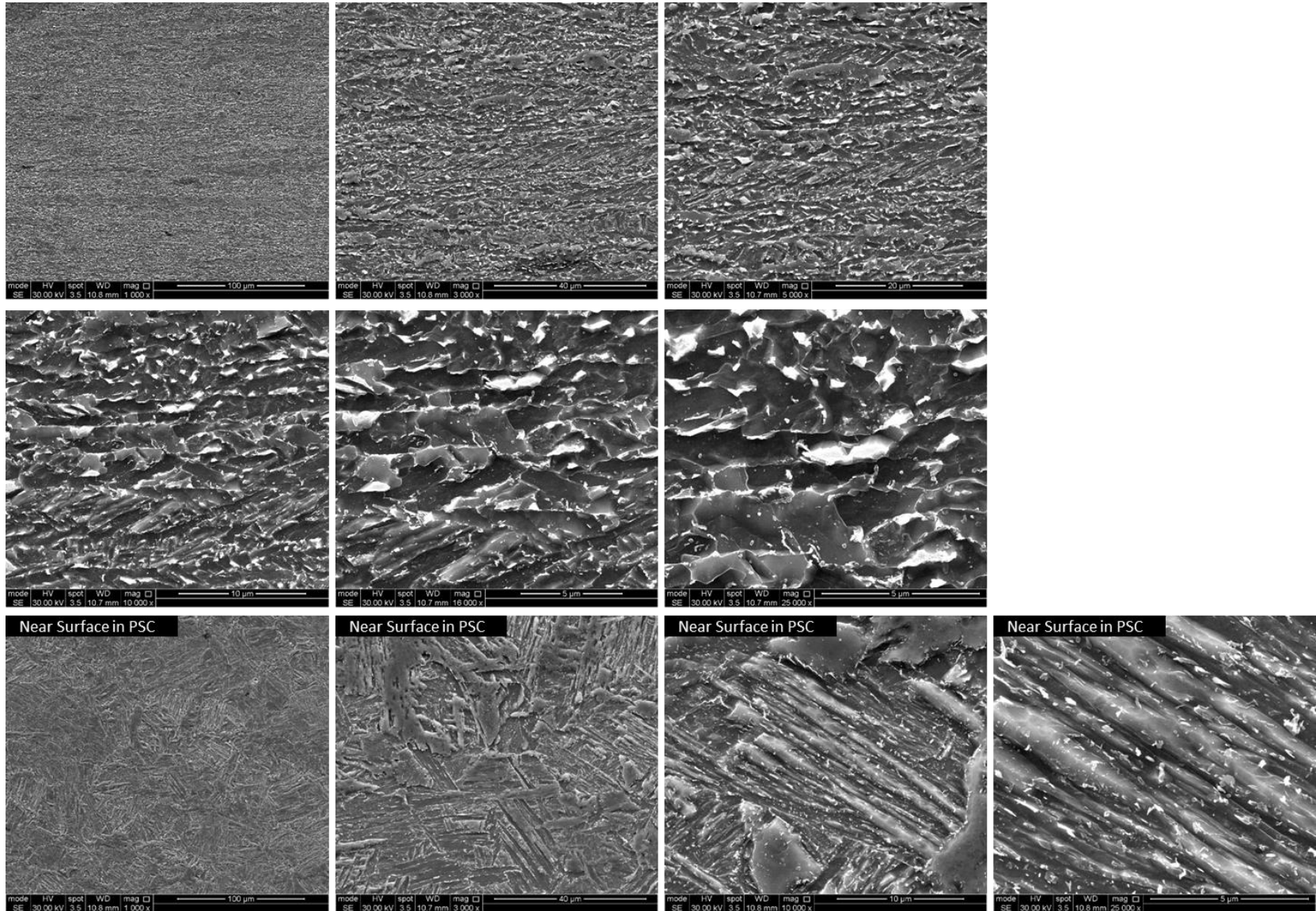


AI.4b. SC4 TEM thin foil



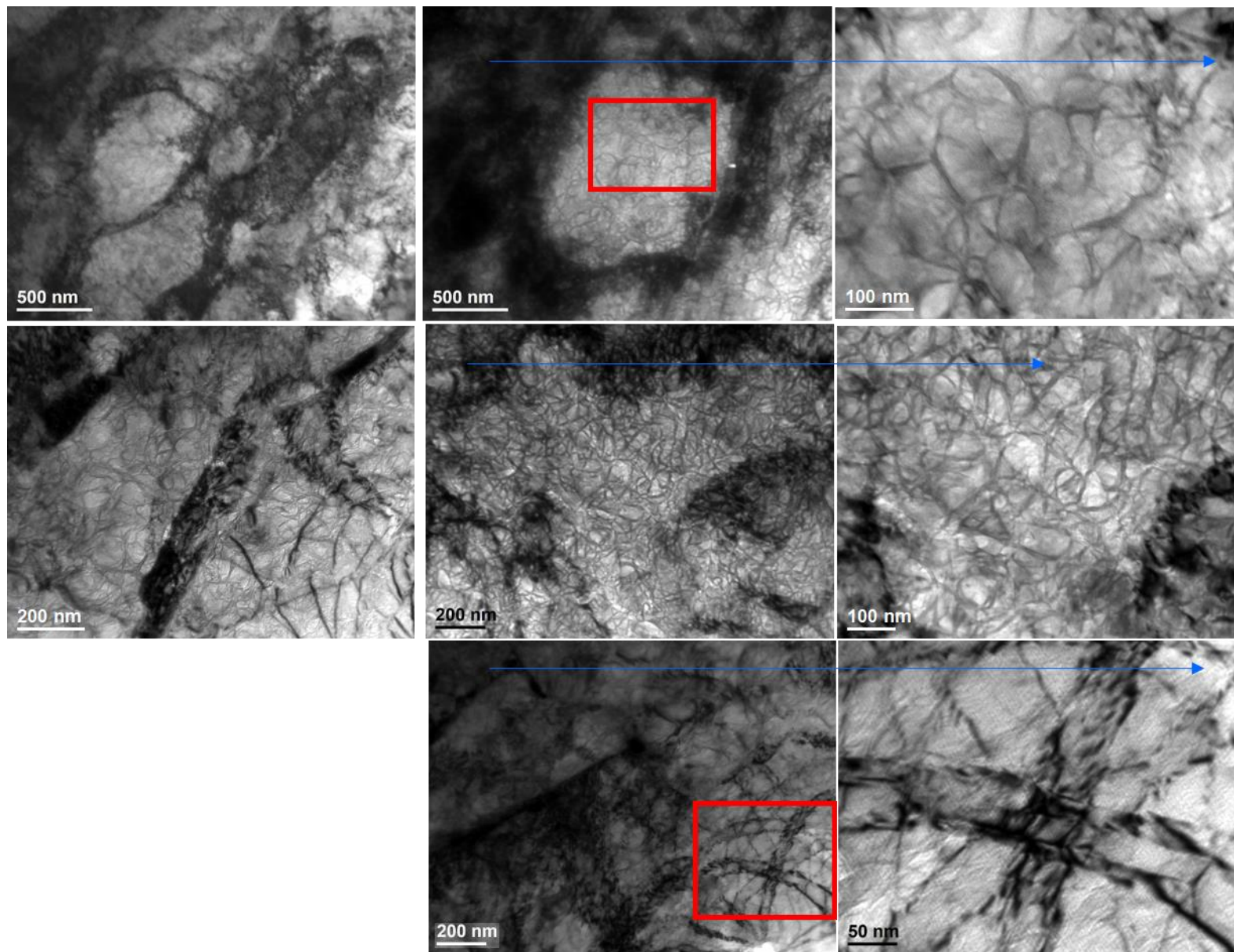
## AI.5. SC5

### AI.5a. SC5 Secondary electrons



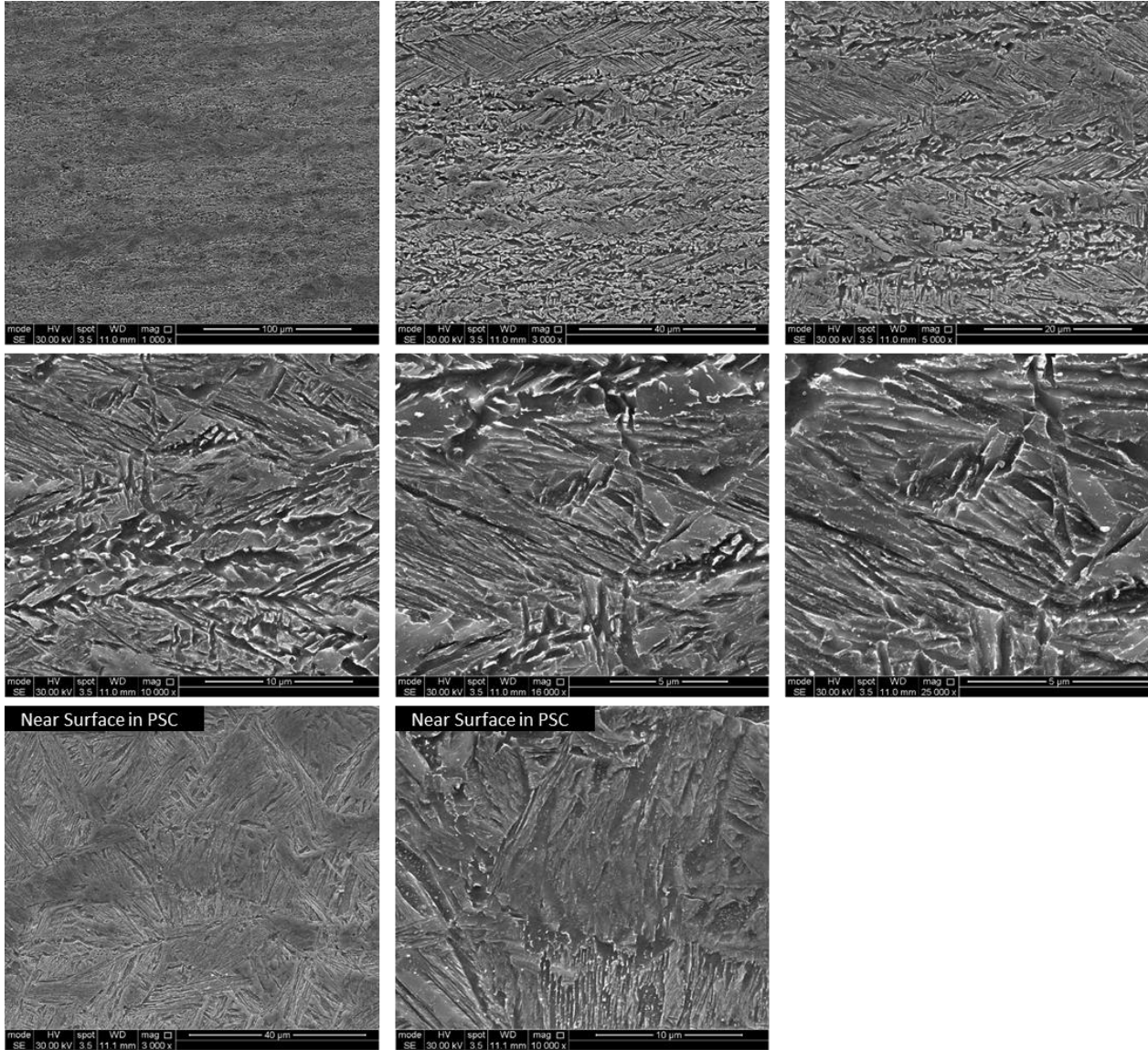


AI.5b. SC5 TEM thin foil



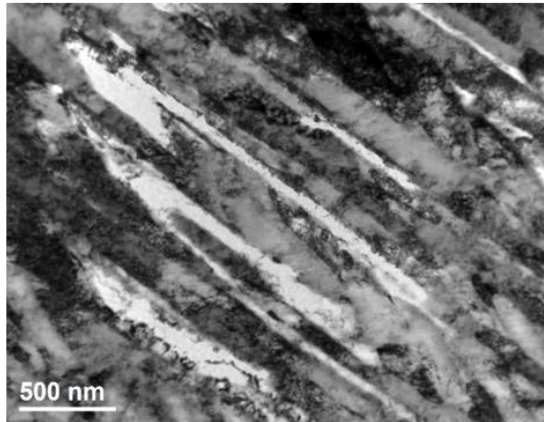
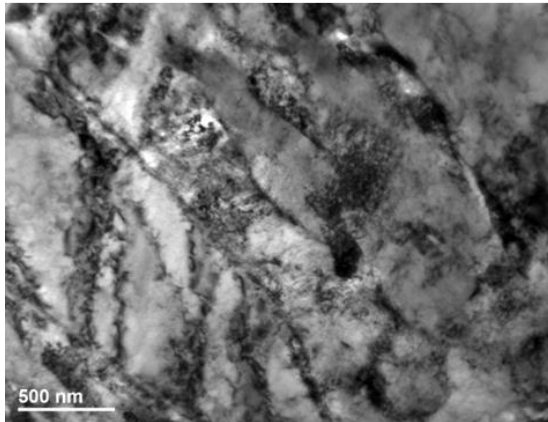
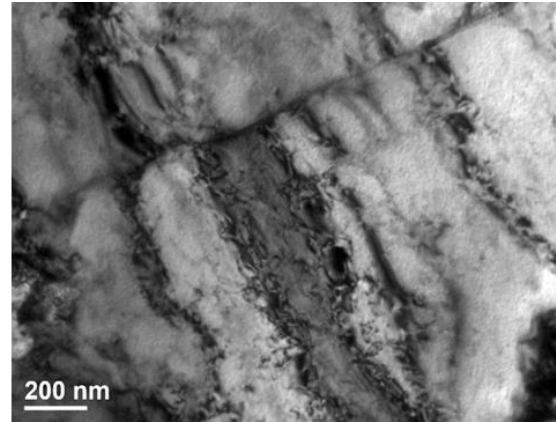
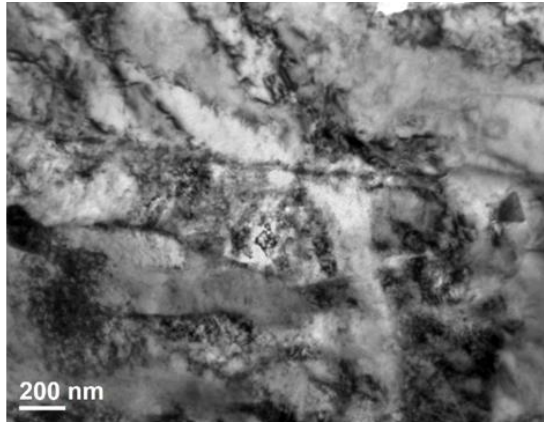
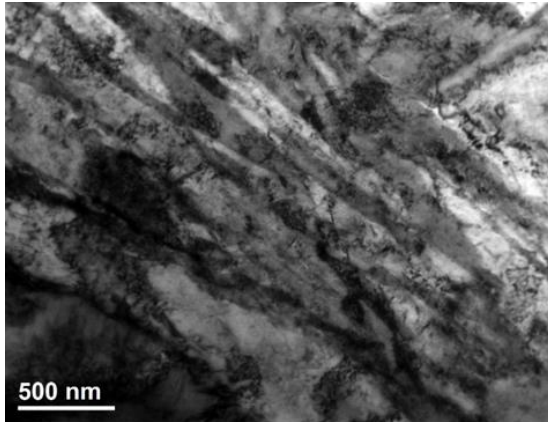
## AI.6 Quench

### AI.6a. Quench Secondary electrons





**Al.6b. Quench TEM thin foil**



# APPENDIX II

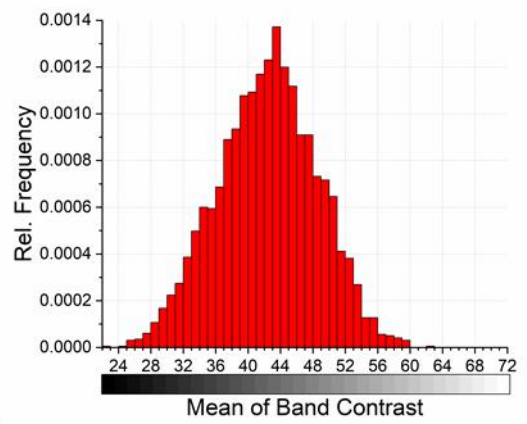
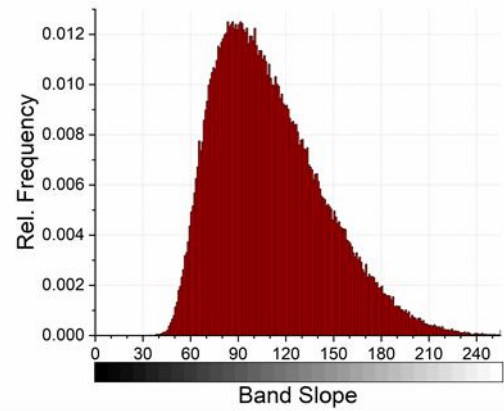
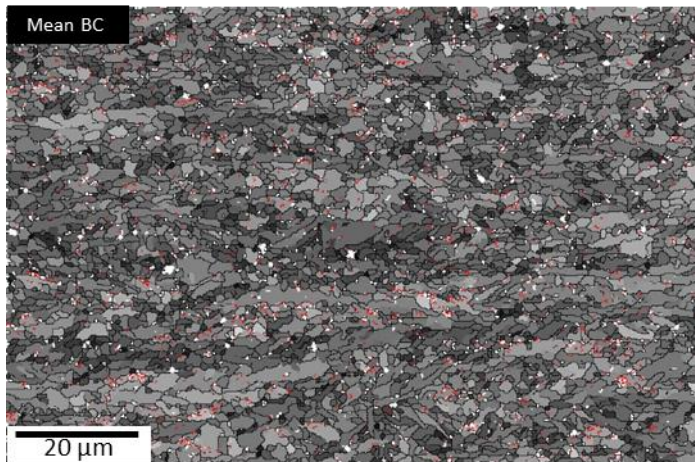
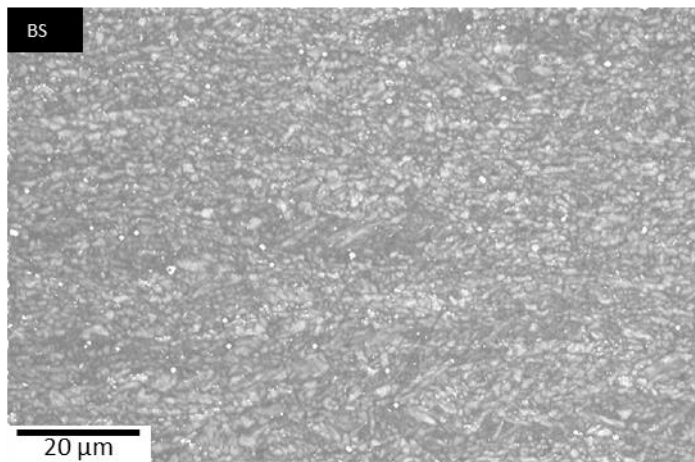
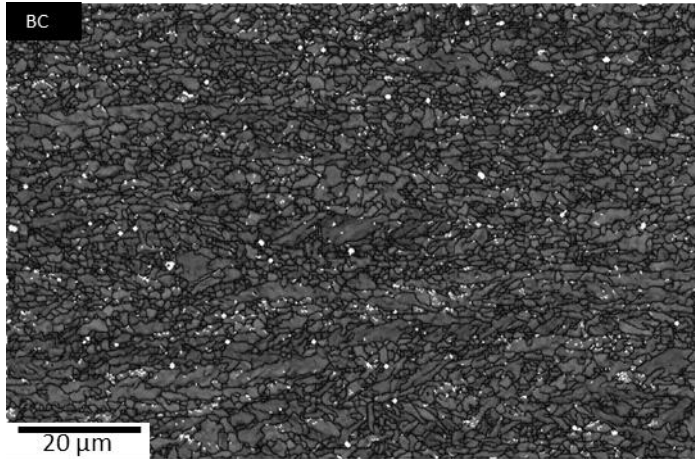
## Electron Backscattered Diffraction

### Mapping

The microstructure, the proportion and distribution of the phases in steel are associated with its mechanical properties. EBSD is a very useful technique to identify and quantify the phases that are present in the microstructure. CP steels microstructure generally consist of a combination of ferrite, bainite, and martensite, and under certain conditions, relatively small amounts of retained austenite may be present in the steel.

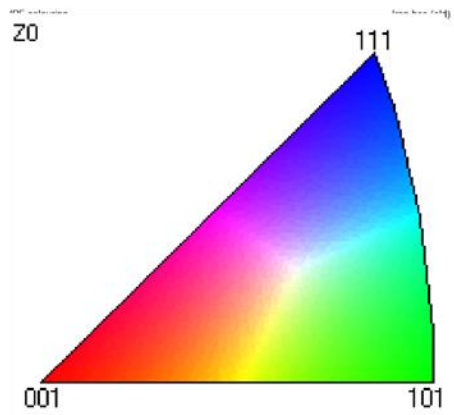
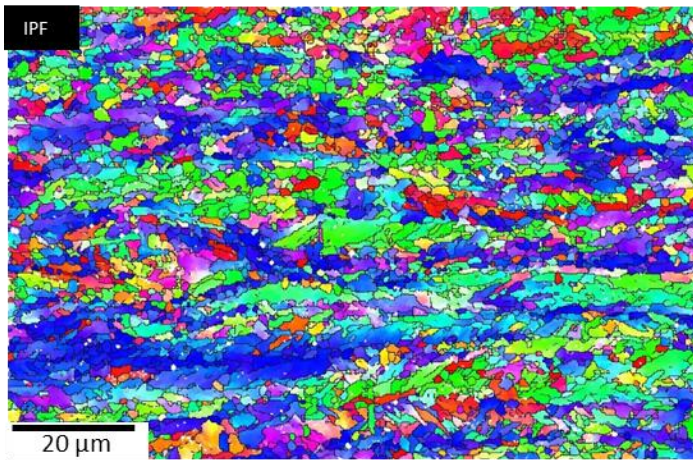
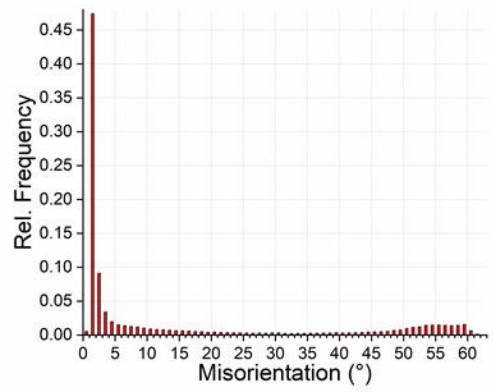
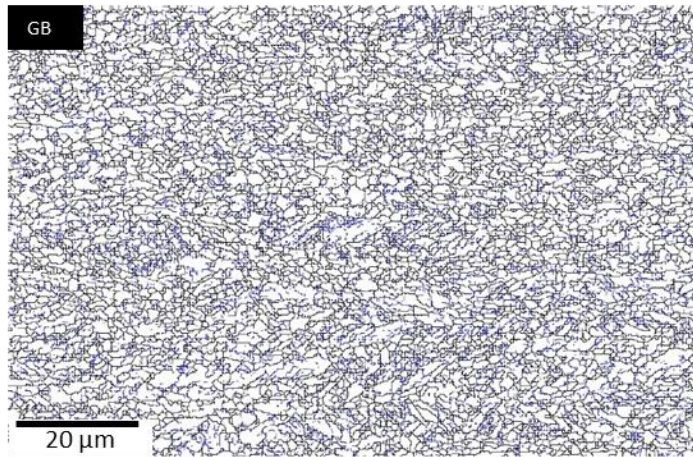
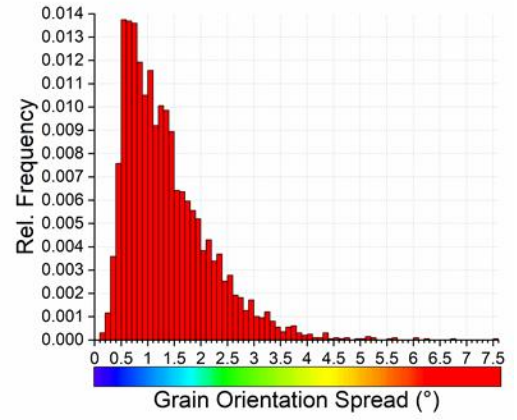
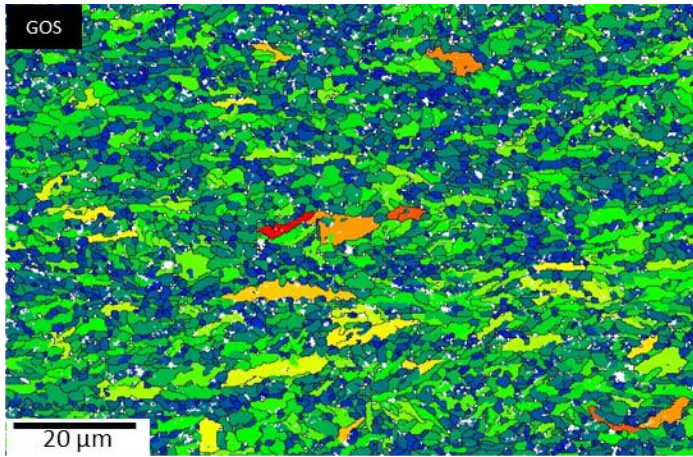
The EBSD maps presented next were constructed to identify and quantify the phases in each of the specimens that followed the full designed TMP route. The procedure to follow was explained in detail in Section 5.5 of this thesis, and consists of phase segmentation based on the crystal structure detected by the EBSD system, the grain averaged band contrast map, the grain orientation spread filter and also the aspect ratio of the grains. The criteria to define a grain was a misorientation angle greater than or equal to  $5^\circ$  and that the minimum area of a grain must be higher than 10 pixels or  $0.4 \mu\text{m}^2$ .

## AII.1 EBSD maps from SC1



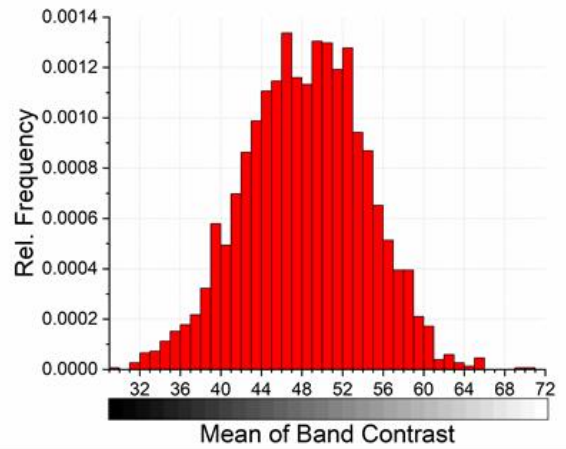
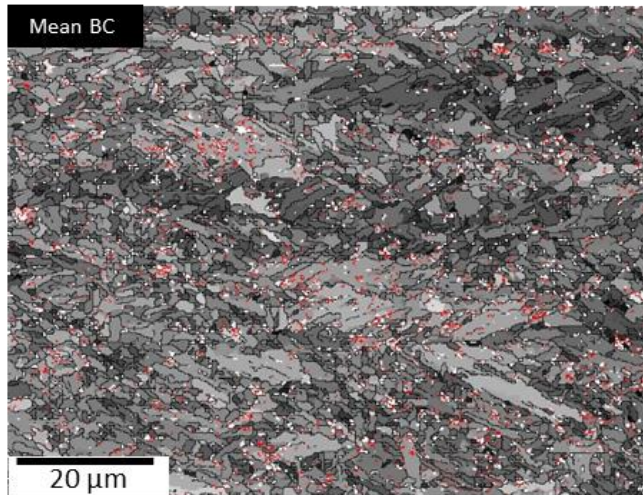
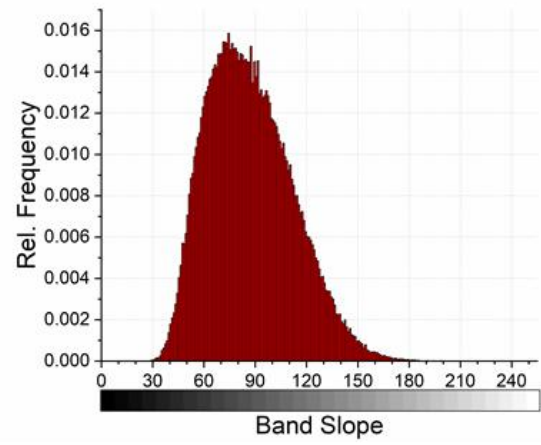
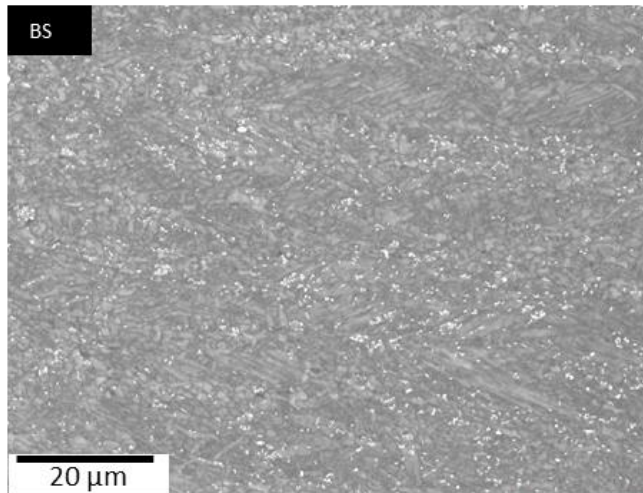
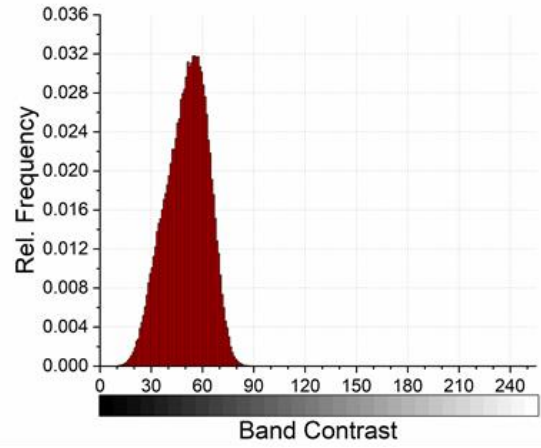
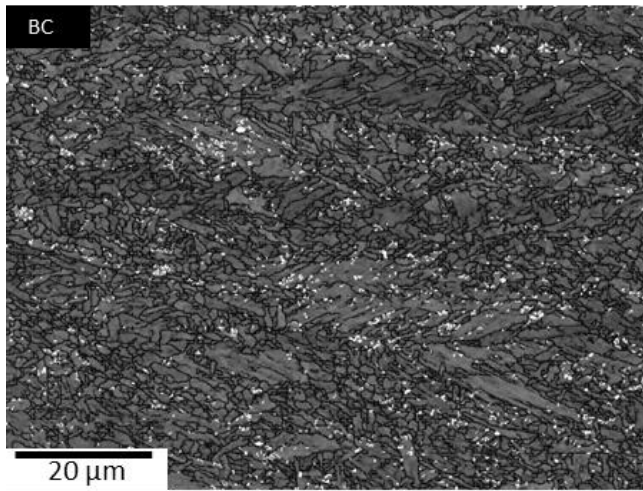


EBSD maps from SC1 (continued)



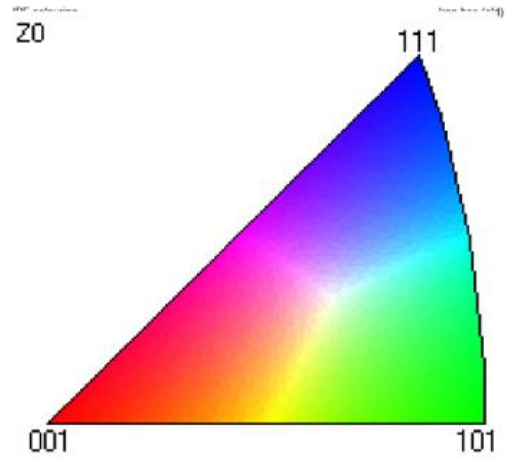
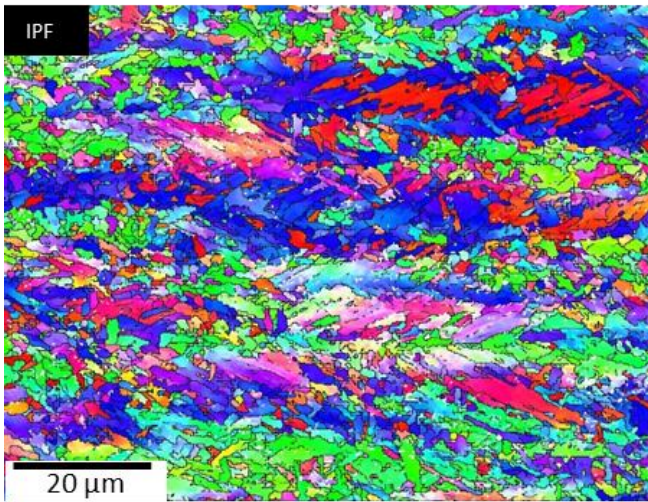
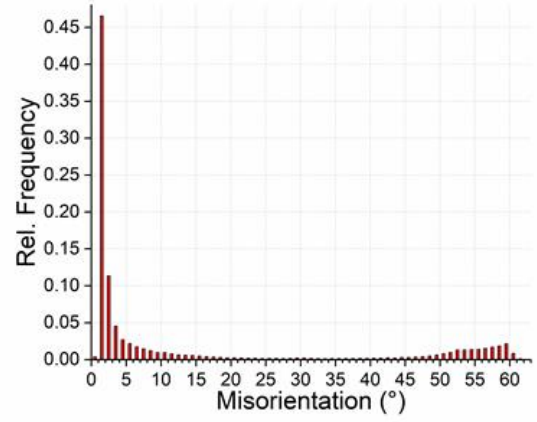
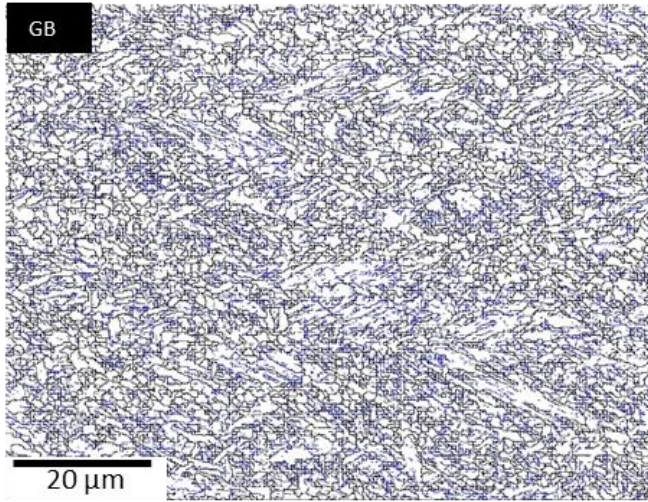
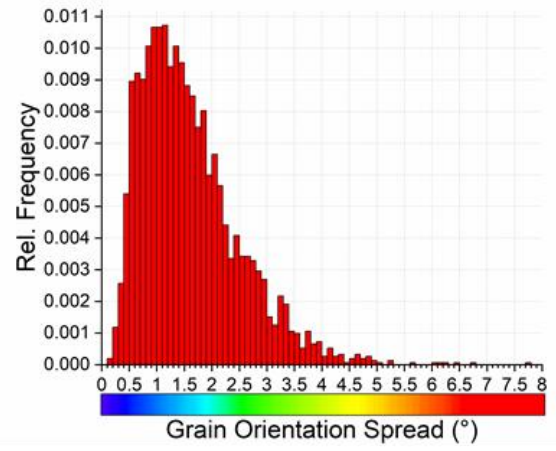
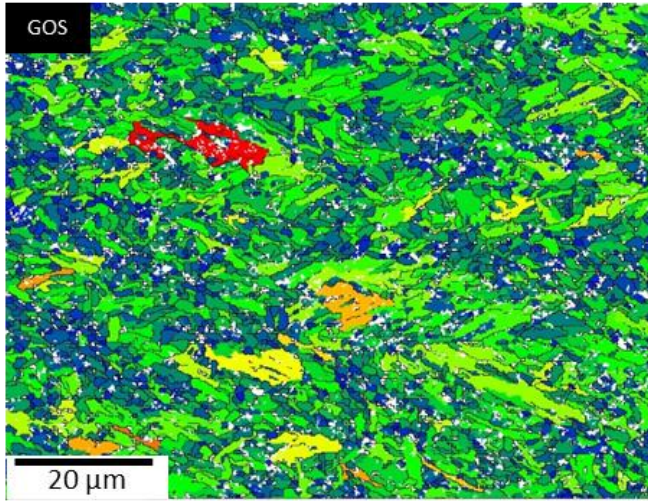


## AII.2 EBSD maps from SC2

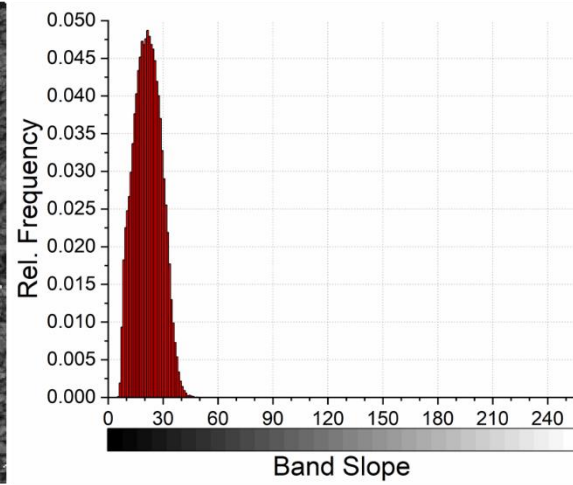
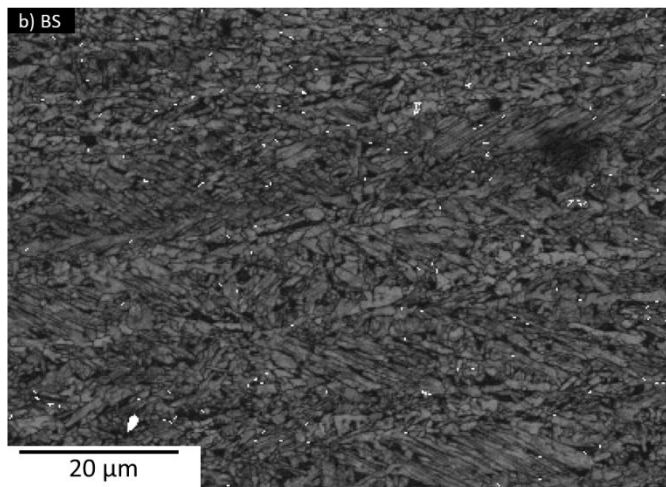
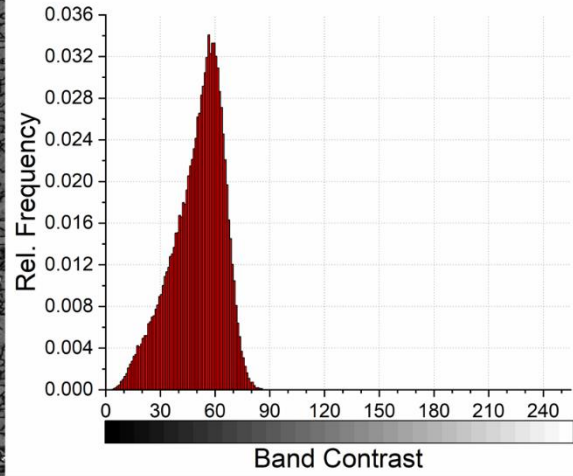
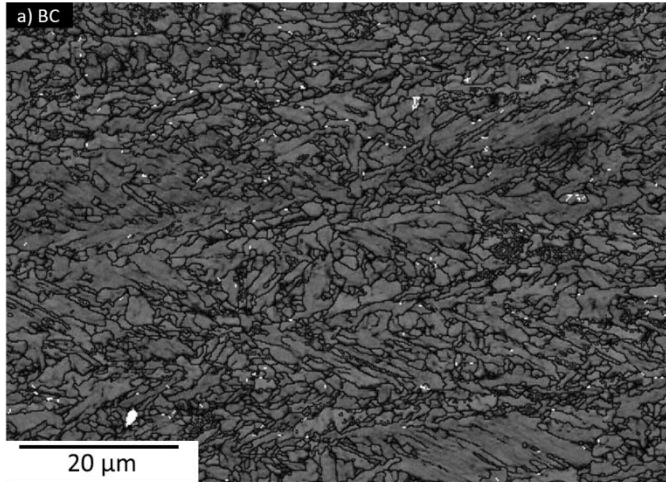




EBSD maps from SC2 (continued)

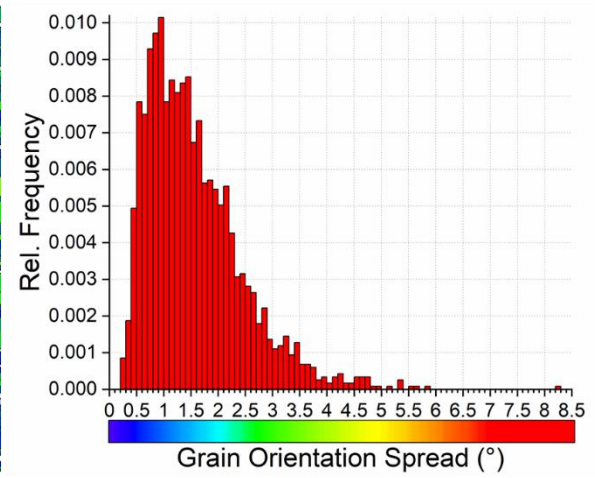
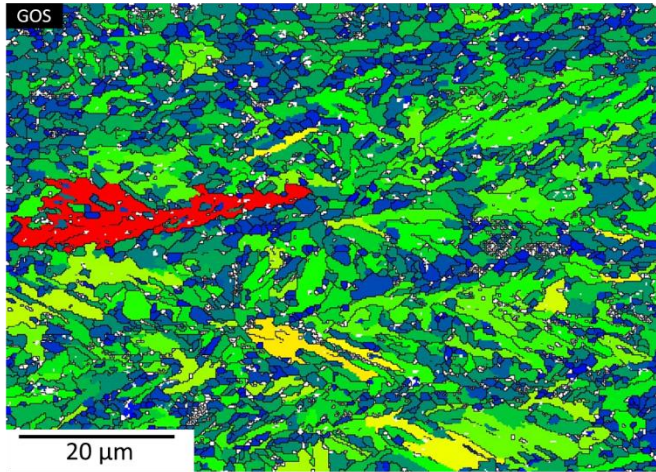
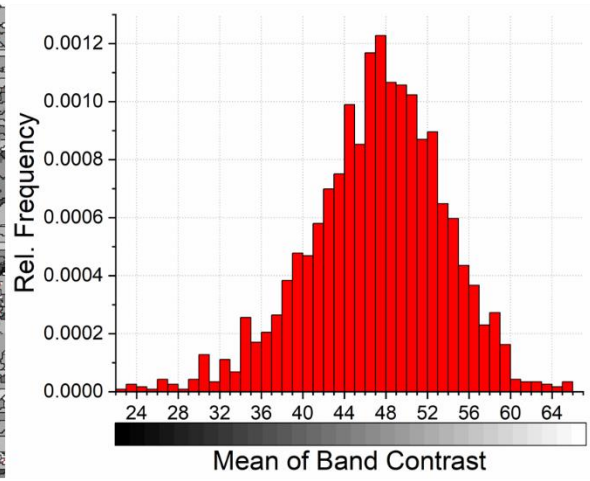
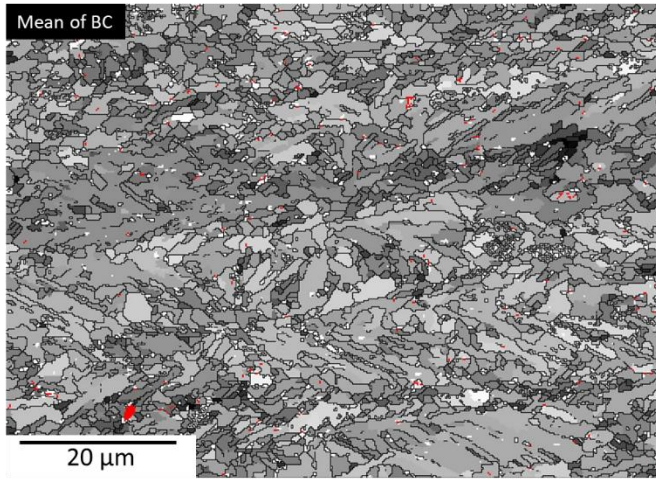


### AII.3 EBSD maps from SC3



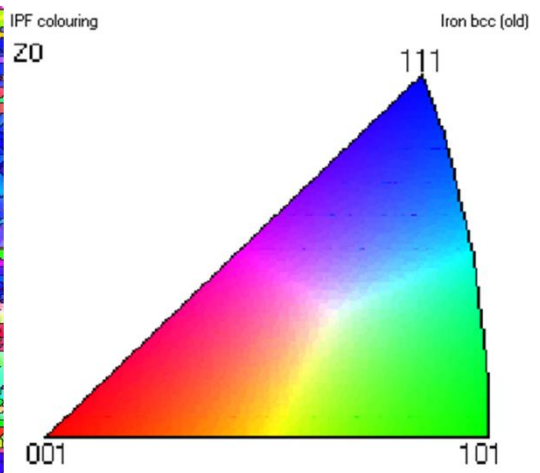
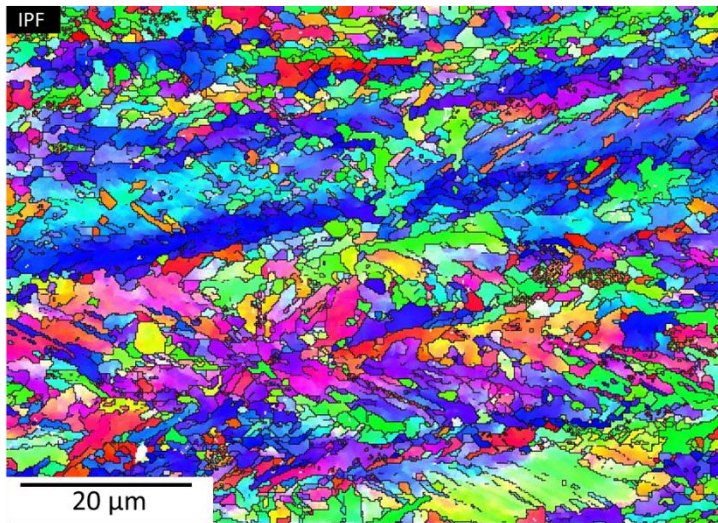
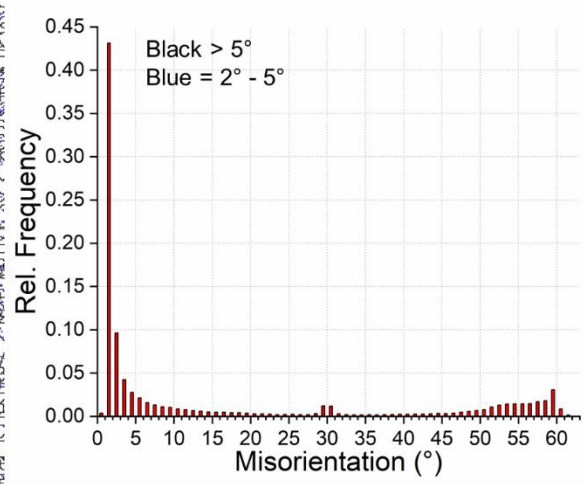
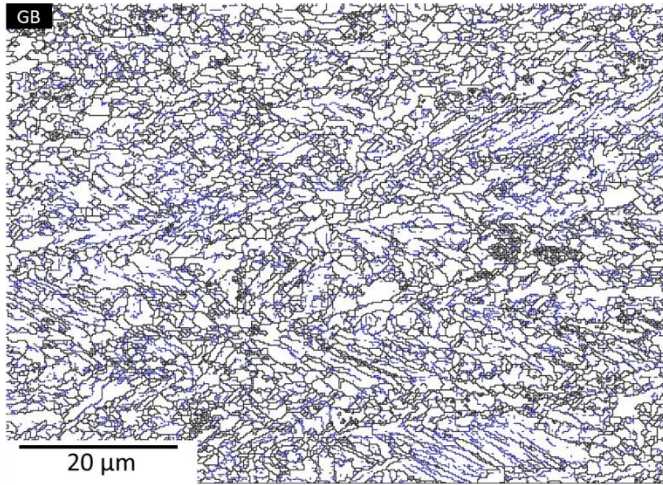


EBSD maps from SC3 (continued)

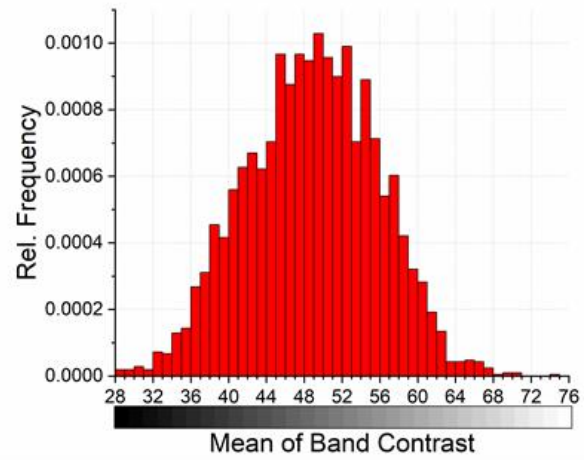
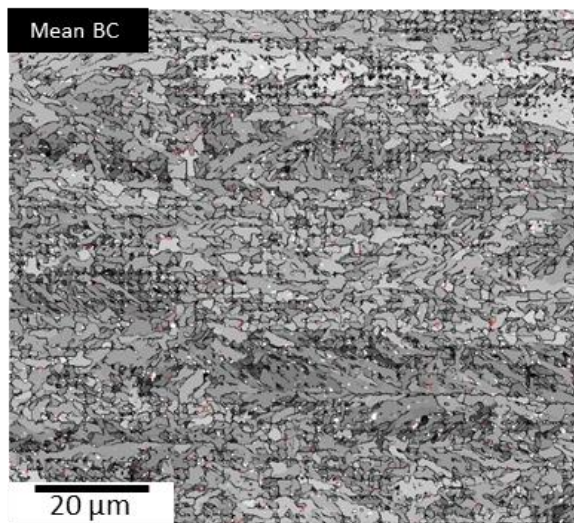
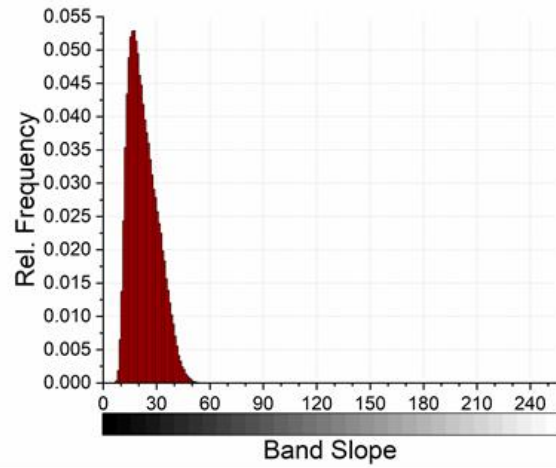
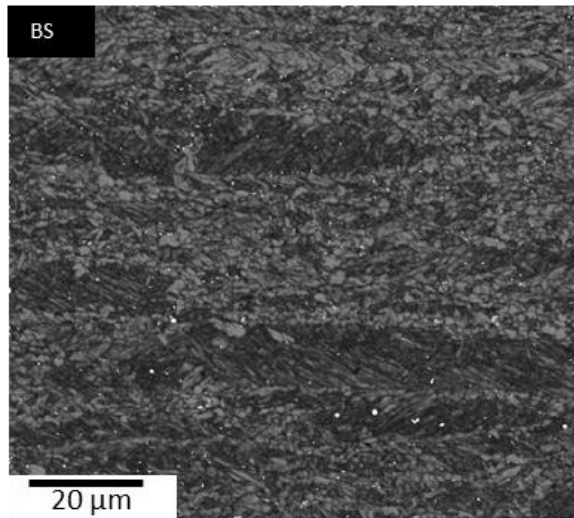
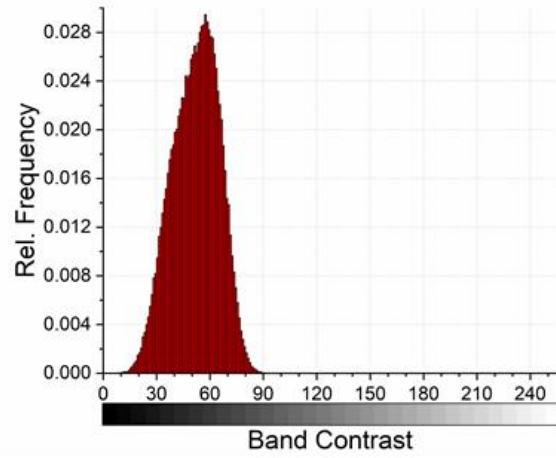
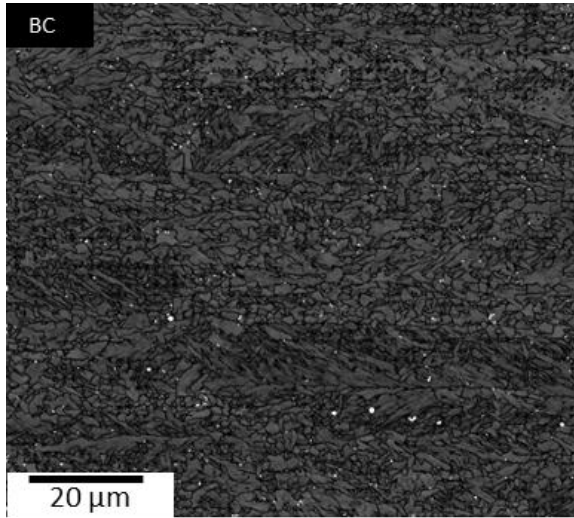




EBSD maps from SC3 (continued)

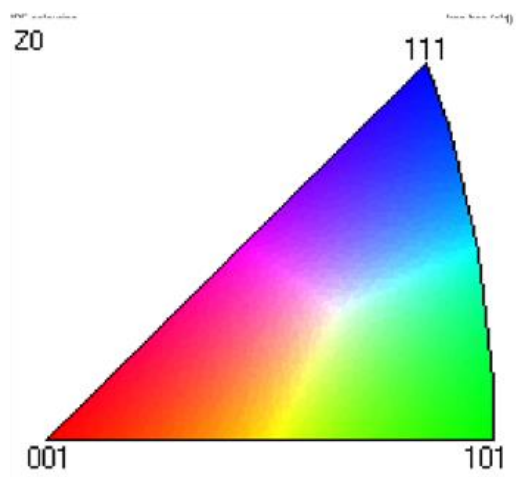
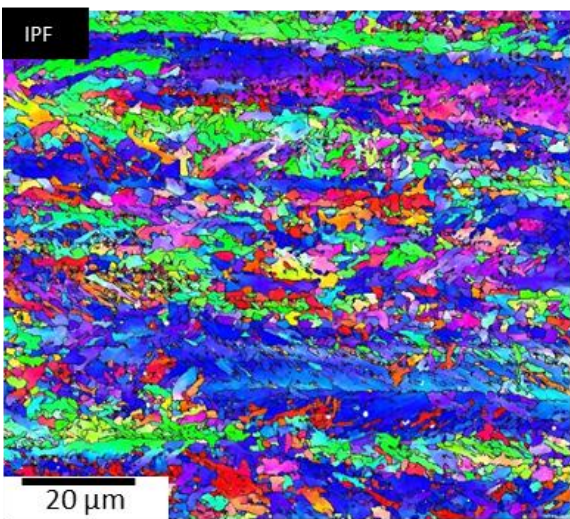
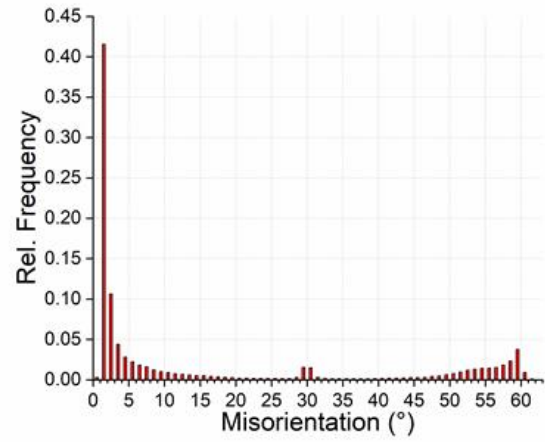
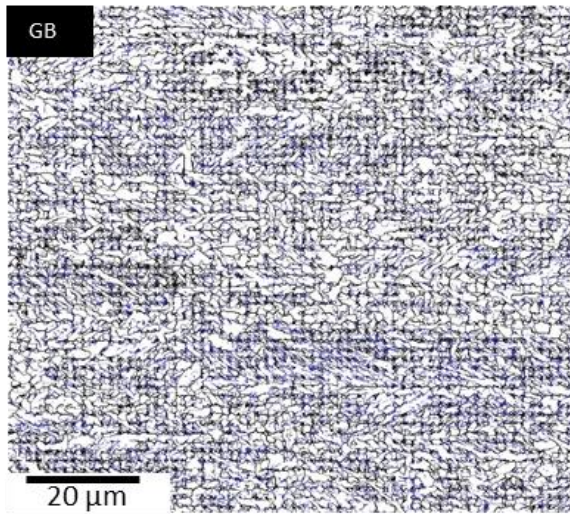
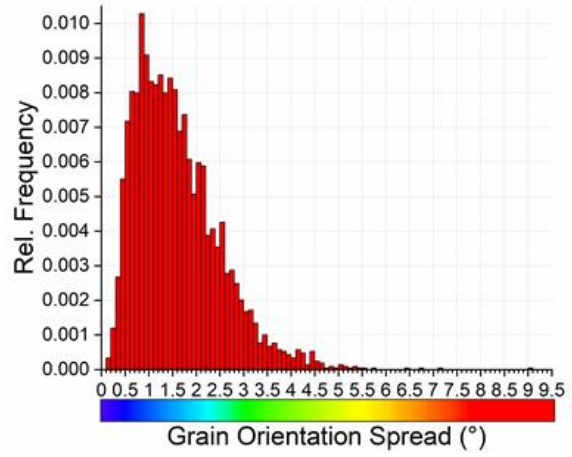
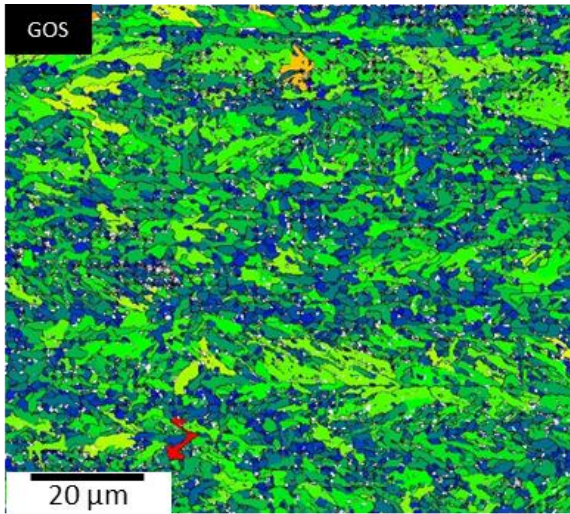


## AII.4 EBSD maps from SC4

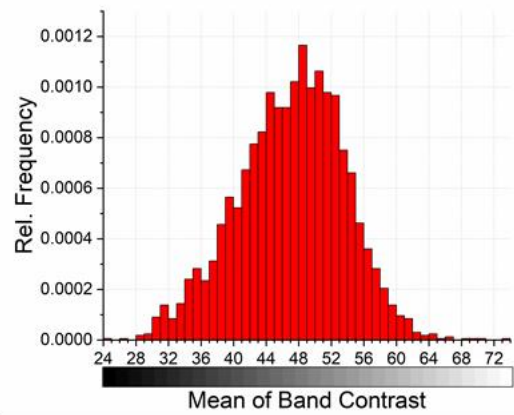
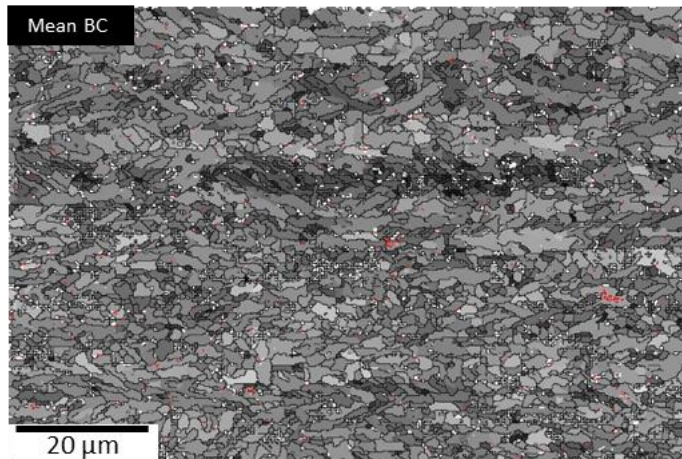
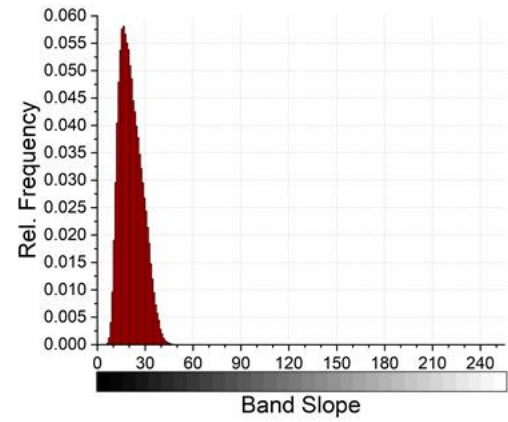
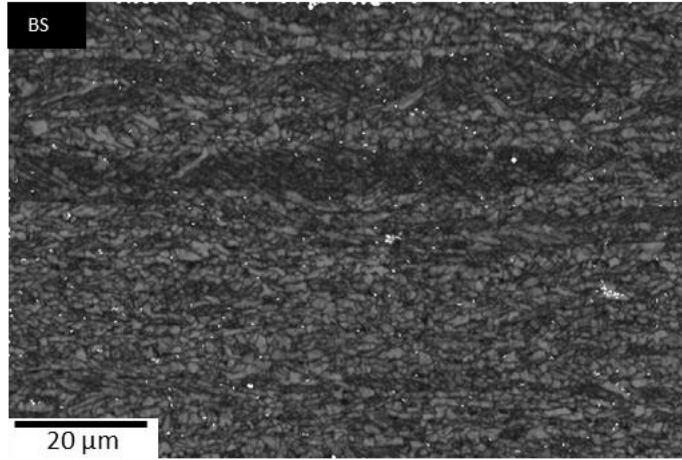
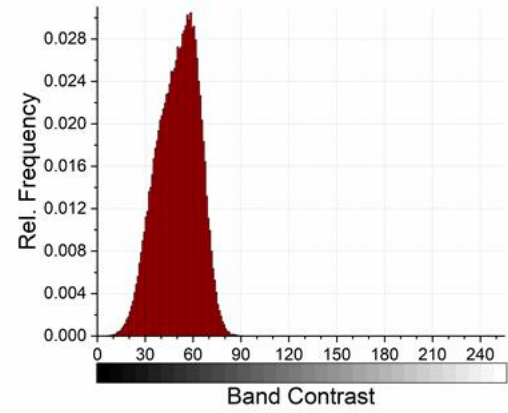
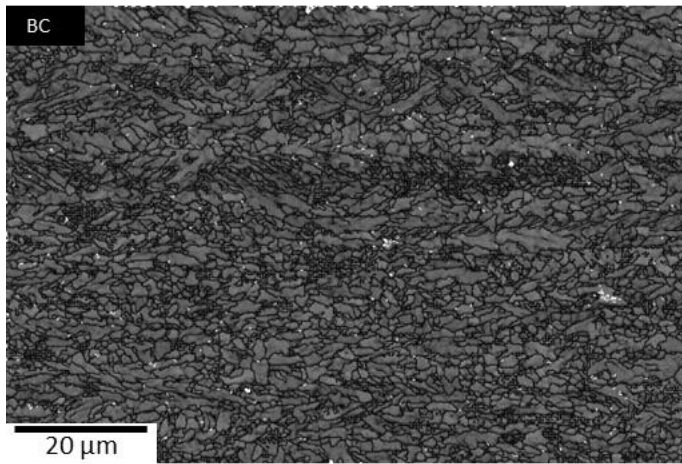




EBSD maps from SC4 (continued)

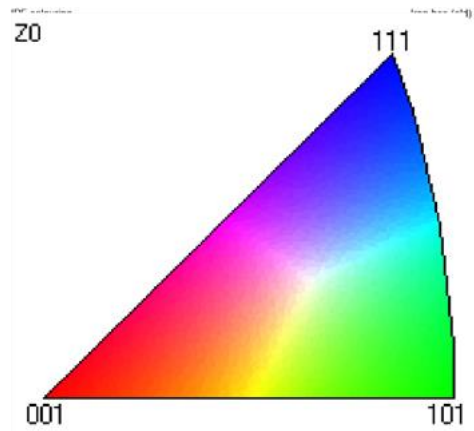
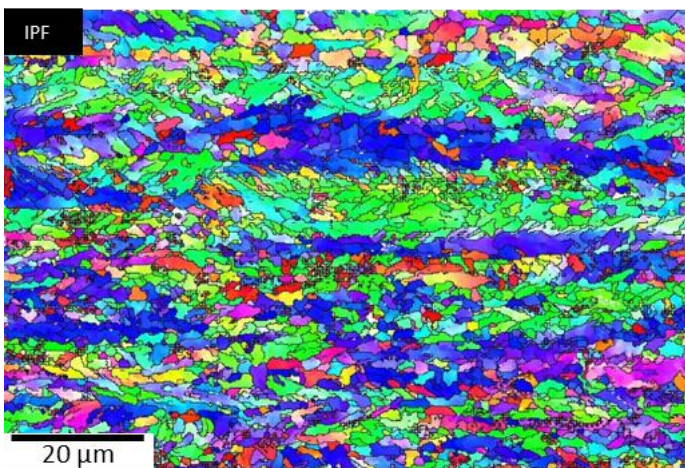
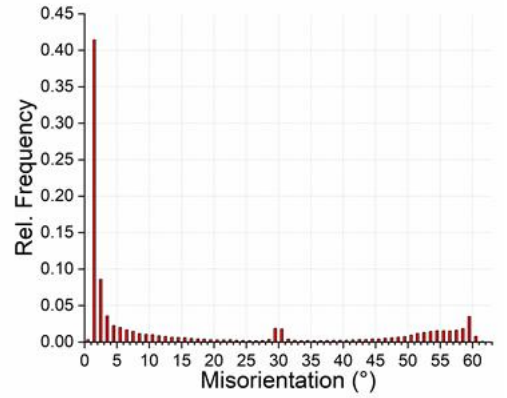
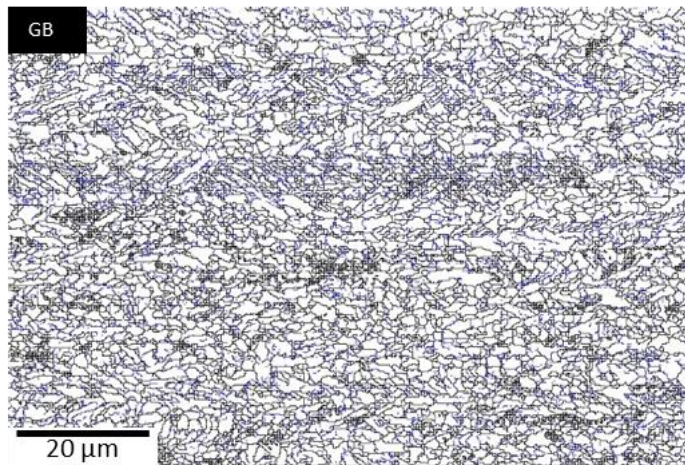
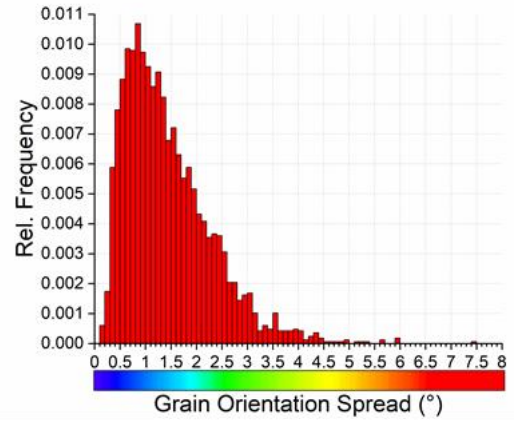
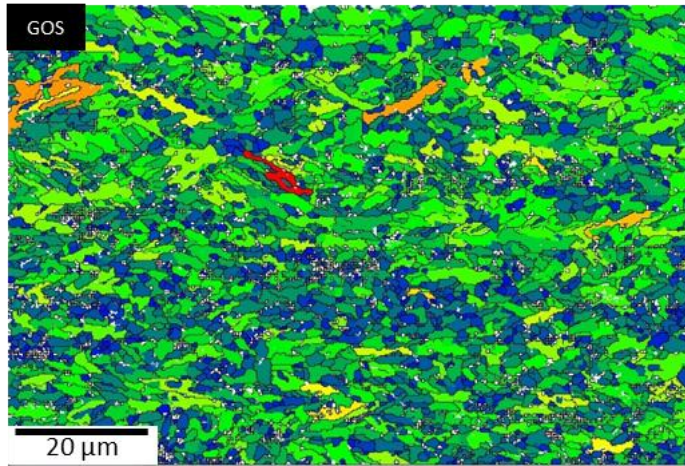


## AII.5 EBSD maps from SC5



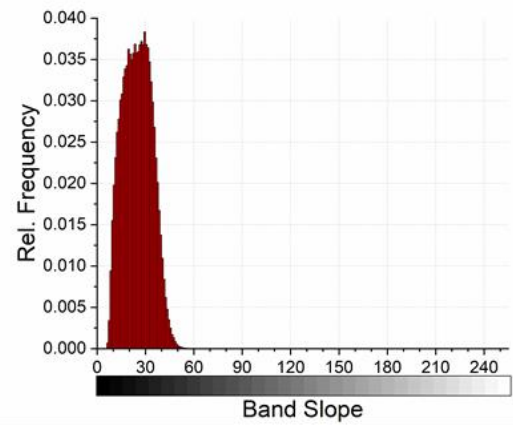
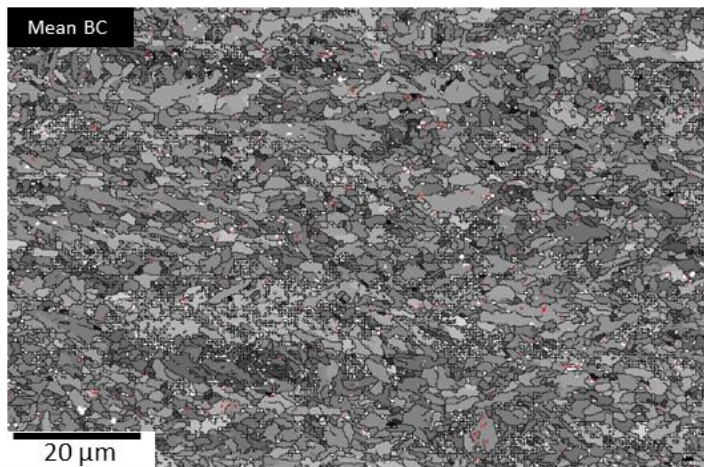
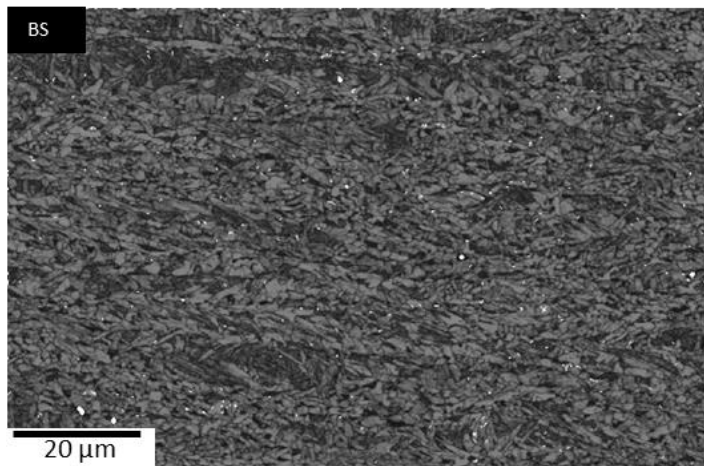
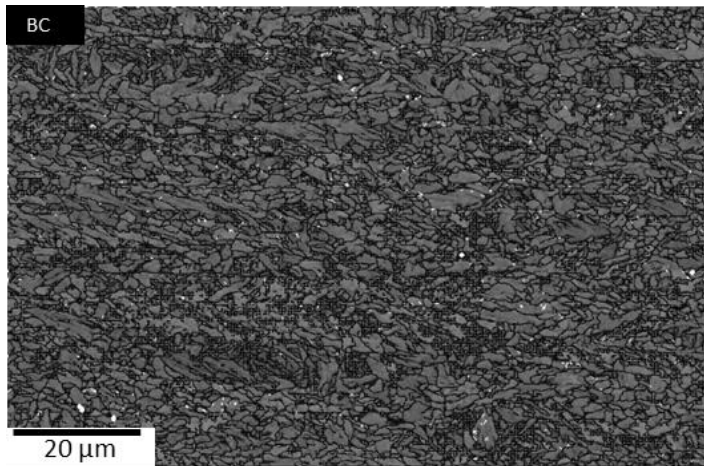


EBSD maps from SC5 (continued)





## AII.6 EBSD maps from Quench after the fourth pass





EBSD maps from Quench after the fourth pass (continued)

